EXPERIMENTAL AND THEORETICAL INVESTIGATION OF A MULTIPHASE REACTION IN A COMPACT HEAT EXCHANGER-REACTOR (HEX REACTOR)

A Dissertation

by

NICHOLAS PAUL NIEDBALSKI

Submitted to the Office of Graduate and Professional Studies of
Texas A&M University
in partial fulfillment of the requirements for the degree of

DOCTOR OF PHILOSOPHY

Chair of Committee,	Debjyoti Banerjee
Committee Members,	Marvin Adams
	Eric Petersen
	Waruna Kulatilaka
Head of Department,	Andreas Polycarpou

August 2017

Major Subject: Mechanical Engineering

ABSTRACT

Heat transfer enhancement research has long been concerned with keeping pace to the rapidly increasing cooling demands of high performance electronics. In addition to requiring the removal of higher heat fluxes as device miniaturization continues, the operating temperature limits remain essentially the same. The rapid removal of large quantities of low quality heat presents a formidable challenge to thermal systems engineers. In such applications, single-phase forced convection thermal management (TM) schemes are no longer adequate. High energy density thermophysical phase change materials, such as the boiling of water, have proven capable of handling high heat fluxes, but suffer the drawback of requiring temperatures that are outside the acceptable range for high-power electronics cooling. Recently, the use of high energy density endothermic chemical reactions as an alternative to thermophysical phase change materials has shown promise. One particularly attractive reaction for thermal management purposes is the endothermic decomposition of ammonium carbamate (AC), due to both its high energy density and comparatively low reaction temperatures that are amenable to electronics cooling.

In this study, we propose to facilitate the development of thermal management systems based on AC (or similar reactions) by a combined experimental and theoretical approach. The objective is to elucidate the combined effect of heat transfer, mass transfer, momentum transfer, and chemical kinetics on the thermal management capabilities of a heat exchanger-chemical reactor (HEX reactor) utilizing an AC-heat transfer fluid slurry. A model to describe the reaction kinetics in the presence of a liquid

solvent, which is presently lacking the literature, is critical to the design and understanding of thermochemical reaction-based TM systems. Further, this model must be rooted in a sound theoretical and empirical basis. Currently, there are no published experimental chemical kinetics data for the decomposition of AC in a heat transfer fluid.

A systematic investigation of the reaction kinetics within the range of temperatures typical for electronics cooling was conducted to obtain real-time calorimetric and species concentration data. Fundamental insights gained from the experimental chemical kinetics study were used to develop a general reaction model framework for AC decomposition in the presence of a solvent. This model serves as the source term in the thermal energy conservation equation, which in turn is required to model and predict HEX reactor performance. The reaction model parameters were estimated from the experimental results using numerical optimization and validated at temperature between 55°C and 70°C, concentrations between 25 g/L an 50 g/L, and particle sizes between 800μm and 100μm. A 1-dimensional, multi-phase HEX reactor model was developed, incorporating the parameterized reaction model and validated against data from the literature.

In this report, we demonstrate the experimental findings and the subsequent model development, comparison to experimental trends, validation, and comparison to published data for HEX reactor thermal performance with AC decomposition. Critical factors of design interest are identified and explored to improve fundamental understanding of the complex thermal, hydrodynamic, and chemical phenomena governing AC HEX reactor performance.

DEDICATION

I dedicate this work to my mother, Lynn Hughes, and father, Robert Niedbalski. Your love, support, and wisdom have made this journey possible.

ACKNOWLEDGEMENTS

I would like to thank Dr. Soumya Patnaik, Dr. Thomas Reitz, and Dr. Larry Byrd at the Air Force Research Laboratory (AFRL) for sponsoring my work at the Thermal Lab in the Aerospace System Directorate, as well as for sponsoring my travel and stipend under the "Co-op" program. I also wish to thank the High Performance Computing Modernization Program (HCMP), who sponsored my research as a National Defense Science and Engineering Graduate (NDSEG) fellow from September 2013 to June 2015. I also wish to thank Doug Johnson, of the University of Dayton Research Institute who providing patient, helpful advice, guidance, ideas, and support toward both my experimental and computational work – I can say with certainty I would not have accomplished anywhere near the amount of experimental work without Doug's mentorship; Dr. Zachary West and Mr. Kris Klingshirn at the Fuels branch of AFRL for allowing me the use of their FTIR analyzer, and Dr. Jamie Ervin. I also thank my advisor, Dr. Debjyoti Banerjee, for his mentorship and guidance during the course of my research. Most importantly, I wish to thank my loving Fiancée, Danielle Dukes, for providing the love, encouragement, and direction that was indispensable in my growth as both a person, a student, and an engineer

There are, of course, many others to whom I am indebted, at both AFRL and Texas A&M University, for making this endeavor possible. Since it is not possible to name everyone here, I wish to extend my greatest thanks to my colleagues at both institutions for their support and advice.

CONTRIBUTORS AND FUNDING SOURCES

This work was supported by a dissertation committee consisting of Professor Debjyoti Banerjee [advisor], Professor Eric Petersen, and Associate Professor Waruna Kulatilaka of the Department of Mechanical Engineering; Professor Marvin Adams of the Department of Nuclear Engineering; and Dr. Soumya Patnaik of the Air Force Research Laboratory, Power and Controls Division, Flight Systems Integration Branch.

This work was funded by the Air Force Research Laboratory (AFRL) under contract number FA8650-12-D-2224, Task Order 1. The student was also supported by the National Defense Science and Engineering Graduate (NDSEG) fellowship from 2013-2015, and the Texas A&M University Department of Mechanical Engineering via graduate research assistanceship in the Spring 2015 semester.

The HEX reactor data used for validation in Chapter VI was provided by AFRL, and was published in 2015 – see references section. All other work conducted for the dissertation was completed by the student independently.

NOMENCLATURE

Abbreviations

AC	Ammonium Carbamate
AFRL	Air Force Research Laboratory
CA	Carbamic Acid
EG	Ethylene Glycol
HCMP	High Performance Computing Modernization Program
MFC	Mass Flow Controller
MFM	Mass Flow Meter
NDSEG	National Defense Science and Engineering Graduate
PCM	Phase Change Material
PG	Propylene Glycol
PHE	Plate Heat Exchanger
RSS	Root Sum Square
TM	Thermal Management
TMS	Thermal Management System

Capital Letters

A	Area (m^2)
A^*	Generic fitting parameter
$\mathbf{A}$	Coefficient matrix
$[Am]$	Amine concentration (mol/L)

B	Generic fitting parameter
$[B]$	Base concentration (mol/L)
Bi	Biot number (dimensionless)
C	Heat capacity (kJ/K)
C^*	Fitting parameter in Eq. (6.43)
D	Diffusion coefficient (mol/m·s)
E	Activation energy (kJ/mol)
F	Objective function
H	Henry's coefficient (mole fraction / mole fraction)
$H_{2,1}$	Henry's coefficient from ref. [30]
ΔH	Enthalpy of reaction (kJ/mol)
I	Specific enthalpy (kJ/kg)
K	Equilibrium Coefficient (dimensionless)
K^*	'Rate coefficient' for state-space approximation of algebraic constraints
L	Length (m)
L_c	Characteristic length scale (m)
Ne	Newton number (dimensionless)
$N_s(t;r_i)$	Integral term defined in Eq. (3.37)
N_{stir}	Agitator speed (s^{-1})

N_{SG}	Critical impeller speed (s^{-1})
P	Pressure (Pa)
Pr	Prandtl number (dimensionless)
M	Molecular weight (kg/mol)
$\dot{Q}$	Heat transfer rate (W)
R	Heater coil sheath radius (m)
$\Re$	Universal gas constant (J/mol·K)
R_o	Heater coil nichrome element radium (m)
Re	Reynolds number (dimensionless)
R_{th}	Thermal resistance (K/W)
S'''	Volumetric thermal energy source term (J/m^3)
Sc	Schmidt number
Sh	Sherwood number
Sh_0	Sherwood number at $Re_s=0$
$[sol]$	Solute concentration in liquid phase (mol/L)
T	Temperature (°C)
$\tilde{T}$	Conditioned batch reactor temperature signal (°C)

U	Superficial velocity (m/s)
V	Volume (m^3)
V_{dead}	Dead volume in absorber (m)
V_{mfc}	Total volume dispensed by mass flow controller (m^3)
$\dot{V}$	Volumetric flow rate (m^3/s)
$\dot{V}_p$	Purge gas flow rate (m^3/s)
We	Weber number (dimensionless)
X	Martinelli Parameter (dimensionless)
Y	Experimental gas-phase mole fraction measurement (dimensionless)
$[Z]$	Zwitterion concentration (mol/L)

Lowercase Letters

a_b'''	Dispersed gas phase area concentration (m^{-1})
a_s'''	Solid phase surface area concentration (m^{-1})
$\mathbf{b}$	Vector of inhomogenous terms in state space form
c	Solid-phase concentration (kg/m^3)

c_p	Specific heat capacity at constant pressure (kJ/kg K)
c_s	Mass density of particles with initial size ranging from r_i to $r_i + \delta r_i$ (dimensionless)
d_b	Bubble diameter (m)
d_h	Hydraulic diameter (m)
d_{stir}	Agitator diameter (m)
f	Particle size distribution function (m^{-1})
g	Gravitational acceleration (m/s^2)
h	Heat transfer coefficient (W/m^2K)
k	Rate coefficient/mass transfer coefficient (variable units)
l	Thickness (m)
$\dot{m}$	Mass flow rate (g/s)
$m^*_{a,abs}$	Apparent mass of NH_3 absorbed (g)
m_{AC}	Initial mass of solid AC (g)
m'''_g	Volumetric mass 'generation' (kg/m^3)
$\dot{n}$	Molar flow rate (mol/s)

$n_s'''(t;r_i)$	Number density of solid phase particles particles with initial size ranging from r_i to $r_i + \delta r_i$ (dimensionless) (m^{-4})
p	Agitator power input (W)
q''	Heat flux (W/m^2)
q'	Channel width averaged heat flux (W/m)
r	Radius (m)
Δr	Radial finite volume increment (m)
$\dot{r}$	Dimensionless reaction/species transfer rate (s^{-1})
Δs	Entropy change (kJ/kg K)
t	Time (s)
t_e	Surface renewal timescale (s)
t_{res}	Residence time (s)
u	Velocity (m/s)
u_s	Settling velocity (m/s)
u_t	Terminal velocity of single bubble (m/s)
u'	Turbulent fluctuating velocity magnitude (m/s)

u'_{min}	Minimum fluctuating velocity required to achieve suspension of solid particles in batch reactor
x	Mole fraction in liquid phase (based on solvent) (dimensionless)
$\tilde{x}$	Surface concentration in terms of solvent mole fraction (dimensionless)
Δx	Concentration gradient of dissolved species in liquid phase (dimensionless)
v	Voltage (V)
w	Weighting factor in objective function (dimensionless)
y^*	Gas inlet concentration for the model in Figure 10
y	Gas-phase mole fraction (based on total moles of gas)
z	Length coordinate (m)

Subscripts

AC	Ammonium carbamate
a	Ammonia
atm	At atmospheric conditions
c	Carbon dioxide

des	Gas desorption
dis	Solid dissolution
eff	Effective value
F	Friction
f	Forward reaction
g	Bulk gas phase
h	Heater coil
het	Heterogeneous reaction
hom	Homogeneous reaction
i	Initial (at $t = 0$)
in	At inlet
j	Generic species index
L	Load-side of HEX reactor
l	Liquid-phase of batch reactor
lm	Logarithmic mean
loss	Losses to environment
obs	Observed/apparent
out	At outer surface
phys	Physical process (e.g., dissolution)
purge	Purge gas
R	Reactant-side of HEX reactor
rxn	Due to reaction

s	Solid-phase
sat	At saturation condition
surf	At surface
tot	Total
TP	Two-phase
SP	Single-phase
w	Wall

Superscripts

b	Bubble/dispersed gas phase
g	Bulk gas phase
l	Bulk liquid phase
$l-b$	Bulk-liquid-dispersed gas interface
$l-g$	Bulk-liquid – bulk gas interface
$l-s$	Bulk-liquid-dispersed solid interface
p	Particle
s	Dispersed solid phase
T	Transpose operator

Greek

Φ_{TP}	Two-phase multiplier (dimensionless)
χ	Mass quality (dimensionless)
α	Thermal diffusivity (m^2/s)
α_m	Mass diffusivity (m^2/s)

β	Void fraction (dimensionless)
$\overline{\beta}$	Channel length-averaged void fraction (dimensionless)
ε	"Balance" parameter $\dot{Q}_{rxn} / \dot{Q}_L$
ε_{ss}	Minimum energy required to achieve suspension (W/m^3)
γ	Supersaturation parameter defined in Eq. (41) (dimensionless)
η	Conversion efficiency $\dot{Q}_{rxn} / \dot{m}_{AC} \Delta H$
$\boldsymbol{\theta}$	Model parameter vector
κ	Thermal conductivity (W/m K)
λ	Darcy friction factor (dimensionless)
ρ	Mass density (kg/m^3)
$\overline{\rho}$	Molar density (mol/m^3)
δ	Film thickness (m)
δ_e	Effective approach distance in Eq. (3.10) (m)
φ_v	Solid phase volume fraction (dimensionless)
μ	Dynamic viscosity (Pa·s)
σ	Surface tension (N/m)

$\boldsymbol{\sigma}$	Cauchy stress tensor (N/m^2)
Ω	Parameter defined as $2P_{eq}M_l / 3\Re T\rho_l$
τ	Time constant (s)

TABLE OF CONTENTS

Page

ABSTRACT ii

DEDICATION iv

ACKNOWLEDGEMENTS v

CONTRIBUTORS AND FUNDING SOURCES vi

NOMENCLATURE vii

TABLE OF CONTENTS xviii

LIST OF FIGURES xxii

LIST OF TABLES xxxv

CHAPTER I INTRODUCTION 1

CHAPTER II EXPERIMENTAL INVESTIGATION 7

2.1 Solubility Study 7
2.1.1 Experimental Design 8
2.1.2 Uncertainty Analysis 11
2.1.2 Results and Analysis 12
2.2 Kinetics Study 19
2.2.1 Experimental Design 19
2.2.2 Uncertainty Analysis 22
2.2.3 Reactor Characterization 24
2.2.4 Results 34
2.2.4.1 Estimation of Dissolved Ammonia Concentration 36
2.2.4.2 Effect of AC Concentration 37
2.2.4.3 Effect of Particle Size 40
2.2.4.4 Effect of Temperature 42
2.2.4.5 Discussion 44

CHAPTER III REACTION RATE MODELING 53

3.1 Mathematical Formulation 55
3.1.1 Solid-Phase Dissolution 58
3.1.1.1 Solid-Liquid Mass Transfer Coefficient 59
3.1.1.2 Diffusion Coefficients of Dissolved Species 66
3.1.2 Heterogeneous Decomposition 70
3.1.2.1 Implementation of the Heterogeneous Reaction Model 73
3.2.2.2 Particle Surface Concentration 78
3.1.3 Homogeneous Decomposition 83
3.1.3.1 Homogeneous Reaction Kinetics with Water as the Solvent 84
3.1.3.2 Selection of a Model for Homogeneous Decomposition in PG 88
3.1.4 Gas Desorption 90
3.1.4.1 General Considerations 90
3.1.4.2 CO_2 Desorption 92
3.1.4.3 NH_3 Desorption 95

CHAPTER IV KINETIC PARAMETER ESTIMATION 101

4.1 Parameter Estimation Methodology 101
4.2 Parameter Estimation Results 105
4.2.1 Mass Transfer-Limited Homogeneous Reaction 108
4.3 Qualitative Model Behavior and Comparison to Experiment 122
4.3.1 Qualitative Trends in Model Predictions 127
4.3.2 Comparison to Experimental Results 133
4.4 Sensitivity Analysis 142
4.4.1 Heterogeneous Parameters 143
4.4.2 Homogeneous Parameters 157

CHAPTER V THERMAL PARAMETER ESTIMATION 162

5.1 Heat of Solution of NH_3 163
5.2 Calorimeter Model 168
5.2.1 Heater Model 168
5.2.1.1 Mathematical Model 169
5.2.1.2 Thermophysical Parameter Estimation 173
5.2.3 Reactor Wall Model 176
5.2.4 Liquid-Phase Thermal Model and Sub-Model Integration 179
5.2.4.1 Thermochemical Energy Balance 185
5.2.4.2 Sensible Energy Storage in the Solid-Phase 187
5.2.4.3 Solution Method 191
5.2.4.4 Endothermic Heat Absorption Estimation 193
5.3 Calorimetric Results and Discussion 198
5.3.1 Wall Heat Transfer and Heater Coil Dynamics 198
5.3.2 Thermal Parameter Estimation Results 200

5.3.2.1 Heterogeneous Reaction 201
5.3.2.2 Homogeneous Reaction 203
5.3.2.3 Comparison to Experiment 203
5.3.2.4 Analysis 210

CHAPTER VI HEX REACTOR MODEL 214

6.1 Mathematical Model 216
6.1.1 Governing Equations 219
6.1.1.1 Conservation of Mass 220
6.1.1.2 Conservation of Species 223
6.1.1.3 Conservation of Momentum 228
6.1.1.4 Conservation of Energy 231
6.1.2 Correlations and Physical Properties 235
6.1.2.1 Mass Transfer Parameters 237
6.1.2.2 Thermal-Hydraulic Parameters 239
6.1.3 Numerical Methodology 249
6.2 Model Predictions and Comparison to Experiment 253
6.2.1 Single-Phase Validation 253
6.2.2 Low Residence Time Validation 259
6.2.3 High Residence Time Validation 262
6.2.4 Discussion 265
6.2.4.1 Low Residence Time 265
6.2.4.2 High Residence Time 268
6.2.4.3 Axial Heat Flux/Absorption Profiles 275
6.3 Parametric Analysis 288
6.3.1 Load-Side Inlet Temperature 289
6.3.2 Reactant-Side Inlet Temperature 290
6.3.3 Solid AC Concentration 295
6.3.4 Particle Size 306
6.3.5 Residence Time 312
6.4 Optimization 314
6.4.1 Assumptions 316
6.4.2 Results and Discussion 317

CHAPTER VII CONCLUSIONS AND RECOMMENDATIONS 321

7.1 NH_3 Sequestration 326
7.2 Residence Time and Heat Transfer Intensification 328
7.3 Improvements to Model Fidelity 331
7.4 Parameter Space Mapping and Uncertainty Quantification 333

REFERENCES 336

APPENDIX 350

A.1 Single-Phase Characterization 350
A.1.1 Load-side heat transfer characterization 352
A.1.2 Reactant-side heat transfer characterization 359
A.1.3 Uncertainty Analysis 361
A.2 Batch Reactor Model Parameter Estimates 366
A.2.1 Mass Transfer and Solubility Parameters 366
A.2.2 Kinetic Parameters 367
A.3 Experimental Comparisons 368
A.3.1 Low Residence Time (10 s) 368
A.3.2 High Residence Time (70 s) 368

LIST OF FIGURES

Page

Figure 1. Sectional view of absorption vessel showing absorption tube, circulation jacket, and sparging tube 10

Figure 2. Schematic of NH_3 absorption experiment 10

Figure 3. Comparison of Eq. (2.12) predictions (dashed line) to experimental measurements (solid line) in a dry absorption tube initially filled with air 16

Figure 4. Comparison of experimental NH_3 solubility measurements (black squares) and correlation predictions (blue line); also plotted on the right axis is the solubility of CO_2 in propylene glycol (red line), calculated from the data of Galvao and Francesoni [30] 18

Figure 5. Solid model of the reaction vessel, lid assembly, agitator drive, and dosing port assembly..... 20

Figure 6. PID diagram of experiment to measure effect of tubing and vacuum pump on a continuous gas sample of known concentration history 24

Figure 7. Gas-phase mass fraction of CO_2 fed into effluent gas sample system (dashed) compared to FTIR readings (solid) for input CO_2 concentrations of 5% (a, top) and 20% (b, bottom)..... 26

Figure 8. PID diagram of experiment to test effect of reactor headspace on a continuous gas sample of known concentration history 27

Figure 9. Gas-phase mass fraction of CO_2 fed into reactor headspace (dashed) compared to FTIR readings (solid) for input CO_2 concentrations of 5% (a, top) and 20% (b, bottom)..... 29

Figure 10. Simplified representation of reactor headspace. $\dot{V}_j$ signifies the volumetric flow rate of a gas source *j*, where *j* = *a* for NH_3, *c* for CO_2, and *p* for the purge gas (N_2). $\dot{V}_{tot}$ signifies the total volumetric flow rate of the effluent gas stream 30

Figure 11. Comparison of CO_2 gas-phase mole fractions read by FTIR (solid) and predicted by Eq. (2.20) (dashed) utilizing a rate

constant of 0.16 s^{-1} for input mass fractions of 5% (a, top) and 20% (b, bottom) 33

Figure 12. CO_2 (solid) and NH_3 (dashed) mole fraction history. Reaction temperature was 70°C, AC concentration was 37.5 g/L, and particle size range was -20 +30 mesh. 35

Figure 13. CO_2 (a, top) and NH_3 gas-phase mole fraction histories for initial AC solids concentration of 25 g/L (solid), 37.5 g/L (dashed) and 50 g/L (dot). Reaction temperature was 70°C and the particle size was in the -30 + 40 mesh range 39

Figure 14. CO_2 (a, top) and NH_3 (b, bottom) gas-phase mole fraction histories for particle size ranges -20 +30 (black), -30 +40 (blue), -40 +50 (red), -50 +60 (green). Reaction temperature was 70°C and concentration was 37.5 g/L 41

Figure 15. CO_2 (a, top) and NH_3 (b, bottom) gas-phase mole fraction histories at different temperatures: 55°C (black), 60°C (blue), 65°C (red) and 70°C (green). AC concentration was 37.5 g/L and particle size range was -30 +40 mesh 43

Figure 16. Dissolved NH_3 mass fraction content at different temperatures: 55°C (black), 60°C (blue), 65°C (red) and 70°C (green). AC concentration was 37.5 g/L and particle size range was -30 +40 mesh 46

Figure 17. CO_2 gas-phase mole fraction, y_c (solid black) compared to the time derivative of NH_3 the gas-phase mole fraction, y_a (dashed red) at a reaction temperature of 70°C, concentration of 37.5 g/L, and particle size range -20 + 30 mesh 48

Figure 18. Schematic of reaction pathways in proposed model for decomposition of AC in PG 56

Figure 19. Estimates of D_a (blue line) and D_c (black line) as obtained with Eq. (3.18); $D_{a,H2O}$ and $D_{c,H2O}$ were obtained from Frank *et al* .[49] and Cadogan *et al.* [48], respectively. In the case of D_a, the data for an NH_3 mole fraction of 20% 68

Figure 20. Diffusion coefficient D_a of NH_3 in PG at different NH_3 mole fractions: 0 (black line), 0.1 (blue line), and 0.2 (red line). D_a estimated with Eq. (3.18) and using Frank *et al.*'s results [49]. 69

Figure 21. Functional breakdown/dataflow diagram of parameter estimation workflow 105

Figure 22. Plot of homogeneous equilibrium coefficient K_{hom} as a function of assumed quiescent desorption coefficient $k_a^{l\text{-}g}$ 110

Figure 23. Plot of estimated homogeneous reaction equilibrium coefficient as function of temperature for three different experimental datasets: m_{AC} = 20g (black diamonds), 30g (blue squares), 40g (red triangles). The "high" and "low" estimates, assuming an Arrhenius dependence on temperature, are plotted as black dotted lines 112

Figure 24. Estimated $k_{f,hom}$ as a function of temperature for m_{AC} = 20g (black diamonds), 30g (blue squares), and 40g (red triangles) for reaction temperatures of 55°C, 60°C, and 70°C. 114

Figure 25. Estimates for effective heterogeneous equilibrium coefficient K_{het} as a function of temperature for three different experimental datasets: m_{AC} = 20g (black diamonds), 30g (blue squares), 40g (red triangles) 115

Figure 26. Solid-liquid desorption coefficient k_{het} estimates as a function of temperature for three different experimental datasets: m_{AC} = 20g (black diamonds), 30g (blue squares), 40g (red triangles) 117

Figure 27. Comparison of k_{het} calculated by Eq. (3.12) for different particle sizes vs. Simulink estimated k_{het}; from Eq. (3.12): 20 mesh (black line), 40 mesh (blue line), 60 mesh (red line) with m_{AC} = 40g for each case; Simulink estimates: m_{AC} = 20g (diamonds), m_{AC} = 30g (triangles), and m_{AC} = 40g (squares). 119

Figure 28. Solid-liquid dissolution coefficient k_{dis} estimates as a function of temperature for three different experimental datasets: m_{AC} = 20g (black diamonds), 30g (blue squares), 40g (red triangles) 119

Figure 29. Logarithmic plot of k_{het} (solid shapes), k_{dis} (hollow shapes), and predictions of Eq. (3.12) (black line) over various temperatures. Simulink-estimated values are marked according to m_{AC} (20g – diamond, 30g – triangle, 40g – square). A value of d_p = 850μm was used in Eq. (3.12). The lines drawn through the markers are to guide the eye 120

Figure 30. Solubility fraction of AC in PG, $x_{AC,sat}$, estimates as a function of temperature for three different experimental datasets: m_{AC} = 20g (black diamonds), 30g (blue squares), 40g (red triangles) 121

Figure 31. Model predictions for homogeneous forward (red curve, left axis) and reverse (blue curve, left axis); gas-phase molar concentration of CO2 yc (black curve, right axis) as functions of time for reaction conditions mAC = 40g, T = 60°C, and initial particle size between 40 and 50 mesh.....124

Figure 32. Model predictions of total gas release rates of CO_2 (red curve) and NH_3 (blue curve), as well as net homogeneous reaction rate (black curve) as functions of time for reaction conditions m_{AC} = 40g, T = 60°C, and initial particle size between 40 and 50 mesh. 125

Figure 33. Model predictions of dimensionless dissolved CO_2 (black curve, right axis) and NH_3 (blue curve, left axis) as a function of time for reaction conditions m_{AC} = 40g, T = 60°C, and initial particle size between 40 and 50 mesh.....126

Figure 34. Comparison of model predictions for gas-phase CO_2 (top) and NH_3 (bottom) mole fraction histories over various mesh sizes for reaction temperature of 70°C and m_{AC} = 30g: 20-30 mesh (black), 30-40 mesh (blue), 40-50 mesh (red) and 70-80 mesh (green).....128

Figure 35. Comparison of model predictions for gas-phase CO_2 (top) and NH_3 (bottom) mole fraction histories for m_{AC} = 30g and particle size range of 40-50 mesh at different temperatures: 55°C (black), 60°C (blue) and 70°C (red). 130

Figure 36. Comparison of model predictions for gas-phase CO_2 (top) and NH_3 (bottom) mole fraction histories for particle size range 30-40 mesh and reaction temperature of 60°C over different initial AC mass loadings; m_{AC} = 20g (black), 30g (blue) and 40g (red). 132

Figure 37. Comparison of experiment (red curve) and model predictions (black curve) for CO_2 (top plot) and NH_3 (bottom plot) gas-phase mole fractions. Reaction conditions were m_{AC} = 40g, T = 55°C, and initial particle size between 40 and 50 mesh. 134

Figure 38. Model predictions for heterogeneous decomposition rate (red curve, right axis), homogeneous decomposition rate (black curve, left axis), and AC dissolution rate (blue curve, right

axis). Reaction conditions were m_{AC} = 40g, T = 55°C, and initial particle size between 40 and 50 mesh.....136

Figure 39. Comparison of experiment (red curve) and model predictions (black curve) for CO_2 (top plot) and NH_3 (bottom plot) gas-phase mole fractions. Reaction conditions were m_{AC} = 40g, T = 60°C, and initial particle size between 40 and 50 mesh. 137

Figure 40. Comparison of experiment (red curve) and model predictions (black curve) for CO_2 (top plot) and NH_3 (bottom plot) gas-phase mole fractions. Reaction conditions were m_{AC} = 40g, T = 70°C, and initial particle size between 40 and 50 mesh. 139

Figure 41. Comparison of experiment (red curve) and model predictions (black curve) for CO_2 (top plot) and NH_3 (bottom plot) gas-phase mole fractions. Reaction conditions were m_{AC} = 40g, T = 70°C, and initial particle size between 60 and 100 mesh. 141

Figure 42. CO_2 (y_c, top) and NH_3 (y_a, bottom) gas-phase concentration histories at different values of k_{het} (baseline – black, x2 – red, x0.5 – blue) with m_{AC} = 40g, T_l= 70°C, and initial particle size range of -40 +50 mesh. 144

Figure 43. Model predictions for heterogeneous reaction rate (solid) and homogeneous reaction rate (dashed) at different k_{het} (x1-black, x2 – red, x0.5 – blue) with m_{AC} = 40g, T = 70°C, and initial particle size range of -40 +50 mesh.....146

Figure 44. Model predictions for CO_2 (y_c, top) and NH_3 (y_a, bottom) gas-phase concentration histories at different values of K_{het} (baseline – black, x2 – red, x0.5 – blue) with m_{AC} = 40g, T_l= 70°C, and initial particle size range of -40 +50 mesh.....148

Figure 45. Comparison of model predictions for CO_2 (y_c,) gas-phase concentration histories in response to perturbations in k_{het} (dashed) and K_{het} (solid) (baseline – black, x2 – red, x0.5 – blue) with m_{AC} = 40g, T_l= 60°C, and initial particle size range of -40 +50 mesh. 150

Figure 46. Model predictions of CO_2 (y_c, top) and NH_3 (y_a, bottom) gas-phase concentration histories at different values of $x_{AC,sat}$ (baseline – black, x2 – red, x0.5 – blue) with m_{AC} = 40g, T_l= 70°C, and initial particle size range of -40 +50 mesh. 152

Figure 47. Model predictions of CO_2 (y_c, top) and NH_3 (y_a, bottom) gas-phase concentration histories at different values of k_{dis} (baseline – black, x2 – red, x0.5 – blue) with m_{AC} = 40g, T_l= 70°C, and initial particle size range of -40 +50 mesh.....153

Figure 48. Comparison of model predictions for dissolution rate in response to perturbations in $x_{AC,sat}$ (solid) and k_{dis} (dashed) - baseline – black, x2 – red, x0.5 – blue. Reaction conditions were m_{AC} = 40g, T_l = 70°C, and initial particle size range of -40 +50 mesh.....155

Figure 49. Model predictions of CO_2 (y_c, top) and NH_3 (y_a, bottom) gas-phase concentration histories at different values of $k_{f,hom}$ (baseline – black, x2 – red, x0.5 – blue) with m_{AC} = 40g, T_l= 70°C, and initial particle size range of -40 +50 mesh. 158

Figure 50. Model predictions of CO_2 (y_c, top) and NH_3 (y_a, bottom) gas-phase concentration histories at different values of K_{hom} (baseline – black, x2 – red, x0.5 – blue) with m_{AC} = 40g, T_l= 70°C, and initial particle size range of -40 +50 mesh. 159

Figure 51. Model predictions for dissolved CO_2 (x_c – dashed lines) and NH_3 (x_a – solid lines) concentration subjected to perturbations of K_{hom} : baseline – black, x2 – red, and x0.5 – blue; input parameters were m_{AC} = 40g, T_l = 70°C, and particles size range was -40 +50 mesh. 160

Figure 52. Plot of ln (x_a) as a function of 1/T as obtained from the solubility studies (black squares), and a least-squares linear regression to the same (dashed line). Linearity over the 50 °C-80°C temperature range suggests that the heat of desorption for NH_3 is not a strong function of temperature.....164

Figure 53. Plot of ln (x_a) as a function of T as obtained from the solubility study data (black squares) and a least-squares linear regression to the same (dashed line). 164

Figure 54. Simplified layout diagram of NH_3 desorption test apparatus 166

Figure 55. Domain for heater coil mathematical model; the Nichrome resistive element is represented by the region from the center to $r = R_o$; the MgO insulation is represented from $r = R_o$ to $r = R$. The presence of the stainless steel sheath was neglected 169

Figure 56. Plot of normalized temperature (T - T_{min}) / (T_{max} – T_{min}) vs. normalized time t / t_{max} for heater inputs of 50W (solid), 100W (dashed), and 500W (dot). 174

Figure 57. Comparison of normalized heater surface temperature measurements (T - T_{min}) / (T_{max} – T_{min}) to model predictions using parametrically optimized α_h and k_h values at two different heater settings: 50W (solid: experiment, dot: model) and 700W (dashed: experiment, short dash: model) 176

Figure 58. Domain for mathematical model of reactor wall 177

Figure 59. Diagram representing the model's three domains (reactor wall, liquid-phase, and heater coil) and the assumed direction of heat flow. 180

Figure 60. Plot comparing temperature ratio $(T - T_i) / (T_i - T_f)$ measured experimentally (red) and predicted by the model (black) as a function of time. Two cases are shown: heating to 55°C (solid) and heating to 70°C (dashed). 185

Figure 61. Simulink block diagram of batch reactor model with reaction rate, thermochemistry, and energy balance sub modules. The 'Liquid-phase energy balance' block contains the state-space models for the heater and reactor wall. 192

Figure 62. Simplified illustration of Simulink block diagram used to calculate experimental endothermic heat absorption. 196

Figure 63. Conditioned temperature data obtained using 1st – order filter with a time constant of 2 seconds (red) and 20th – order polynomial fit (blue); the actual T_l data is also depicted (black). 196

Figure 64. Calculated endothermic heat absorption obtained using 1st – order filter with a time constant of 2 seconds (red) and 20th – order polynomial fit (blue) 197

Figure 65. Plot of model-calculated heat flow from heater surface (black) and wetted reactor wall (red) compared to experimental heater input (blue). The positive direction of heat flow is defined in Figure 59. Source of the experimental data was the test m_{AC} = 40g, T = 70°C, 40 – 50 mesh particle size 199

Figure 66. Born-Haber Cycle for decomposition of solid AC suspended in PG 202

Figure 67. Comparison of temperature histories measured experimentally (black) and predicted by the model (red) for m_{AC} = 40g, T = 70°C, 40 – 50 mesh particles 205

Figure 68. Comparison of heat absorbed by the reaction calculated using calorimetric calculations (black) and predicted by the model (red) for m_{AC} = 40g, T = 70°C, 40 – 50 mesh particles 205

Figure 69. Comparison of temperature histories measured experimentally (black) and predicted by the model (red) for m_{AC} = 30g, T = 70°C, 50 – 60 mesh particles 206

Figure 70. Comparison of heat absorbed by the reaction calculated using calorimetric calculations (black) and predicted by the model (red) for m_{AC} = 30g, T = 70°C, 50 – 60 mesh particles 206

Figure 71. Comparison of temperature histories measured experimentally (black) and predicted by the model (red) for m_{AC} = 30g, T = 60°C, 40 – 50 mesh particles 208

Figure 72. Comparison of heat absorbed by the reaction calculated using calorimetric calculations (black) and predicted by the model (red) for m_{AC} = 40g, T = 60°C, 40 – 50 mesh particles 208

Figure 73. Comparison of temperature histories measured experimentally (black) and predicted by the model (red) for m_{AC} = 30g, T = 55°C, 40 – 50 mesh particles 209

Figure 74. Comparison of heat absorbed by the reaction calculated using calorimetric calculations (black) and predicted by the model (red) for m_{AC} = 30g, T = 55°C, 40 – 50 mesh particles 209

Figure 75. Heat absorption predicted by model for heterogeneous decomposition (red), dissolution (black), and homogeneous decomposition (blue) for m_{AC} = 40g, T = 70°C, 40 – 50 mesh particle size 210

Figure 76. – Heat absorption by homogeneous decomposition as a function of time at different temperatures: T = 70°C (blue), 60°C (red), and 55°C (black). In all three cases, m_{AC} = 40g with 40 – 50 mesh particle size 212

Figure 77. Fraction of heat absorbed by homogeneous decomposition relative to total heat absorbed as a function of time at different

temperatures: T = 70°C (blue), 60°C (red), and 55°C (black). In all three cases, m_{AC} = 40g with 40 – 50 mesh particle size.....212

Figure 78. Heat absorption due to NH_3 desorption into CO_2 bubbles as a function of time at different temperature: T = 70°C (blue), 60°C (red), and 55°C (black). In all three cases, m_{AC} = 40g with 40 – 50 mesh particle size.....213

Figure 79. Diagram depicting pair of reactant and load channels; the long dashed lines represent symmetry adiabats; the vector g is in the direction of gravity. The white particles represent the gas-phase; green particles represent the solid-phase 216

Figure 80. Plot of Eq. (6.47) (solid line) and Eq. (6.48) (dashed line) as a function of Reynolds number in single phase flow. 243

Figure 81. AFRL's Alfa Laval HEX reactor as configured for single-phase heat transfer characterization.....255

Figure 82. Heat absorbed by endothermic reaction as a function of solid AC concentration predicted by model (black squares) and from Johnson *et al.* 's 10 second residence time experiments [70] (red triangles). Particle size was between 420μm and 250μm (40-60 mesh).....261

Figure 83. Load-side heat rejection as a function of solid AC concentration predicted by model (black squares) and from Johnson *et al.*'s 10 second residence time experiments [70] (red triangles). Particle size was between 420μm and 250μm (40-60 mesh).....261

Figure 84. Heat absorbed by endothermic reaction as a function of solid AC concentration predicted by model (black) and from Johnson *et al.*'s 70 second residence time experiments [70] (red); load-side inlet temperature was 70°C (triangle), 80°C (square), and 90°C (circle); particle size was between 420μm and 250μm (40-60 mesh).....263

Figure 85. Load-side heat rejection as a function of solid AC concentration predicted by model (black) and from Johnson *et al.*'s 70 second residence time experiments [70] (red); load-side inlet temperature was 70°C (triangle), 80°C (square), and 90°C (circle); particle size was between 420μm and 250μm (40-60 mesh).....263

Figure 86. Estimated average void fraction as a function of solid AC concentration predicted by model (black) and from Johnson *et al.*'s 70 second residence time experiments [70] (red); load-side inlet temperature was 70°C (triangle), 80°C (square), and 90°C (circle); particle size was between 420μm and 250μm (40-60 mesh).....264

Figure 87. Axial gas-phase mass flux (j_g – dashed line) and dimensionless solid-phase concentration (c/c_i – solid line) simulated for different 10 second residence time tests: c_i = 22 (black), 32 (blue), and 50 (red) g/L.....266

Figure 88. Axial gas-phase mass flux (j_g – dashed line) and dimensionless solid-phase concentration (c/c_i – solid line) simulated for different 70 second residence time tests: c_i = 85 (black), 169 (blue), and 211 (red) g/L.....270

Figure 89. Sensitivity of predicted Q_L (black) and Q_{rxn} (blue) as a function k_{dis} . k_{dis}* is the nominal value of k_{dis} for the experiment c_i = 211 g/L, t_{res} = 70 s; Q* is the model-predicted value of Q_L or Q_{rxn} corresponding to k_{dis}*. 272

Figure 90. Sensitivity of predicted Q_L (black) and Q_{rxn} (blue) as a function k_{het} . k_{het}* is the nominal value of k_{het} for the experiment c_i = 211 g/L, t_{res} = 70 s; Q* is the model-predicted value of Q_L or Q_{rxn} corresponding to k_{het}*. 272

Figure 91. Average void fraction predicted by model for the 70 second residence time case as a function of assumed C^* in Eq. (6.43); c_i = 169 g/L and $T_{L,in}$ = 80°C.....274

Figure 92. x_c as a function of z/L for assumed values of C^* in Eq. (6.43): 0.001 1/s (black), 0.1 1/s (blue) and 1.0 1/s (red); the dashed black line indicates local $x_{c,sat}$. All other simulation conditions were for a 70 second residence time test with c_i = 169 g/L and $T_{L,in}$ = 80°C. 275

Figure 93. Local heat flux per-unit-length-per-channel for c_i = 50 g/L, $T_{L,in}$ = 80°C, $T_{R,in}$ = 50°C, t_{res} = 10 s; contribution of load-side rejection (blue solid line) and reaction (blue dashed line) compared to load-side rejection of single-phase case with identical inlet conditions (solid black line).....277

Figure 94. Local fraction of heat absorbed by reaction to heat rejected by load-side for c_i = 50 g/L, $T_{L,in}$ = 80°C, $T_{R,in}$ = 50°C, t_{res} = 10 s 278

Figure 95. Local heat flux per-unit-length per channel due to dissolution (black), heterogeneous decomposition (blue) and homogeneous decomposition (red) for c_i = 50 g/L, $T_{L,in}$ = 80°C, $T_{R,in}$ = 50°C, t_{res} = 10 s. 279

Figure 96. Local reactant-side temperature for c_i = 50 g/L, $T_{L,in}$ = 80°C, $T_{R,in}$ = 50°C, t_{res} = 10 s (red) and corresponding single-phase case (black) 281

Figure 97. Local load-side heat rejection (solid blue: with reaction, solid black: single-phase baseline) and heat absorption by reaction (dashed blue) for for c_i = 211 g/L, $T_{L,in}$ = 80°C, $T_{R,in}$ = 50°C, t_{res} = 70 s.....283

Figure 98. Local fraction of heat absorbed by reaction to heat rejected by load-side for c_i = 211 g/L, $T_{L,in}$ = 80°C, $T_{R,in}$ = 50°C, t_{res} = 70 s 284

Figure 99. Local heat flux per-unit-length per channel due to dissolution (blue), heterogeneous decomposition (black) and homogeneous decomposition (red) for c_i = 211 g/L, $T_{L,in}$ = 80°C, $T_{R,in}$ = 50°C, t_{res} = 70 s 285

Figure 100. Local reactant-side temperature for c_i = 211 g/L, $T_{L,in}$ = 80°C, $T_{R,in}$ = 50°C, t_{res} = 70 s (solid black) and corresponding single-phase case (solid blue) compared to the case c_i = 50 g/L, $T_{L,in}$ = 80°C, $T_{R,in}$ = 50°C, t_{res} = 10 s (dashed black) 286

Figure 101. Total load-side heat rejection (black), conversion (red) and balance (blue) as a function for reactant-side inlet temperature; all other parameters were fixed according to Table 11.....291

Figure 102. Local heat absorption due to homogeneous decomposition (dashed) and combined heterogeneous and dissolution mechanisms (solid) at various $T_{R,in}$: 50°C (black), 60°C (blue), 70°C (red) and 80°C (green).....293

Figure 103. Dimensionless reactant-side temperature profiles at different $T_{R,in}$: 50°C (black), 70°C (blue), and 80°C (red). Negative values of T^* indicate a heat transfer-limited condition 294

Figure 104. Local heat absorption rate due to reaction/dissolution in an "infinite length" reactor for different solid AC concentrations: 20 g/L (black), 50 g/L (blue), and 100 g/L (red) 296

Figure 105. Local dissolved AC mole fraction x_{AC} for "infinite length reactor" at different solid AC concentrations: 20 g/L (black), 50 g/L (blue), and 100 g/L (red) 299

Figure 106. Local dissolved NH_3 mole fraction x_a for "infinite length reactor" at different solid AC concentrations: 20 g/L (black), 50 g/L (blue), and 100 g/L (red) 299

Figure 107. Total load-side heat rejection (black), conversion (red) and balance (blue) as a function of solid AC concentration; all other parameters were fixed according to Table 12 300

Figure 108. Local heat flux (solid line) and heat absorption (dashed line) at various solid AC concentrations: 20 g/L (black), 40 g/L (blue), 100 g/L (red), and 200 g/L (green) 301

Figure 109. Local heat absorption by homogeneous reaction (solid black line), all processes combined (dashed black line), and load-side heat rejection for t_{res} = 70 seconds and c_i = 200 g/L. All other parameters are as listed in Table 13 303

Figure 110. Total load-side heat rejection (black), conversion (red) and balance (blue) as a function of solid AC concentration; all other parameters were fixed according to Table 6.7, but with residence time set to 70 seconds 305

Figure 111. Total load-side heat rejection (black), conversion (blue), and balance (red) as a function of mean mesh size; all simulations used the fixed parameters listed in Table 14 308

Figure 112. Local heat absorption rate due to reaction/dissolution (solid lines) and solid-phase concentration ratio c/c_i at different mean particle sizes: 20 - 30 mesh (black), 40 - 50 mesh (blue), and 90 - 100 mesh (red) 309

Figure 113. Local heat absorption rate due to homogeneous decomposition (solid lines) and due to combined heterogeneous reaction and dissolution (dashed lines) at different particle sizes: 20 - 30 mesh (black), 40 - 50 mesh (blue), and 90 - 100 mesh (red) 309

Figure 114. Total load-side heat rejection (black), conversion (blue), and balance (red) as a function of mean mesh size; all simulations used the fixed parameters listed in Table 14 but with residence time set to 70 seconds 311

Figure 115. Total load-side heat rejection as a function of residence time for different solid AC concentrations: 0 g/L (dashed), 25 g/L (green), 50 g/L (black), 100 g/L (blue), and 200 g/L (red) 313

Figure 116. Conversion as a function of residence time for different solid AC concentrations: 0 g/L (dashed), 25 g/L (green), 50 g/L (black), 100 g/L (blue), and 200 g/L (red) 313

Figure 117. Optimal $\dot{Q}_L / \dot{Q}_{rxn,\max}$ (red squares), conversion (black squares), and balance (blue squares) as a function of AC feed rate. 318

Figure 118. Diagram of experimental apparatus used in single-phase heat transfer characterization 351

Figure 119. Wilson plot obtained from water-water single-phase testing 357

Figure 120. Plot of $NuPr^{1/3}(\mu/\mu_w)$ as function of Re for the load side of the HEX reactor 357

Figure 121. Parity plot comparing overall heat transfer coefficient *U* calculated experimentally with predictions using Eq. (11) 358

Figure 122. Plot of reactant-side Nusselt number as a function of Reynolds-Prandtl product 360

LIST OF TABLES

Page

Table 1. Instrumentation and associated uncertainty used in NH_3 solubility experiments 11

Table 2. Instrumentation and associated uncertainties used in batch reactor kinetic and calorimetric studies 23

Table 3. Experimental results for $\Delta H_{a,des}$ spot-check using both FTIR (2) and gravimetric (1) measurement methods 167

Table 4. Thermochemical parameters used in model for validation. Asterisks indicate the value was obtained from experiment 203

Table 5. Load-side heat rejection measured during single-phase heat transfer characterization experiments compared to model predictions 257

Table 6. Predicted maximum attainable heat transfer, per Eq. (6.68), for 70 s residence time single-phase validation experiments 258

Table 7. Load-side heat rejection measured during 70s residence time single-phase heat transfer characterization experiments compared to model predictions; $\dot{m}_R$ was estimated using Eq. (6.68) and setting experimental $\dot{Q}_L = \dot{Q}_{\max}$ 259

Table 8. Experimental conditions for low residence time (10 second) tests reported in [70] 260

Table 9. Experimental conditions for high residence time (70 second) tests reported in [70] 262

Table 10. Range of conditions considered for parametric study 289

Table 11. Fixed parameters for $T_{R,in}$ study 291

Table 12. Fixed parameters for solid AC concentration study 296

Table 13. Calculated thermal performance values for “infinite length reactor” cases plotted in Figure 105 297

Table 14. Fixed parameters in particle size study 307

Table 15. Optimization results using Eq. (6.72) for different AC feed rates....318

Table 16. Instrument uncertainties claimed by manufacturer....361

Table 17. Estimated relative uncertainties for water-water characterization tests....365

Table 18. Estimated relative uncertainties for water-glycol characterization tests....365

Table 19. Estimated mass transfer and solubility parameters as a function of temperature at different solid AC loadings....366

Table 20. Estimated kinetic (rate and equilibrium coefficients) as a function of temperature at different solid AC loadings....367

Table 21. Comparison between results of Johnson *et al.* [70] and HEX reactor model predictions for heat absorbed by endothermic reaction (Q_{rxn}) and heat transferred by convection (Q_L) ; 10 second residence time.....368

Table 22. Comparison between results of Johnson *et al.* [70] and HEX reactor model predictions for heat absorbed by endothermic reaction (Q_{rxn}) and heat transferred by convection (Q_L) ; 70 second residence time.....368

CHAPTER I

INTRODUCTION

It is a well-known issue in the area of electronics and power systems cooling that conventional thermal management schemes reliant on forced convection are not amenable to the continued trend of device miniaturization and the consequent increase in heat flux demands [1]. In such applications, there are severe constraints on the allowable operating temperature (typically between 30 - 80°C) even as the heat flux demands continue to increase. Thermophysical approaches such as phase-change materials (PCMs) [2,3] have offered some reprieve by increasing the effective energy density of the heat transfer medium within the working temperature range restrictions. Nevertheless, it has been pointed out that thermochemical reactions, possessing fundamentally higher latent heat [4] than thermophysical PCMS, have the potential to serve as vastly superior thermal management materials. Justification for pursuing a thermochemical-based TMS would require there to be a significant advantage over, say, boiling of water (with a latent heat of ~2000 kJ/kg). For certain highly endothermic reactions – namely, the endothermic decomposition of ammonium carbamate [5,6] – this advantage comes in the form of reaction temperatures in the neighborhood of 60°C at atmospheric pressure, with an enthalpy of reaction between 1800 – 2000 kJ/kg [7-9]. In contrast, boiling of water – which might be considered as the "gold standard" method for addressing high heat flux thermal loads – requires temperatures in excess of 100°C at atmospheric pressure.

The early work with AC conducted by Schmidt *et al.* [10] in a batch reactor showed that - even at laboratory scales - the decomposition of AC was capable of rapidly absorbing appreciable quantities of heat in a 1 L batch reactor at temperatures between 30 – 60°C (with the aid of a vacuum pump). However, the batch reactor apparatus used in the aforesaid work is not realistic for practical, scaled-up thermal management systems due principally to the poor volumetric heat transfer capabilities of stirred tank reactors, a drawback that has spurred no small degree of research effort by chemical engineers [11]. In effect, full realization of the thermal management potential for high energy density reactions is to a large extent limited by the equipment used to serve as an interface between the thermal load and the reacting species. Thankfully, there is a substantial body of research showing unequivocally that open flow chemical reactors that combine channel geometry optimized for mixing intensity and high surface area-per-unit-volume are capable of leveraging chemical reactions with high enthalpies of reaction [12], a practice that falls under the realm of what the chemical engineering literature has dubbed "process intensification". Such reactors are commonly referred to as Heat EXchanger reactors, or HEX reactors [12]. The obvious merit is that the high heat transfer performance capabilities of compact heat exchangers serve as enabling vehicles to match high heat transfer demands with high energy density chemical reactions.

For the case of AC decomposition, Johnson *et al.* [13] proposed a chevron plate heat exchanger (PHE) as a HEX reactor to form the basis for a TMS system utilizing a slurry of milled solid AC particles and propylene glycol (PG). Chevron PHEs have been

well-studied in both single phase flows [14-17] and more recently, multiphase flows (especially in the case of boiling and condensation of refrigerants) [18-22]. Channels are formed by two stacks of stamped wavy pattern plates, where the troughs and crests of the stamped plates are oriented in a chevron pattern with respect to the axial direction. Within a single channel, the upper and lower chevron patterns are in opposing directions, which has been shown to promote intense mixing by inducing secondary swirl flows [23, 24]. The secondary swirl flows enhance both mixing and heat transfer, both of which are important aspects for chemical reactors [12]. Additionally, chevron PHEs are modular and can be disassembled for maintenance and inspection relatively easily when compared to shell and tube heat exchangers and their capacity can be increased merely by installing additional stamped plates onto the frame. Johnson *et al.*'s [13] reactor design was, at the time of its publication, the only known three-phase HEX reactor design comprised of a chevron plate heat exchanger that was used for thermal management purposes. The system they developed was capable of continuously generating and feeding a reacting slurry with inline solid-liquid mixing and dispersion; the solids concentration of the slurry could be varied in real-time to match heat load demands. The design also incorporated solid-liquid separation. The concept was essentially to change what was a heat transfer problem into a mass transfer problem – the heat load was used to drive the decomposition reaction, after which the gas products were separated and removed from the process.

Niedbalski *et al*. [25] conducted an experimental investigation of the reacting multiphase flow characteristics in the reactor design developed by Johnson *et al* [13]

utilizing the neutralization reaction of sodium bicarbonate and acetic acid in a PG-water mixture to represent a generic gas-generating reacting flow. The flow visualization and pressure drop analysis presented showed that the chevron PHE was capable of handling a large volume of gas generation without developing conditions that would prove a barrier to heat transfer. They also observed that for both low and high gas generation rates the multi-phase flow appeared to be well dispersed. Based on these observations, Niedbalski *et al.* [26] developed a plug flow model for the chevron PHE HEX reactor to estimate the thermal performance of the reactor with the decomposing AC slurry. The reactor model proposed yielded calculations suggesting favorable scale-up attributes due to both the efficient thermal performance of the chosen HEX reactor equipment, and the high energy density and rapid chemical kinetics of AC decomposition. However, the model had not been validated against experimental data for AC decomposition in PG, and its relatively simple nature raises questions as to its applicability to arbitrarily broad operating conditions and HEX reactor types. Lastly, the decomposition kinetics was presumed to be described satisfactorily by a single algebraic relation that was developed for AC decomposition in the absence of a solvent. As it will be shown in this report, a much more nuanced approach is necessary to adequately capture the chemical kinetics. In summation, the early work [5,6,10,13,25,26] investigating the viability of utilizing endothermic reactions (AC decomposition in particular) show remarkable potential from a proof-of-concept viewpoint. To advance this approach to thermal management to a more technically mature level, greater scrutiny must be applied toward understanding the underlying coupled transport phenomena and chemical kinetics. Therefore, in this work,

we address two areas of need in order to enable further development of an ammonium carbamate-based HEX reactor as a viable thermal management platform:

- The present lack of experimental data characterizing the decomposition kinetics in the presence of an inert carrier fluid, and;
- A model that incorporates these experimental insights toward predicting the coupled chemical kinetics, mass transfer, momentum transfer, and heat transfer.

The first point is accomplished by an experimental characterization of the solvent and decomposition product interactions, coupled with a calorimetric and spectroscopic kinetic study. The fundamental insights gained from the experimental effort form the basis for a reaction rate model for the decomposition of AC in PG; this model then serves as a source term in the energy transport equation for the HEX reactor. Experimental data reported by Johnson *et al* [13] will be used to validate both the flow model developed for the HEX reactor, and the coupling with the chemical kinetics model.

Accordingly, this report is comprised of seven chapters:

- Chapter II describes the experimental work that has been conducted to characterize the decomposition of AC in a heat transfer fluid (propylene glycol, or PG);
- Chapter III discusses the theoretical foundation developed from the experimental observation of Chapter II, which serves as the basis for modeling the decomposition of AC in PG;

- Chapter IV develops the methodology to estimate the kinetic parameters for the model presented in Chapter III. The estimated parameters are discussed and the associated model predictions are compared to *in situ* spectroscopic measurements of gas released by the decomposition of AC in PG;

- Chapter V introduces a combined experimental and a dynamic lumped element modeling technique to obtain calorimetry measurements of an unsteady, energetic reaction. This technique is combined with the kinetic model parameterized with the results obtained in Chapter IV to estimate the heats of reaction and dissolution for each step in the decomposition reaction;

- Chapter VI adapts the kinetic model to a modular plug flow HEX reactor model. The new HEX reactor model is validated against data in the open literature for AC decomposition in a chevron plate heat exchanger HEX reactor. The model's ease of integration with numerical optimization techniques is demonstrated through an operating condition optimization study.

- Chapter VII discusses conclusions to be drawn from the present body of work, and possibilities for future research are suggested.

CHAPTER II

EXPERIMENTAL INVESTIGATION

As it stands, only a narrow range of published works have considered the decomposition kinetics of AC when exposed only to its gas products (e.g., [27,28]). Schmidt *et al.* [10] conducted the first (and presently, only) experimental study of AC decomposition immersed in a solvent, but offered only qualitative observations and did not explore the kinetics in detail. The experimental work conducted in this study addresses the present lack in understanding of the mechanisms governing the rate of AC decomposition when immersed in a solvent (PG). There were two complementary experimental studies accomplished: a study of the interaction between the gaseous decomposition products and the solvent, and a calorimetric and spectroscopic study of a reacting AC slurry within temperature and pressure ranges relevant to electronics cooling applications. Quantitative and qualitative data were obtained that proved instrumental in developing the reaction model framework presented in Chapter II.

2.1 Solubility Study

In the previous theoretical study by Niedbalski *et al.* [26], the interactions between the decomposition products NH_3 and CO_2 was ignored. However, as will be shown, the hold-up of gas products in solution acts as a potential hindrance to the reaction rate, and thus an understanding of solvent's capacity to retain the decomposition products is necessary to understanding the chemical kinetics. In this section, we discuss the NH_3-PG equilibrium study that was conducted to ascertain the solubility limits of

NH_3 in PG at atmospheric pressure and temperatures between 55°C and 75°C. It was determined that CO_2 had negligible solubility in PG compared to that of NH_3, and thus the scope of these experiments was limited NH_3.

2.1.1 Experimental Design

Figure 1 shows a diagram of the absorption apparatus. Anhydrous NH_3 is metered by a thermal mass flow controller (MFC) (MKS Instruments 1479A) at approximately 7.3 SCCM (referenced at 0°C) into a stainless steel jacketed absorption tube containing a 25, 30, or 40 ml sample of PG, wherein absorption occurs as the gas is bubbled through the liquid sample by means of a small sparging tube. Excess (i.e., NH_3 bubbles that are not completely absorbed) exit the absorption tube and pass through a differential pressure-based mass flow meter (MFM) (Alicat Scientific MS-series) before venting into the fume hood exhaust. The mass absorbed is calculated by integrating the difference between the MFC and MFM. The PG sample temperature is regulated by a 300W laboratory thermostat (Thermo Scientific Neslab RTE17) circulating water. This arrangement is shown in Figure 2. The absorption vessel consisted of a 1" OD stainless steel tube ("absorption tube") with two KF25 high vacuum rated flanges at the inlet and outlet, having a total overall volume of 110 ml. The absorption tube was mated with a 4.5" stainless steel flange by a ¾" NPT adapter welded just below its outlet arm; this flange was in turn mated with the circulation jacket flange and sealed with a Buna-N gasket. Approximately 70 ml of the absorption tube volume extended into the circulation

jacket, and hence even the largest PG sample would be within the heated region of the tube.

The absorption process occurred within 0.2-0.4 psi of atmospheric pressure. Once the differential mass flow was less than 0.1 sccm, the PG sample was declared to have reached a saturated state; this condition was further verified by closing the isolation valves to seal the absorption tube and monitoring the change in pressure – if a measurable (0.05 psi) drop in pressure occurred, the valves were opened and flow resumed. This pressure-checking procedure was repeated until no additional changes could be measured. This experimental method showed excellent repeatability.

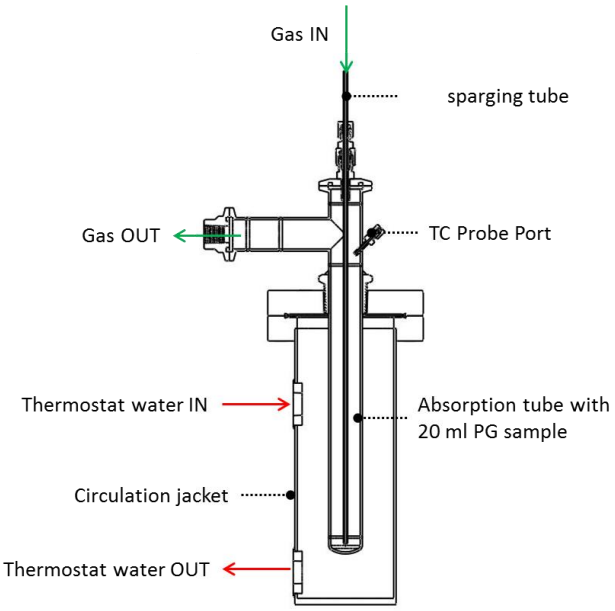

Figure 1. Sectional view of absorption vessel showing absorption tube, circulation jacket, and sparging tube

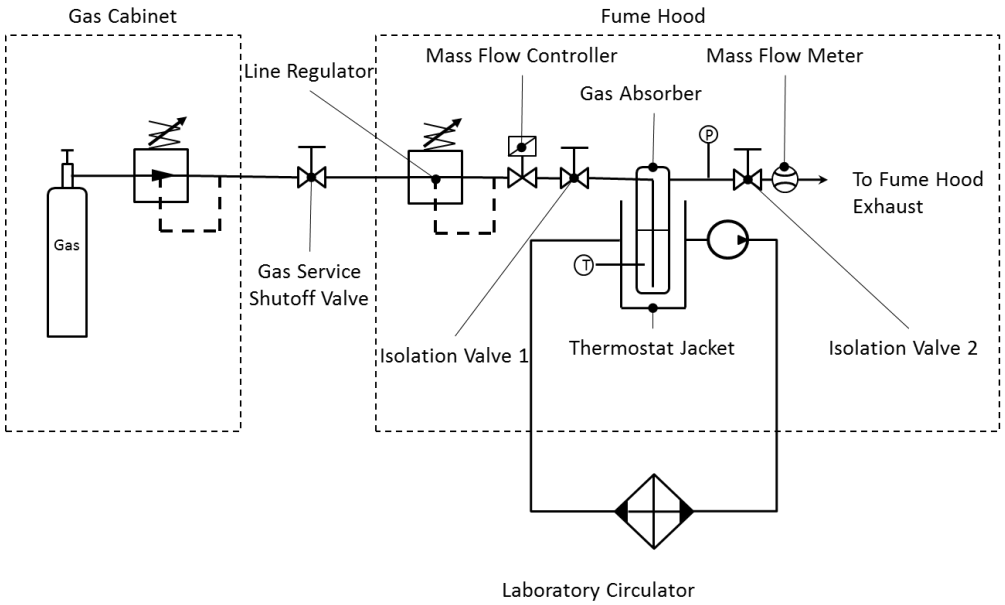

Figure 2. Schematic of NH_3 absorption experiment

2.1.2 Uncertainty Analysis

Table 1 shows the instrumentation used as part of the absorber and their associated uncertainties:

Table 1. Instrumentation and associated uncertainty used in NH_3 solubility experiments

Instrument	Make / Model	Uncertainty
Mass Flow Controller (MFC)	MKS 1479	+/- 1.2%
Mass Flow Meter (MFM)	Alicat MS-10	+/- 1.3% (0.8% reading + 0.2% FS)
Temperature Probe	Omega Eng. T-type	+/- 0.1°C
Pressure Transducer	Omega Eng. PX409	+/- 1.0% Reading
Pressure Calibrator	Heisse PTE-2	+/- 0.05%

The total internal volume of the absorber, including the tubing, was measured at 175 ml by sealing the vessel and feeding a fixed flow rate of NH_3 while monitoring the change in pressure; the volume was then calculated using the relation:

$$V_{abs} = \frac{\dot{n}_{MFC}}{\dot{P}}\left(\Re T\right) \tag{2.1}$$

The error in the rate of pressure increase was estimated from the leak integrity of the sealed vessel at 10 psig, which amounted to 0.1 ml/min. Thus, we have $\delta\dot{P}/\dot{P}$ = +/-

0.7%. From Table 1, it follows that $\delta\dot{m}/\dot{m}$ = +/-1.3%. Applying the Klein-McKlintok method to Eq. (2.7), one obtains:

$$\delta m_{abs} = \sqrt{\left(\delta\dot{V}_{MFC}\right)^2 + \left(\delta\dot{V}_{MFM}\right)^2 + \left(\delta V_{dead}\right)^2} \tag{2.2}$$

which evaluates to +/- 4.0% if one takes the smallest absorbed mass at 75°C (~1.1 g).

2.1.2 Results and Analysis

First, we address that the volume between the absorption tube and the MFM contained air at the start of the experiment, and the differing viscosities of air and NH_3 introduces an error in the differential mass transfer measurement. A simple correction factor was applied to the total calculated NH_3 absorption, assuming that by end of the experiment all air in the headspace of the absorption tube and the tubing leading to the MFM was completely displaced by NH_3. The MFM used in this study incorporated a laminar flow element in a microchannel to measure the differential pressure of the flow, and thence compute the mass flow rate [29]. Therefore, from the well-known equation for fully-developed laminar flow in a channel of constant cross section, the voltage signal v_j generated by the MFMs differential pressure transducer is directly proportional to the viscosity μ_j of the fluid species j and its volumetric flow rate $\dot{V}_j$:

$$v_j = A^* \mu_j \dot{V}_j \tag{2.3}$$

Where A^* is a detector constant which includes the $\Delta v/\Delta P$ calibration coefficient. It is assumed for this analysis that NH_3 and air form a binary gas mixture whose viscosity μ_g is given by:

$$\mu_g = \mu_a y_a + \mu_{air} y_{air} \tag{2.4}$$

where y_a is the mole fraction of NH_3, y_{air} is the mole fraction of air, μ_a is the dynamic viscosity of NH_3 and μ_{air} is the dynamic viscosity of air. It shall be demonstrated shortly that this mixture viscosity model is appropriate. Let $\dot{V}_a^*$ signify the flow rate computed by the MFM (the raw data recorded during the experiment) where the fluid is assumed to be NH_3. Let $\dot{V}_{mfc}$ and $\dot{V}$ be the flow rate of NH_3 introduced by the MFC and the *actual* flow rate of the air-NH_3 mixture through the MFM, respectively. The voltage signal generated by the mixture flowing through the MFM is,

$$v^* = A^* \mu_g \dot{V} \tag{2.5}$$

In principle, the MFM converts v^* into the apparent NH_3 flow rate by substituting it into the left-hand side of Eq. (2.3) and solving for the flow rate:

$$\dot{V}_a^* = \frac{\mu_g}{\mu_a}\dot{V}_g = \left(y_a + \frac{\mu_{air}}{\mu_a}\left(1 - y_a\right)\right)\dot{V} \tag{2.6}$$

where $\dot{V}_a^*$ is the "apparent" volume flow rate of NH_3 as reported by the MFM, without compensation for the presence of air. The total apparent mass absorbed, $\dot{m}_{a,abs}^*$, is calculated by,

$$m_{a,abs}^* = \rho_a \int_0^{t_f} \left[\dot{V}_{mfc} - \dot{V}_a^*\right] dt \tag{2.7}$$

Substituting Eq. (2.6) into Eq. (2.7), re-arranging, and using the fact that the air is completely displaced by the end of the experiment, we obtain:

$$m_{a,abs}^* = \rho_a \left[V_{mfc} - \int_0^{t_{test}} \dot{V}_a dt - \frac{\mu_{air}}{\mu_a} V_{dead} \right] \tag{2.8}$$

where V_{mfc} is the cumulative volume of NH_3 dispensed by the MFC, and V_{dead} is the dead volume of the absorber which was initially completely filled with air. The last term in the brackets on the right-hand side of Eq. (2.8) is the correction factor, which is simply added to $m_{a,abs}^*$ to obtain the correct quantity of absorbed NH_3. The validity of Eq. (2.4) was tested by allowing the MFC to dispense a constant flow rate of NH_3 through the dry, initially air-filled absorber (without the PG sample) and comparing the MFM output to the known input. Assuming, initially at least, that Eq. (2.4) describes the gas

mixture viscosity, the ratio $\dot{V}_a^* / \dot{V}_{mfc}$ is simply that of μ_g / μ_a, and it follows from Eq. (2.6) that,

$$\frac{\dot{V}_a^*}{\dot{V}_{mfc}} = \frac{\mu_{air}}{\mu_a} + y_a \left(1 - \frac{\mu_{air}}{\mu_a} \right) \tag{2.9}$$

If the gas mixture in the absorption tube is well-mixed, the NH_3 in the dead volume of the absorption tube is calculated by:

$$\frac{dy_a}{dt} = \frac{\dot{V}_{mfc}}{V_{dead}} \left(1 - y_a \right) \tag{2.10}$$

This is readily integrated to yield,

$$y_a = 1 - \exp\left(- \frac{\dot{V}_{mfc}}{V_{dead}} t \right) \tag{2.11}$$

Invoking Eq. (2.9),

$$\dot{V}_a^* / \dot{V}_{mfc} = 1 + \left(1 - \frac{\mu_{air}}{\mu_a} \right) \exp\left(- \frac{\dot{V}_{mfc}}{V_{dead}} t \right) \tag{2.12}$$

Inherent in this equation is the assumption that the viscosity of the air-NH_3 mixture is a linear mixing rule per Eq. (2.4); the validity of the MFM correction in Eq. (2.8) is therefore tied directly that of Eq. (2.11). An inspection of the $\dot{V}_a^* \big/ \dot{V}_{mfc}$ data from the experiment described above, shown in Figure 3, follows the functional dependence predicted by Eq. (2.11), and thus validates the assumption underlying Eq. (2.8).

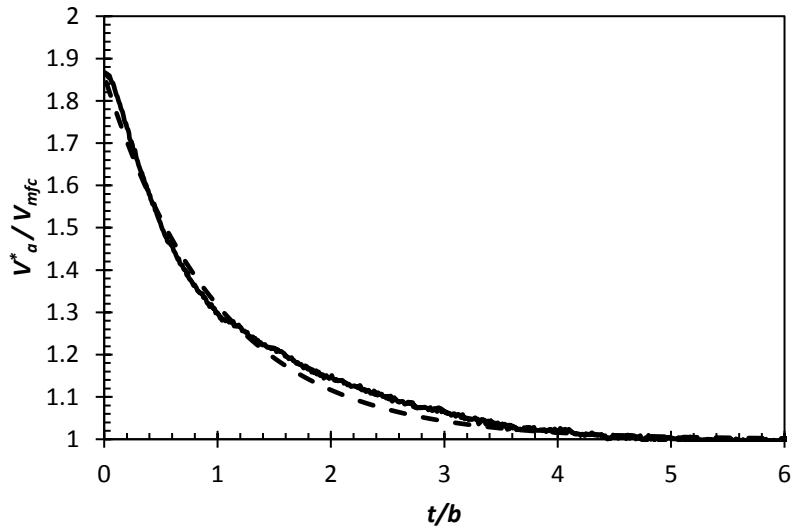

Figure 3. Comparison of Eq. (2.12) predictions (dashed line) to experimental measurements (solid line) in a dry absorption tube initially filled with air

The dashed curve in Figure 3 required a slight adjustment by giving $\dot{V}_{mfc} \big/ V_{dead}$ a value of 0.00155 s^{-1} instead of its nominal value of 0.000788 s^{-1}, which is based on an MFC input of 7.34 sccm (the maximum controllable flow rate of NH_3 for the particular model used in this study) and an absorber dead volume of 155 ml. Despite this discrepancy, likely due to the gas mixture not adhering completely to the well-mixed

approximation, the overall agreement between the absorption tube filling experiment and predictions by Eq. (2.12) is excellent and we are justified in adopting the mass absorption correction in Eq. (2.8) for interpreting the following results.

The mass absorption of NH_3 in PG was measured over a temperature range of 50°C and 75°C at atmospheric pressure. shows a plot of the mole fraction at saturation of NH_3 in PG as a function of temperature, and also a plot of the best fit line to the data. The blue line in Figure 4 is represented by the equation

$$x_{a,sat} = \exp\left[\frac{A}{T + 273.15} + B\right] \tag{2.13}$$

Where T is the temperature in °C and the fitting parameters A and B take the values of 3212 K and -12.744, respectively. This correlation could reproduce the experimental data with an average error of 2.1% and a maximum error of 5%. In the interest of the gas-solvent interactions relevant to AC decomposition in PG, it is useful to compare the solubility of NH_3 against that of CO_2, which is also generated during the reaction. Galvao and Francesoni [30] studied experimentally the solubility of CH_4 and CO_2 in PG at temperatures ranging from 30°C to 150°C and pressures between 0.36 and 4.5 MPa. This data can be extrapolated to atmospheric pressure using the Henry's coefficient ($H_{2,1}$) values one may obtain from the slope of mole fraction vs. pressure at various temperatures, and used to calculate the solubility of CO_2 in terms of mole fraction (also plotted in Figure 4):

$$x_{c,sat} = \frac{P_{atm}}{H_{2,1}} \frac{M_c}{M_{AC}} \tag{2.14}$$

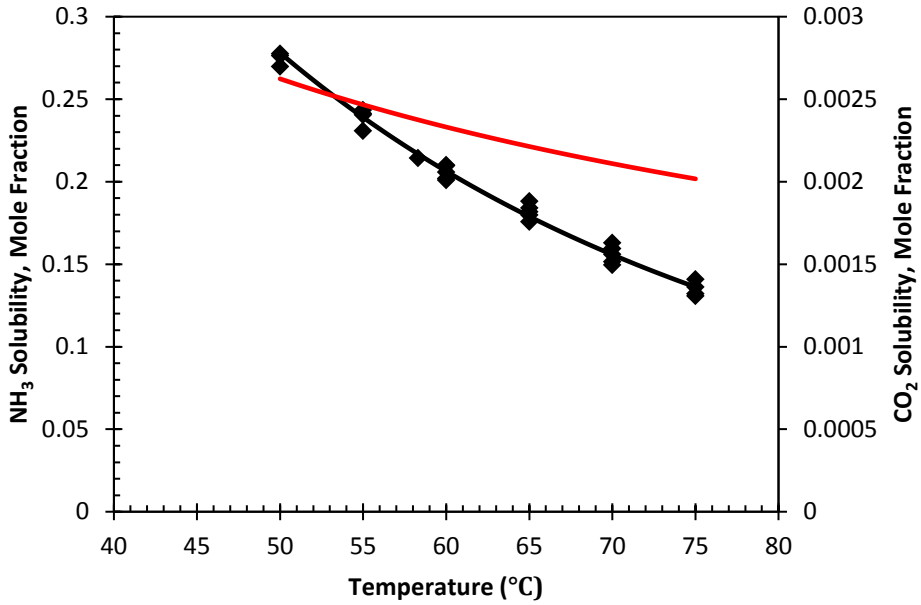

Figure 4. Comparison of experimental NH_3 solubility measurements (black squares) and correlation predictions (black line); also plotted on the right axis is the solubility of CO_2 in propylene glycol (red line), calculated from the data of Galvao and Francesoni [30]

Comparing the data of Galvao and Francesoni and the results from this study, the solubility of NH_3 in PG is, at the very least, nearly a factor of 30 greater than that of CO_2.

2.2 Kinetics Study

There are two objects of interest pursued in the chemical kinetics investigation that was conducted in this work: the rate of heat absorption and the rate gas release by the decomposition reaction. The heat balance data and FTIR spectroscopic analysis of the desorbed decomposition products form the basis for development of the chemical kinetics model, both in terms of validation points and physical insight into the dominant mechanisms governing the reaction. In this subsection, we discuss the experimental methodology employed and an analysis of the quantitative data to serve as validation bases for the model.

2.2.1 Experimental Design

A batch reactor apparatus (Figure 5) was built to study the decomposition of ammonium carbamate under controlled temperature and pressure conditions. The gasses produced by the reaction (NH3 and CO2) are conveyed from the reaction vessel into a Fourier Transform Infrared (FTIR) gas analyzer (MKS instruments MultiGas 3000) for real-time NH3 and CO2 concentration monitoring. The reaction is allowed to occur within a 1-liter jacketed glass vessel, with an additional liter of headspace to allow for the introduction of solid ammonium carbamate into a heated, mechanically agitated sample of propylene glycol. All wetted materials (aluminum, borosilicate glass, PTFE, and Nitrile) within the reaction vessel, including the headspace and seals, were selected to be impermeable and chemically inert with respect to the carrier fluid, reactants, and byproducts. Stirring is accomplished by a rotary agitator having a propeller diameter of

38mm; the agitator is driven by a magnetically coupled DC motor attached to the reactor stand. Effluent reaction gasses are removed by a diaphragm vacuum pump (Vacuubrand MD1C), which, combined with a solenoid valve and a digital vacuum controller (Vacuubrand CVC3000), permit real-time control of the reactor pressure. To prevent recombination of ammonium carbamate in the exhaust lines between the reactor, vacuum, and FTIR sample inlet, a dry nitrogen purge is introduced into the reactor headspace at 9 – 10 SLPM by means of a thermal mass flow controller (MKS Instruments 1790A). The nitrogen purge dilutes the NH3 and CO2 discharge and acts as an inert carrier gas for the FTIR analyzer.

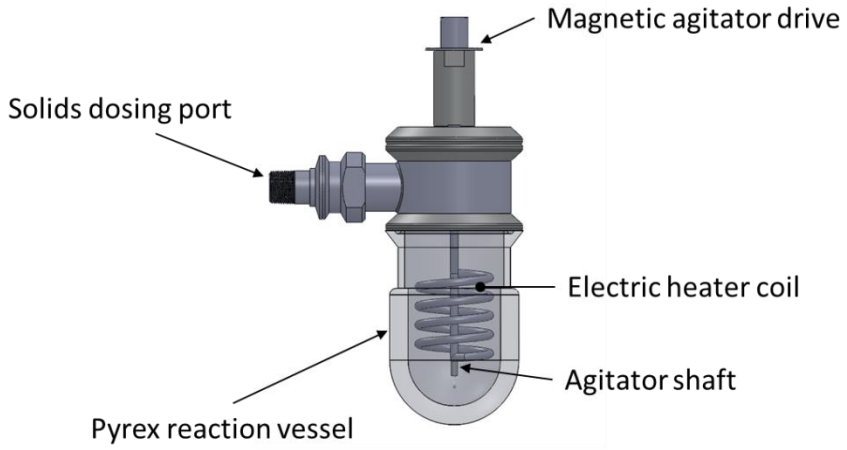

Figure 5. Solid model of the reaction vessel, lid assembly, agitator drive, and dosing port assembly.

A large bore solids dosing port was welded to the side of the reactor lid to accommodate a removable 25 mm dosing tube, into which the solid ammonium carbamate sample is loaded. The dosing tube contains a manually operated piston with a

PTFE ram to push the sample into the reaction vessel and initiate the decomposition reaction.

Prior to each experiment, the glass reaction vessel is washed with acetone, followed by a 4-6 hour vacuum purge of the entire reactor assembly. Propylene glycol (Sigma Aldrich, 99.5% purity) is measured with a 1-L graduated cylinder and dispensed into the reaction vessel without further purification. The experimental procedure consists of a "heating" phase and "decomposing" phase. During the heating phase, the reactor is sealed while the agitator and heater coil bring the clean propylene glycol sample to the specified reaction temperature (between 55°C and 70°C). The heater output is regulated by a digital DC power supply (Agilent Technologies model 5770) with a 1500W capacity. Once the set-point temperature is obtained, the reactor is allowed to 'stabilize' until the heater output remains constant, indicating equilibrium with the surroundings has been attained. At this point, the vacuum pump and nitrogen purge is activated to deliver a baseline (i.e., no AC decomposition) to the FTIR. Throughout all tests performed, the CO2 and NH3 content of the clean propylene glycol samples did not rise above background levels, indicating the absence of volatile components that would provide false readings or otherwise interfere with the computation of gas-phase NH3 and CO2 concentrations.

A sample of ammonium carbamate is massed and fed into the dosing tube with the piston in the fully retracted position. The dosing tube is subsequently clamped into the dosing port. The reaction is initiated by introducing the ammonium carbamate sample into the heated propylene glycol contained in the reactor, coinciding with the

activation of the vacuum pump and nitrogen purge occurring after a user-triggered time delay on the LabVIEW control panel. The reactor is again sealed once the piston is fully engaged. A T-type thermocouple probe is used to monitor the fluid temperature and provides the feedback signal for the heater control. Typically, the fluid temperature was able to be maintained within 1.5°C of the set point temperature during the course of the reaction, with the largest temperature excursions occurring immediately upon the introduction of the AC sample into the reactor.

2.2.2 Uncertainty Analysis

Following the same procedure as in Section 2.1.2, the Klein-McKlintok method [31] was used to estimate the uncertainty in the quantities derived from the FTIR concentration measurements. Table 2lists the instrumentation employed in the batch reactor apparatus and their associated uncertainties as obtained by calibration or from the manufacturer

Table 2. Instrumentation and associated uncertainties used in batch reactor kinetic and calorimetric studies

Instrument	Make / Model	Uncertainty
Pressure Transducer	Vacuubrand VSK3000	+/- 0.75 Torr
Temperature	Omega Engr. T-type	+/- 0.1 °C
FTIR Analyzer	MKS Instruments MG3000	+/- 5% (max deviation in calibration curve)
Nitrogen Flow Meter	Omega FMA2710	+/- 1.0%

The molar flow rate of any species in the effluent gas stream is given by

$$\dot{n}_j = \dot{V}_p \frac{y_j}{y_p} \tag{2.15}$$

The associated uncertainty is therefore [31]:

$$\frac{\delta \dot{n}}{\dot{n}} = \sqrt{\left(\frac{\delta \dot{V}_p}{\dot{V}_p}\right)^2 + 2\left(\frac{\delta y}{y}\right)^2} \tag{2.16}$$

The purge flow rate uncertainty is $\delta \dot{V}_p / \dot{V}$ = +/-1.0% and the uncertainty in mole fraction measurement is $\delta y / y$ = +/- 5.0% according to Table 2 Thus, we have a total estimated uncertainty of +/-7.0% associated with the calculated molar flow rates.

2.2.3 Reactor Characterization

FTIR measurements conducted throughout the kinetic study are ultimately to determine the instantaneous rate of gas release due to desorption and chemical reaction, $\dot{n}_a$ and $\dot{n}_c$. The rapid solids dosing capability of the reactor necessitated a significant (approx. 1 liter) of dead volume in the head space above the AC-PG slurry. Therefore, the concentration trace measured by the FTIR analyzer represents the combined effect of mixing dynamics occurring in the reactor headspace, tubing and equipment leading to the analyzer and the process stream, in addition to the reaction kinetics generating the gasses. Therefore, a relationship must be established between the quantities of interest, $\dot{n}_A$ and $\dot{n}_C$, and the concentration of gaseous species in the reactor headspace.

First, a simple experiment was devised to establish the effect of the tubing, fittings, and vacuum pump that convey the effluent gas sample to the FTIR analyzer, shown in Figure 6:

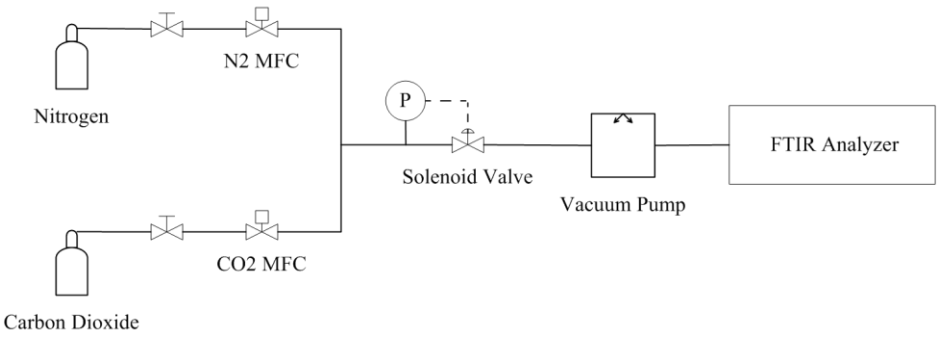

Figure 6. PID diagram of experiment to measure effect of tubing and vacuum pump on a continuous gas sample of known concentration history

The batch reactor effluent gas sample system (tubing, vacuum transducer, vacuum valve, pump, and fittings) were attached, without modification, to the outlet of a y-fitting with 1/8" NPT connections joining two controlled streams of N_2 and CO_2 gas. This arrangement permitted a known pulse of CO_2 to be introduced into the sampling system, with the output measured by the FTIR analyzer to be compared to the input to check for distortion from transport delay, axial dispersion, and mixing. Initially, the N_2 was allowed to flow at a constant rate while the CO_2 MFC was commanded to maintain a set point of 0 slm; at time $t = t_o$, the CO_2 MFC setpoint was changed to a value $\dot{V}_c > 0$, which was maintained for the duration of the pulse. At time $t = t_f > t_o$, the CO_2 MFC set point was again set to 0. The values of $\dot{V}_c$ were varied to give mole fractions of $0.05 \le y_c \le 0.2$, while the flow rate of the N_2 MFC was maintained at 9 slm – the same as that which was to be used in the kinetic study experiments. Results showing the CO_2 concentration set points y_c = 5% and y_c = 20% are shown, respectively, in Figure 7a and Figure 7b

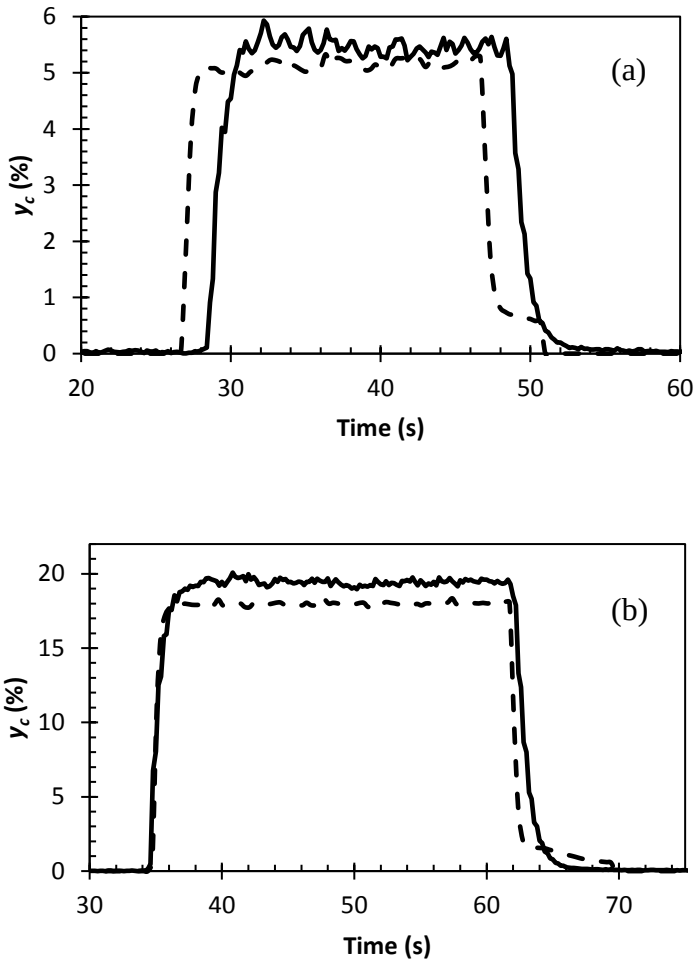

Figure 7. Gas-phase mass fraction of CO_2 fed into effluent gas sample system (dashed) compared to FTIR readings (solid) for input CO_2 concentrations of 5% (a, top) and 20% (b, bottom)

It is immediately apparent that the output curve measured at the FTIR analyzer suffers no significant distortion with respect to the input curve; for the case of y_c = 5%, a slight delay (roughly 1.8 seconds) is observed, whereas no discernable delay occurs in the case y_c = 20%. These observations establish that the method of gas sample delivery between the reactor and FTIR analyzer do not contribute appreciable dynamics to real-time concentration measurement.

Next, the same experiment was repeated, but with the y-fitting replaced by the reaction vessel, as shown in Figure 8

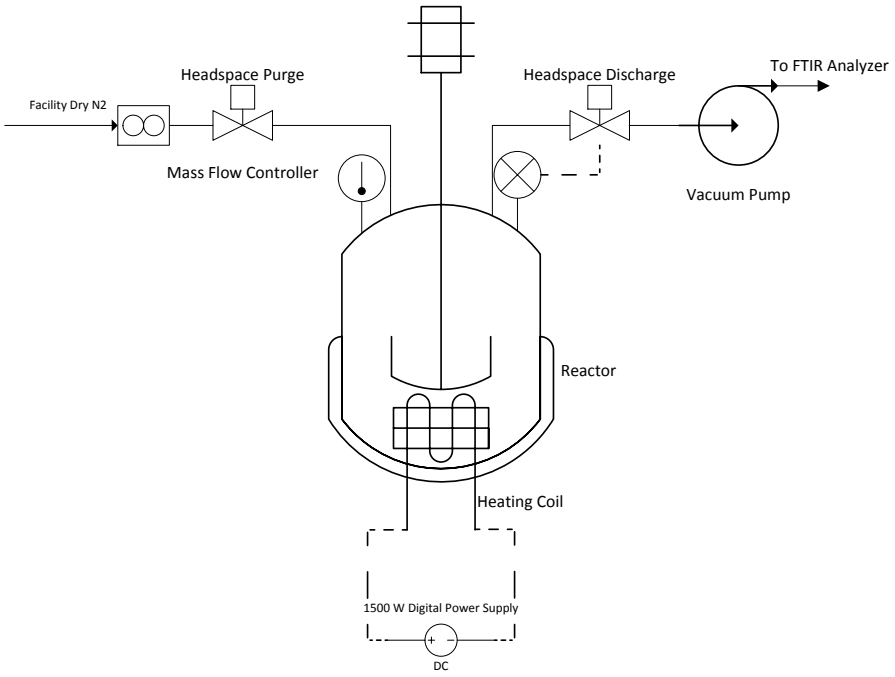

Figure 8. PID diagram of experiment to test effect of reactor headspace on a continuous gas sample of known concentration history

The N_2 stream was connected to the reactor through a 1/8” port connector on the top lid flange, directing a downward jet toward the gas-liquid interface 4 inches below,

duplicating the gas purge arrangement used in the kinetic study experiments. The CO_2 stream was connected to the reactor via the 6 o'clock side instrumentation port, which was oriented at 45° with respect to the horizontal. The CO_2 gas stream impinged on the gas-liquid interface 1 inch below the aforesaid instrumentation port, simulating gas release from a reacting AC-PG slurry. The reaction vessel was filled with 800 ml of clean PG, and the agitator set to 1000 RPM to replicate decomposition test conditions. The CO_2 pulsing procedure was identical to that used in the test previously discussed. Figure 9a and Figure 9b show the results for y_c = 5% and y_c = 20%, respectively:

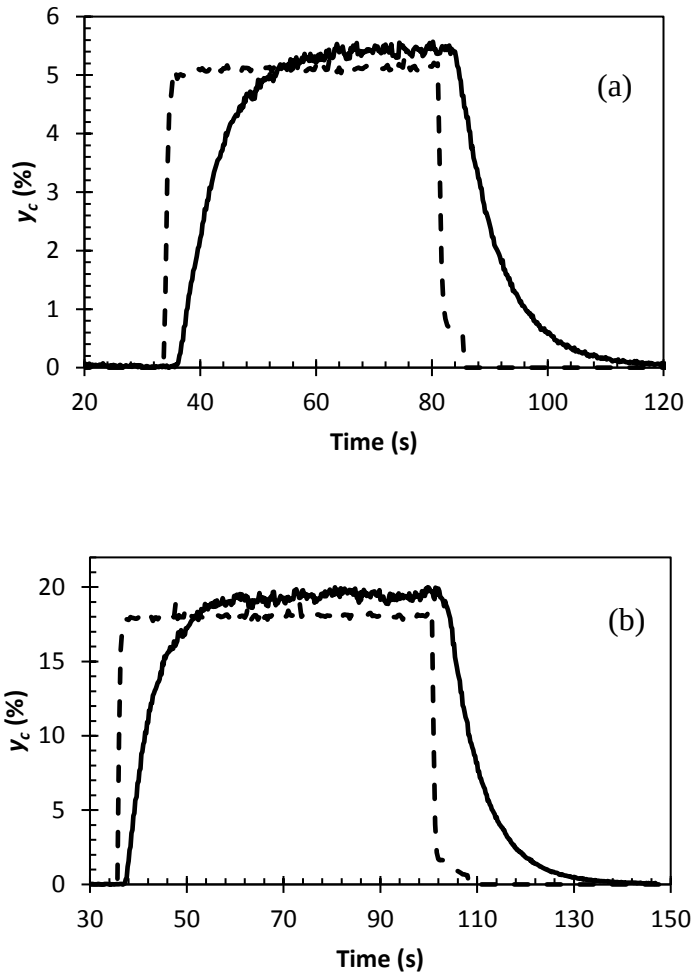

Figure 9. Gas-phase mass fraction of CO_2 fed into reactor headspace (dashed) compared to FTIR readings (solid) for input CO_2 concentrations of 5% (a, top) and 20% (b, bottom)

It is clear from the comparisons in Figure 9a and Figure 9b that the mixing dynamics in the reactor headspace must itself be modeled in order to relate the instantaneous release of NH_3 and CO_2 to the FTIR measurements. Toward this end, we may model the reactor headspace as a well-mixed (i.e., no spatial inhomogeneity in concentration) chamber, represented in Figure 10

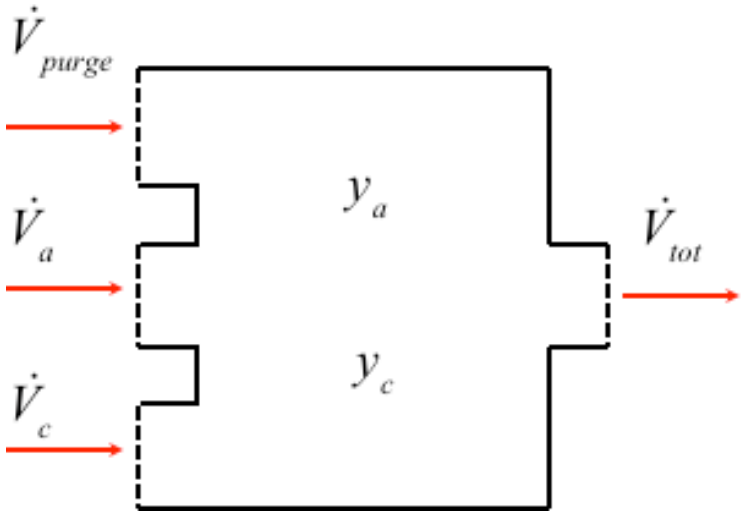

Figure 10. Simplified representation of reactor headspace. $\dot{V}_j$ signifies the volumetric flow rate of a gas source *j*, where *j* = *a* for NH3, *c* for CO_2, and *purge* for the purge gas (N_2). $\dot{V}_{tot}$ signifies the total volumetric flow rate of the effluent gas stream

Applying conservation of mass to the control volume in Figure 10 and assuming that no gas-phase reactions occur in the reactor headspace, and that the pressure remains well controlled, the total molar flow rate to the analyzer is:

$$\dot{n}_{tot} = \sum_{j=1}^{k} \dot{n}_j \tag{2.17}$$

Defining the 'inlet' gas mole fraction as for species *j* as $y_j^* = \dot{n}_j / \dot{n}_t$, and exploiting the fact that $\frac{dy_j}{dt} = 0$, the integral species balance for the headspace is:

$$\frac{\partial y_j}{\partial t} = \frac{1}{\tau_{hs}} \left(y_j^* - y_j \right) \tag{2.18}$$

Where $\tau_{hs} = \dot{n}_j / n_t$ is the residence time of a gaseous species *j* in the reactor headspace. To account for departure from the 'perfectly mixed' idealization, we introduce the empirical coefficient k_{hs} in place of τ_{hs}:

$$\frac{\P y_j}{\P t} = k_{hs} \left(y_j^* - y_j \right) \tag{2.19}$$

In the absence of gas-phase chemical reaction, and assuming the ideal gas law is obeyed by the mixture, k_{hs} is a function solely of advection (mixing) and diffusion phenomena. While the rate of gas release due to desorption and chemical reaction occurring in the reacting slurry is not time invariant, the volume flow rate of purge gas is constant, because it is the dominant source of gas, the hydrodynamic interactions

between the mixture constituents is approximately constant. Therefore, at least initially, k_{hs} is assumed to constant with respect to time. This assumption allows Eq. (2.19) to be integrated to obtain the solution for a step input at $t = t_o$:

$$y_c(t) = \begin{cases} y_c^* \left[1 - \exp\left\{ -k_{hs} \left(t - t_o \right) \right\} \right] & t_o \le t \le t_f \\ y_c^* \exp\left\{ -k_{hs} \left(t - t_f \right) \right\} & t_f < t \end{cases} \tag{2.20}$$

After parametric adjustment, a value of $k_{hs} = 0.16\ s^{-1}$ was found to give good agreement between Eq. (2.20) and the data. Comparison between Eq. (2.20) and experiment for $y_c^* = 0.05$ and $y_c^* = 0.20$ are shown in Figure 11a and Figure 11b, respectively.

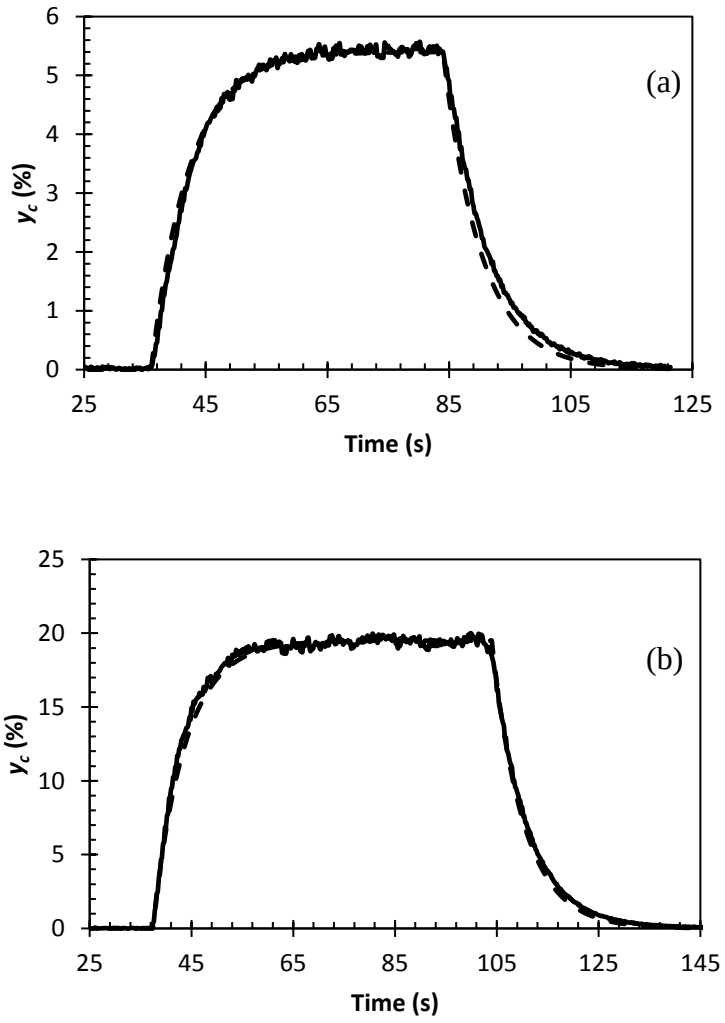

Figure 11. Comparison of CO_2 gas-phase mole fractions read by FTIR (solid) and predicted by Eq. (2.20) (dashed) utilizing a rate constant of 0.16 s-1 for input mass fractions of 5% (a, top) and 20% (b, bottom)

2.2.4 Results

The general trends shown in Figure 12 are representative of the time-dependent behavior observed throughout the range of temperatures, particle sizes, and initial AC concentrations studied. The reaction rate (as seen by the mass fraction of effluent CO_2) exhibits an initial peak, followed by a brief plateau, and finally followed by a steep decline. With respect to the character of the effluent NH_3 histories measured, there are essentially two types of curves that were observed:

1) A gradual, monotonic rise to a maximum limiting value

2) An initial peak wherein a maximum is attained followed by a gradual decline to a limiting value (termed "NH3 limit" hereafter).

Typically, type (1) occurs with coarser grained particle sizes and lower temperatures (for the tests conducted at 55°C, all NH_3 histories presented this way), whereas type (2) tends to occur at higher temperatures and finer particle sizes. The CO_2 mass fraction behavior with time is remarkably similar to the reaction rates reported by Ramachandran *et al*. [28] in their experimental investigation of AC decomposition in the absence of a solvent. Specifically, the CO_2 curves observed in this study and the dP/dt curves – P being the total pressure of NH_3 and CO_2 above the decomposing AC - presented in [28] both show an initially steep slope, followed by an inflection point and steep decline toward zero. Claudel and Boulamri [27] also reported a P(t) curve for the decomposition of dry AC whose derivative also followed this pattern.

The highest reaction rates occur within the first 100 seconds upon introducing AC into the reactor. Immediately after AC introduction, a vigorous white froth with fine bubbles is produced and expands the volume of the slurry by roughly 50 ml before settling shortly thereafter into a steady froth with marginally larger bubble sizes. Eventually, solid AC is no longer visible and the reacting mixture reaches clarity comparable to clean PG; the majority of bubbles appear to be born in the vicinity of the agitator blades. At this point, the NH_3 mass fraction does not change noticeably while the CO_2 mass fraction for all cases tested appear to decrease asymptotically toward zero. The CO_2, mass fractions converge onto a common line, whereas the NH_3 mass fractions will 'level off' at a value that depends on the reaction temperature and the initial concentration of solid AC.

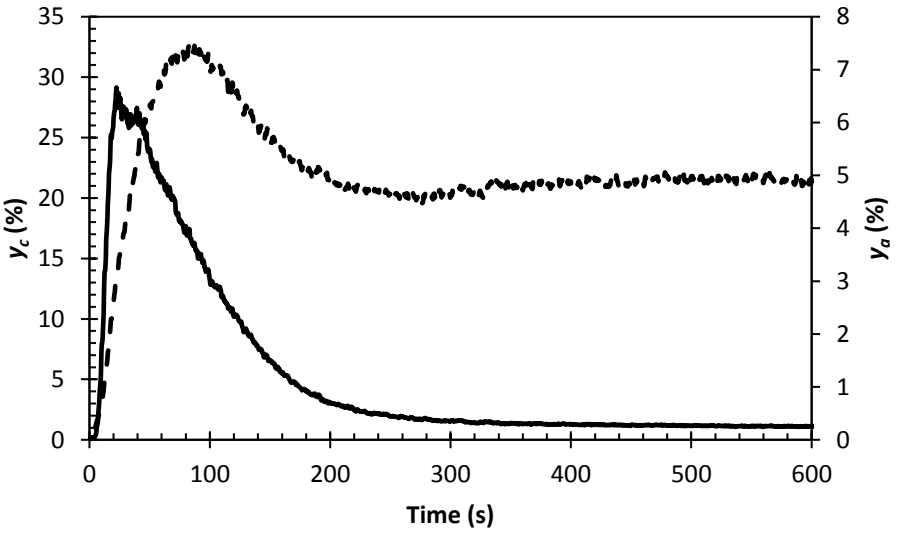

Figure 12. CO_2 (solid) and NH_3 (dashed) mole fraction history. Reaction temperature was 70°C, AC concentration was 37.5 g/L, and particle size range was -20 +30 mesh.

2.2.4.1 Estimation of Dissolved Ammonia Concentration

It was demonstrated in the previous experimental section that the solubility of CO_2 in PG is low compared to that of NH_3. This observation implies that the CO_2 mass fraction history also serves as a reliable indicator of the AC decomposition rate, as only a relatively small fraction would remain trapped in solution. Conversely, the NH_3 release rate can be seen to occur in non-stoichiometric proportions since one would expect twice the abundance as that of CO_2 if there were no interaction between the PG and reaction products. Indeed, assuming the solubility of CO_2 may be neglected, one may calculate the NH_3 holdup at time *t* after the onset of the reaction as follows:

$$x_a(t) = \int_0^t \left(\dot{n}_a - 2\dot{n}_c\right) ds \Big/ V_l M_l \tag{2.21}$$

The molar flow rates of NH_3 and CO_2 are calculated using the mole fractions computed by the FTIR analyzer:

$$\dot{n}_a = \dot{V}_{tot} y_a^* \tag{2.22}$$

$$\dot{n}_c = \dot{V}_{tot} y_c^* \tag{2.23}$$

Where,

$$\dot{V}_{tot} = \dot{V}_{purge} \Big/ y^*_{purge} \tag{2.24}$$

Where the values for y_a^*, y_c^*, and y_{purge}^* are acquired by directly solving Eq. (2.19) using the raw FTIR readings (i.e., y_a, y_c, and y_{purge}). Due to the low vapor pressure of PG [32], its contribution to the total gas flow rate is neglected. We reiterate here that there is certainly a non-zero quantity of dissolved CO_2, albeit a small one, otherwise the reverse (reformation) reaction of dissolved ammonium carbamate would not occur, which is obviously contrary to the experimental observations.

2.**2.4.2 Effect of AC Concentration**

First, it is stressed that the term 'AC concentration' refers to the initial mass of solid AC per unit volume of PG. Figure 13a and Figure 13b show the impact of initial AC concentration on the gas-phase mole fractions of CO_2 and NH_3, respectively, for a reaction temperature of 70°C and particle sizes in the -30 + 40 mesh range. Increasing the AC concentration tends to broaden the base of the CO_2 peak while enhancing the height of the peak by nearly the same proportion, thus preserving the overall shape of the curve. The maxima also appear to shift slightly to the left with increasing AC concentration.

The NH_3 mole fraction histories (Figure 13b) show that the NH_3 limit settles at progressively higher mass fractions in direct proportion to the increase in AC concentration. At 25 g/L, no peak is present, but at 37.5 g/L and 50 g/L, the peak can be

seen to rise above the horizontal line demarcating the NH_3 limit. The relative peak height to NH_3 limit distance also increases, making the peak appear as a more distinct curve feature. Unlike the CO_2 maxima, the NH_3 maxima shift toward the right.

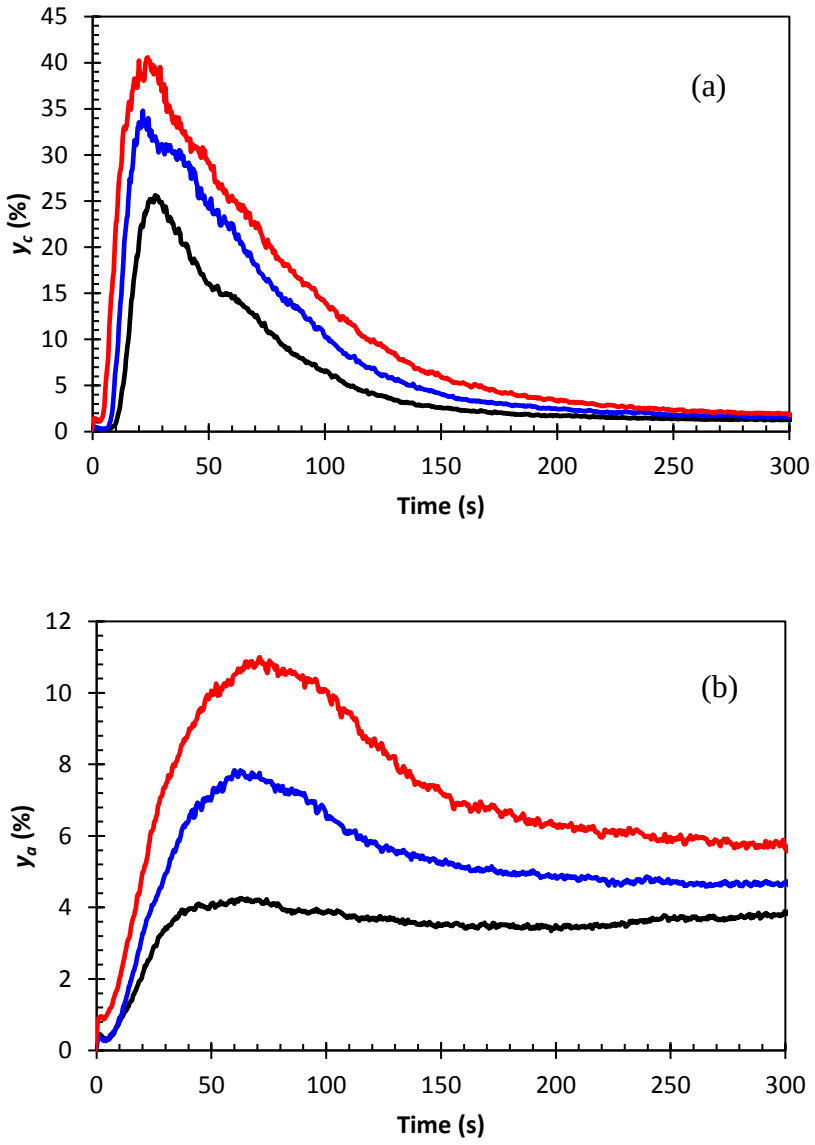

Figure 13. CO_2 (a, top) and NH_3 gas-phase mole fraction histories for initial AC solids concentration of 25 g/L (solid), 37.5 g/L (dashed) and 50 g/L (dot). Reaction temperature was 70°C and the particle size was in the -30 + 40 mesh range

2.2.4.3 Effect of Particle Size

Reducing the particle size likewise raises the maximum CO_2 and NH_3 mass fractions; however, the peaks become narrower both at the base and the apex while the maxima are shifted left, giving the appearance that the curve is being squeezed to the upper left as the particle size is decreased. The area under the CO_2 curve does not change appreciably as compared to the effect of increased AC concentration. The maximum NH_3 mass fractions are also shifted left – the opposite trend compared to increasing initial AC concentration. The NH_3 limit does not appear to change; as the NH_3 peak heights increase, the width of the peak narrows considerably. A comparison of the CO_2 and NH_3 concentrations of four different particle size ranges is presented in Figure 14a and Figure 14b, respectively.

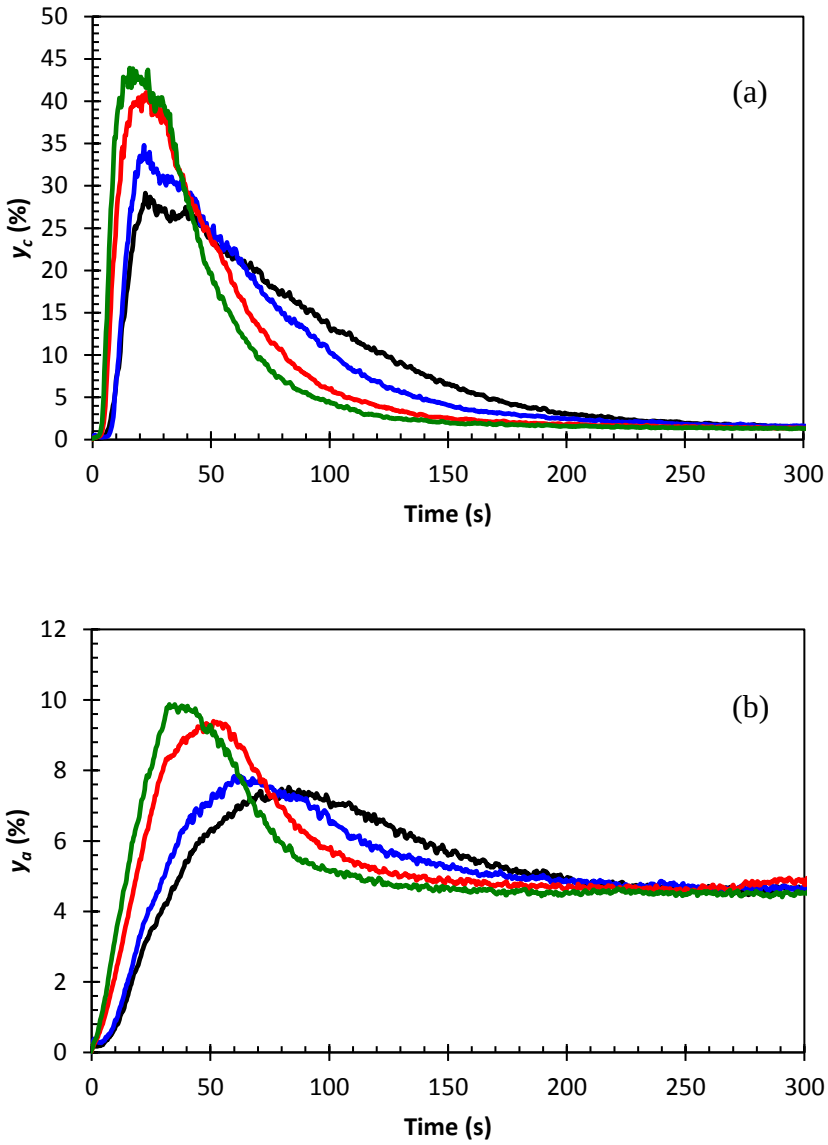

Figure 14. CO_2 (a, top) and NH_3 (b, bottom) gas-phase mole fraction histories for particle size ranges -20 +30 (black), -30 +40 (blue), -40 +50 (red), -50 +60 (green). Reaction temperature was 70°C and concentration was 37.5 g/L

2.2.4.4 Effect of Temperature

As one would expect, increasing the reaction temperature greatly enhances the height of the initial CO_2 peak, as shown in Figure 15a. The dependence on reaction temperature of the gas-phase CO_2 mass fraction is qualitatively similar to that of particle size, wherein the curve is sharpened near the peak and narrowed at the base (albeit to a far lesser extent) while its maximum is shifted to the left. The gas-phase NH_3 mass fractions (Figure 15b) show initial peaks that narrow at the base and apex, with maxima shifting up and to the left as temperature is increased in a similar manner to that of decreasing particle size; in comparison, however, the leftward shift is smaller in magnitude when compared to the enhancement in peak height. The NH_3 limits occur at successively higher values in approximately direct proportion to the reaction temperature in a manner nearly identical to when concentration is increased.

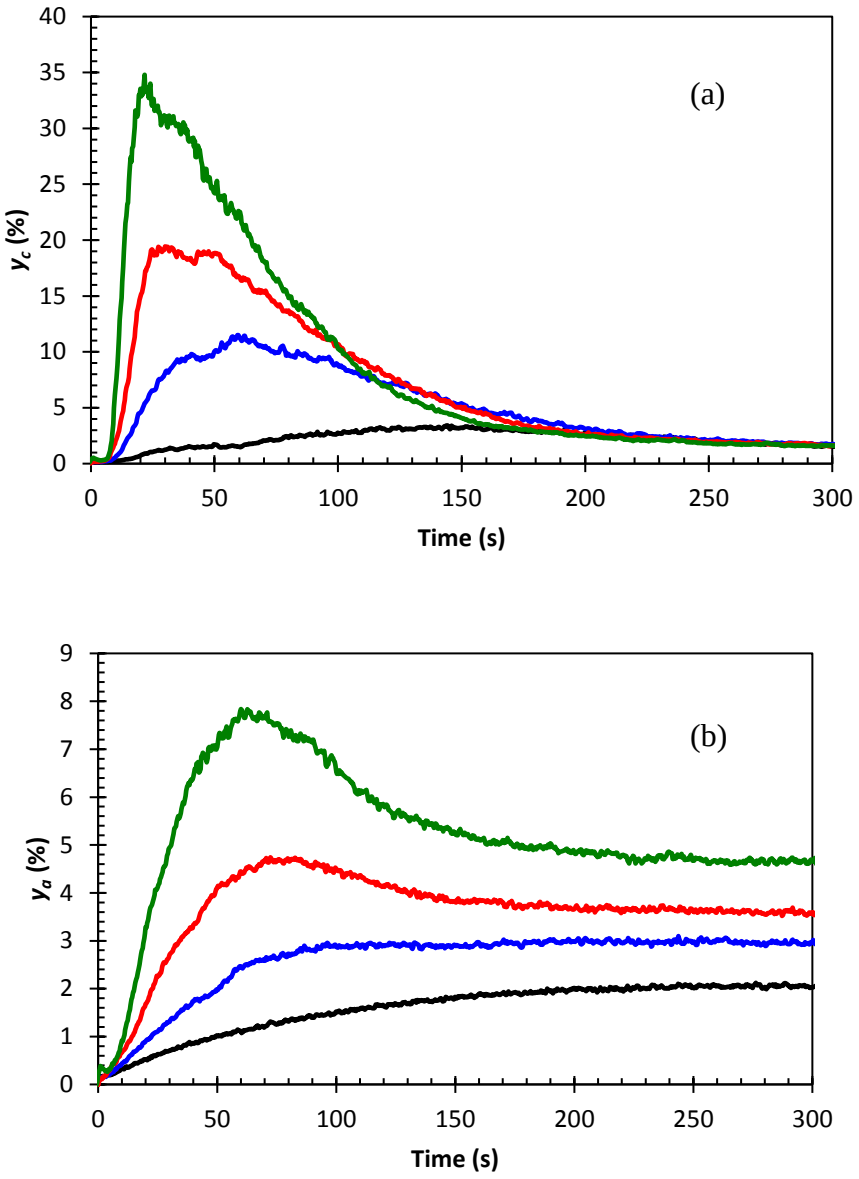

Figure 15. CO_2 (a, top) and NH_3 (b, bottom) gas-phase mole fraction histories at different temperatures: 55°C (black), 60°C (blue), 65°C (red) and 70°C (green). AC concentration was 37.5 g/L and particle size range was -30 +40 mesh

2.2.4.5 Discussion

The importance of gas-solvent interactions in the global reaction kinetics is immediately apparent in the asymptotic behavior of the CO_2 and NH_3 FTIR data in Figure 13 - Figure 15. The vastly differing solubilities of CO_2 and NH_3 indicate that the former is more readily released – hence the sharp initial peak followed by asymptotic decline toward 0% - whereas the latter tends to accumulate in the PG and is released gradually, reflected in the relatively high plateau/NH_3 limit. The consequences of reaction products retained in solution are dictated by Le Chatlelier's principle: the driving force for the reverse reaction will increase. The gradual buildup of NH_3 acts to retard the decomposition (forward) reaction rate. After reaction times between 250-300 seconds have elapsed, the CO_2 mass fraction lingers at approximately 1% (although it is still decreasing very slowly), while the NH_3 mass fraction remains essentially constant, indicating the system is very close to achieving chemical equilibrium. That this stage of the reaction coincides with the maximum level of dissolved NH_3 is a strong indicator that the release rate of NH_3 has become the rate-limiting step in the overall reaction.

A representative plot of the dissolved NH_3 content estimated with Eq. (2.21) is given in Figure 16. This hypothesis is further corroborated by the increase in the NH_3 limits with respect to temperature and AC concentration. It is well-understood that increasing temperature universally accelerates reaction rates; in particular, AC decomposition is hastened by increasing temperature and thus shifting equilibrium in favor of the forward reaction. As a result, a higher concentration of dissolved NH_3 must accumulate before equilibrium is established, which in turn presents as a greater NH_3

mole fraction in the effluent gas stream. It is for this same reason that the NH_3 limit is enhanced with increasing AC concentration, as greater proportions of reactant also shift equilibrium in favor of the forward reaction. On the other hand, changing the initial AC particle size does not affect the equilibrium condition.

The particle size comparisons in Figure 14a and Figure 14b show that finer AC granules, and by extension greater solid-phase surface area per unit volume at fixed AC concentration, will enhance the rate of reaction *initially* in exchange for approaching equilibrium more rapidly, which accounts for the narrowed CO_2 peaks. The short-term enhancement in reaction rate causes x_a to climb quickly and thus accelerate the reverse reaction; without additional un-reacted material or higher temperature, there is no chemical impetus to change the balance between the forward and reverse reaction rates in solution beyond t = 300 seconds. It is worth noting that the initial reaction rate dependence on particle surface area reveals the presence of a heterogeneous step in the global kinetics. At this juncture it is not yet clear whether the homogeneous and heterogeneous steps are parallel or sequential.

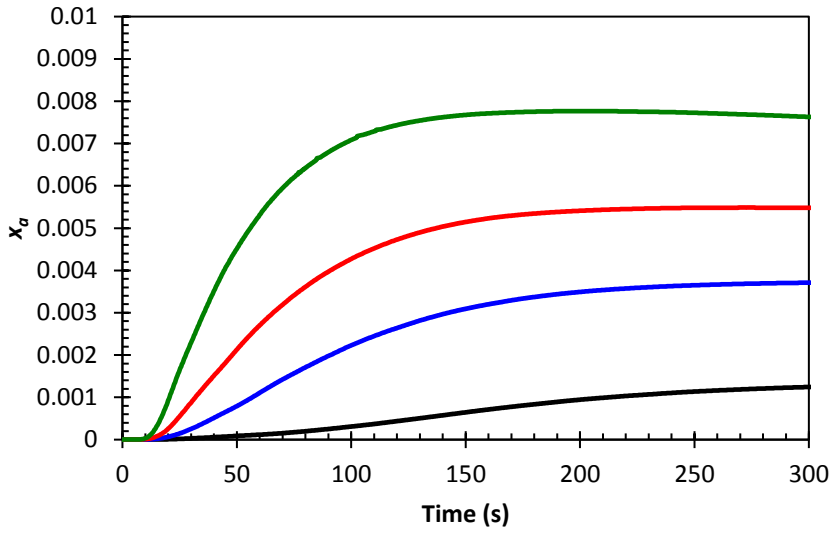

Figure 16. Dissolved NH_3 mole fraction content at different temperatures: 55°C (black), 60°C (blue), 65°C (red) and 70°C (green). AC concentration was 37.5 g/L and particle size range was -30 +40 mesh

The presence of the initial peaks in many of the NH_3 FTIR data points to three curious facets of the reaction. First, in general, the NH_3 peaks (when present) do not coincide temporally with the CO_2 peaks. These peaks often differ by 15 seconds or more, the NH_3 peaks occurring as the CO_2 mass fraction is declining. Second, by comparing the representative curves of y_a in Figure 15b to the x_a curves in Figure 16, there are no peaks in x_a that correlate to the peaks in y_a. And third, x_a was never found to exceed 30% of the NH_3 solubility limit. With these details taken into consideration, it is evident that NH_3 release is not solely accomplished by convective mass transfer to the reactor's gas-liquid interface, nor is it likely to be forming bubbles, and therefore must be aided by an additional mechanism(s).

A survey of the gas-scrubbing literature showed that bubble columns [33] and sparged stirred tank reactors (STRs) [34-36] were capable of very high mass transfer rates due to localized turbulent mixing produced by bubble agitation and high gas-liquid contact area. It is plausible, then, that bubbles released during the course of AC decomposition – particularly in the first 100 seconds – may enhance the removal rate of NH_3 through similar mechanisms. This hypothesis is corroborated by the close (qualitative) correlation between the concentration of bubbles in the reacting slurry and the gas-phase mass fraction of CO_2, from which it may also be inferred that CO_2 is primarily responsible for bubble formation. Such an inference is consistent with the relatively low solubility of CO_2 in PG at atmospheric pressure.

Hence, bubbles that are generated will initially have very low concentrations of NH_3, which provides a strong driving force for mass transfer from the liquid phase. This driving force is further enhanced by the high specific gas-liquid contact area owing to the small and numerous bubbles produced at high CO_2 release rates (such that $y_c > 15\%$, approximately).

Lastly, to address the offset between the NH_3 peaks and CO_2 peaks, one need only inspect Figure 17; the plot in Figure 17 is emblematic of the relationship between the NH_3 and CO_2 peaks (when applicable) observed in this study – the maxima of the CO_2 peak occurs at the same time as an inflection point in the NH_3 peak. After the inflection point, a gentle crest is formed as the NH_3 mass fraction reaches its maximum value and begins to decline.

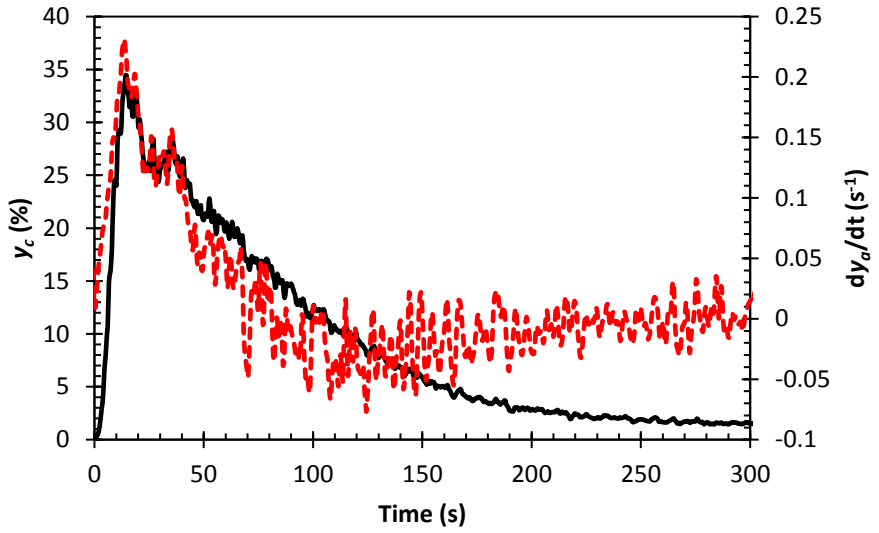

Figure 17. CO_2 gas-phase mole fraction, y_c (solid black) compared to the time derivative of NH_3 the gas-phase mole fraction, y_a (dashed red) at a reaction temperature of 70°C, concentration of 37.5 g/L, and particle size range -20 + 30 mesh

The two key driving forces for gas-liquid mass transfer in STRs to consider are the volumetric mass transfer coefficient ka''', (where a''' is the total gas-liquid interfacial area per unit volume, including bubbles and the free surface between the bulk liquid and reactor headspace) and the concentration gradient between gas and liquid phases, $H_j x_j - y_j$ [36], where H_j is Henry's constant for gas species j and y_j is the concentration of species j present in the medium into which the gas is desorbing. At the y_a inflection point shown in Figure 17, y_c has reached its maximum and is beginning to decrease. Consistent with the correlation between y_c and bubble generation, the bubble concentration begins to decline, and with it, the volumetric mass transfer coefficient. At the same time, the concentration gradient is also increasing as x_a continues to rise rapidly, opposing the decrease in ka''' and causing the NH_3 peak to round gently, as

evidenced by the gradual decrease in dy_a/dt after achieving its maximum. However, the buildup of NH_3 in solution continues to slow the net reaction rate, which further reduces the volumetric mass transfer coefficient in addition to decelerating the rise in concentration gradient. Stated concisely, the 'offset' between the NH_3 and CO_2 peaks is attributable to the two driving forces for NH_3 desorption changing in opposite directions, which effectively delays the drop in y_a until several seconds after y_c has begun to fall. The immediate implication of these conclusions is that the release rate of CO_2 is governed by the intrinsic kinetics of AC decomposition, whereas the release rate of NH_3 is governed by mass transfer.

This same dynamic framework can also be used to explain the qualitative differences between the y_c and y_a curves produced by changing the three experimental variables (AC concentration, temperature, particle size) considered in the kinetics study. It is useful for the purpose of this discussion to outline the following:

- Increases in the reaction rate, which are indicated directly by y_c, are accompanied by increases in dx_a/dt and, when y_c is above 15%, enhances the volumetric mass transfer coefficient by means of vigorous bubble generation;

- Increases in dx_a/dt tends to decrease (or at least slow the increase of) dy_c/dt as a result of Le Chatelier's principle, acting in opposition to the volumetric mass transfer coefficient, but also increases the concentration gradient driving force for NH_3 desorption;

- As x_a approaches the NH_3 limit, both y_c and dx_a/dt appears to decay exponentially

These aspects, taken together, allow several possibilities for the temporal evolution of y_c and y_a depending on the relative magnitudes of the kinetic (rate coefficients, equilibria) and mass transfer parameters (ka''' , concentration gradient). Suppose, for instance, that changing the reaction temperature causes an enhancement in reaction rate that is large compared to the increase in the NH_3 limit. In this case, x_a grows quickly and approaches the NH_3 limit sooner than at lower temperatures, also causing a rapid decline in y_c ; while the growth in the concentration gradient is faster initially, it is also short-lived, and is therefore sooner overwhelmed by the decline in ka''' , causing the y_a peaks to shift leftward as seen in Figure 15b. Indeed, it can be seen in Figure 15a while the maximum y_c is enhanced considerably, its rate of decline is more pronounced, which is consistent with the above scenario. This effect occurs to a greater extreme in the case of the particle size study, where the greater solid surface area concentration enhanced the height of the y_c peak, but did not bring about a change in the NH_3 limit. The accelerated growth of x_a, and hence the decline in y_c, is not tempered by a greater distance to equilibrium; a steep slope in y_c is produced as the forward reaction quickly decelerates, which produces the y_c peak-narrowing effect seen in Figure 15a. It then follows that the decrease in ka''' quickly overwhelms the brief (but expedient) increase in concentration gradient, dramatically shifting the y_a peaks to the left and narrowing them per Figure 14b.

A similar analysis of the kinetics/mass transfer balance can be employed to account for the behavior produced by varying AC concentration. Suppose instead that the increase in the reaction rate is of a *comparable* magnitude to the increase in NH_3

limit. As before, the rate of x_a growth increases, but the resulting decline in y_c is not significant as the case considered before due to the relatively greater distance from equilibrium (see point 3 above). This would present in the y_c curve as a nearly parallel slope (compared to other curves in the plot) during the decline from the peak y_c value, and this is indeed the pattern seen in Figure 13a as AC concentration increases. With the decline in ka'' essentially unchanged, and the concentration gradient growing faster as well as over a longer time period, the point after which the overall mass transfer driving force begins to fall is delayed, causing a rightward shift in the y_a peaks that is consistent with the trends noted in Figure 13b.

The findings discussed in the chapter have allowed a general physical framework for the combined reaction and mass transfer kinetics to be deduced; it was found that NH_3 has a relatively high solubility compared to that of CO_2, and thus there will be a greater tendency for NH_3 produced by the decomposition reaction to be retained as a dissolved species on the bulk liquid phase. By Le Chatelier's principle, the accumulation of reaction products in solution will tend to increase the prevalence of the reverse (reformation) reaction, which will in turn tend to slow the net reaction rate. In contrast, the low solubility of CO_2 implies that it will tend to be released into the gas phase almost as soon as it is produced by the decomposition reaction. After the reaction progresses to the point where NH_3 retention in solution is appreciable, it is likely that the chemical kinetics enter a mass transfer-limited regime where the decomposition rate is dictated almost entirely by the rate at which NH_3 is desorbed from the liquid phase. Another important implication of this hypothesis is that the release rate of CO_2 observed

experimentally is closely tied to the chemical kinetics, whereas the release rate of NH_3 is indicative of the mass transfer kinetics. Lastly, the inflection points in the gas-phase concentration histories imply a multi-step reaction [28].

In the following chapter, a multi-step reaction model is developed to incorporate these findings. It is postulated that the differing interactions between the solvent and the reaction products leads to two disparate timescales, and renders the mass transfer kinetics as a consideration of equal importance to the chemical kinetics.

CHAPTER III

REACTION RATE MODELING

The thermo-hydraulic performance of a multiphase HEX reactor consisting of *k* coexisting phases is predicated upon energy, mass, and momentum transfer within a given phase and across the various phases present. The local, instantaneous balance of thermal energy in three dimensions is expressed by the relation:

$$\frac{\partial(\mathbf{u}\rho I)}{\partial t} + \mathbf{u}\cdot\nabla(\mathbf{u}\rho I) = \mathbf{u}\cdot(\nabla\cdot\tilde{\boldsymbol{\sigma}}) + \nabla\cdot\mathbf{q} + S''' \tag{3.1}$$

where ρ is the density, I is the specific enthalpy, $\mathbf{u}$ is the velocity field, $\boldsymbol{\sigma}$ is the Cauchy stress tensor, $\mathbf{q}$ is the heat flux field, and S''' is a (scalar) volumetric source term. The first term on the right hand side of Eq. (3.1) represents the effect of flow work, including viscous dissipation. In most industrial heat transfer applications, this term is typically neglected because it is small compared to the second term; the energy equation is driven by the heat flux and, depending on the situation, the source term. The source term S''' encompasses the energy sink/source contributions of chemical reactions and other volumetric phenomena such as radiation absorption/emission. In this work, the highly endothermic and rapid chemical kinetics of ammonium carbamate (AC) means that S''' is equally as important as $\nabla\cdot\mathbf{q}$. If constitutive relations for $\mathbf{q}$ are known and the velocity field $\mathbf{u}$ is also known, the solution of Eq. (3.1) is predicated upon proper representation and understanding of S'''.

It is at this point that the complicated issue of coupled chemical kinetics, heat transfer, and momentum transfer arises. Before any attempt is made toward understanding the nature of this coupling and how it applies specifically to AC decomposition in a flow environment, it is absolutely crucial to ensure that the chemical kinetics of the reaction can be modeled. As it stands, no report in the literature yet exists that can adequately address this question; previous research [26] has explored rudimentary models for AC decomposition in a HEX reactor, but as was cautioned in the introductory chapter, a more sophisticated model of the chemical kinetics of AC decomposition in PG is needed.

The approach considered here is a multiple step, multiple pathway formulation that assumes the simultaneous occurrence of heterogeneous AC decomposition, AC dissolution into the solvent, homogeneous AC decomposition, and desorption of dissolved gasses. For each process, candidate rate laws are adopted from the latest data for AC decomposition available in the literature, with modifications as needed to for consistency with the experimental data obtained in this study.

At present, the focus is upon explaining the apparently disparate timescales for CO_2 and NH_3 release that were observed in the experiments in Chapter II. The heat transfer considerations, and hence also fitting the model to the calorimetric measurements, will be addressed in subsequent work. Indeed, since the temperature was held constant to within 1°C for a majority of the experiments, it is safe to assume for the chemical kinetics are approximately isothermal. The chemical parameters (e.g. rate and

equilibrium coefficients) may therefore be deduced separately from the thermal parameters (e.g., enthalpy of reaction, enthalpy of absorption/desorption).

3.1 Mathematical Formulation

The experimental results suggest an overall reaction that is comprised of several steps. In the most general sense, the following simultaneous phenomena are present:

- Heterogeneous chemical reaction (solid-to-gas)
- Homogeneous chemical reaction
- Dissolution of solid AC particles
- Gas desorption
- Bubble nucleation, growth, and release

The combined dynamics of these phenomena are represented in terms of a resistance network analogy in Figure 18. The physical states of the various species present are shown as boxed items in Figure 18, while the arrows represent a dynamic process (e.g. chemical reaction, desorption, and so forth) conveying the species between physical states.

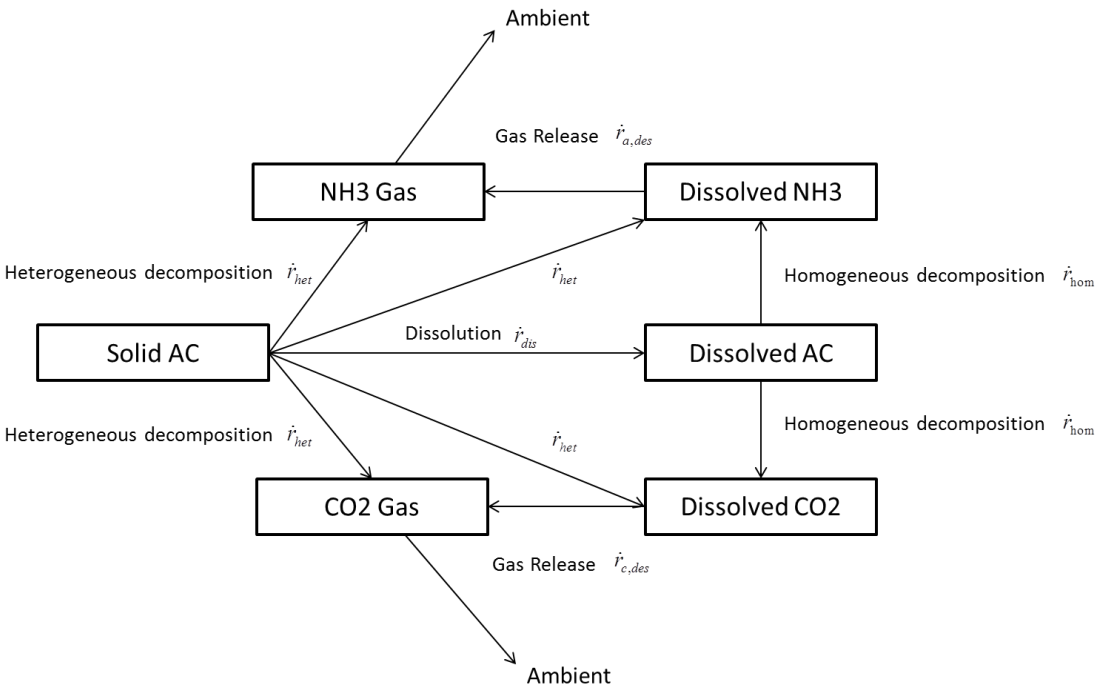

Figure 18. Schematic of reaction pathways in proposed model for decomposition of AC in PG

The model depicted in Figure 18 allows for the possibility that the heterogeneous and homogeneous reaction pathways are not strictly parallel or sequential. For instance, it is possible that both the heterogeneous and homogeneous reactions contribute to the population of dissolved gas species directly. At the same time, the solid AC may also experience dissolution, which contributes to the dissolved AC population, which in turn contributes to the dissolved gas species. The only assumption made at this point is that no other chemical reactions apart from the decomposition and reformation of AC occur In principle, the arrows in Figure 18 may be expressed as rate equations to yield a mathematical representation of the system. As is typical in the analysis of mass transfer in agitated vessels, all dissolved species in the bulk liquid phase are assumed to be

uniformly distributed [37]. The temperature field is also assumed to be without spatial variation, as was also verified experimentally. The species balance equations for solid AC, dissolved AC, dissolved NH_3, and dissolved CO_2 respectively are written (in terms of solvent mole fraction) as follows:

$$\frac{dc}{dt} = -\dot{r}_{dis} - \dot{r}_{het} \tag{3.2}$$

$$\frac{dx_{AC}}{dt} = \dot{r}_{dis} - \dot{r}_{\text{hom}} \tag{3.3}$$

$$\frac{dx_a}{dt} = 2\left(\dot{r}_{\text{hom}} + \dot{r}_{het}\right) - \dot{r}_{a,des} \tag{3.4}$$

$$\frac{dx_c}{dt} = \dot{r}_{\text{hom}} + \dot{r}_{het} - \dot{r}_{c,des} \tag{3.5}$$

where Eqs. (3.2)-(3.5) are represented in terms of solvent (PG) mole fraction. The terms $\dot{r}$ represent the processes depicted in Figure 18. The gas-phase species balance in the reactor headspace (in terms of gas phase mole fraction) is given by:

$$\frac{dy_c^g}{dt} = \frac{\dot{V}_{tot}}{V_g} y_c^g \tag{3.6}$$

$$\frac{dy_a^g}{dt} = \frac{\dot{V}_{tot}}{V_g} y_a^g \tag{3.7}$$

The subscript g is introduced to distinguish the gas-phase mole fractions in the reactor headspace from those present in bubbles in the liquid phase. The following sections present an analysis of the individual rate terms $\dot{r}$ and a discussion of their appropriate formulation.

3.1.1 Solid-Phase Dissolution

The dissolution of a soluble solid material into a bulk solvent is fundamentally a heterogeneous convective mass transfer process. The mass transfer rate from such a material may be written thusly:

$$\dot{r}_{dis} = k_j^{s-l} a_s'''\left(x_j^{s-l} - x_j\right) \tag{3.8}$$

where, k_j^{s-l} is the solid-liquid mass transfer coefficient for species *j*, a_s''' the total surface area of solid particles per unit volume , x_j^{s-l} the concentration of dissolved species *j* at the solid-liquid interface (for dissolution, this is the saturation concentration [37]), and x_j the dissolved species concentration in the bulk liquid. The following discussion shall explore the proper representation of the mass transfer coefficient; treatment of the particle number density is considered in the next section.

3.1.1.1 Solid-Liquid Mass Transfer Coefficient

The complicated hydrodynamics involved with mass transfer between suspended solid particles and a mechanically agitated liquid bulk is rendered even more complex by the presence of multiple species of differing solubility and chemical reaction occurring within both phases. Further still, the characteristic timescale for solid-liquid mass transfer observed in this study (i.e. the longevity of visible solid particles suspended in the liquid phase) is on the order of 30 – 40 seconds, whereas the stirred tank reactor applications for which mass transfer correlations are typically developed are on the order of several minutes or even hours [38]. There is also the possibility that bubbles may nucleate on the particle surface due to localized supersaturation of dissolved gas products in the concentration boundary layer at the particle-liquid interface, which can produce considerable enhancement in the convective mass transfer coefficient [39]; there is evidently no similar instance in the open literature from which mass transfer coefficients were obtained. In either case, we can only regard the conventional convective mass transfer correlations available for solid-liquid mass transfer in stirred tank reactors as providing a first approximation.

Therefore, we approach estimation of the solid-liquid mass transfer coefficients with two expectations in mind:

1) Provide a baseline estimate for numerical parameter estimation – significant departure from values predicted by convective mass transfer correlations can give insight into the dominant physical mechanism in this complex process.

2) Provide a qualitative understanding of how relevant process parameters (e.g. particle size, temperature) will impact solid and liquid phase interaction.

An extensive review of the approaches employed in correlating mass transfer coefficients of suspended solid particles in stirred tank reactors (STRs) is presented by Pangarkar *et al.* [38]. They classified the approaches as follows:

1) Dimensional analysis
2) Kolmogoroff's theory of isotropic turbulence
3) Terminal slip velocity theory
4) Momentum-mass transfer analogies

Dimensional analysis, though it yields correlations that are simple in form, suffers the drawback of being applicable only to the system from which it was derived; the use of Kolmogoroff's theory to obtain spatially average turbulent energy dissipation rates was also criticized by Pangarkar *et al.* as inappropriate on the basis that actual STR conditions have been shown repeatedly to possess considerable spatial variation in turbulence intensities [38, 40]. Thus, it would also be unwise to assume a uniform distribution of turbulence intensities here.

Steinberger and Treybal [41], in their experimental investigation of soluble spheres in a liquid stream, represented the rate of mass loss (dissolution) via the dimensionless Sherwood number $Sh = k_j^{s-l} L_c \big/ D_j$. Here, L_c is a characteristic length, and

D_j the diffusion coefficient for a soluble species *j*. The correlation they proposed has the general form

$$Sh_s = Sh_0 + B\left(\mathrm{Re}_s\, Sc^{1/3}\right)^m \tag{3.9}$$

where, $\mathrm{Re}_s = u_s L_c \rho_l / \mu_l$ is the Reynolds number of the dispersed solid phase, Sh_0 accounts for natural convection at low Re_s, $\mathrm{Re}_s = u_s L_c \rho_l / \mu_l$ is the Schmidt number, and *B* and *m* are constants. The authors found that Sh_s was best correlated with the characteristic length as the diameter of the sphere, with the characteristic velocity *u* being the relative velocity between the particle and liquid phase. The extension of these results to those of agitated vessels is not a trivial task, for in the aforementioned reference the velocity was a fixed, known quantity. Obviously, in agitated vessels, the velocity field varies with space [40] and the hydrodynamic interactions between liquid and solid phases are far more complex than the experimental conditions in [41]. For agitated vessels, Harriot [42] noted that the characteristic velocity for use in correlations such as those proposed by Steinberger and Treybal may be obtained by one of two ways:

1) the terminal velocity of the particle as though it was falling in static liquid, and;

2) the average turbulent fluctuating velocity in the vicinity of the particle.

Harriot also cautioned that such correlations, which are based on steady-state mass transfer, assume a fully-developed concentration boundary layer and are therefore more

applicable to particle sizes that are large compared to the length scale of turbulent eddies.

Harriot observed that a transient component will also be present in the mass transfer coefficient; in the case of penetration theory [42], where mass transfer is dominated by the transient term, the mass transfer coefficient varies according to:

$$k_j^{s-l} = \sqrt{\frac{D_j}{\pi t_e}} \tag{3.10}$$

where, t_e is the timescale for surface renewal, or the inverse of the rate at which the boundary layer is disrupted due to turbulent eddies. What Harriot [42] proposed was a compromise between steady-state mass transfer models and penetration theory. The boundary layer is modeled as a stagnant region of fluid which is only *partially* renewed every t_e seconds. This model is represented as

$$k_j^{s-l} = \frac{D_j}{\delta_e} + \frac{1}{2}\sqrt{\frac{D_j}{\pi t_e}} \tag{3.11}$$

In this case, the parameter δ_e is the effective approach distance of turbulent eddies to the particle surface, which is conceptually the surface area-averaged concentration boundary layer thickness. While this approach is theoretically sensible, the difficulty remains in

determining t_e and δ_e, which Harriot admits does not lend itself easily to quantitative description.

Pangarkar *et al.* [38] offered a correlation that agreed well for both solid-liquid and solid-liquid-gas (i.e., sparged STRs):

$$k_j^{s\text{-}l} = 1.8\times10^{-3}\left(\frac{N_{stir}}{N_{SG}}\right)\left(Sc\right)^{-0.53} \tag{3.12}$$

where, N_{stir} is the agitator speed, N_{SG} is the minimum agitator speed – termed as the "critical impeller speed" in the literature - at which complete particle suspension is first achieved. The term N_{SG} carries the information about fluid properties, solid properties, and STR geometry in addition to representing the relative intensity of turbulence [38]. The fact that this correlation was able to provide accurate predictions of a variety of conditions, including with the presence of gas bubbles, makes it suitable for use in this work. It is apparent from this correlation that N_{SG} is presumed known, or must otherwise be itself modeled in order to implement Eq. (3.12). It was not possible to reliably determine N_{SG} for AC in PG under the temperatures tested because the gas generated by the decomposition reaction obscured the view of particles settling at the bottom of the reaction vessel, and lifetime of the solid-phase would not be sufficient to permit systematic variation of the agitator speed in search of N_{SG}. Under such conditions, there was no reliable way to judge the onset of suspension. Therefore, recourse is made to using semi-theoretical models to predict the critical impeller speed.

A great deal of consideration has been given to predicting critical impeller speeds for STRs with solid suspensions due its industrial significance [43, 44]. Mersmann *et al.* [45] conducted a theoretical analysis of the conditions necessary for solid particle suspension in STRs. In essence, the local turbulent kinetic energy of the flow field must be sufficient to overcome the settling energy of a particle; for a volume of fluid containing a volume fraction ϕ_v of solid particles, this energy threshold is [45]

$$\varepsilon_{ss} = u_s \phi_v \left(1-\phi_v\right)^n g \frac{\Delta\rho}{\rho_l} \tag{3.13}$$

where u_s is the settling (terminal) velocity, and $\Delta\rho$ the difference in density between the solid and liquid phases. Assuming uniform density, we calculate the solid-phase volume fraction as:

$$\phi_v = \frac{c_s}{\rho_s} \tag{3.14}$$

Expressed in terms of the local fluctuating velocity u', the minimum fluctuating velocity intensity is:

$$u' = \left(3u_s^2 d_s c_D \phi_v (1-\phi_v)^n g(\Delta\rho / \rho_s)\right)^{1/4} \tag{3.15}$$

where, c_D is the drag coefficient, d_s is the particle diameter, and ρ_s is the particle density. The authors assumed that the distribution of turbulent dissipation ε followed a normal logarithmic law, and cited that it has been well-established that local fluctuating velocity u' is directly proportional to the tip velocity of the agitator blades. For the suspension of settled particles on the bottom of the reaction vessel, Mersmann *et al.* [45] argued that the minimum fluctuating velocity (in their work, the lower 0.1% tail of the fluctuating velocity PDF); utilizing the aforesaid assumptions on the character of the turbulent energy spectrum, they predicted the following functional relationship between the stirrer tip speed and the minimum fluctuating velocity:

$$\frac{u'_{\min}}{u_{tip}} = 0.088 Ne^{7/18} \left(\frac{d_{stir}}{d_{vessel}} \right)^{3/2} \tag{3.16}$$

where, d_{stir} is the agitator diameter, d_{vessel} is the reactor diameter, and $Ne = p / \rho_l N_s^3 d_{stir}^5$ is the Newton number, where p represents the mechanical power input of the agitator. It was not possible using the batch reactor apparatus to reliably and accurately measure the stirrer power delivered to the liquid-phase, and so a representative value of Ne = 0.35 was chosen, which is typical of marine-type propellers [45].

Reasonable agreement was shown between the published experimental results of several other investigators and the theoretical model proposed by Mersmann *et al*. Lacking experimental data specific for the critical agitator speed in this study, the model

of Mersmann *et al.* [45] in conjunction with the model recommended by Pangarkar *et al.* [38] was chosen to initially estimate the solid-liquid mass transfer coefficient.

3.1.1.2 Diffusion Coefficients of Dissolved Species

Evaluating Eq. (3.12) requires knowledge of the binary diffusion coefficient D_{AC} in order to calculate the Schmidt number *Sc*. Hence, to obtain bounding estimates for k_{dis}, it is also necessary to estimate the diffusion coefficient of AC in PG. The high solubility of both AC and NH_3 in PG presents a possible complication in determining a well-defined value for D_{AC}, which we shall consider as part of the analysis that follows. For a mixture of *N* components, neglecting the Soret effect and ion diffusion, Fick's Law is [46]:

$$\mathbf{j}_i = -D_{ii}\nabla C_i - \sum_{j\neq i}^{N} D_{ij}\nabla C_j \tag{3.17}$$

where $\mathbf{j}$ is the molar flux vector and *C* is the molar concentration for the *i*-th or *j*-th component as indicated; the term D_{ii} is the Fickian diffusion coefficient of the *i*-th component with respect to a concentration gradient of the *i*-th component (termed 'self diffusion coefficient'), while the off-diagonal elements D_{ij} are the Fickian diffusion coefficients of the *i*-th component with respect to a concentration gradient with the *j*-th component. These parameters are also functions of temperature and pressure [46, 47]. In dilute solutions, the solutes interact primarily with the solvent rather than other solutes, and thus the D_{ij} terms are small compared to D_{ii} [48]. It is assumed, in this model, that

the dissolved concentrations of AC, NH_3, and CO_2 are small compared to the molar concentration of the solvent – this is certainly true in the batch reactor experiments, where the total solute concentrations were relatively small (a theoretical maximum mole fraction of ~6%).

To establish the model's suitability beyond the conditions in the batch reactor, we argue that the concentration of dependence of D_a and D_{AC} is small enough (at temperatures necessary for AC decomposition) that they can be well approximated as functions of temperature only. Because CO_2 is only sparingly soluble in PG, it is not necessary to consider concentration effects on its diffusivity. Several investigators have published self-diffusion coefficients for CO_2 [47,49,50], NH_3 [51], and both CO_2 and NH_3 [52] in various solvents at different solute concentrations; however, there is no data in the open literature available for the diffusion coefficients of AC, NH_3, and CO_2 in PG. The diffusion coefficients for NH_3 and CO_2 are estimated based on a modified Stokes-Einstein relation, as was used in a similar case by Deerks and Versteeg [53]:

$$D_j \approx D_{j,H_2O}\left(\frac{\mu_{H_2O}}{\mu_{PG}}\right)^{0.8} \tag{3.18}$$

where D_j is the self diffusion coefficient of species j in PG, $D_{j,H2O}$ is the self diffusion coefficient of species j in water, and μ is the dynamic viscosity. The values of D_a and D_c estimated with Eq. (3.18) over a temperature range of 45°C - 80°C, depicted in Figure 19, show only minor difference between the two:

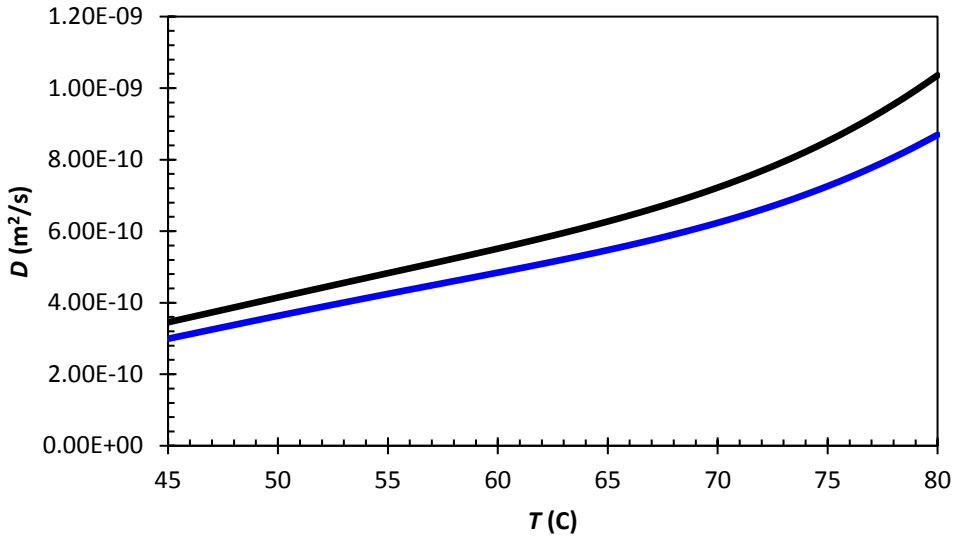

Figure 19. Estimates of D_a (blue line) and D_c (black line) as obtained with Eq. (3.18); $D_{a,H2O}$ and $D_{c,H2O}$ were obtained from Frank *et al* .[49] and Cadogan *et al.* [48], respectively. In the case of D_a, the data for an NH_3 mole fraction of 20%

As to the question of concentration dependency, the data published by Frank *et al.* [51] for NH_3 in water showed an increase in $D_{a,H2O}$ of approximately 30% between infinite dilution ($x_a \approx 0$) and $x_a = 20\%$, which corresponds to the saturation limit of NH_3 at 55°C. Plots of D_a estimated with Eq. (3.18) for NH_3 mole fraction of 0%, 10%, and 20% are provided in Figure 20.

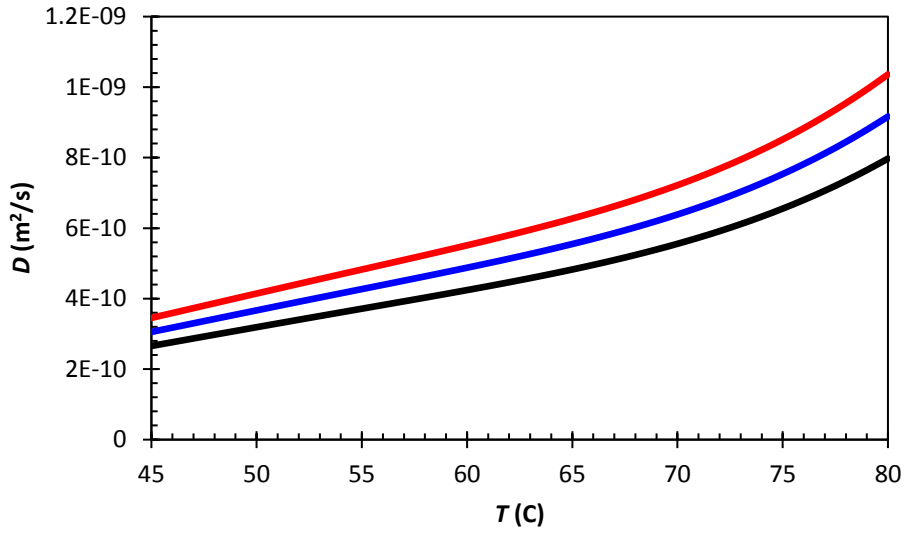

Figure 20. Diffusion coefficient Da of NH3 in PG at different NH3 mole fractions: 0 (black line), 0.1 (blue line), and 0.2 (red line). Da estimated with Eq. (3.18) and using Frank et al.'s results [49].

From Eq. (3.12), one finds that the corresponding difference in k_{dis} (assuming changes in viscosity and density are small, as they appear to be in [51]) is only 14%. In practice, temperatures well in excess of 55°C will be necessary for rapid decomposition, and so the concentration dependence of k_{dis} on x_a or x_{AC} is expected to be lower. If we assume that a similar dependence on concentration exists with PG as the solvent, we are justified in our assumption of small concentration dependence; indeed, Iskrenova and Patnaik [52] determined that the effect of NH_3 concentration in ethylene glycol (which is chemically similar to PG) was weak, although they did not account for chemical reactions in their molecular dynamics simulations. Since there is no known chemical reaction occurring between AC and PG, it is reasonable to expect this pattern to hold with respect to the concentration dependence of D_{AC}. Since there is no data available for

D_{AC} in any fluid system, we shall assume, at present, that $D_{AC} \approx D_a$ with the understanding we will likely overestimate D_{AC} – and thus k_{dis} – since AC is a larger molecule than NH_3. As we are only relying on Eq. (3.12) to provide an informative estimate to guide the parameter estimation process, such compromises in accuracy are acceptable.

3.1.2 Heterogeneous Decomposition

There have been very few studies that examined the kinetics of solid-phase AC decomposition, and no definitive evidence offered as to the reaction pathways and the elementary steps of the reaction. Nevertheless, Ramachandran *et al.* [28] considered three possible models that could plausibly account for the vapor pressure histories obtained during solid-phase AC decomposition in a sealed vessel. Of the three models considered, they judged the following mechanism to be the most promising:

$$\begin{aligned}
&\left(NH_4COONH_2\right)_s \underset{k_{-1}}{\overset{k_1}{\rightleftharpoons}} (NH_2COOH)_s + (NH_3)_s \\
&(NH_2COOH)_s \underset{k_{-2}}{\overset{k_2}{\rightleftharpoons}} (NH_3)_s + (CO_2)_s \\
&(NH_3)_s \underset{k_{-3}}{\overset{k_3}{\rightleftharpoons}} (NH_3)_g \\
&(CO_2)_s \underset{k_{-4}}{\overset{k_4}{\rightleftharpoons}} (CO_2)_g
\end{aligned} \tag{3.19}$$

where the subscript *s* denotes a surface-bound (i.e. on the solid AC surface) species. In this particular scheme, decomposition takes place entirely on the surface: an ammonium ion, which is adjoined to neighboring carbamate ions via hydrogen bonding, is

deprotonated by one of the carbamate anions. The resulting carbamic acid molecule then further decomposes into an NH_3 and CO_2 molecule, which may then desorb from the surface [28].

Ramachandran *et al.* point out that that this process may also occur within the bulk material. They cite the crystalline structure of AC and the ability to qualitatively reproduce their experimental kinetic data (using assumed rate coefficients) as indicators of the proposed model's plausibility. The rate law for this model, subject to the assumption that $k_3 \approx k_4 = k_f$ and $k_{-3} \approx k_{-4} = k_r$

$$\frac{dP}{dt} = k_f \left([NH]_3 + [CO_2] \right) - k_r P \tag{3.20}$$

where, k_f is the forward rate constant and k_r is the reverse rate constant, and P is the total pressure of gas-phase CO_2 and NH_3. Among the scant few models reported in the open literature, the heterogeneous reaction scheme posited by Ramachandran *et al.* is by and large the best supported and appears to be consistent with spectroscopic and crystallographic data available [28]. However, it may be argued that this mechanism can also account for the kinetic behavior observed in more recent studies of AC decomposition in a fluid environment.

Schmidt [10] observed that the decomposition of AC suspended in fluid medium in which it is poorly soluble (Tetraglyme) is exceedingly slow compared to solvents such as ethylene glycol or propylene glycol. Assuming, for the time being, that

Ramachandran *et al.*'s solid-gas decomposition mechanism still holds, the desorption steps in Eq. (3.19) are

$$\begin{aligned} (NH_3)_s &\underset{k_{-3}}{\overset{k_3}{\rightleftharpoons}} (NH_3)_l \\ (CO_2)_s &\underset{k_{-3}}{\overset{k_3}{\rightleftharpoons}} (CO_2)_l \end{aligned} \tag{3.21}$$

where the subscript *l* denotes liquid-phase absorbed species. If the solid AC is poorly soluble in the liquid-phase, then it is reasonable to also assume that NH_3 and CO_2 are poorly soluble as well. This implies that $k_3 << k_{-3}$ and $k_4 << k_{-4}$, and it follows that the overall reaction rate is limited by the steps in Eq. (3.21).

Hence, the rate of AC decomposition would be a function of the transfer of desorbed gases away from the solid surface, which is controlled by diffusion and hydrodynamic considerations rather than chemical kinetics. This situation is analogous to the "NH_3 limit" condition observed experimentally in this work, the difference being that this limit would be reached almost instantly if a poor solvent were used. These facets make the scheme proposed by Ramachandran *et al.* a favorable first step in modeling the heterogeneous decomposition mechanism in the presence of PG.

The other aspect that needs to be addressed is the applicability of this model when both a surface reaction and dissolution process occur simultaneously. As dissolution occurs, the production of the surface bound species will most assuredly be affected since the exchange of protons and re-arrangement of hydrogen bonds with neighboring molecules in the crystal structure are involved [28]. Additionally, the NH_3,

CO_2, and dissolved AC concentration boundary layer in the vicinity of the AC solid particle may induce local diffusivity, viscosity, and liquid-phase density gradients. The present lack of experimental evidence elucidating the relative effect of dissolution to that of heterogeneous decomposition of AC renders a precise account of such highly nonlinear phenomena virtually impossible. Therefore, as an initial approximation, we shall not attempt to model these nonlinearities explicitly and instead assume that dissolution and heterogeneous decomposition are parallel, independent processes. It is certainly conceptually and physically reasonable to presume that the overall rate of solid AC consumption is a parallel combination of dissolution and chemical reaction. The rate coefficients for both mechanisms will be incorporated with empirical correction factors to provide adjustment for these non-idealities.

3.1.2.1 Implementation of the Heterogeneous Reaction Model

The differing solubility of NH_3 and CO_2 in PG, requires that desorption of the surface bound species be treated with two separate rate equations, as it is to be expected that the forward (and reverse) rate coefficients k_4 and k_3 will not be comparable as was assumed in Eq. (3.20). Also, the total pressure can no longer be used to represent the combined desorbed gas concentrations. The presence of dissolved NH_3 and CO_2 within the liquid film permits the possibility that the homogeneous reaction will occur; this will be examined in the next section – concerning the homogeneous reaction model – where it will be shown to be of minor importance.

The first question to address is the species balance equations for the surface-bound species $(NH_3)_s$, $(CO_2)_s$ and $(NH_2COOH)_s$. According to Ramachandran *et al.*'s [28] model, the forward reaction $(AC)_s \rightarrow (CA)_s + (A)_s$ is zero-order and the dissociation of carbamic acid is a pseudo first-order process. With the eventual intent of interfacing the surface reaction model with the liquid and gas-phase transport models, it is convenient to define dimensionless surface concentrations $\tilde{x}$ as

$$\tilde{x}_c = [CO_2]_s \frac{M_l}{\bar{d}_i \rho_l} \tag{3.22}$$

$$\tilde{x}_a = [NH_3]_s \frac{M_l}{\bar{d}_i \rho_l} \tag{3.23}$$

$$\tilde{x}_{CA} = [CA]_s \frac{M_l}{\bar{d}_i \rho_l} \tag{3.24}$$

Where $\bar{d}_i$ is the mean initial solid-phase particle diameter, and M_l is the molar mass of the liquid phase. Assuming that carbamic acid formation is zero-order and its decomposition into CO_2 and NH_3 is pseudo first-order, and incorporating the remaining elementary steps in Eq. (3.19), the corresponding differential equations for the evolution of $\tilde{x}_a$, $\tilde{x}_c$ and $\tilde{x}_{CA}$ are:

$$\frac{d\tilde{x}_a}{dt} = k_1\left(1 - \frac{1}{K^s_{a-CA}}\tilde{x}_{CA}\tilde{x}_a\right) + k_2\left(\tilde{x}_{CA} - \frac{1}{K^s_{a-c}}\tilde{x}_a\tilde{x}_c\right) - k_3\left(\tilde{x}_a - \frac{x_a^{s-l}}{\bar{d}_i K_a^{s-l}}\right) \tag{3.25}$$

$$\frac{d\tilde{x}_c}{dt} = k_2\left(\tilde{x}_{CA} - \frac{1}{K^s_{a-c}}\tilde{x}_a\tilde{x}_c\right) - k_4\left(\tilde{x}_c - \frac{x_c^{s-l}}{\bar{d}_i K_c^{s-l}}\right) \tag{3.26}$$

$$\frac{d\tilde{x}_{CA}}{dt} = k_1\left(1 - \frac{1}{K^s_{a-CA}}\tilde{x}_{CA}\tilde{x}_a\right) - k_2\left(\tilde{x}_{CA} - \frac{1}{K^s_{a-c}}\tilde{x}_a\tilde{x}_c\right) \tag{3.27}$$

Where k_1, k_2, k_3 and k_4 are the forward rate coefficients for the individual elementary steps; x_a^{s-l} and x_c^{s-l} are the concentrations of dissolved NH_3 and CO_2 at the particle surface, respectively; $K_a^{s-l} = k_3/k_{-3}$ and $K_c^{s-l} = k_4/k_{-4}$ are the equilibrium constants for the solid-liquid desorption of NH_3 and CO_2, respectively; $K^s_{a-c} = k_2/k_{-2}$ and $K^s_{a-CA} = k_1/k_{-1}$ are the equilibrium coefficients for the decomposition and formation of carbamic acid, respectively. With eight unknown parameters and a total of five non-linear terms, the heterogeneous reaction model is by far the most complicated and difficult to adjust parametrically since none of the rate and equilibrium coefficients are known *a priori*. Note that the terms involving k_3 and k_4 represent solid-to-liquid film desorption. Note also that carbamic acid is a fundamentally *unstable* intermediate [28], which was implicit in the assumption by Ramachandran *et al*. that $[CA]_s << [NH_3]_s$ and

$[CO_2]_s$. Thus, we may invoke the quasi-steady assumption with respect to carbamic acid, i.e. $\tilde{x}_{CA}$ is small and approximately constant.

The volumetric rate equations for the desorption of surface bound species into the liquid film are

$$\dot{r}_c^{s-l} = k_5 a_s'''\left(\tilde{x}_c - \frac{x_c^{s-l}}{\bar{d}_i K_c^{s-l}}\right) \tag{3.28}$$

$$\dot{r}_a^{s-l} = k_6 a_s'''\left(\tilde{x}_a - \frac{x_a^{s-l}}{\bar{d}_i K_a^{s-l}}\right) \tag{3.29}$$

As discussed in the previous section, the transfer of species through the liquid film is described by

$$\dot{r}_c^{s-l} = k_c^{s-l} a_s'''\left(x_c^{s-l} - x_c\right) \tag{3.30}$$

$$\dot{r}_a^{s-l} = k_a^{s-l} a_s'''\left(x_a^{s-l} - x_a\right) \tag{3.31}$$

Since there can be no mass storage at solid-liquid interface, Eqs. (3.28) and (3.29) equate to Eqs. (3.30) and (3.31), respectively.

The solid-phase reaction kinetics are simplified in this study by assuming that desorption of CO_2 and NH_3 is the rate limiting step – i.e, the process is mass transfer-limited. Accordingly, the surface concentrations of CO_2 and NH_3 are quasi-steady and approximately equal to their equilibrium values, obviating the need to estimate the four equilibrium coefficients and rate coefficients in Eqs. (3.25) – (3.27), and leaving only the mass transfer coefficients and surface concentrations in Eq. (3.30) and (3.31). Assuming that the solvent does not influence the surface-level chemical interactions between AC, carbamic acid, and the adsorbed gas molecules, the equilibrium adsorbed surface concentrations are identical to the case of dry AC as in [28]:

$$x_a^{s-l} = \frac{2}{3}\frac{P_{eq}}{\Re T K_a^{s-l}}\left(\frac{M_l}{\rho_l}\right) \tag{3.32}$$

$$x_c^{s-l} = \frac{1}{3}\frac{P_{eq}}{\Re T K_c^{s-l}}\left(\frac{M_l}{\rho_l}\right) \tag{3.33}$$

where, in accordance with Ramachandran *et al*'s [28] assumption, $K_a^{s-l} \approx K_c^{s-l} = K_{het}$ in the absence of a solvent, and P_{eq} is the dissociation pressure of dry AC – a function of temperature only [7-9]. The difference in the respective solubilities of CO_2 and NH_3 in PG means that the equilibrium coefficients K_a^{s-l} and K_c^{s-l} are most likely interdepenent functions of the complex solid-phase equilibria asserted by Eqs. (3.25) – (3.29). It is, however, possible to eliminate either Eq. (3.30) or Eq. (3.31) and consider only K_c^{s-l} or

K_a^{s-l} (respectively) as a function of temperature only without a substantial loss in fidelity; this will be discussed further in Chapter IV.

3.2.2.2 Particle Surface Concentration

We now grant consideration to the particle surface area concentration, a_s''' . The surface area dependence of both the dissolution kinetics and heterogeneous reaction requires that the distribution of particles sizes must be accounted for. Mathematically, the total, instantaneous rate of dissolution or heterogeneous reaction is the sum of the contributions from the different particle sizes present in the slurry. The fundamental relationship that must be ascertained is the manner in which the surface area of particles belonging to different size classes varies as the solid phase is depleted. We seek to obtain a differential equation or system of differential equations describing how the characteristic size of particles in an infinitesimal size range is changing with time. To proceed with the analysis, let us assume that

1) The total number of particles in the reactor at any time *t* does not change. As dissolution (or decomposition) occurs, the particles shrink in size; particles that obtain a diameter of zero are considered "depleted" and no longer contribute to the total rate of mass transfer. There is of course the possibility that particles may split into smaller particles due to mechanical stresses, or agglomerate to from larger particles. The AC salt particles used in this study were visibly fine crystalline hexahedra that flowed easily as long they were kept free of moisture, and required significant force to break into smaller pieces (say, a mortar and pestle

or extremely prolonged agitation in the sieves). It is unlikely that there is sufficient shear or impact force in the reactor to cause particle break-up. The possibility of agglomeration is also unlikely because of the rapid rate of dissolution.

2) The particles are spherical in shape. Harriot [42] pointed out that the effect of shape on the mass transfer coefficient is unimportant compared to other parameters affecting solid-liquid mass transfer.

3) The dissolved species concentration and temperature field in the liquid phase are spatially uniform.

From assumption (1), the number density for any particle size is easily computed using knowledge of the initial particle size distribution and other easily obtainable parameters. Consider the number density of a population of spherical particles having initial radii r_i between r_i and $r_i + dr_i$:

$$n_s''' = \frac{3 f\left(r_i\right) m_{AC}}{4\pi r_i^3 \rho_s} \tag{3.34}$$

where, m_{AC} is the total mass of solid AC introduced into the reactor and $f\left(r_i\right)$ is the particle size distribution function, which gives the fraction of m_{AC} having an initial radius between r_i and $r_i + dr_i$, per unit radius. For particles belonging to this differential size range, the instantaneous rate of solid-phase depletion (for particles in this size range) due to both heterogeneous reaction and dissolution is

$$\frac{dc_s}{dt} = \pi r_s^2 n_s''' \left(\frac{M_{AC}\rho_l}{M_l} \right) \left(\frac{1}{3} k_c^{s-l} \Delta x_c + \frac{2}{3} k_a^{s-l} \Delta x_a + k_{AC}^{s-l} \Delta x_{AC}^{s-l} \right) \tag{3.35}$$

where $c_s = c_s(r_i;t)$ is the solvent mole fraction of solid particles and $r_s = r_s(r_i;t)$ is the instantaneous radius, both of which are with reference to particles whose initial radius is in the neighborhood of r_i; $\Delta x_{AC} = x_{AC,sat} - x_{AC}$ is the concentration driving force for dissolution mass transfer, $\Delta x_a = x_a^{s-l} - x_a$ is the driving force for surface desorption of NH_3, and $\Delta x_c = x_c^{s-l} - x_c$ is the driving force for surface desorption of CO_2. We note here that pursuant to assumption (3), Δx_{AC}, Δx_a and Δx_c are not functions of particle size. More importantly, because any give particle is exposed to the same conditions at any location in the reactor, the distribution of solid particles within the reactor is unimportant.

One may also write the mass concentration of solid particles with initial sizes about r_i as

$$c_s = \frac{4\pi}{3} r_s^3 \rho_s n_s''' \tag{3.36}$$

Eq. (3.34) can be differentiated to obtain another expression for the depletion rate of the differential particle population:

$$\frac{dc_s}{dt} = 4\pi r_s^2 n_s''' \rho_s \frac{dr_s}{dt} \tag{3.37}$$

Equating Eqs. (3.36) and (3.37) and integrating the resulting expression for the rate of particle diameter change, we obtain

$$r_s\left(t; r_i\right) = r_i - \int_0^t \frac{\dot{r}_s}{\pi r_s n_s'''} dt = r_i - N_s\left(t\right) \tag{3.38}$$

To ensure that Eq. (3.38) is physically realistic, a restriction must be placed on the function $N(t)$ such that particles whose size has shrunk to zero no longer contribute to the total depletion rate:

$$N_s(t; r_i) = \begin{cases} \int_0^t \frac{dc_s}{\rho r_s n_s'''} & \int_0^t \frac{dc_s}{\rho r_s n_s'''} \le r_i \\ r_i & \int_0^t \frac{dc_s}{\rho r_s n_s'''} > r_i \end{cases} \tag{3.39}$$

Hence, the total surface area concentration is a superposition of all particle sizes:

$$a_s''' = \frac{3 m_{AC}}{r_s} \int_0^\infty \frac{f(r_i) r_s^2}{r_i^3} dr_i \tag{3.40}$$

A useful simplification is achieved by noting that

1) the AC particle sizes considered were within a known range, so the limits of integration in Eq. (3.40) can be replaced with $r_{i,\min}$ and $r_{i,\max}$ (the smallest remaining particles and largest, respectively) and;
2) for a given particle size range, the distribution of particle sizes was observed to be approximately constant, which is to say $f\left(r_i\right) = 1/\Delta r_i$.

Hence,

$$a_s''' = 3\frac{m_{AC}}{r_s \Delta r_i}\int_{r_{i,\min}}^{r_{i,\max}} \frac{\left(r_i - N_s(t)\right)^2}{r_i^3} dr_i \tag{3.41}$$

According to Harriot's [42] experimental observations, the relatively narrow range of particle sizes allows the mass transfer coefficient to be approximated as constant with respect to particle size class – although it may change with time. To satisfy the constraint dictated by Eq. (3.39), the lower limit of integration in Eq. (3.41) is replaced with $r_{i,\min}^* = \max(r_{i,\min}, N_s(t; r_{i,\min}))$, yielding

$$a_s''' = \frac{3m_{AC}}{r_s \Delta r_i}\left[\ln\left(\frac{r_{i,\max}}{r_{i,\min}^*}\right) + 2N_s\left(\frac{1}{r_{i,\max}} - \frac{1}{r_{i,\min}^*}\right) - \frac{1}{2}N_s^2\left(\frac{1}{r_{i,\max}^2} - \frac{1}{r_{i,\min}^{2*}}\right)\right] \tag{3.42}$$

3.*1.3 Homogeneous Decomposition*

At present, there has been no investigation reported in the literature concerning the kinetics of homogeneous AC decomposition (i.e. in the dissolved state). Schmidt [10] had previously observed that AC decomposition occurred in solution with both ethylene glycol and PG, but no rate law or analysis of the chemical kinetics was published. There is, however, a substantial body of research reported about AC in the system NH_3-CO_2-H_2O, which does offer insight into the equilibria and kinetics in the presence of a liquid solvent. Without the availability of experimental data for the solution chemistry of NH_3 and CO_2 in PG, recourse is made to this chemically similar and well-studied solvent-solute system for guidance in the choosing the appropriate rate law. It is important to bear in mind that the objective is ultimately to produce a model that can be fitted to the batch reactor data over a wide range of operating conditions. And while the chemical kinetics model should be physically reasonable, an exact account of the chemistry is not necessary to accomplish the goals of this work.

3.1.3.1 Homogeneous Reaction Kinetics with Water as the Solvent

Quantitative spectroscopic studies [54, 55] of the chemistry of NH_3-CO_2-H_2O have revealed a complex system of simultaneous reversible reactions and solution speciation that includes ammonium carbamate, ammonium carbonate, ammonium ions, carbonate ions, hydroxide ions, in addition to free NH_3 and CO_2. Naturally, this invites the complication of additional side reactions being possible with NH_3 and CO_2 in PG, particularly the decomposition of AC to ammonium carbonate, $(NH_4)\ CO_3$ [56]. Before addressing this issue, the kinetics of AC reformation in aqueous solution will be reviewed.

Pinset *et al.* [57] claimed that in an aqueous solution, the net reaction between CO_2 and NH_3 to form NH_4^+ and NH_2COO^- (dissolved AC) followed a second-order rate law, viz. $\dot{r} \propto \left[NH_3\right]\left[CO_2\right]$. The same claim was echoed later by Hatch and Pigford [53]. Essentially, it was assumed that a CO_2 molecule and an NH_3 molecule formed a carbamate ion, $NH_2COO^{—}$, and a free proton. The H^+ would instantaneously react with a free NH_3 molecule to form NH_4^+ and thence give AC. Danckwerts [58], building upon the work of Caplow [59], proposed that carbamate formation with CO_2 occurred by a two-step process wherein a zwitterion is formed by the combination of CO_2 and an amine *R*, followed by rapid deprotonation by a base *B*:

$$CO_2 + R_2NH \underset{k_{-1}}{\overset{k_1}{\rightleftharpoons}} R_2^+NHCO_2^- \tag{3.43}$$

$$R_2^+NHCO_2^- + B \underset{k_{-B}}{\overset{k_B}{\rightleftharpoons}} R_2NCO_2^- + BH^+ \tag{3.44}$$

The rate equations for this scheme are:

$$-\frac{d[CO_2]}{dt} = k_1[CO_2][R_2NH] - k_{-1}[Z] \tag{3.45}$$

$$-\frac{d[Z]}{dt} = \sum k_B[B][Z] - \sum k_{-B}[BH^+][Z] \tag{3.46}$$

Where [Z] is the concentration of the zwitterion $R_2NCO_2^{-1}$ and the term $\sum k_B[B]$ accounts for any bases present in the system that deprotonate the zwitterion. Danckwerts cited "… a close analogy between the formation of carbamates by CO_2 and the formation of substituted ureas by cyanic acid" as justification for this generalization. According to this mechanism, if one assumes that the concentration of the zwitterion is quasi-steady and the deprotonation is irreversible (i.e. $k_B >> k_{-B}$), then the apparent second order rate coefficient $k_{obs} \equiv \left(d[CO_2]/dt\right)/[CO_2][Am]$ is

$$k_{obs} = \frac{k_1}{1 + \dfrac{k_{-1}}{\sum k_B[B]}} \tag{3.47}$$

Danckwerts argued that this reaction scheme accounted for the apparently second-order kinetics reported when strong bases were present in the solution -- when $k_{-1} / \sum k_B[B] << 1$. On the opposite extreme, if the aforesaid term is significantly greater than unity, then the protonation rate and zwitterion formation rate are of similar magnitude, yielding,

$$k_{obs} = \frac{k_1}{k_{-1}} \sum k_B[B] \tag{3.48}$$

This asymptotic behavior allowed Danckwerts' model to encompass a host of conditions, and has been frequently adopted [60, 61] for modeling simultaneous absorption and chemical reaction phenomena with CO_2 in aqueous NH_3 solutions. Danckwerts' zwitterion mechanism was criticized by Crooks and Donnellan [62], who attempted to apply it to the reaction with CO_2 and the amine 2,2'-iminodiethanol, considering the two possible cases where either the amine or water serves as the base B. Using this model, their estimation for the rate coefficients k_1, k_{-1} and k_B, k_{-B} based on known values of the equilibrium constants for this system were shown to be implausible. Crooks and Donnellan instead argued that, rather than a two-step zwitterion reaction, the CO_2 will react with an amine by forming a "…loosely-bound encounter complex" which either break up or are deprotonated by an amine or water molecule [62]. Thus, the reaction is a single-step termolecular reaction, and the apparent rate coefficient (with respect to CO_2) is [62]

$$k_{obs} = k_{Am}[Am] + k_w[H_2O] \quad (3.49)$$

where $[H_2O]$ is the concentration of water, taken as 55 mol/dm^3 by Crooks and Donnellan, k_{Am} is the deprotonation rate coefficient for the particular amine under consideration, and k_w is the deprotonation rate coefficient for water. The three amines studied in their experiments utilizing the conductimetric stopped-flow technique were in good agreement with their model. A particularly illuminating discussion was given by da Silva and Svendsen [63], revisiting the two conflicting models from a computational angle by performing *ab initio* calculations on two CO_2-amine-H_2O systems: monoethanolamine (MEA), known to exhibit second-order kinetics overall, and diethanolamine (DEA), which showed third-order kinetics overall. They concluded that the single-step, third-order reaction was the most likely in view of both their *ab initio* calculations and the experimental data published for MEA and DEA. Interestingly, according to da Silva and Svendsen, the solvent itself may act as a base that assists in the deprotonation of the CO_2-amine complex. This model was applied successfully by Liu *et al.* [61] in an experimental study of CO_2 absorption in aqueous NH_3 with a wetted wall contactor. They were able to correlate their data well with the termolecular reaction model over a wide range of temperatures (10°C - 40°C) and NH_3 concentrations (1% - 7.5% by weight).

3.1.3.2 Selection of a Model for Homogeneous Decomposition in PG

The most prominent issue is the fact that the formation of AC in solution was assumed by so many authors to be irreversible, which contradicted the spectroscopic kinetics work of Wang *et al.* [64]. Indeed, if we were to assume this to be the case here, it would imply that homogeneous decomposition of AC is not possible, and the experimentally observed gas release was purely desorption of dissolved NH_3 generated by the heterogeneous reaction. At first glance this may appear to be a reasonable explanation, but it does not account for the high rates of CO_2 release that were observed experimentally even after all visible solid AC had disappeared. It can therefore be said with a high degree of confidence that -- for the conditions considered here at least -- AC decomposition is occurring homogeneously. The other immediate concern is that the models introduced above have not been tested with other solvents. The preceding literature review suggests that, due to its generality and ability to address the shortcomings (as pointed out by Crooks and Donnellan [62]) of the zwitterion model, the termolecular model is the most promising framework from which to approach the homogeneous decomposition of AC in a PG solvent environment. Furthermore, regardless of solvent choice, it is clear that in order for a carbamate molecule to form, an NH_3 molecule must be deprotonated while another must gain a proton. This is exactly the case if the amine (NH_3 in this case) serves as one of the bases in the termolecular model that deprotonates the encounter complex between NH_3 and CO_2, which subsequently becomes a carbamate. As an initial assumption, we posit that PG does not

participate as a base, and thus the reverse reaction according to the termolecular model is, in terms of solvent mole fraction,

$$\dot{r}_{r,\mathrm{hom}} = k_{r,\mathrm{hom}} x_a^2 x_c \tag{3.50}$$

Thus the net homogenous reaction is written

$$\dot{r}_{\mathrm{hom}} = k_{f,\mathrm{hom}} \left(x_{AC} - \frac{1}{K_{\mathrm{hom}}} x_a^2 x_c \right) \tag{3.51}$$

Where, $K_{\mathrm{hom}} \equiv k_{f,\mathrm{hom}} / k_{r,\mathrm{hom}}$ is the equilibrium coefficient for the decomposition/reformation of dissolved AC, $k_{f,\mathrm{hom}}$ is the forward reaction coefficient, and $k_{r,\mathrm{hom}}$ is the reverse reaction coefficient. These rate coefficients are not known *a priori*; they must be deduced parametrically by fitting the overall model to the experimental data.

3.1.4 Gas Desorption

The dissimilar solubilities of CO_2 and NH_3 in PG requires that two separate approaches be taken in the analysis of gas desorption phenomena. It was stated before that, due to its low solubility, bubble formation would be driven primarily by CO_2, whereas for NH_3 desorption would primarily occur to rising CO_2 bubbles and the interface between the bulk liquid and gas phases. A relationship between the concentration of dissolved CO_2, the solvent properties, and saturation conditions is required to predict the rate of nucleation and release. Secondary to this are relations to predict the volumetric mass transfer coefficient between the liquid and dispersed gas phase. In the case of NH_3, since it did not reach its saturation limit in PG under the conditions studied, we require only a means to predict the volumetric mass transfer coefficient.

3.1.4.1 General Considerations

Hikita *et al.* [65] and more recently Kierzkowska-Pawlak and Chacuk [66] approached the analysis of gas desorption by separating the total mass transfer rate into two parallel modes of desorption: bubble desorption (superscript *b*) and quiescent fluid desorption (superscript *g*), which we adopt here:

$$\dot{r}_{c,des} = \dot{r}_c^b + \dot{r}_c^g \tag{3.52}$$

$$\dot{r}_{a,des} = \dot{r}_a^b + \dot{r}_a^g \tag{3.53}$$

Quiescent desorption is fairly straightforward to model, requiring only knowledge of the gas-liquid interfacial area between the liquid phase and reactor headspace, and the overall mass transfer coefficient, $k_j^{l\text{-}g}$, for a volatile species *j* defined by:

$$\frac{1}{k_j^{l\text{-}g}} = \frac{1}{k_j^l} + \frac{1}{H_j k_j^g} \tag{3.54}$$

where, k_j^l is the liquid-side mass transfer coefficient and k_j^g is the gas-side mass transfer coefficient. The quiescent desorption rate for a gas species *j* is then

$$\dot{r}_j^g = \frac{k_j^{l-g} A_g}{V_l}\left(x_j - \frac{y_j^g}{H_j}\left(\frac{PM_l}{\rho_l \Re T_g}\right)\right) \tag{3.55}$$

where, A_g is the surface area of the bulk liquid-bulk gas phase interface. For bubble desorption, the task is decidedly more complicated. When a solution with volatile components becomes supersaturated, bubble nucleation occurs. With the addition of bubbles in contact with the liquid phase, additional surface area becomes available for desorption mass transfer to occur. The hydrodynamic interactions between the bulk

liquid and rising bubbles also produces an enhancement in the gas-liquid mass transfer coefficient [65].

3.1.4.2 CO_2 Desorption

Kierzkowska-Pawlak and Chacuk [66] found that these three processes combined to produce a non-linear function of the degree of supersaturation in their measurements of the release of CO_2 from propylene carbonate dimethyl ether of polyethylene glycol and N-methyl-2-pyrrolidone solutions in a baffled, agitated vessel. They represented the desorption process as

$$\frac{\dot{n}_{des}}{V_l} = k_{c,des} A_{tot} \left([sol]_l - [sol]_{l-g} \right) \tag{3.56}$$

where $[sol]_l$ is the bulk solute concentration, $[sol]_{l-g}$ is the liquid-side solute concentration in mol/L at the gas-liquid inerface. In the case of a supersaturated solution near atmospheric pressure, $[sol]_{l-g} = [sol]_{sat}$. They reasoned that at low supersaturation (at the "low bubbling region"), the volumetric mass transfer coefficient could be approximated as a combination between quiescent desorption and bubble desorption, which they represented in their paper as:

$$k_{c,des} A_{tot} = \frac{k_c^{l-g} A_g}{V_l} + k_c^{l-b} a_b''' \tag{3.57}$$

This is essentially a re-statement of Eq. (3.55), with the caveat that the concentration driving force $[sol]_l - [sol]_{l-g}$ is between the bulk liquid and bulk gas phase. Thus, Eq. (3.57) assumed that the gas-liquid equilibrium conditions between the bulk liquid and bulk gas phase is comparable to that between the bulk liquid and dispersed gas phase. Since the bulk gas-phase is continuously flushed with N_2, it is not advisable to use Eq. (3.57) as written; rather, the quiescent desorption contribution will be proportional to $[sol]_l - [sol]_g$ (where the subscript *g* indicates the bulk gas-phase), and the bubble desorption contribution will be proportional to the degree of supersaturation, *i.e.* $[sol]_l - [sol]_{sat}$.

If the dispersed gas phase consists of fine bubbles, then the disjoint pressure due to surface tension forces means that, in general, the gas-liquid equilibrium conditions for fine gas bubbles will be different from that of the flat gas-liquid interface. In this case the error incurred by assuming the two phase equilibria to be comparable is small; for an average bubble diameter d_b on the order of 2 mm, and taking the surface tension σ of PG to be 0.036 N/m [67], the disjoint pressure between the dispersed gas phase and liquid phase is

$$\Delta P = \frac{4\sigma}{d_b} \approx 70 Pa \tag{3.58}$$

This is a small value, and may reasonably be neglected. Henceforth, *P* shall mean the pressure in both dispersed gas phase and bulk gas phase (neglecting the small

hydrostatic pressure component in the bulk liquid phase). We have assumed here that the nucleation-growth-release cycle of a typical bubble is rapid compared to the residence time of the bubble in the liquid phase following detachment. The larger disjoint pressures associated with bubbles immediately following nucleation will not play a significant role in the overall desorption process.

From dimensional analysis and curve fitting to their experimental desorption data, Kierzkowska-Pawlak and Chacuk [66] derived an expression for the bubbling component of the volumetric mass transfer coefficient:

$$\frac{k_c^{l-b} a_b'''}{N_{stir}} = \left(1.22E-6\right) \mathrm{Re}_{stir}^{0.69} We^{0.42} \gamma^{2.2} \tag{3.59}$$

where Re_{stir} is the stirrer Reynolds number, N_{stir} is the stirrer speed in s^{-1}, $We = \rho_l N_{stir}^2 d_{stir}^3 / \sigma$ is the Weber number, and $\gamma = \left([sol]_l - [sol]_{sat}\right)/[sol]_{sat}$. Kierzkowska-Pawlak and Chacuk claimed a mean error of 18.4% within the ranges $3.08 < We < 29$, $262 < Re_{stir} < 3987$, and $0 < \gamma < 4$. The success of this correlation for predicting supersaturated desorption of CO_2 from different solvents with a single equation (within a reasonable error margin) recommends it as a first step for predicting the desorption rate of CO_2 from PG. The drawback is that it is impossible to discern the relative contributions to the total mass transfer rate due to bubble generation (including nucleation, growth, and release) and mass transfer to existing bubbles. The fraction of the total CO_2 release rate due solely to bubble nucleation is an important parameter since

knowledge of the bubble population is required to estimate the total gas-liquid contact area and the gas-liquid mass transfer coefficient. These calculations are, as will be shown, vital to modeling the bubble-desorption component $\dot{r}_a^b$ for NH_3. We assume that due to the low average bubble residence time (< 1 s approximately), the dominant contributor to the CO_2 desorption rate is the generation of bubbles.

3.1.4.3 NH_3 Desorption

NH_3 release is expected to play only a minor role in the nucleation of bubbles in the slurry; to model NH_3 bubble-desorption, we have

$$\dot{r}_{a,des} = k_a^{l-b} a_b''' \left(x_a - y_a^b \left(\frac{PM_l}{H_a \rho_l \Re T_g} \right) \right) \tag{3.60}$$

where, a_b''' and y_a^b are the average volumetric gas-liquid contact area and gas-phase concentration of the bubble population. The average volumetric gas-liquid contact area may be estimated if the void fraction β and the average bubble diameter are known, assuming spherical bubbles [36]:

$$a_b''' = \frac{6\beta}{d_b} \tag{3.61}$$

A correlation developed by Kudrewizki [68] was recommended by Garcia-Ochoa *et al.* [36] to predict the void fraction, with a viscosity correction:

$$\frac{\beta}{1-\beta} = 0.819 \frac{U_g^{2/3} N_{stir}^{2/5} d_{stir}^{4/15}}{g^{1/3}} \left(\frac{\rho_l}{\sigma}\right)\left(\frac{\rho_l}{\rho_l - \rho_g}\right)\left(\frac{\rho_l}{\rho_g}\right)^{-1/15}\left(\frac{\mu_l}{\mu_g}\right)^{-1/4} \tag{3.62}$$

where U_g is the superficial gas velocity and d_{stir} is the agitator blade diameter (ca. 50 mm in this study). Note that this correlation was developed for *sparged* stirred tanks, viz. the gas is introduced at a single point, whereas in this case gas is generated throughout the liquid volume. Since in turbulent agitated vessels the bubble size and hold-up is most strongly influenced by the agitator speed [36] (which is also the assumption made by Kudrewizki [68]), the void fraction should still depend on the same variables as in Eq. (3.60). Allowance is made for the possibility that the leading multiplier and exponents on d_{stir}, $N_{stir,}$ and perhaps U_g may need to be adjusted to fit the experimental data in this study. The average bubble diameter d_b is assumed to be on the same order of the maximum stable bubble size in turbulent conditions [36]:

$$d_b \sim d_{b,\max} = 0.7 \frac{\sigma^{0.6}}{\left(p/V_l\right)^{0.4} \rho_l^{0.2}} \left(\frac{\mu_l}{\mu_g}\right)^{0.1} \tag{3.63}$$

where p is the power input to the agitator. Power inputs of ~0.1 W were typical in this work, and using representative values for μ_l, μ_g, σ, and ρ_l, Eq. (3.63) gives a bubble

diameter of ~3 mm. This prediction is consistent with qualitative observations from Chapter II.

The determination of the overall mass transfer coefficient between the dispersed gas phase and bulk liquid phase is simplified by the assumption that the gas-side mass transfer resistance (in the bubbles) is negligible. The liquid-side mass transfer coefficient for bubbles in an agitated vessel is based on penetration theory, with the effective exposure time t_e from Eq. (3.10) estimated with the ratio of eddy length-scale to the Kolmogoroff fluctuating velocity [36]:

$$k_a^{l\text{-}b} = 2\sqrt{\frac{D_a}{\rho}}\left(\frac{p}{V_l \eta_l}\right)^{1/4} \tag{3.64}$$

It is fortunate that in Eq. (3.64) only a crude estimate of the average turbulent energy dissipation p/V is required, since its exponent of ¼ renders $k_a^{l\text{-}b}$ fairly insensitive to errors in measuring p.

In summary, Eqs. (3.52) and (3.53) become:

$$\dot{r}_{c,des} = \frac{k_a^{l-g} A_g}{V_l}\left(x_c - y_c^g\left(\frac{PM_l}{H_c \rho_l \Re T_g}\right)\right) + k_a^{l-b} a_b'''\left(x_c - x_{c,sat}\right) \tag{3.65}$$

$$\dot{r}_{a,des} = \left(\frac{k_a^{l-g} A_g}{V_l} + \frac{6\beta}{d_b} k_a^{l-b} \right) x_a - \left[y_a^g \left(\frac{k_a^{l-g} A_g}{V_l} \right) + y_a^b \left(\frac{6\beta}{d_b} k_a^{l-b} \right) \right] \left(\frac{PM_l}{H_a \rho_l \Re T_g} \right) \tag{3.66}$$

where is assumed that the contribution to the desorption rate by bubble formation may be embodied in the term $k_c^{l\text{-}b} a_b'''$, which is determined from the Kierzkowska-Pawlak and Chacuk [66] correlation.

The forgoing analysis is applicable to stirred batch reactors in general under a wide range of operating conditions and working fluids; however, in the conditions investigated in this study, it is possible to simplify Eq. (3.66) considerably – this offers the advantage of reducing the number of correlations from the literature upon which the kinetic parameter estimation will be dependent, thereby also reducing the degree of uncertainty. Since it has been established that bubble formation is initiated by CO_2 owing to its poor solubility, then we may estimate the time necessary for a CO_2 bubble to become saturated with NH_3 by analyzing a single CO_2 bubble in contact with an expanse of PG. Because NH_3 is more soluble than CO_2 by over an order of magnitude, it is also permissible to assume that the bubble's total pressure (and hence also it's volume) is primarily due to the presence of CO_2. Therefore, we may analyze this bubble as an approximately fixed volume sphere; moles of NH_3 accumulate in the bubble according to the following rate:

$$\frac{dn_a}{dt} = \frac{k_a^{l-b} A_b}{H_a V_b}\left(x_a \left(\frac{V_b \rho_l}{M_l} \right) - n_a \right) \tag{3.67}$$

where n_a is the number of moles of NH_3 in the bubble, which at $t = 0$ is 0. For a spherical bubble, we have

$$\frac{A_b}{V_b} = \frac{6}{d_b} \tag{3.68}$$

We now define:

$$\tau = \frac{H_a d_b}{6 k_a^{l-b}} \tag{3.69}$$

$$n_{a,sat} = x_a H_a \left(\frac{V_b \rho_l}{M_l} \right) \tag{3.70}$$

Hence, upon substitution of Eqs. (3.68) and (3.70) into (3.67) and subsequent integration, we obtain:

$$n_a = n_{a,sat}\left(1 - \exp\left\{ -\frac{t}{\tau} \right\} \right) \tag{3.71}$$

The average NH_3 content of this bubble over the course of its residence time t_{res} (i.e., time in contact with the bulk liquid-phase) is

$$\bar{n}_a = n_{a,sat}\left[1-\frac{\tau}{t_{res}}\left(\exp\left\{-\frac{t_{res}}{\tau}\right\}-1\right)\right] \tag{3.72}$$

Using Eq. (3.64) and assuming a temperature of 60°C, one obtains $k_a^{l-b} \approx 4E-4$ $m^{-2}s^{-1}$, and $H_a = 0.014$ from the solubility data discussed in Chapter II; Eq. (3.63) furnishes an estimated bubble diameter of ~2 mm, with which we calculate the time constant via Eq. (3.68) as $\tau \approx 0.01\text{s}$. From observation of the batch reactor experiments, typical bubble residence times were on the order of 1 second, and so the expected average NH_3 content is nearly equal to $n_{a,sat}$. We may therefore adopt the follow simplification of Eq. (3.58):

$$\dot{r}_a^{l-b} = \dot{r}_c^{l-b}\left(H_a x_a\right) \tag{3.73}$$

For the batch reactor, the maximum estimated mole fraction of NH_3 that remained in solution was ~0.007, which, when calculated the basis of partial pressure (and assuming $P_b \approx P_{atm}$) amounts to about 7% of a bubble's total gas content. This validates the assumption that $P_c >> P_a$, which was the basis of the preceding analysis.

CHAPTER IV

KINETIC PARAMETER ESTIMATION

Great care was taken with the batch reactor experiments to ensure that the thermal and kinetic behavior could be analyzed independently. The FTIR gas-phase concentration measurements presented in Chapter II were used to construct an objective function to numerically estimate the unknown parameters as a function of temperature, solids concentration, and particle size distribution. The parameter obtained through the method discussed in this chapter showed good agreement with the experimental data and with theoretical expectations, with only a few exceptions at low temperature and large particle sizes.

4.1 Parameter Estimation Methodology

The task of parameter estimation was approached as a multi-dimensional optimization problem wherein the objective function representing the root-sum-squared (RSS) error between model predictions and experimental measurement is minimized. Here, the objective function F is written as:

$$F(\theta) = \sum_{n=1}^{N} \sqrt{\left(y_a(t_n;\theta) - Y_a(n)\right)^2 + \left(y_c(t_n;\theta) - Y_c(n)\right)^2} \tag{4.1}$$

where, $y(t_n;\boldsymbol{\theta})$ and $Y(n)$ is the gas-phase mole fraction measured experimentally and predicted by the model, respectively, at time $t_n = n\Delta t$ corresponding to the n-th data

point. The subscripts *a* and *c* designate NH_3 and CO_2, respectively. The relation $F = F(t_n; \boldsymbol{\theta})$ is a scalar function of the model parameters represented by the vector $\boldsymbol{\theta}$. If the parameter space is unbounded, then *F* is at a minimum when [69]

$$\nabla F = \mathbf{0} \tag{4.2}$$

The reactor model possesses seven coupled, dynamic states with 12 adjustable parameters; hence, a digital computer program was developed using the MatLab/Simulink (MathWorks, ver. 2015a) programming language. The Simulink environment is integrated with a suite of parameter estimation tools and optimized numerical ODE solution algorithms for rapid simulation execution. The governing equations were integrated using an adaptive 2^{nd}-3^{rd} order Runge-Kutta method (rk23-tb) in conjunction with adaptive time-step sizes. To simulate 500 seconds, Simulink required only ~0.1 seconds of wall clock time. Simulink's parameter estimation tool was used to minimize Eq. (4.1).

Initially, the parameter estimation was carried out for each experiment, i.e. a dataset comprised of the gas-phase mole fractions $y(n; \boldsymbol{\theta})$ measured by FTIR for a particular initial mass of AC (m_{AC}), reaction temperature, and initial particle size range. The parameter estimation tool was capable of achieving very close fits between experiment and model predictions; however, when the estimated parameters for several different experimental data sets were compared, the trends observed with respect to the experimental variables were not physically plausible. Additionally, depending on the

initial parameter estimates used, the optimization routine could potentially arrive at an alternate set of best-fit parameters.

The presence of local minima in the objective function $F(\boldsymbol{\theta})$was addressed in two ways:

1) "Realistic" upper and lower bounds were placed on the parameter set $\boldsymbol{\theta}$. While the appropriate ranges for kinetic parameters $K_a^{s\text{-}l}$, $K_c^{s\text{-}l}$, $k_{f,\mathrm{hom}}$and K_{hom} were not known (other than to require that they be positive, real numbers), the mass transfer parameter range was chosen to center on a nominal value minimum value, described in the section that follows, with the upper bound one order of magnitude greater than said minimum value. The solubility of solid AC in PG, $x_{AC,sat}$, allowed to vary between +/- 100% of the solubility of AC in ethylene glycol reported in [Schmidt]. Placing these restrictions on the permissible values of $\boldsymbol{\theta}$ reduced the number of local minima within reach of the optimization routine.
2) As the temperature is increased, chemical equilibrium shifts in favor of products, and the overall rate of reaction increases. This implies that the homogeneous rate coefficient $k_{f,hom}$ and the homogeneous equilibrium coefficient K_{hom} increase with temperature. The heterogeneous reaction will also experience a chemical equilibrium shift in favor of products, thus the heterogeneous equilibrium coefficients are expect to decrease with increasing temperature. Changes in initial AC mass and initial particle size range do not alter the kinetic behavior of the reactants and products, and so the forgoing kinetic parameters are not expected to change appreciably with respect to m_{AC} or particle size.

To reflect the fact that the kinetic parameters are not functions of m_{AC} or initial particle size range $f(r_i)$, experiments having the same reaction temperature were grouped in order to run the parameter estimation routine in parallel, and thus ensure that the kinetic parameters are consistent across initial particle masses and sizes. Experimental data corresponding to a given set of experimental conditions $[m_{AC}, f(r_i)]$ supply the reference signals $[y_a, y_c]$ to the Simulink parameter estimation tool; each instance of the reactor model corresponding to this experimental dataset is parameterized accordingly (i.e., with m_{AC} and $f(r_i)$), and executed to obtain the predictions $[Y_c, Y_a]$, which are also supplied to the Simulink parameter estimation tool. Each experimental dataset and model prediction is used to construct the objective function to be minimized. This flow of data is represented pictorially in Figure 21.

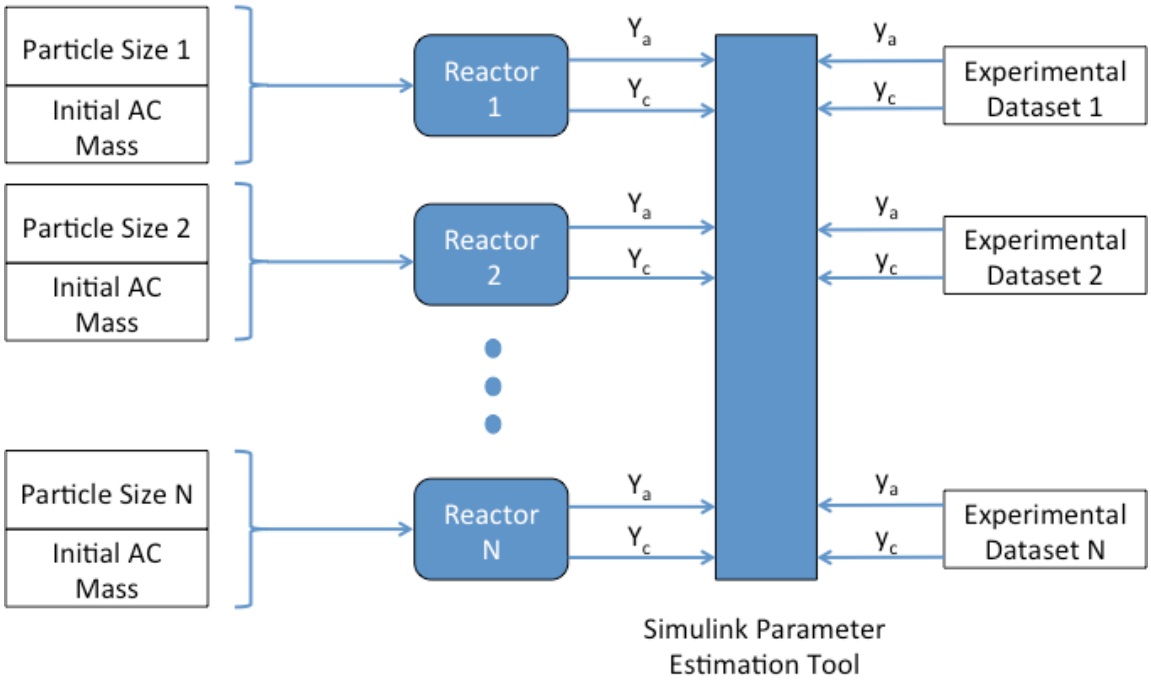

Figure 21. Functional breakdown/dataflow diagram of parameter estimation workflow

4.2 Parameter Estimation Results

The initial set of results obtained utilizing method 2 described above was qualitatively correct, but the overall fit was poor; it was conjectured that this may have been due to forcing a constant quiescent mass transfer coefficient across a wide range of m_{AC} and initial particle sizes, which may have been enhanced in cases where higher gas generation rates were present (such as with higher m_{AC}) due to greater bulk liquid-bulk gas interface renewal frequency. The overall fit to the experimental data was improved by applying the same method, but restricting the datasets used to experiments having the same m_{AC} and reaction temperature, but different initial particle sizes.

The choice of "reasonable" parameter ranges for the kinetic parameters and equilibrium coefficients depends largely upon one's assumption of the dominant mechanisms and/or pathways. In particular, the following possibilities were considered:

1) The dissolution process is much faster than the heterogeneous pathways, and the homogeneous reaction is fast;
2) The dissolution and heterogeneous pathways are of comparable magnitude, and the homogeneous reaction is fast;
3) The dissolution and heterogeneous pathways are as described in case (2), but the homogeneous reaction is slow

Case (1) provided acceptable fits for reaction temperatures of 55°C and 60°C, but was unable to match the initial rising slopes of the CO_2 mass fraction curves at T = 70°C. Conversely, cases (2) and (3) provided considerably better quality fits at T = 70°C, and hence case (1) was not considered further. From this comparison, it is clear that heterogeneous AC decomposition is an important determining factor in the process' behavior at short residence times (less than 40 seconds), and cannot be approximated via a single pathway.

Case (3) was also dismissed when it was observed that acceptable fits could only be obtained if $\dot{r}_{a,het}$ and $\dot{r}_{c,het}$ were assumed to be independent processes; while the quality of fit obtained was remarkably good, the heterogeneous reaction did not satisfy conservation of species, viz.,

$$\int_0^{t_{het}} \dot{r}_a^{s-l}(s)ds = 2\int_0^{t_{het}} \dot{r}_c^{s-l}(s)ds \tag{4.3}$$

where t_{het} is the duration of the heterogeneous reaction. Enforcing this constraint by setting $\dot{r}_a^{s-l} = 2\dot{r}_c^{s-l}$ is perhaps the simplest approach, but comes at the expense of agreement with the data at low (60°C or less) reaction temperatures. Physically, this assumption means that any small imbalance between $\dot{r}_a^{s-l}$ and $\dot{r}_c^{s-l}$ is resolved in a near-instantaneous adjustment in the equilibrium concentrations of NH_3, CO_2, AC, and any intermediates adsorbed on the solid-phase. This would be an acceptable approximation if the solid-phase decomposition kinetics occurs at a far smaller timescale than the rate of solid-liquid phase convective mass transfer, i.e., the process is mass transfer limited. Notwithstanding the compromise in fidelity, reasonable agreement was attained, and certain qualitative behavior observed experimentally was mimicked by the model that had not been reproducible with the independent, parallel pathway assumption.

The assertion $\dot{r}_a^{s-l} = 2\dot{r}_c^{s-l}$ was realized by replacing K_a^{s-l}, K_c^{s-l} with a single parameter K_{het}; likewise, the solid-liquid mass transfer coefficients k_a^{s-l} and k_c^{s-l} were replaced with k_{het}. The simplified representation for the heterogeneous reaction is:

$$\dot{r}_a^{s-l} = 0.5\dot{r}_c^{s-l} = \dot{r}_{het} = \frac{k_{het} a_s'''}{V_l}\left(x_a^{s-l} - x_a\right) \tag{4.4}$$

where x_a^{s-l} represents the saturated concentration of adsorbed NH_3 at the solid-liquid interface. Generally, even under the assumption of quasi-equilibrium heterogeneous decomposition kinetics, x_a^{s-l} is a function of time since the (adsorbed) surface concentrations of reactants and products must adjust concurrently with changes in $\dot{r}_{het}$. However, implementing the functional dependence of x_a^{s-l} on $\dot{r}_{het}$ would introduce (at least) four additional unknown equilibrium coefficients, significantly complicating the parameter estimation task. Therefore, the approximation $x_a^{s-l} = 2P_{eq}(T_l)M_l / 3r_l\hat{A}T_lK_{het}$ was adopted, which represents an effective average over the duration of the heterogeneous reaction. It shall be demonstrated in the following discussions that this is an acceptable approximation.

4.2.1 Mass Transfer-Limited Homogeneous Reaction

Assuming a fast reversible homogeneous reaction that is mass transfer limited, the estimated kinetic parameters, particularly the homogeneous equilibrium coefficient, were very sensitive to the search range chosen for the quiescent mass transfer coefficients between the bulk liquid and bulk gas phases. The reason for this can be seen by examining the y_a curves late in the reaction (typically when $t > 300$ seconds), which reach a plateau. According to the model (subject to the aforesaid assumptions), this is a mass transfer dominated regime where the homogeneous reaction is nearly in equilibrium, and thus the homogeneous equilibrium coefficient may be written:

$$K_{\text{hom}} \approx \frac{[NH_3]^2[CO_2]}{[AC]} \tag{4.5}$$

The "equilibrium" concentration for NH_3 in the bulk liquid phase are estimated by:

$$[NH]_3 \approx \frac{\dot{n}_a}{A_g k_a^{l-g}} + \frac{y_a}{H_a}\left(\frac{P}{\Re T_g}\right) \tag{4.6}$$

where it is assumed that the sparse population of bubbles late in the reaction do not appreciably affect the rate of NH_3 desorption; $\dot{n}_a$ and y_a were evaluated as the average of the last 10 data points for each for each experiment. The remaining concentration of un-dissociated AC, [AC], and the dissolved NH_3 concentration, [NH_3], may be estimated as discussed in Chapter II.

Because of the low saturation limit for CO_2 in solution, the method shown in Eq. (4.6) will not yield reliable estimates for [CO_2] since it does not account for bubble desorption, which is still present even beyond t = 300 seconds. As will be shown in the sensitivity studies in discussed in the section to follow, this is likely the reason why there was only a negligibly small impact on the gas-phase concentration predictions with respect to perturbations in k_c^{l-g}; hence, no bounds were placed on the search range for k_c^{l-g}. For the present analysis to estimate K_{hom}, we recognize from the persistent but slow release of bubbles that [CO_2] is very close to its saturation limit, i.e. [CO_2] ≈ [CO_2]$_{sat}$.

The estimated value for K_{hom} as a function of assumed value for k_a^{l-g} is shown in Figure 22, which demonstrates a rapidly diminishing sensitivity with increasing k_a^{l-g}.

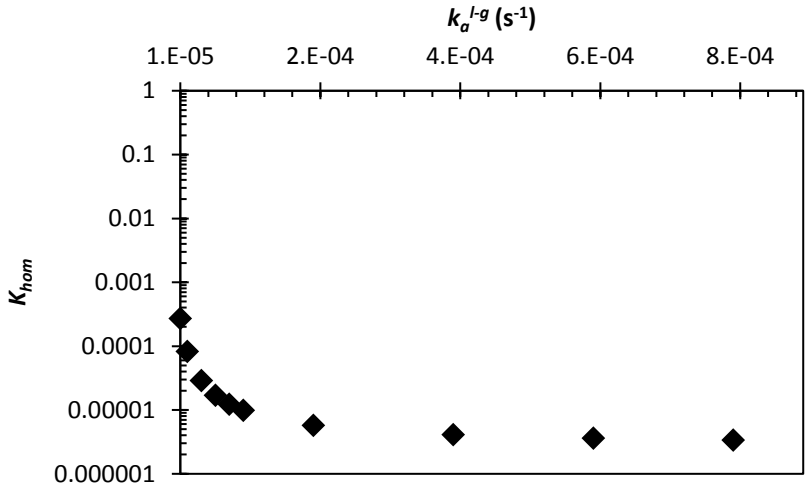

Figure 22. Plot of homogeneous equilibrium coefficient K_{hom} as a function of assumed quiescent desorption coefficient

If one assumes that $[CO_2] = [CO_2]_{sat}$ and $[NH_3]$ as obtained in Chapter III, typical values of k_a^{l-g} are on the order of 5.0 - 9.0E-5 s^{-1}. This would suggest 1.0E-5 s^{-1} to 1.0E-4 s^{-1} to be a reasonable bound on k_a^{l-g}, and this is reinforced further by noting in Figure 22 that K_{hom}'s sensitivity to k_a^{l-g} is drastically reduced beyond 2.0 E-4 s^{-1}. A corresponding set of maximum and minimum bounding curves for K_{hom} can be constructed thus: "high" and "low" estimates for K_{hom} were obtained by assuming, respectively, k_a^{l-g} = 1.0E-5 s^{-1} and k_a^{l-g} = 2.0E-4 s^{-1}, and utilizing the experimental data for $[CO_2]_{sat}$ and [AC] for temperatures of 55°C, 60°C, and 70°C to evaluate Eq. (4.5). This data was obtained from all tests with an initial AC mass of 30g.

The consistency of these bounds with theoretical expectations was checked by assuming a Van 't Hoff dependence with respect to temperature for both the forward and reverse homogeneous reaction:

$$K_{\hom} = \frac{k_{f,\hom}}{k_{r,\hom}} = B \exp\left(- \frac{E_f - E_r}{\Re T_l} \right) \tag{4.7}$$

where *B* is the pre-exponential factor (assumed to be independent of temperature), E_f is the activation energy of the forward reaction, and E_r is the activation energy for the reverse reaction. Eq. (4.7) was fit to the "high" and "low" estimates for K_{hom} utilizing a least-squares linear regression of $\ln\left(K_{\hom}\right)$ as a function of $1/T$; the fits are plotted in Figure 23 and compared against the parameter estimation results for K_{hom}

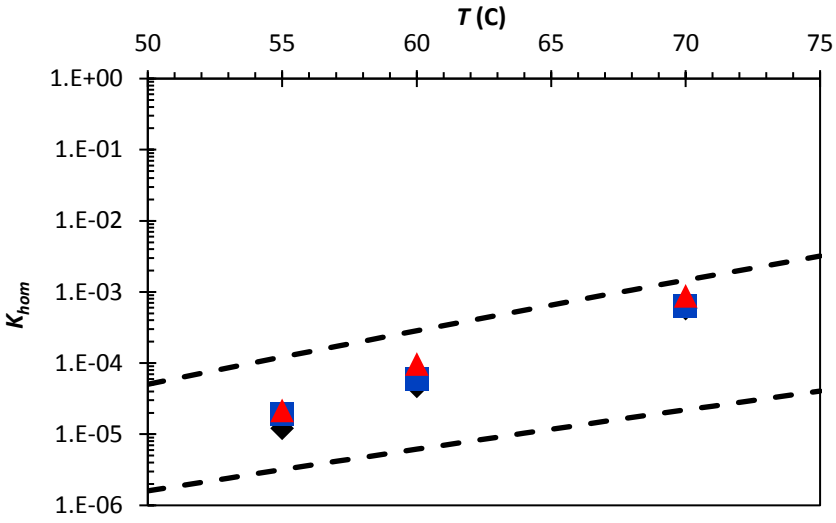

Figure 23. Plot of estimated homogeneous reaction equilibrium coefficient as function of temperature for three different experimental datasets: m_{AC} = 20g (black diamonds), 30g (blue squares), 40g (red triangles). The "high" and "low" estimates, assuming an Arrhenius dependence on temperature, are plotted as black dotted lines

The difference between the forward and reverse reactions is equal to the molar heat of reaction $\Delta\bar{H}$. Assuming, conservatively, ΔH ~ 1800 kJ/kg per Johnson *et al*. [70], the slope of $\ln\left(K_{\text{hom}}\right)$ is approximately 18100 K; the slopes $\ln\left(K_{\text{hom}}\right)_{\max}$ and $\ln\left(K_{\text{hom}}\right)_{\min}$ as shown in Figure 23 are 18700 K (corresponding to ΔH = 2040 kJ/kg) and 13000 K (corresponding to ΔH = 1590 kJ/kg) respectively. Thus, the range of $k_a^{l\text{-}g}$ chosen to initially bound the parameter estimation procedure are consistent with theoretical expectations, i.e. the expected temperature dependence of K_{hom} lies within the bounds of possible best-fit values. The estimated K_{hom} depicted in Figure 23 were within the expected range. Applying a linear regression fit to these estimates yields ΔH = -3006 kJ/kg, which is far in excess of the higher literature values (approximately 2200

kJ/kg) for dry AC [10]. This unrealistically high value suggests that the Van ‘t Hoff behavior postulated previously may not be applicable to the homogeneous reaction, and its use here should only be regarded as an empirical correlation insofar that it provides reasonable (i.e., close to or within the bounding curves in Figure 23) estimations for *K* between 55°C and 80°C.

The forward rate coefficient for the homogeneous reaction, unlike $K_{hom,}$, could not be estimated analytically. For the purpose of correlating the data without any implicit assumptions pertaining to the chemical physics, $k_{f,\mathrm{hom}}$ was assumed to follow an Arrhenius temperature dependence:

$$k_{f,\mathrm{hom}} = A\exp\left(-\frac{E_f}{\Re T_l}\right) \tag{4.8}$$

where, E_f is the activation energy of the forward (decomposition) reaction. A curve fit to the estimated $k_{f,\mathrm{hom}}$ values having this form is plotted in Figure 24

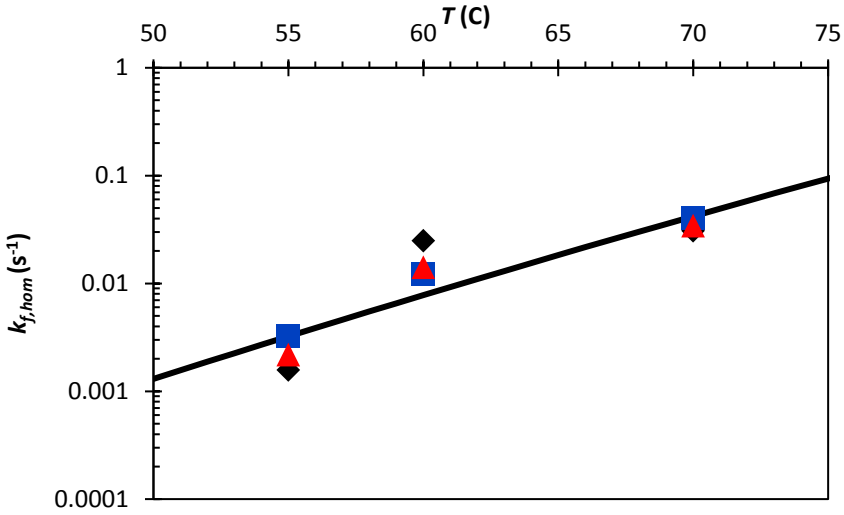

Figure 24. Estimated $k_{f,hom}$ as a function of temperature for m_{AC} = 20g (black diamonds), 30g (blue squares), and 40g (red triangles) for reaction temperatures of 55°C, 60°C, and 70°C.

The values of the fit parameters are $A = \exp(51.466)\,s^{-1}$ and $E_f / \Re = 18730\,K$. The literature reports the activation energy of the decomposition reaction for dry, powder form AC to be 76 kJ/mol [10] – this gives $E_f / \Re = 9141K$. Similar to the case with the estimates for K_{hom}, the term E_f is significantly greater than the case with dry AC in contact with only NH_3 and CO_2 gas. While the use of Eq. (4.8) was intended solely as a correlation of the data, the possibility also exists that there is a greater energy barrier to the homogeneous reaction in PG compared to heterogeneous decomposition of dry solid AC. The solvent cage effect [71] is a plausible explanation for the discrepancy between theoretically predicted $E_f / \Re$ and the fit to the estimated $k_{f,\mathrm{hom}}$. Without experimental measurements of the dissolved species in the bulk liquid phase to confirm the

appropriateness of the homogeneous reaction mechanism used in this model, it is not possible at this point to posit a definitive explanation.

The effective heterogeneous equilibrium coefficient K_{het}, which was assumed to be constant over the course of the reaction, was successfully fit to the three different sets of experimental data (m_{AC} = 20g, 30g, 40g) over T = 55°C, 60°C, and 70°C with only a single outlier and otherwise very little scatter. The estimates are depicted in Figure 25:

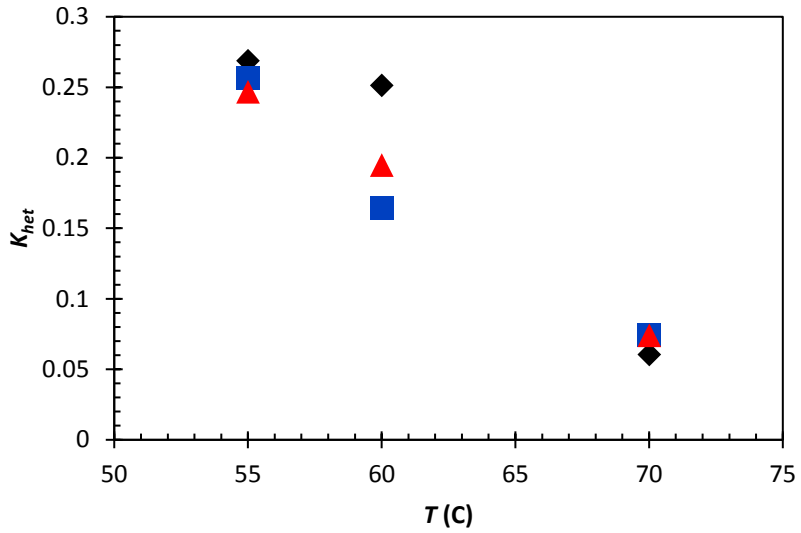

Figure 25. Estimates for effective heterogeneous equilibrium coefficient K_{het} as a function of temperature for three different experimental datasets: m_{AC} = 20g (black diamonds), 30g (blue squares), 40g (red triangles)

Since no analytical estimates or data from the literature could be obtained for the heterogeneous decomposition of AC in PG, no attempt was made to place bounds on the value of K_{het}, save for the obvious requirement that it should be a positive number greater than zero. As expected, K_{het} decreases with increasing temperature, denoting

increasing concentrations of desorbed NH_3 and CO_2 at the surface of the solid-phase, and hence a faster net heterogeneous decomposition rate per Eq. (4.4). The outlier in Figure 25 corresponds to the best-fit estimate to the datasets containing all experiments with m_{AC} = 20g at T = 60°C. Generally, tests with initial particle sizes in the 20 – 30 mesh range (the largest particle sizes used), were difficult to fit compared to the smaller particle sizes. For tests with m_{AC} = 20g, this difficulty was compounded, especially at lower temperatures, since smaller quantities of gas were produced and thus secondary effects – such as absorption of NH_3 onto condensed PG adhering to the reactor headspace walls or poor mixing with the N_2 carrier gas therein – had a more pronounced effect on repeatability. The differences between estimates obtained for the 30g and 40g tests were much smaller overall and less repeatability issues were observed, which lends credence to this explanation. We therefore expect to encounter greater scatter in the estimates obtained from the 20g datasets (at least at lower temperatures) than the 30g and 40g tests, hence the presentation of the outlier.

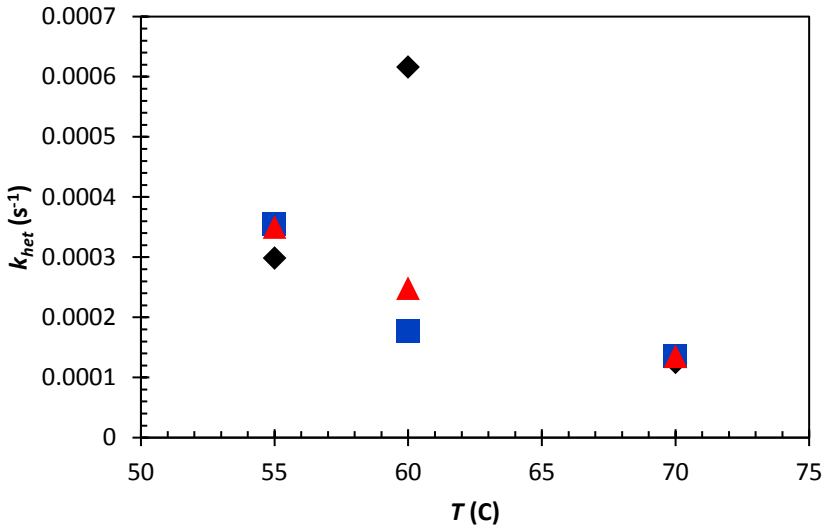

Figure 26. Solid-liquid desorption coefficient k_{het} estimates as a function of temperature for three different experimental datasets: m_{AC} = 20g (black diamonds), 30g (blue squares), 40g (red triangles)

Overall, there is an apparent tendency for k_{het} to decrease as temperature increases, but only slightly after T = 60°C. As the viscosity of the liquid phase decreases with temperature, one might expect k_{het} to increase with temperature, contrary to what is shown in Figure 26. We suspect that this is due to a breakdown in the assumption of a mass transfer-limited heterogeneous reaction at lower temperatures, and hence decreasing accuracy in the estimation of any associated parameters. This is reflected by the marked improvement in scatter with the experimental gas-phase concentration data as temperature increases.

The disparity between the characteristic timescales of solid-liquid mass transfer and the preceding chemical reaction step(s) grows with temperature, and thus approaches the idealized case of a quasi-equilibrium, mass transfer-limited process (i.e.,

more consistent with the model). On the other hand, as temperature decreases, the timescales of chemical reaction *on* the solid phase and mass transfer *from* the solid phase will eventually become comparable. The solid-gas equilibrium data from the literature [7-9] as well as experimental observations from Johnson *et al.* [70] and Schmidt [10] suggest that the reaction proceeds "rapidly" only if the equilibrium vapor pressure exceeds the local pressure; hence, one would expect significantly slower heterogeneous kinetics below 60°C (at atmospheric pressure) and thus departure from the mass transfer-limited idealization. In this case the heterogeneous reaction rate is governed by the complicated dynamic interactions (differential equations as opposed to simple algebraic relations) of both chemical reaction and mass transfer steps, requiring the inclusion of additional state equations and parameters. Therefore, the asymptotically decreasing k_{het} is due to a combination of the model's inability to reproduce this complex nonlinear behavior and the parameter estimation routine's attempt to fit the model to data at temperatures where solid-phase kinetics are likely important.

When compared against the predictions of the Pangarkar [38] correlation, plotted in Figure 27, the estimated values for k_{het} fall roughly within the range predicted by Eq. (3.12) for the particle sizes used in this study. On the other hand, the estimated values for k_{dis} (Figure 28) are nearly an order of magnitude lower.

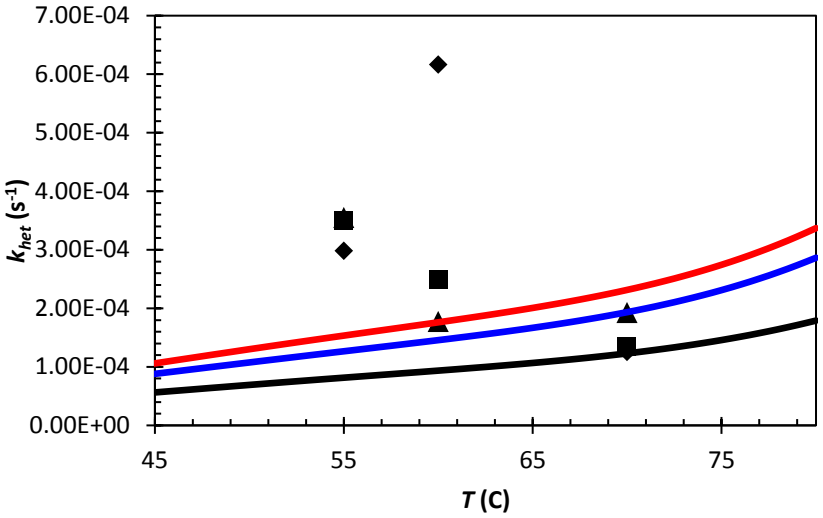

Figure 27. Comparison of k_{het} calculated by Eq. (3.12) for different particle sizes vs. Simulink estimated k_{het}; from Eq. (3.12): 20 mesh (black line), 40 mesh (blue line), 60 mesh (red line) with m_{AC} = 40g for each case; Simulink estimates: m_{AC} = 20g (diamonds), m_{AC} = 30g (triangles), and m_{AC} = 40g (squares).

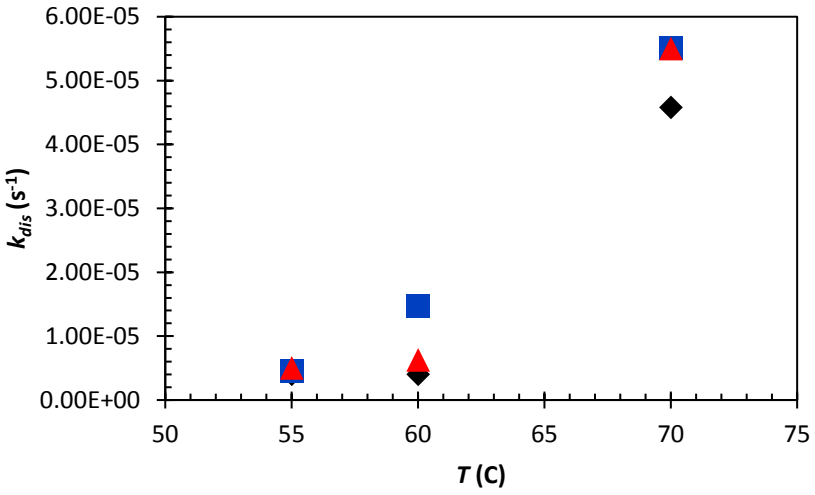

Figure 28. Solid-liquid dissolution coefficient k_{dis} estimates as a function of temperature for three different experimental datasets: m_{AC} = 20g (black diamonds), 30g (blue squares), 40g (red triangles)

Simulink-estimated k_{dis} values follow the expected trend as temperature increases, i.e. lower liquid-phase viscosity at constant agitation speed tends to enhance diffusion and thus convective mass transfer processes. The comparatively low values of k_{dis} are likely – at least in part – a consequence of the assumption that $D_{AC} \approx D_a$, which would result in Eq. (3.12) over-predicting k_{dis}. At T = 70°C, both k_{dis} and k_{het} give the impression of converging to similar magnitudes as temperature increases further; a plot of k in Figure 29 comparing k_{het} , k_{hom}, and Eq. (3.12) (assuming a 20 mesh particle size) illustrates this trend:

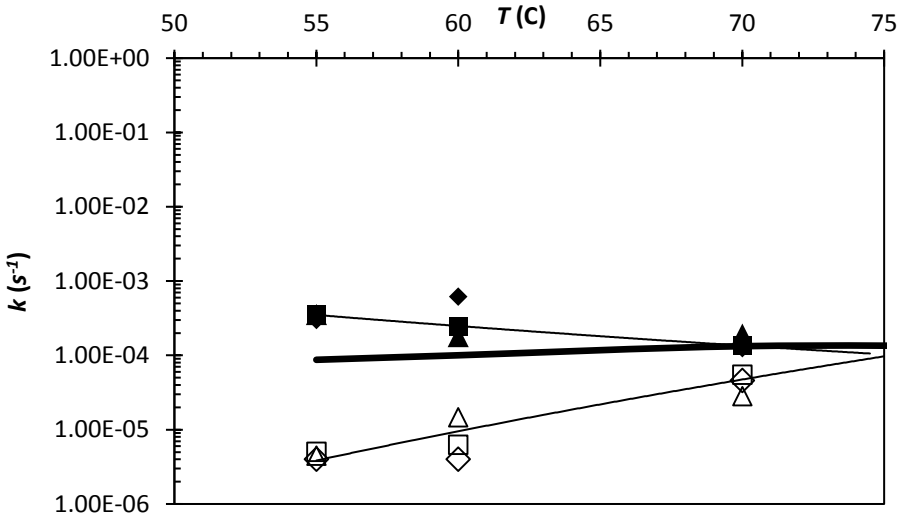

Figure 29. Logarithmic plot of k_{het} (solid shapes), k_{dis} (hollow shapes), and predictions of Eq. (3.12) (black line) over various temperatures. Simulink-estimated values are marked according to m_{AC} (20g – diamond, 30g – triangle, 40g – square). A value of d_p = 850µm was used in Eq. (3.12). The lines drawn through the markers are to guide the eye

As the reaction aligns with the assumption of mass transfer-limited heterogeneous decomposition, k_{het} is approximately described by the convective mass

transfer model of Pangarkar [38]. We hypothesize that further increases in temperature beyond 70°C can eventually be expected to cause k_{het} to diverge significantly from the predictions of Eq. (3.12) as large surface-bound NH_3 and CO_2 concentrations on the solid-phase would cause bubble nucleation sufficient to eclipse the rate of convective mass transfer. The cycle of bubble nucleation, growth, and release on the AC particle surface would disrupt the concentration boundary layer and thus cause a secondary enhancement in k_{dis}.

With regard to the estimated solubility of AC in PG ($x_{AC,sat}$), a distinctly decreasing trend can be observed at greater reaction temperatures, per Figure 30:

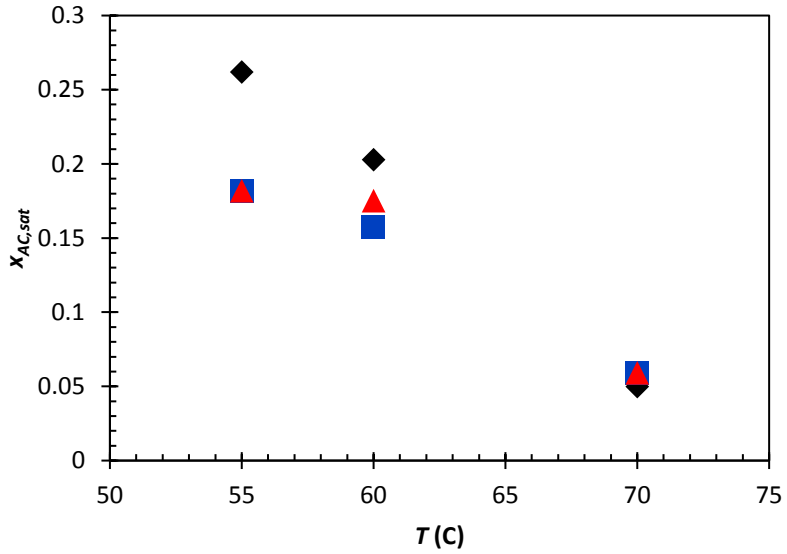

Figure 30. Solubility fraction of AC in PG, $x_{AC,sat}$, estimates as a function of temperature for three different experimental datasets: m_{AC} = 20g (black diamonds), 30g (blue squares), 40g (red triangles)

The observed trend is suspect, given that most solids with a negative heat of solution will exhibit a rising solubility with temperature [72, 73]. Because of the slow

overall reaction rate at lower temperatures, if the concentrations studied are far enough removed from the AC saturation limit, the fitting routine will settle on inordinately high values of $x_{AC,sat}$. This is further complicated by the similar effect that perturbations of k_{dis} have on $\dot{r}_{dis}$, as was found in the sensitivity analysis discussed in Section 4.4.1. This would explain, at least in part, why good agreement was obtained with the calorimetry results (to be discussed in Chapter V), which are dependent on correctly predicting $\dot{r}_{dis}$, but not on the individual estimates for k_{dis} or $x_{AC,sat}$. Schmidt [10] measured the solubility of AC in ethylene glycol (EG) at 25°C and 1 atm, which he found to be 0.185 g/ml (or 0.134 on a solvent mole fraction basis). Since EG and PG are chemically similar, one can assume that the solubility of AC in each should also be similar; thus, the estimated values in Figure 30 are indeed reasonable.

4.3 Qualitative Model Behavior and Comparison to Experiment

In this section, the qualitative trends predicted by the model for NH_3 (y_a) and CO_2 (y_c) concentration histories at different reaction temperatures, initial solid AC mass, and initial particle size range is analyzed. In all cases considered hence, the parameter set used was obtained via method 2 described in the previous section, with an experimental dataset consisting of all tests with m_{AC} = 30g. Further, it was observed that using parameter values averaged for each of the three initial AC loadings (20g, 30g, and 40g) at each temperature did not give satisfactory agreement with the experimental results, whereas using the parameter fits obtained from the m_{AC} = 40g series of experiments gave excellent agreement. It is likely that use of averaged parameters upset

the balance between the reaction mechanisms that was attained with any individual fitted parameter set.

A comparison of the early behavior of the reaction when rapid bubbling was observed to late in the reaction when the total gas release rate slowed significantly had led to the designation of two distinct regimes for the decomposition of AC in PG:

1) **Irreversible Regime**: the reaction rate is primarily forward, and reaction/species transfer dynamics from reverse reaction(s) are negligible.
2) **Mass Transfer-Limited Regime:** The heterogeneous reaction and dissolution processes have ceased completely due to disappearance of the solid-phase. The forward and reverse reactions are of comparable magnitude, and proceeds only at the rate permitted by liquid-gas mass transfer.

Since the existence of these two reaction regimes - and their causes - have critical implications for reactor design, it shall be demonstrated here that the model predictions support these hypotheses before the comparisons to experiment are discussed.

Figure 31 shows the model predictions for the forward and reverse homogeneous reaction rates with m_{AC} = 40g, T = 60°C, and an initial particle size range between 40 and 50 mesh. Additionally, the predicted gas-phase mole fraction of CO_2 is plotted on a secondary axis. Early in the reaction, the forward homogeneous reaction outpaces the reverse reaction by approximately five-fold, consistent with conditions postulated for the irreversible regime. This continues until $t \approx 100$ s, after which the reverse reaction rapidly closes the gap and thereby heralds the end of the irreversible regime. Both curves proceed to decrease linearly and parallel to one another, separated by a narrow gap.

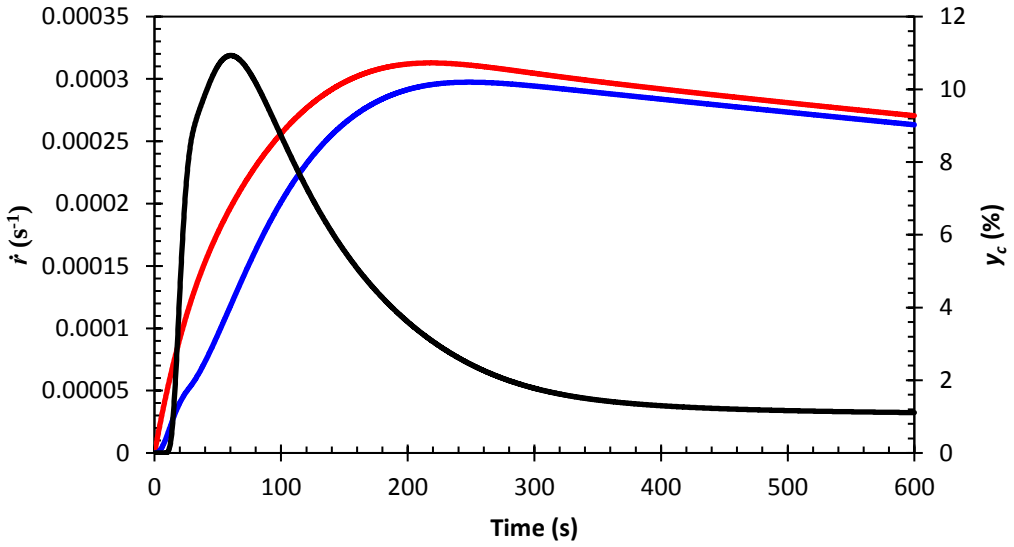

Figure 31. Model predictions for homogeneous forward (red curve, left axis) and reverse (blue curve, left axis); gas-phase molar concentration of CO_2 (y_c, black curve, right axis) as functions of time for reaction conditions m_{AC} = 40g, T_l = 60°C, and initial particle size between 40 and 50 mesh.

One also notices that the rapid decline in CO_2 release corresponds approximately to the period of time over which the curves representing the forward and reverse heterogeneous reactions converge. As Figure 31 shows, there is a nearly constant gas-phase concentration of CO_2 coinciding with the forward and reverse reaction rates being parallel (for times exceeding ~300 seconds). The small, persistent difference between the forward and reverse reactions indicates that the escape of decomposition products from solution is preventing chemical equilibrium from being completely achieved. Since this difference is small and the only subsequent step is desorption from the liquid-phase, mass transfer-limited conditions exist. Figure 32 shows that when the reaction enters into the mass transfer-limited regime, the release rate of CO_2 and NH_3 become nearly equal

to the net homogeneous reaction rate, approximating steady-state conditions and yielding practically constant gas-phase concentrations of CO_2 and NH_3.

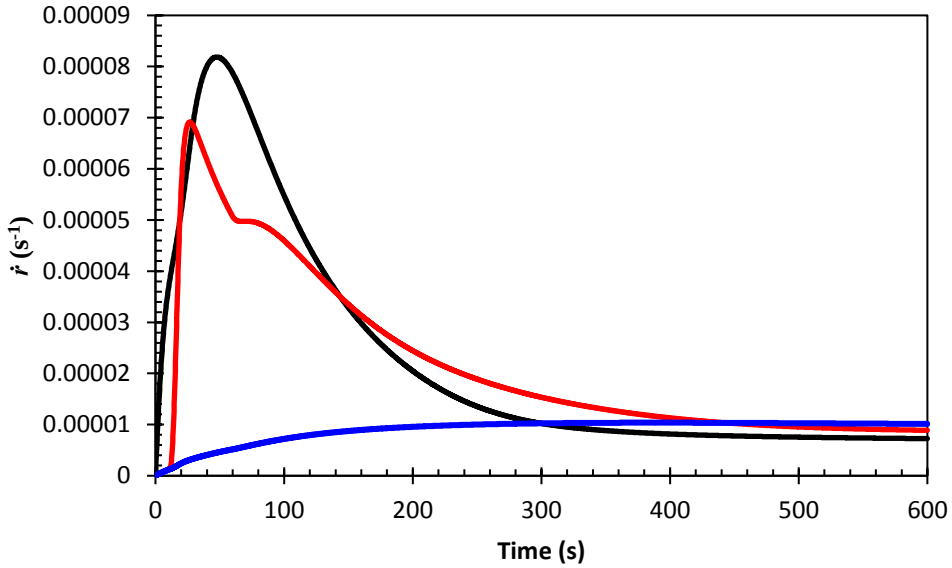

Figure 32. Model predictions of total gas release rates of CO_2 (red curve) and NH_3 (blue curve), as well as net homogeneous reaction rate (black curve) as functions of time for reaction conditions m_{AC} = 40g, T_l = 60°C, and initial particle size between 40 and 50 mesh.

The concentrations of dissolved CO_2 (x_c), NH_3 (x_a), and AC (x_{AC}) corresponding to the conditions in Figure 32 are plotted in Figure 33; x_c is approximately an order of magnitude smaller than x_a, as was anticipated on account of their vastly differing solubility in PG.

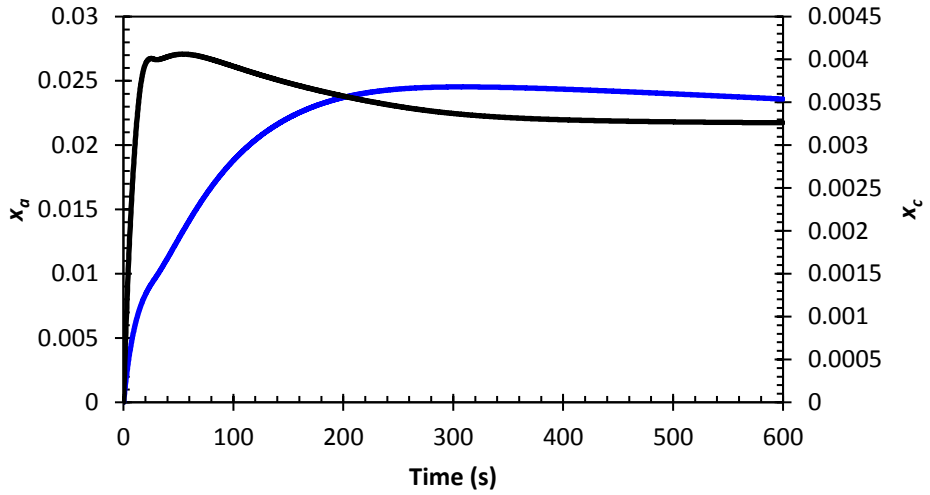

Figure 33. Model predictions of dimensionless dissolved CO_2 (black curve, right axis) and NH_3 (blue curve, left axis) as a function of time for reaction conditions m_{AC} = 40g, T_l = 60°C, and initial particle size between 40 and 50 mesh.

The reverse reaction, according to the model, is directly proportional to the product $x_a^2 x_c$. Since, from the plots in Figure 33, $x_a >> x_c$, it follows that the reverse reaction is indeed predominantly impacted by dissolved NH_3. The model predictions confirm that the mass transfer-limited regime is due almost exclusively to the buildup of NH_3 in solution.

4.3.1 Qualitative Trends in Model Predictions

The model's suitability as an engineering design tool is coupled directly to its ability to be used in "off-design" (i.e., outside of conditions tested experimentally) conditions. We therefore require first and foremost that general trends with respect to concentration, temperature, and particle size can be reproduced satisfactorily. Satisfaction of this criterion was demonstrated insofar as qualitative agreement between model and experiment with respect to reaction temperature, mass loading, and particle size trends is remarkably good. Calculated gas-phase CO_2 and NH_3 concentration trends with decreasing particle sizes at fixed temperature (70°C) and initial mass (30 g) are shown in the top and bottom of Figure 34, respectively. Consistent with experimental trends, CO_2 peak height increases, narrows in width, and shifts leftward as particle size decreases. The NH_3 peaks depicted in Figure 34 follow a similar pattern.

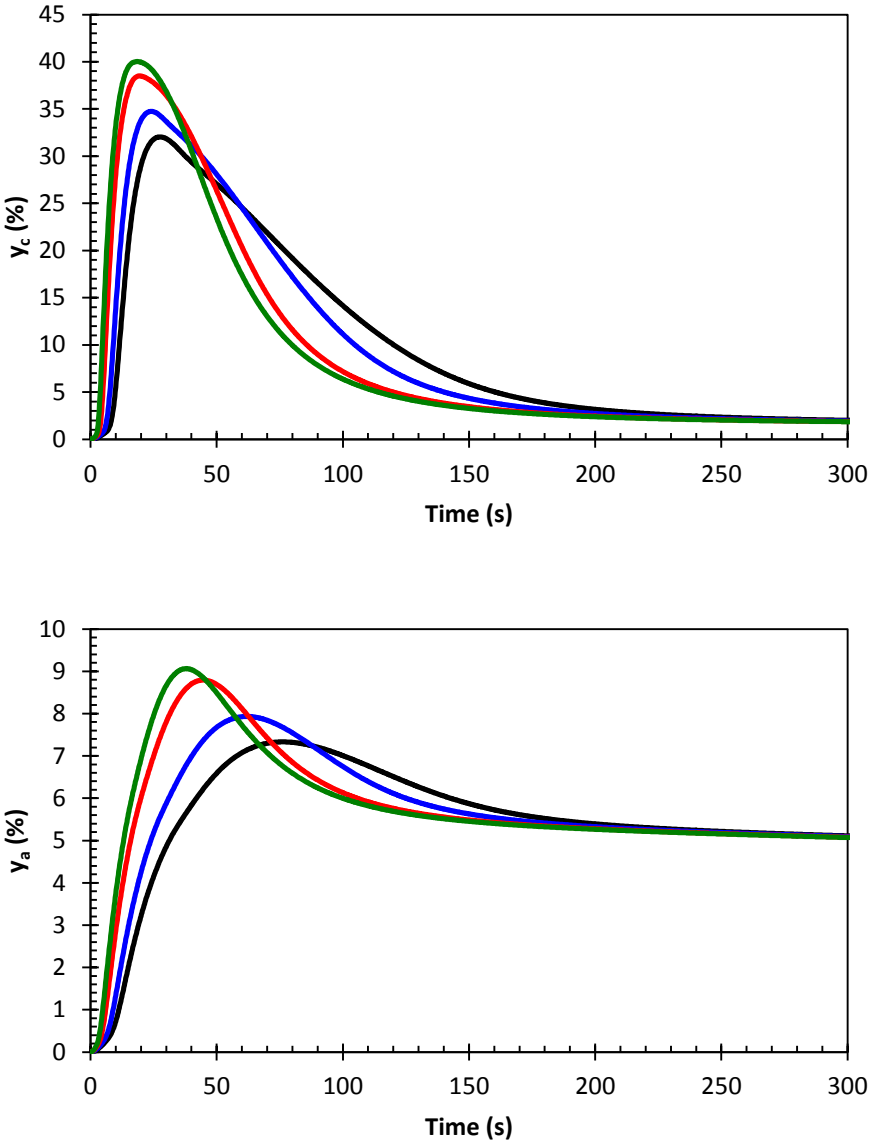

Figure 34. Comparison of model predictions for gas-phase CO_2 (top) and NH_3 (bottom) mole fraction histories over various mesh sizes for reaction temperature of 70°C and m_{AC} = 30g: 20-30 mesh (black), 30-40 mesh (blue), 40-50 mesh (red) and 70-80 mesh (green)

As the kinetic parameters are not linked to particle size, this behavior is indicative of increased surface area available for the heterogeneous reaction mechanism, which tends to accelerate the transfer of solid AC and surface bound reaction products to dissolved species in the bulk liquid phase. Subsequently, the dissolved species populating the liquid phase undergo the reversible homogeneous reaction and/or release to the bulk gas phase via bubble-desorption and convective mass transfer. Referring to Figure 34 again, the calculated NH_3 curves converge toward a single line, as was also observed experimentally. It is evident that the model is capable of capturing the near-equilibrium, mass transfer dominated condition that was posited to account for this behavior.

Gas-phase NH_3 and CO_2 mole fractions were also calculated for reaction temperatures of 55°C, 60°C, and 70°C while m_{AC} and initial particle size range were fixed at 30g and 30 mesh – 40 mesh, respectively. Predicted gas-phase concentration histories y_c and y_a are plotted in Figure 35 at different temperatures. It is clear in both figures that the net reaction rate is accelerated considerably with increasing temperature.

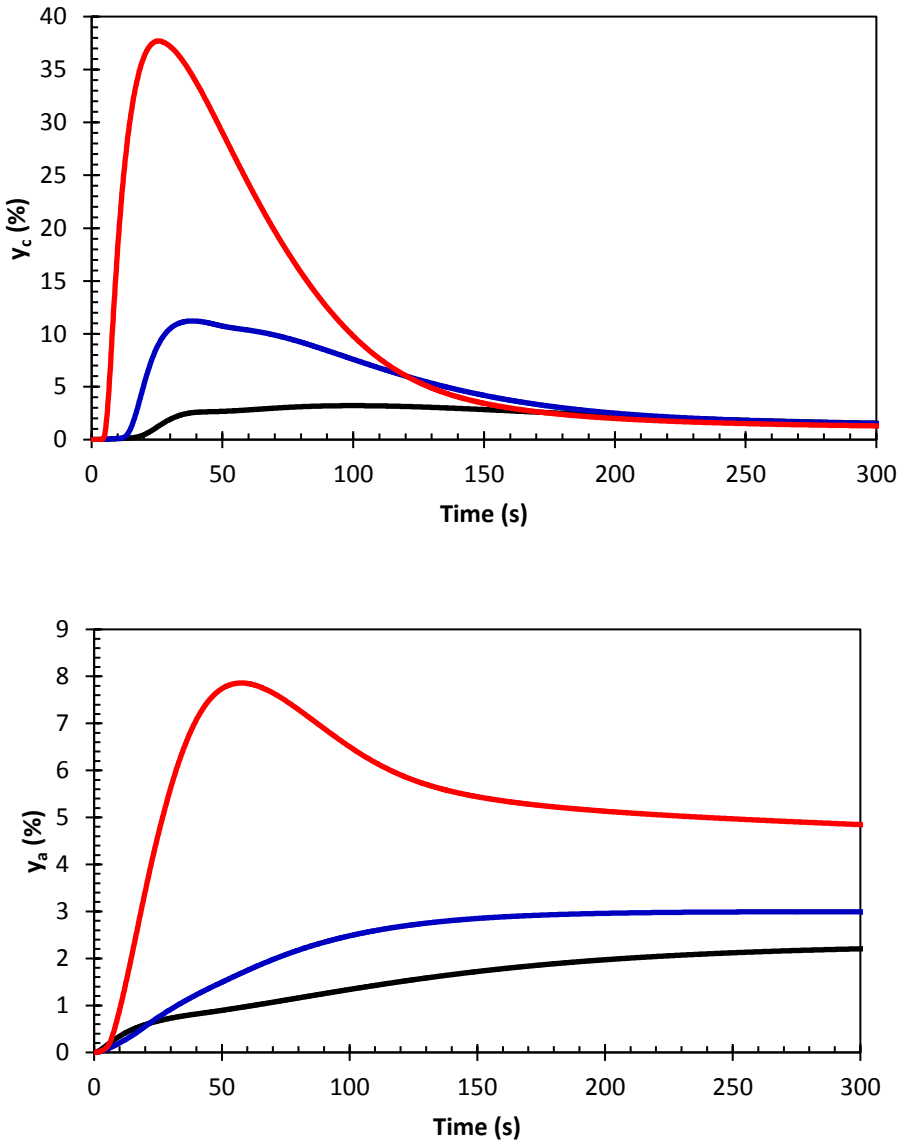

Figure 35. Comparison of model predictions for gas-phase CO_2 (top) and NH_3 (bottom) mole fraction histories for m_{AC} = 30g and particle size range of 40-50 mesh at different temperatures: 55°C (black), 60°C (blue) and 70°C (red).

As the reaction temperature is increased, both y_c and y_a undergo a significant increase in initial slope and peak height (with an accompanying decrease in width), with the peak apex also shifting leftward. The dramatic increase in peak height is a consequence of accelerating the forward reaction kinetics (both in the heterogeneous and homogeneous mechanism), which is true for virtually all chemical reactions when subjected to increases in temperature. At the same time, chemical equilibrium of the dissolved species in the bulk liquid phase shifts increasingly in favor of the reaction products NH_3 and CO_2. While this would seem at first to suggest that the peaks should shift to the right at higher temperatures, the leftward shift indicates that the rate of increase (with respect to temperature) in the forward homogeneous rate coefficient outpaces that of the homogeneous equilibrium coefficient, which also increases with temperature.

Figure 36 shows gas-phase mole fraction histories for CO_2 and NH_3 for m_{AC} = 20g, 30g, and 40g with a 60°C reaction temperature and 40-50 mesh particle size range. The parameter set used was obtained by fitting to the 40g, 60°C datasets for y_a and y_c.

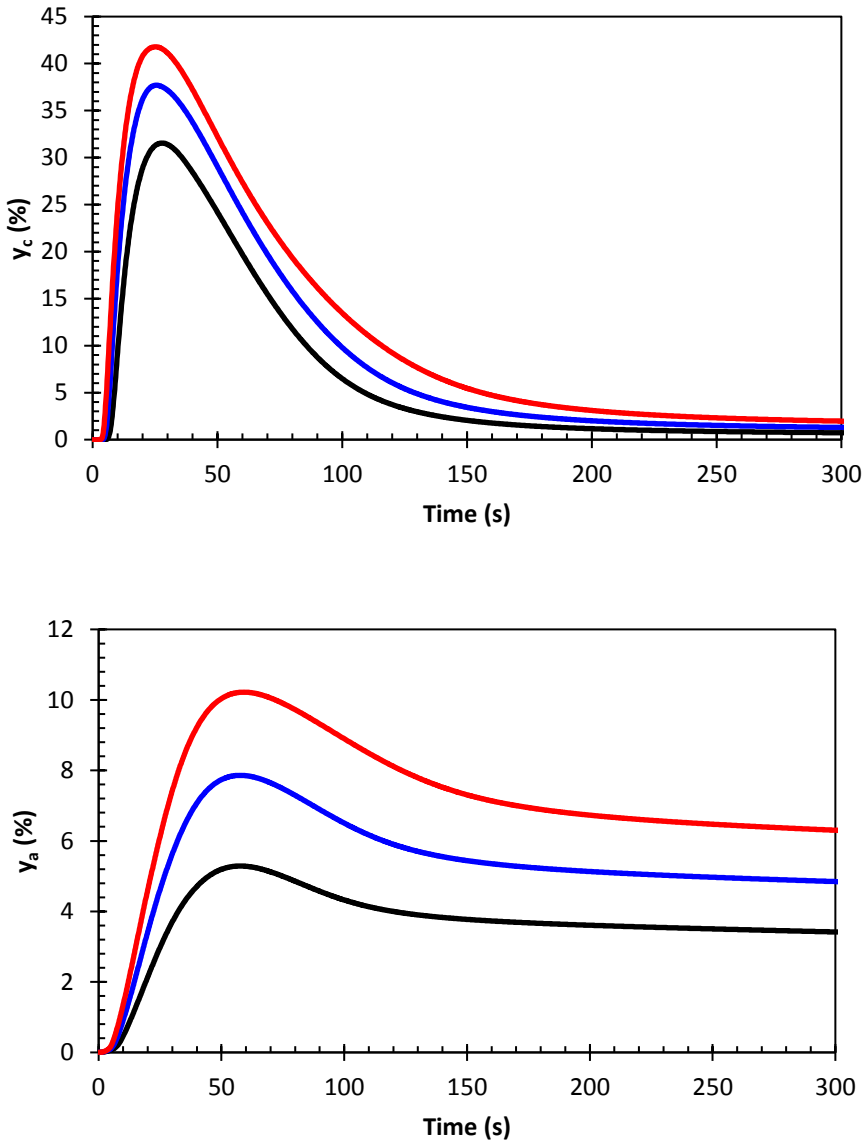

Figure 36. Comparison of model predictions for gas-phase CO_2 (top) and NH_3 (bottom) mole fraction histories for particle size range 30-40 mesh and reaction temperature of 60°C over different initial AC mass loadings; mAC = 20g (black), 30g (blue) and 40g (red).

Again, the trends predicted by the model are consistent with experimental observations: increasing m_{AC} increases y_c peak width and height, without the leftward-shift seen with increasing temperature or decreasing particle size; the y_a peak height increases and the plateau "NH_3 limit" also increases, while the peak apex shifts to the right.

4.3.2 Comparison to Experimental Results

Agreement between model predictions for gas-phase concentration traces and FTIR measurements improves with both increasing temperature and decreasing particle size. As was mentioned previously, this trend is most likely tied to the simplistic nature of the heterogeneous reaction model: increasing temperature tends to make the process mass transfer limited. The trend with respect to particle size arises from the complicated mass transfer behavior associated with larger particles [42]. Smaller particles are better represented by a single *average* mass transfer coefficient, as boundary layers are more likely to be uniform and particle motion has little influence on the surrounding flow field and/or the behavior of other nearby particles. Figure 37 shows a comparison to data from a test with m_{AC} = 40g, T = 55°C, and an initial particle size range of 40 – 50 mesh.

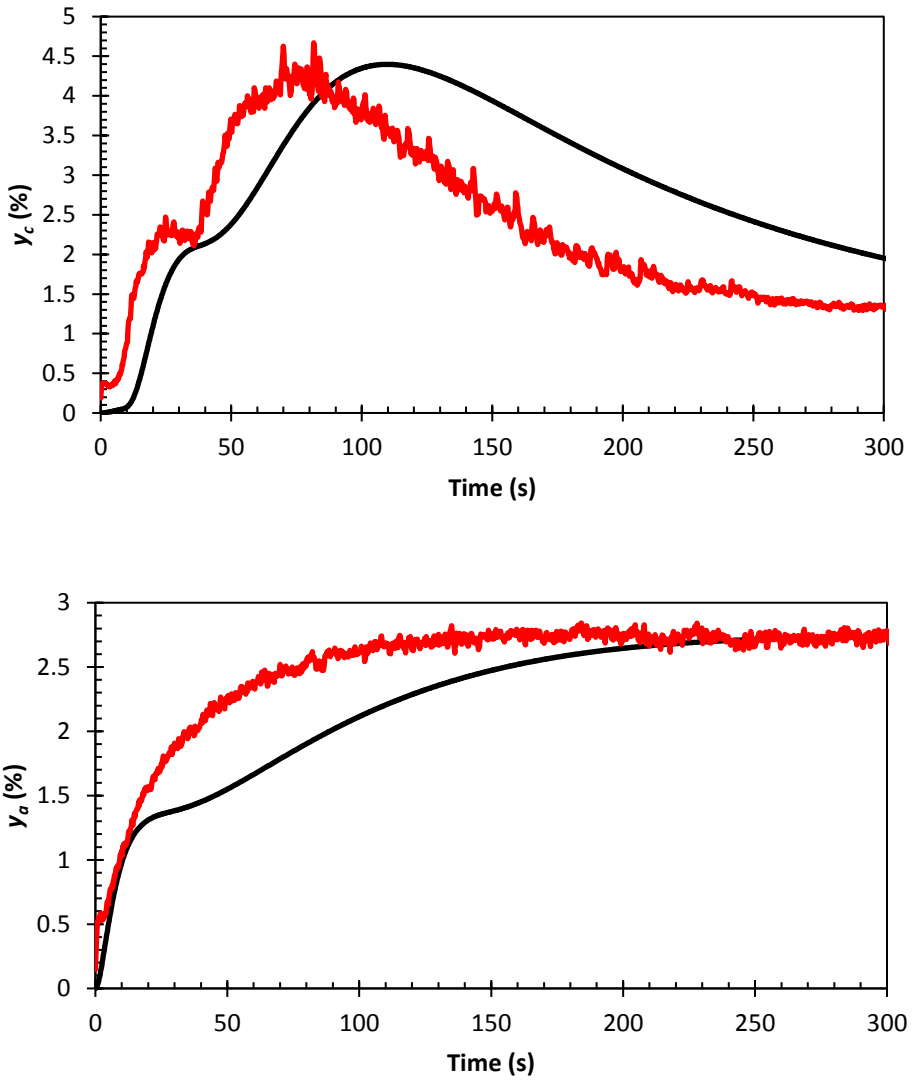

Figure 37. Comparison of experiment (red curve) and model predictions (black curve) for CO_2 (top plot) and NH_3 (bottom plot) gas-phase mole fractions. Reaction conditions were m_{AC} = 40g, T_l = 55°C, and initial particle size between 40 and 50 mesh.

The agreement shown in Figure 37 is quite rough, but not to the point where it would be considered unacceptable. It is, however, noteworthy that the "notch" in the initial slope of y_c recorded by the FTIR between approximately t = 22 s and t = 30 s is also present – albeit considerably smoother – in the model prediction. In the model, the notch coincides with the termination of the heterogeneous reaction as x_a approaches $x_{a,s}$ while dissolution of solid un-reacted AC continues. As more AC dissolves, it accelerates the homogeneous reaction and again causes the slope of y_c to increases and eventually peak as additional CO_2 is liberated. The heterogeneous reaction rate, homogeneous reaction rate, and AC dissolution rate ($\dot{r}_{het}$, $\dot{r}_{hom}$, and $\dot{r}_{dis}$ respectively) corresponding to the model predictions in Figure 37 are plotted in Figure 38– this shows that the "notch" occurs precisely when $\dot{r}_{het}$ reaches zero.

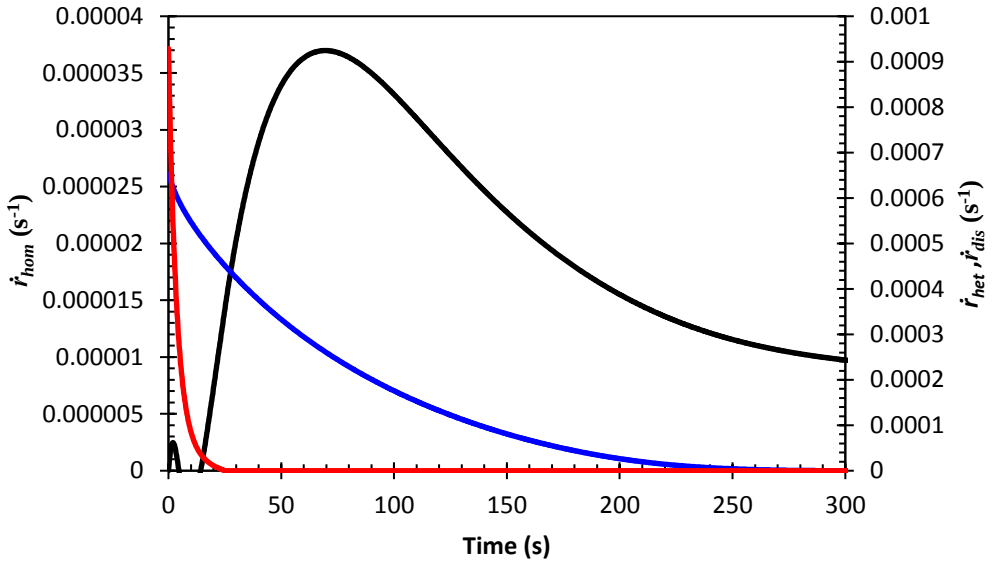

Figure 38. Model predictions for heterogeneous decomposition rate (red curve, right axis), homogeneous decomposition rate (black curve, left axis), and AC dissolution rate (blue curve, right axis). Reaction conditions were m_{AC} = 40g, T_l = 55°C, and initial particle size between 40 and 50 mesh.

Figure 39 compares gas-phase concentration data for a test having m_{AC} = 40g, T = 60°C, and an initial particle size range of 40 – 50 mesh. There is significant improvement in the quality of fit to the CO_2 gas-phase concentration data – and to a lesser extent NH_3 gas-phase concentration – compared to T = 55°C.

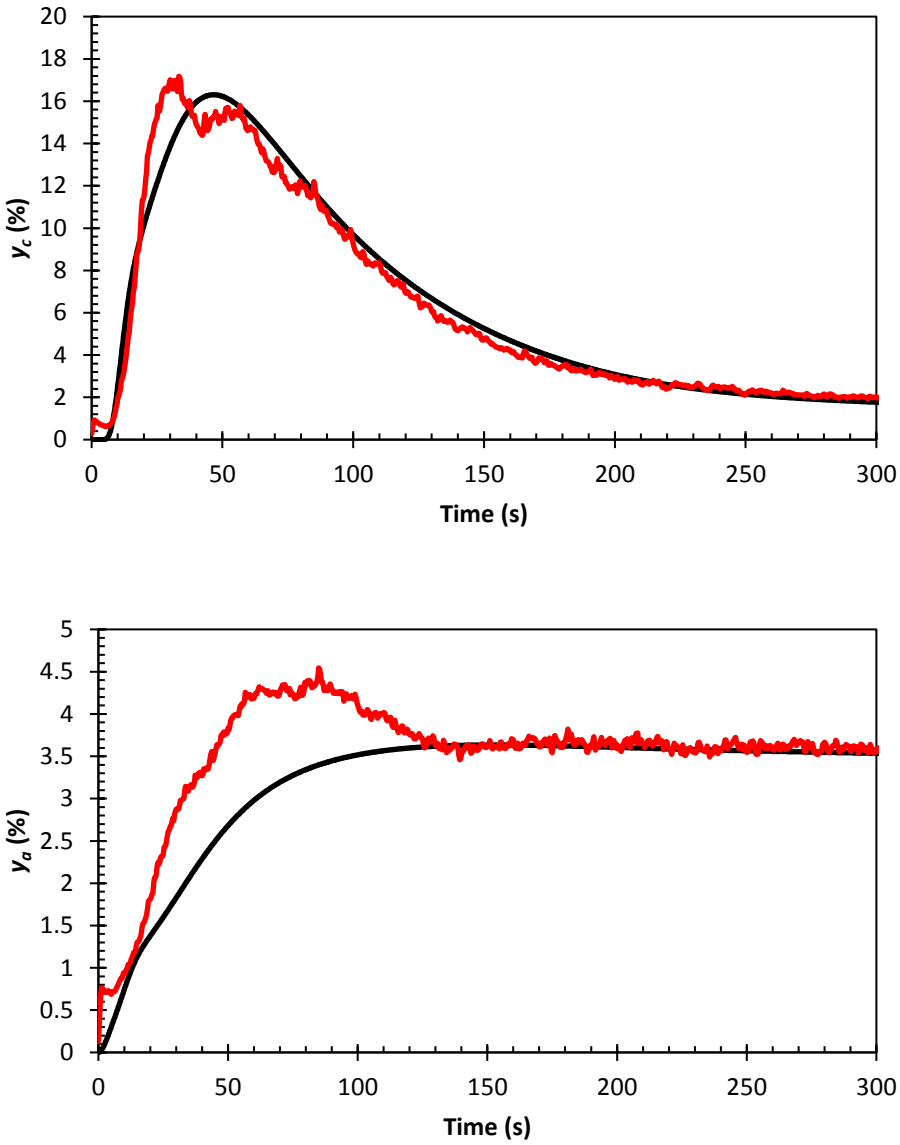

Figure 39. Comparison of experiment (red curve) and model predictions (black curve) for CO_2 (top plot) and NH_3 (bottom plot) gas-phase mole fractions. Reaction conditions were m_{AC} = 40g, T_l = 60°C, and initial particle size between 40 and 50 mesh.

In a manner similar to the T = 55°C case illustrated in Figure 37, the model prediction for y_a underestimates the initial slope, and was thus unable to reproduce the peak observed at t = 60 s, although it appears to approach the correct plateau height late in the reaction, indicating an appropriate balance between K_{hom} and $k_a^{l\text{-}g}$. The under-prediction of dy_a / dt during the course of the heterogeneous reaction indicates that the NH_3 bubble desorption rate is not being captured in its entirety; either x_a is too low, and/or the bubble desorption rate of CO_2 is too low. We can eliminate the second possibility since y_c closely matches the data, and so it follows that the concentration of absorbed NH_3 in the liquid-phase is not growing at a rate consistent with experiment. Hence, we conclude per Eq. (4.4) that the sum $2(\dot{r}_{het} + \dot{r}_{hom})$ is underestimated by the model. Since at 60° the vapor pressure of AC is just slightly above atmospheric pressure [7-9], it is probable that the heterogeneous reaction had not yet reached the mass transfer limited condition. As was the case with T = 55°C, this gives rise to otherwise unexpected behavior in the experiment due to reaction dynamics on the solid-phase, such as a time period over which $\dot{r}_a^{s-l} > 2\dot{r}_c^{s-l}$. This would explain the excellent match to the CO_2 gas-phase concentration data in Figure 39 but comparatively poor match to the gas-phase NH_3 concentration data from the same experiment.

Good agreement was also observed across all datasets at 70°C; a representative comparison with a reaction temperature of 70°C, an initial AC mass of 40g, and an initial particle size range between 40 and 50 mesh is shown in Figure 40

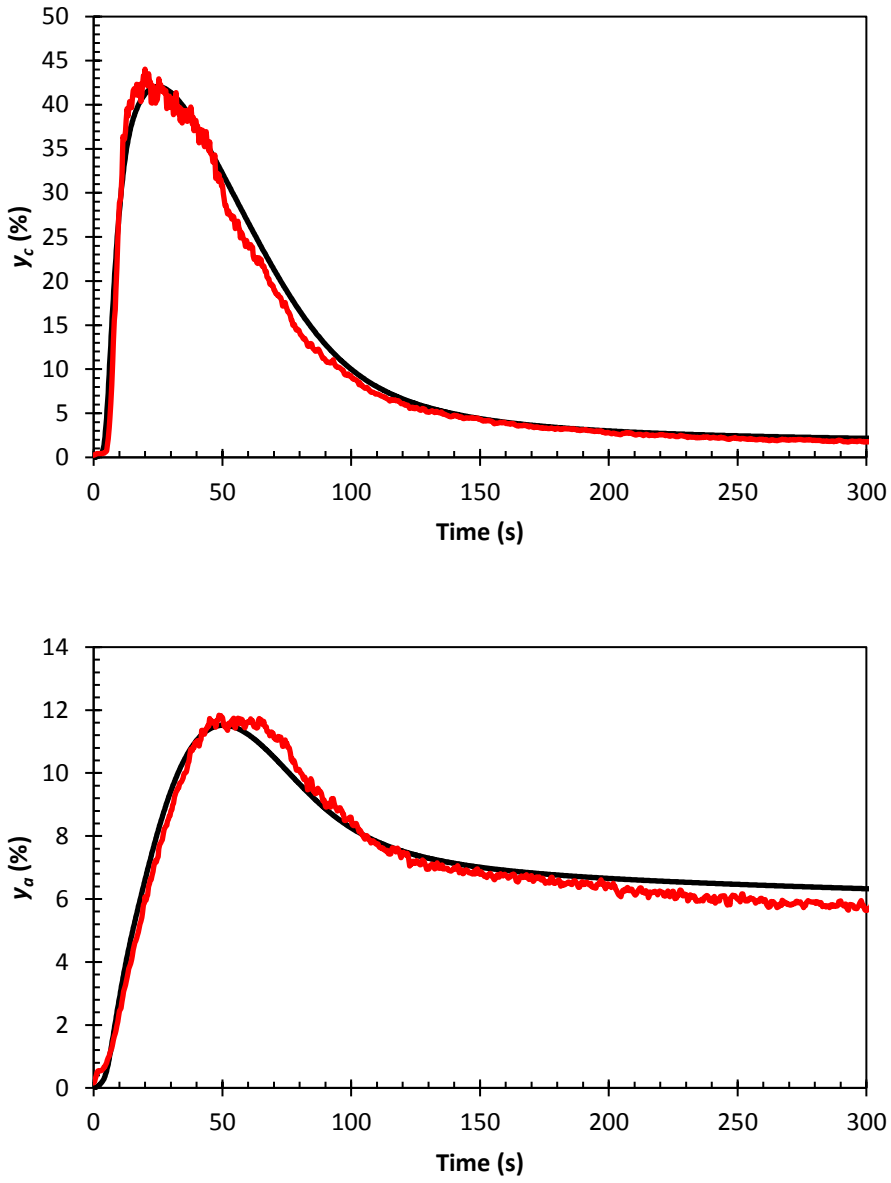

Figure 40. Comparison of experiment (red curve) and model predictions (black curve) for CO_2 (top plot) and NH_3 (bottom plot) gas-phase mole fractions. Reaction conditions were m_{AC} = 40g, T_l = 70°C, and initial particle size between 40 and 50 mesh.

Figure 40 demonstrates similarity in curve height, slope, and overall shape between model and experiment, with a marked improvement in agreement with the y_a data. The model predictions show small deviations from the shape of the CO_2 curve (top plot) are present, namely the flat apex and narrow peak width in the FTIR measurements. Overall, these slight departures from the experimental results do not appear significant, and could perhaps be improved by adjusting the bubble release-rate correlation, which was used here without any modification, to encompass the specific vessel, agitator, and operating conditions in the batch reactor vessel. The NH_3 gas-phase concentration curves in Figure 34 show much better alignment compared to the predictions for 60°C (Figure 39), and the model demonstrates the narrow peak region that is a salient characteristic of the y_a data when especially vigorous bubble release was observed.

As a more detailed demonstration of the model's suitability for use in "off-design" conditions, the model predictions were also compared to an experiment that was not used as part of the parameter estimation. This particular experiment utilized an initial particle size range of 60 to 100 mesh, with an AC sample size of 40g at a reaction temperature of 70°C. The results of the comparison in y_a and y_c predictions are presented in Figure 41

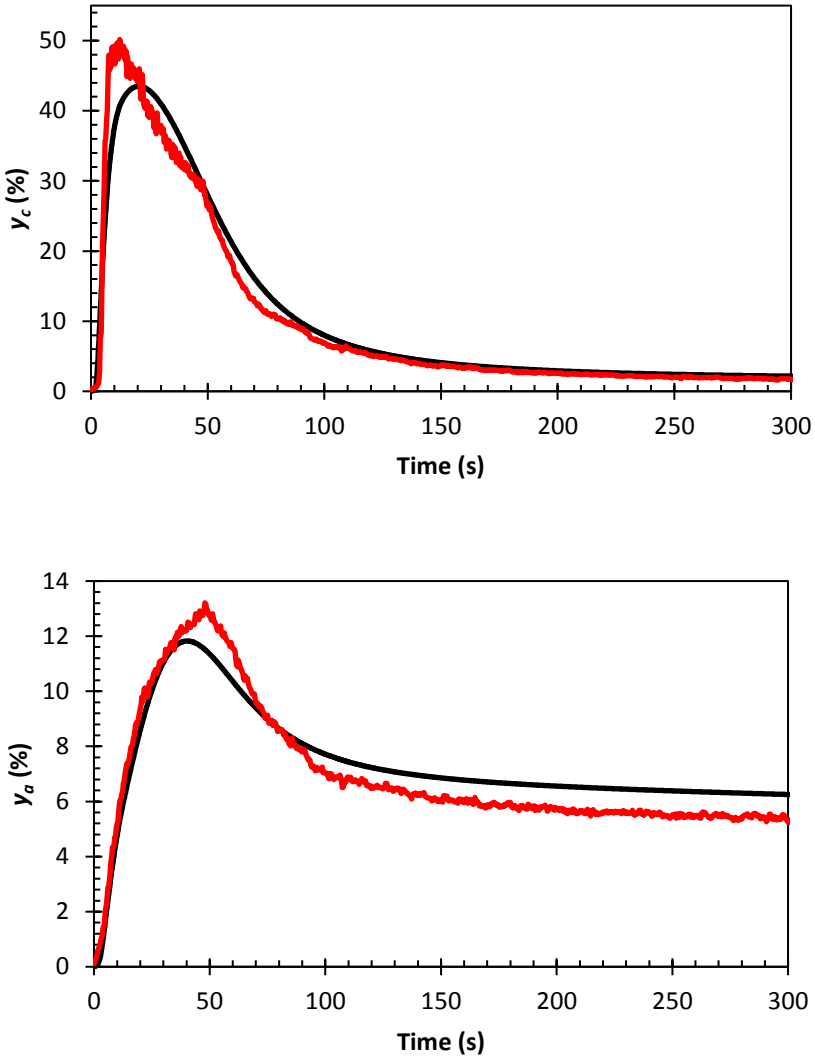

Figure 41. Comparison of experiment (red curve) and model predictions (black curve) for CO_2 (top plot) and NH_3 (bottom plot) gas-phase mole fractions. Reaction conditions were m_{AC} = 40g, T_l = 70°C, and initial particle size between 60 and 100 mesh.

Figure 41 shows good agreement between model and experiment for the off-design dataset. The CO_2 peaks are very close in terms of height and overall width, but with an underestimation in the slope leading up to the peak's apex. The model also does not reproduce the piecewise slopes as y_c begins to decline. The NH_3 also show fair agreement, with the only significant deviations being a ~10% under-prediction in peak height and the failure to produce the unusual peak shape.

4.4 Sensitivity Analysis

In this section, we consider the effect of parametric perturbations on the prediction of CO_2 (y_c) and NH_3 (y_a) gas phase concentrations. This analysis provides an estimate of the relative effect of uncertainty in the kinetic parameters, in addition to insights as to behavior of the parameter estimation routine. The 'baseline' model predictions (i.e. y_a or y_c without perturbed parameters) are obtained using the conditions m_{AC} = 40g, T_l = 70°C, and initial particle size range -40 +50 mesh. Parameters are adjusted by magnitudes of +/- 100% of their baseline value. This perturbation magnitude was chosen so as to be "large" enough to assess the impact of an individual mechanism on the observed gas-phase concentration history and the strength of its coupling to other mechanisms in the hypothesized reaction scheme.

To provide a conceptual framework to more clearly discuss the results that follow, it is useful to consider the net reaction rate as being composed of two parallel pathways, i.e.,

1) Desorption of CO_2, NH_3 to liquid-phase ($\dot{r}_{het}$) → Desorption from liquid-phase to gas-phase
2) Dissolution of AC to liquid-phase ($\dot{r}_{dis}$) → Homogeneous decomposition → Desorption from liquid-phase to gas-phase

According to the reaction scheme, these pathways are coupled since the liquid-phase concentrations enter into all steps of the reaction. However, when the net reaction rate is predominantly forward (namely, during the first 100 seconds of the reaction when heat absorption is maximum), the accumulation of NH_3 in solution has only a secondary effect. In such instances, the parameters involved in a particular reaction/species transfer mechanism are coupled only to subsequent steps within the same pathway. This allows one to link changes induced in one of the two pathways to certain trends and characteristics in the output of CO_2 and NH_3 gas-phase concentration histories.

4.4.1 Heterogeneous Parameters

Adjustments were first made to the heterogeneous reaction and dissolution parameters – K_{het}, k_{het}, $x_{AC,sat}$, and k_{dis} – in the manner described above. Comparisons of the gas-phase concentration histories for CO_2 and NH_3 are shown in Figure 42 and Figure 44 as a response to variations in K_{het}, k_{het}, which govern the heterogeneous decomposition mechanism.

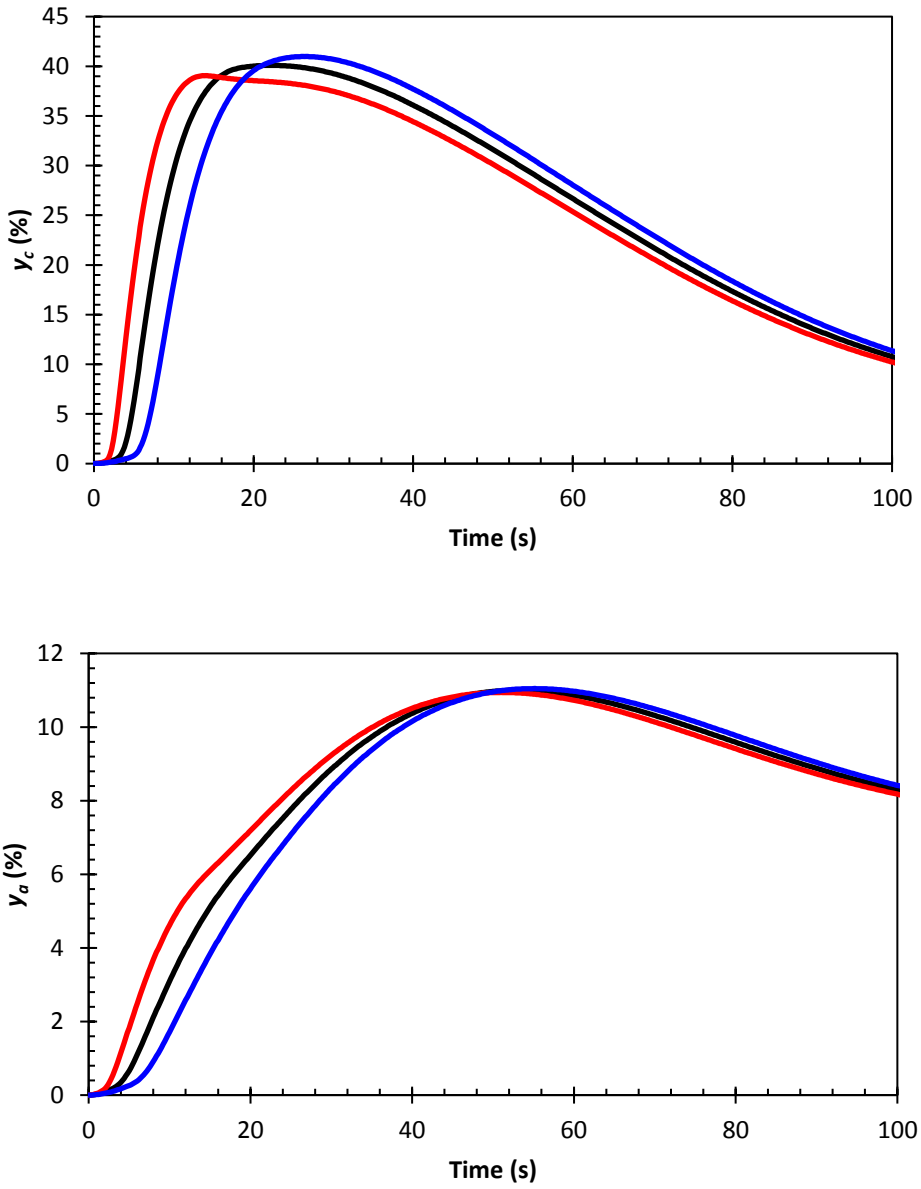

Figure 42. CO_2 (y_c, top) and NH_3 (y_a, bottom) gas-phase concentration histories at different values of khet (baseline – black, x2 – red, x0.5 – blue) with m_{AC} = 40g, T_l = 70°C, and initial particle size range of -40 +50 mesh.

The solid-phase parameters primarily affect the y_a and y_c shapes in the initial stage of the reaction, with diminishing influence following the occurrence of the peak value in y_c. The y_a curves are comparatively less affected due to the high solubility of NH_3 in PG, resulting in a capacitive effect on the species transfer dynamics. Increasing/decreasing k_{het} shifts y_c to the left/right without changing the initial slope (following introduction of AC into the reactor).

Curiously, there is a slight increase in y_c peak height with a 0.5x perturbation of the baseline k_{het}, while the peak height decreases with a 2x perturbation; to understand this, we recall the two pathways feeding the level of CO_2 supersaturation, and thus driving the release of dissolved CO_2 gas – the overall shape and height of y_c can be thought of (qualitatively) as a superposition of "sub-curves" due to paths (1) and (2), each with their own characteristic magnitude and timescale. For the purpose of this discussion, we shall refer to the time at which the peak contribution for path (1) or (2) occurs as the *phase* and the height of this peak contribution as the *magnitude*. Accordingly, the degree to which these two processes are in/out of phase and their *relative* magnitudes largely influences the width of the y_c peak near the apex and to a lesser extent the maximum y_c value attained. Stated more precisely, when path (1) is occurs significantly faster than path (2) (but they are of similar magnitude) the rate of CO_2 release attains two local extrema, each of which corresponds to paths (1) and (2) – this is exhibited by the red curve in Figure 32. As the two pathways become more in-phase, the two peaks gradually merge into a single peak; the intermediate curve between these two extremes appears as a broad peak with either a flat or slightly sloped top

depending the on the relative magnitudes of paths (1) and (2). Figure 43 illustrates the changes in $\dot{r}_{het}$ (path (1)) and $\dot{r}_{hom}$ (path (2)) corresponding to an increase/decrease in k_{het}.

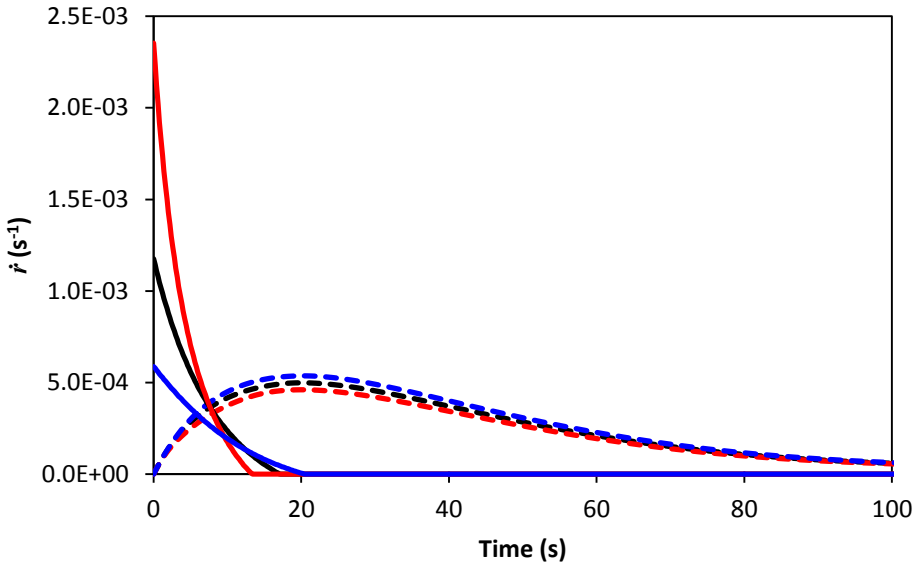

Figure 43. Model predictions for heterogeneous reaction rate (solid) and homogeneous reaction rate (dashed) at different k_{het} (x1-black, x2 – red, x0.5 – blue) with m_{AC} = 40g, T_l = 70°C, and initial particle size range of -40 +50 mesh.

At the onset of the reaction, $\dot{r}_{het}$ is at a maximum (the "pause" before the rapid increase in slope is due to the buildup of CO_2 until it exceeds the saturation limit and bubbles form) and decreases rapidly, whereas $\dot{r}_{hom}$ starts at zero and continues to build as dissolved AC accumulates in the liquid-phase. Increasing k_{het} increases the magnitude of $\dot{r}_{het}$ and slightly reduces its duration since the saturation limit $x_{a,s}$ is attained faster. There is only a minor change in the magnitude of $\dot{r}_{hom}$, and the location of its peak appears unaltered. The increase in $\dot{r}_{het}$'s magnitude and the curve's overall shift leftward results in the path (1) peak occurring further in advance than that of path (2); this results in a

peak that is broader, but also slightly shorter than the baseline. As k_{het} is reduced, the magnitude of path (1) is reduced and the lag is increased, aligning its peak closely with path (2) and thus producing a single curve with a narrower peak than the baseline, but a slightly higher maximum value since the two pathways are effectively in-phase.

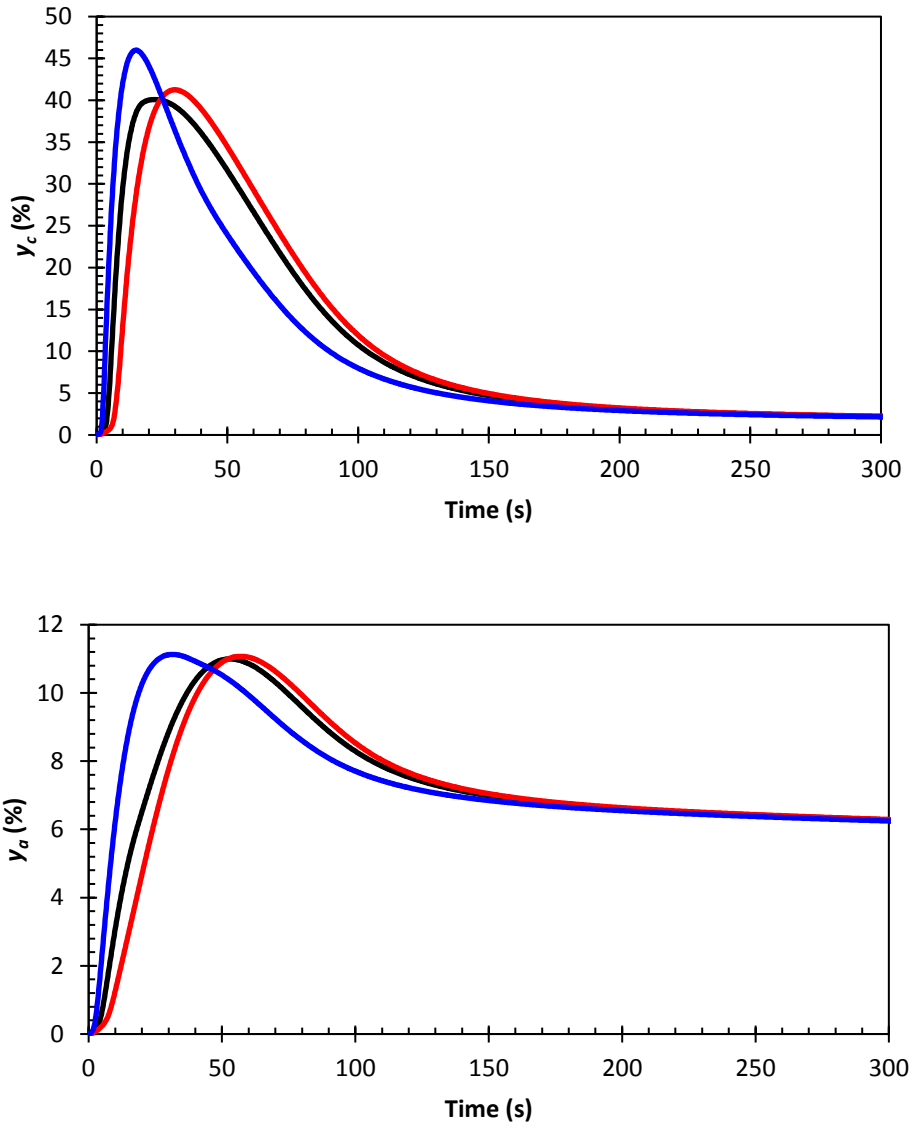

Figure 44. Model predictions for CO_2 (y_c, top) and NH_3 (y_a, bottom) gas-phase concentration histories at different values of K_{het} (baseline – black, x2 – red, x0.5 – blue) with m_{AC} = 40g, T_l = 70°C, and initial particle size range of -40 +50 mesh.

Decreasing/increasing K_{het} increases/decreases the *effective* saturated concentration of NH_3 and CO_2 at the solid-liquid interface, and thence the driving force for desorption into the liquid-phase. The separation (or alignment) of phase and relative magnitudes of paths (1) and (2) are considerably more sensitive to changes in K_{het}. Accordingly, it is expected that the estimation routine does not need to affect large changes in K_{het} to adjust the shape of the y_c curve. The lower sensitivity of y_c to changes in k_{het} implies comparatively larger perturbations are required to adjust the curve shape. Hence, there will generally be less scatter in the estimations of K_{het} compared to that of k_{het} for a given temperature across the three initial AC concentrations tested.

It is also worth noting that at lower temperatures, the sensitivity to changes in K_{het} is amplified while the sensitivity to k_{het} is muted. This can be seen in Figure 45, where the effects of perturbations in K_{het} and k_{het} on y_c are compared.

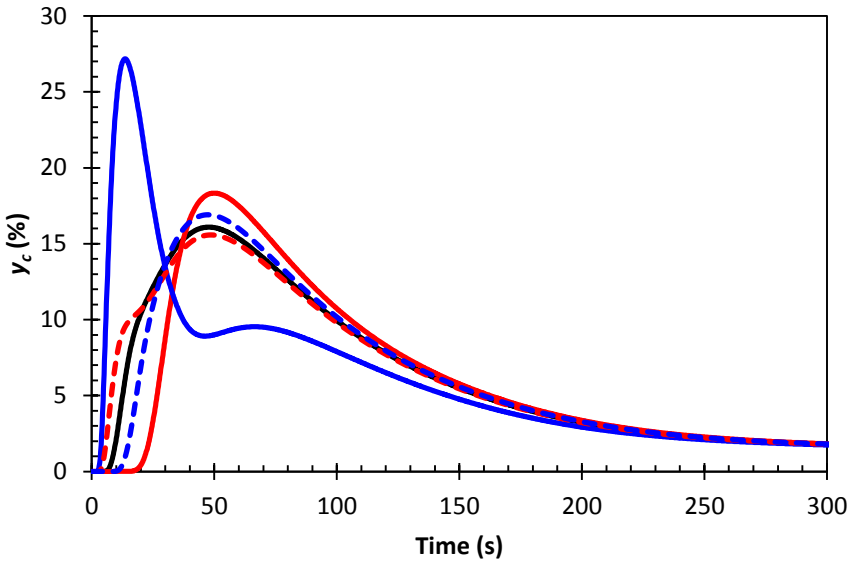

Figure 45. Comparison of model predictions for CO_2 (yc,) gas-phase concentration histories in response to perturbations in k_{het} (dashed) and K_{het} (solid) (baseline – black, x2 – red, x0.5 – blue) with m_{AC} = 40g, T_l = 60°C, and initial particle size range of -40 +50 mesh.

This tendency stems directly from the rapid change of K_{het} with respect to temperature and the assumption that desorption and dissolution from the solid-phase is irreversible: at lower temperatures, K_{het} is large and thus the driving force for desorption of NH_3 and CO_2, $x_{a,s} - x_a$ quickly reaches nil. In this condition, the longevity of the heterogeneous reaction is such that very little CO_2 is released via path (1). With this limitation in place, changing k_{het} only accelerates the dynamics of path (1), but does not influence the reaction's preference for path (1). Therefore, the gross effect on CO_2 release is small. When K_{het} is small, as it would be at higher temperatures, the preference for path (2) is comparable to path (1), or even greater. As a result, changing the dynamics associated with the first step of path (1) has a more pronounced effect. It is also evident in Figure 45 that at T = 60°C, further increases in K_{het} have a moderate,

albeit non-trivial, impact on y_c, whereas there is a dramatic change when K_{het} is decreased by the same proportion. Again, this can be explained based on how K_{het} changes the preference for paths (1) or (2). The situation in Figure 45 is consistent with a reaction that predominantly follows path (1), as further reductions in the contribution of path (2), i.e. increases in K_{het}, have a diminishing effect on y_c and y_a. However, reducing K_{het} by half yields a ~50% increase in the peak value of y_c and simultaneously shifts the peak location by about 30 seconds to the left. This perturbation of K_{het} renders the reaction preferential to path (2), as evidenced by the high initial peak due to heterogeneous reaction and the smaller secondary peak due to the homogeneous reaction. This same logic also dictates that with increasing temperature, y_c and y_a will become less sensitive to K_{het}, but more sensitive to k_{het}.

Changing $x_{AC,sat}$ and k_{dis}, which control the solid-liquid dissolution of un-reacted AC, have a qualitatively similar effect with respect to changes in the shape of the y_c peak early in the reaction; in this case, the magnitude and phase shift of path (2) experience large variations while those of path (2) are effectively unchanged. We are essentially preserving the inherent timescale of the homogeneous reaction while changing those of the preceding dissolution step. A comparison of the effects of changes to $x_{AC,sat}$ and k_{dis} on the gas-phase mole fractions are shown, respectively, in Figure 46 and Figure 47.

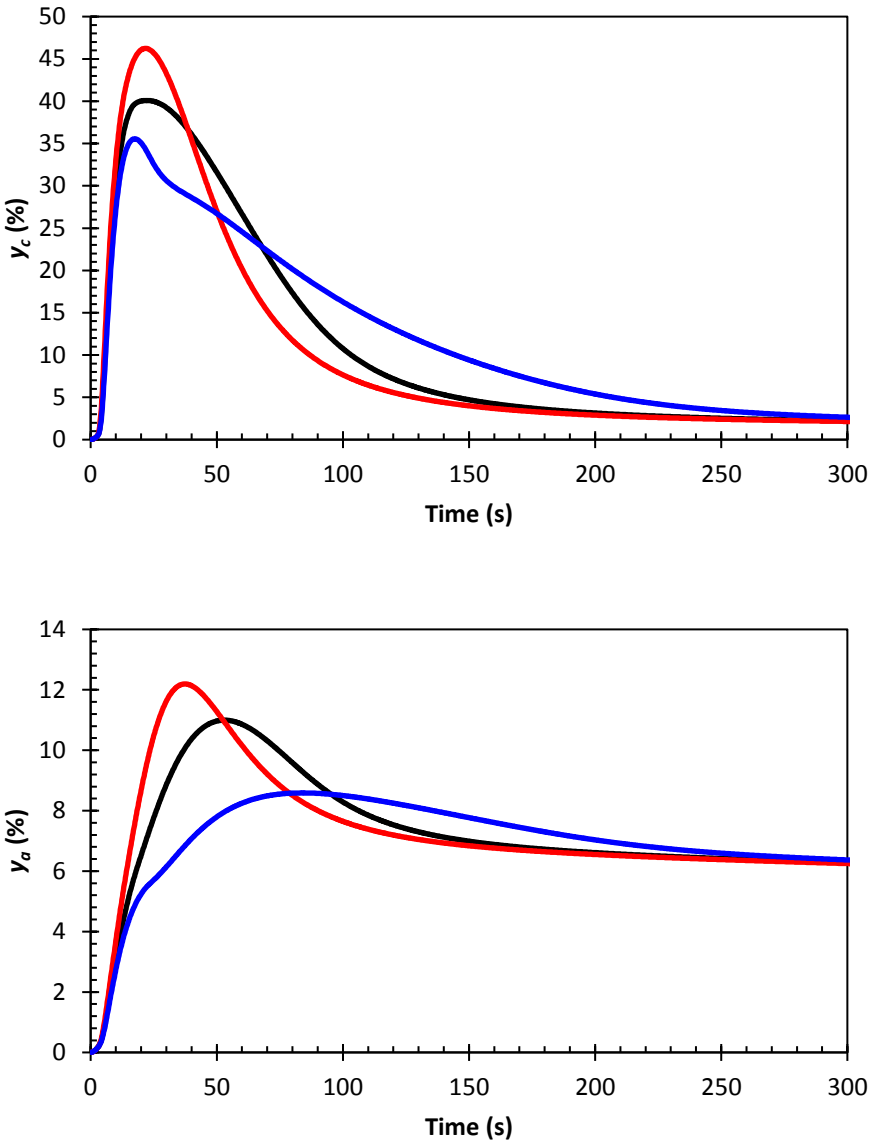

Figure 46. Model predictions of CO_2 (y_c, top) and NH_3 (y_a, bottom) gas-phase concentration histories at different values of $x_{AC,sat}$ (baseline – black, x2 – red, x0.5 – blue) with m_{AC} = 40g, T_l = 70°C, and initial particle size range of -40 +50 mesh.

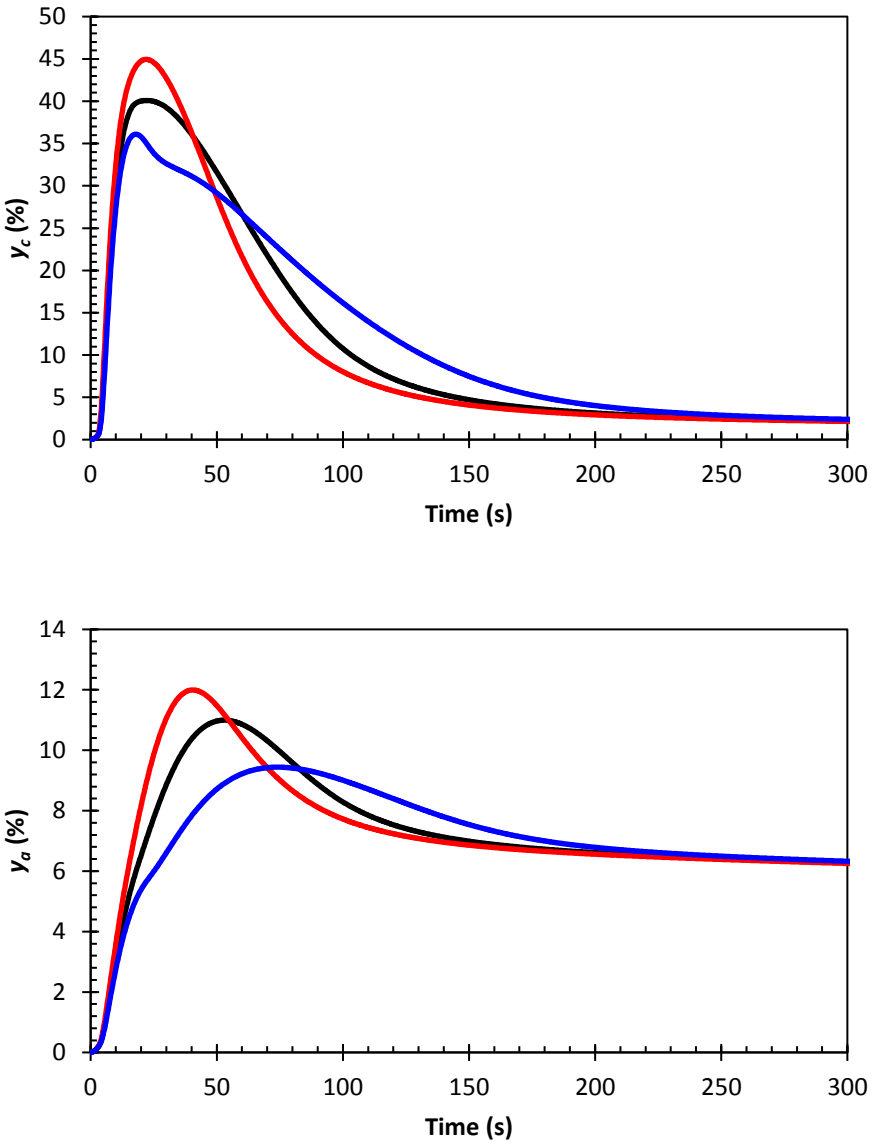

Figure 47. Model predictions of CO_2 (y_c, top) and NH_3 (y_a, bottom) gas-phase concentration histories at different values of k_{dis} (baseline – black, x2 – red, x0.5 – blue) with m_{AC} = 40g, T_l= 70°C, and initial particle size range of -40 +50 mesh.

The y_c trends in Figure 47 with respect to perturbations in k_{dis} show formation of a step and widening of the peak as k_{dis} is decreased, whereas a single peak is formed and the peak is narrowed as k_{dis} is increased. Similar to the explanation for the pattern observed by varying the parameters controlling the first step of path (1), it is clear that decreasing k_{dis} causes both a diminished magnitude and rightward phase shift (i.e. further separation from the peak associated with path (1)), causing the path (1) peak to emerge. As k_{dis} is increased, path (2) experiences both a magnitude enhancement and a leftward phase shift, bringing it into phase with path (1) and thus producing a single, narrower peak. As would be expected, increases/decreases in the initial slopes of y_a accompany increases/decreases in k_{dis}. We also recognize that the "NH_3 limit" (plateau as $t \rightarrow \infty$) introduced in Chapter II remains approximately unchanged, since none of the equilibria (K_{het}, $x_{AC,sat}$, and K_{hom}) or liquid-gas mass transfer coefficients have been altered. Upon further comparison of Figure 46 and Figure 47 against Figure 42 and Figure 44, one notices that changes to $\dot{r}_{dis}$ have a comparatively minor effect on the initial slopes of y_c and y_a (generally within the first 30 seconds of the reaction), but have an increasingly pronounced effect thereafter. Changes to $\dot{r}_{het}$, in contrast, exert the strongest influence during the initial ~30 seconds, but the effect diminishes afterward. Thus, the sudden rise in CO_2 activity is initiated by heterogeneous decomposition, which is eventually supplanted by the contribution from the homogeneous reaction.

Additionally, comparing the trends shown in Figure 46 to those of Figure 47 show a nearly identical effect of doubling/halving $x_{AC,sat}$ to that of doubling/halving k_{dis}.

The route cause is the similar variation in $\dot{r}_{dis}$ with respect to changes in the two parameters, a comparison of which is shown in Figure 48:

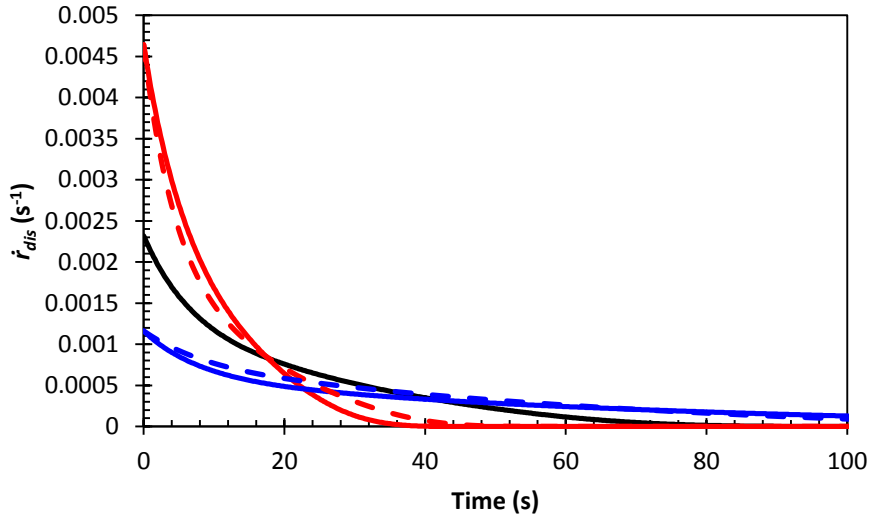

Figure 48. Comparison of model predictions for dissolution rate in response to perturbations in $x_{AC,sat}$ (solid) and k_{dis} (dashed) - baseline – black, x2 – red, x0.5 – blue. Reaction conditions were m_{AC} = 40g, T_l = 70°C, and initial particle size range of -40 +50 mesh.

The reason for this becomes clear upon examination of Eqs. (4.9) and (4.10). If the initial solid concentration of AC is far smaller than its saturation limit in the liquid-phase, we may invoke the following approximations:

$$\frac{\partial \dot{r}_{dis}}{\partial k_{dis}} \approx \frac{a_s'''}{V_l} x_{AC,sat} \tag{4.9}$$

$$\frac{\partial \dot{r}_{dis}}{\partial x_{AC,sat}} \approx \frac{a_s'''}{V_l} k_{dis} \tag{4.10}$$

The sensitivity of $\dot{r}_{dis}$ with respect to k_{dis} is directly proportional to $x_{AC,sat}$, and vice-versa. Hence, the effect on $\dot{r}_{dis}$ of doubling/halving k_{dis} is approximately equivalent to doubling/halving $x_{AC,sat}$. This would explain the scatter in the estimations for k_{dis} and $x_{AC,sat}$: since only small differences are present in the effect of both parameters, large changes were necessary to affect small curve alterations.

It was shown that the height, breadth, and general shape (single peak, step, twin peak) of the y_c curve can be manipulated by adjusting the overall reaction's preference for two parallel pathways. Nearly independent adjustment of the relative magnitude and characteristic timescale of each pathway was affected via their corresponding heterogeneous parameters. Broadly speaking, the tendency of the y_c peaks to become taller, narrower, and left-shifted with increasing temperature shows that the two pathways are overlapping to a greater extent. We therefore conclude that the temporally dependent preference between paths (1) and (2) becomes more equitable and uniform at greater temperatures (note that the increase in the homogeneous rate and equilibrium coefficients with temperature also contribute to this effect, to be discussed next).

4.4.2 Homogeneous Parameters

The timescale and magnitude of the homogeneous decomposition process is dictated by the forward rate coefficient, $k_{f,hom}$ and the equilibrium coefficient K_{hom}. Primarily, the homogeneous reaction is expected to influence the path (2) contribution to the overall reaction, with secondary effects on the solid-liquid desorption step of path (1). Figure 49 and Figure 50 show the effect of $k_{f,hom}$ and K_{hom}, respectively, on y_c and y_a.

There is a general qualitative similarity in the effect of both homogeneous parameters on y_c and those controlling the dissolution process (Figure 46 and Figure 47), insofar as the peak associated with path (2) is shifted left/right and its magnitude enhanced/diminished, while there is little difference in the slopes early in the reaction, indicating that the heterogeneous reaction remains relatively unaffected.

The rate coefficient effectively sets the time constant for the homogeneous reaction, which will cause its peak contribution of CO_2 and NH_3 to shift leftward and increase in magnitude as k_{hom} increases. This manifests as the broad "step" in the overall y_c peak becoming a single, narrower peak. K_{hom} does not appear to alter the phase difference between paths (1) and (2), but does produce a sizeable change in the path (2) magnitude. At this point in the reaction the heterogeneous reaction has ceased and the only available pathway is path (2).

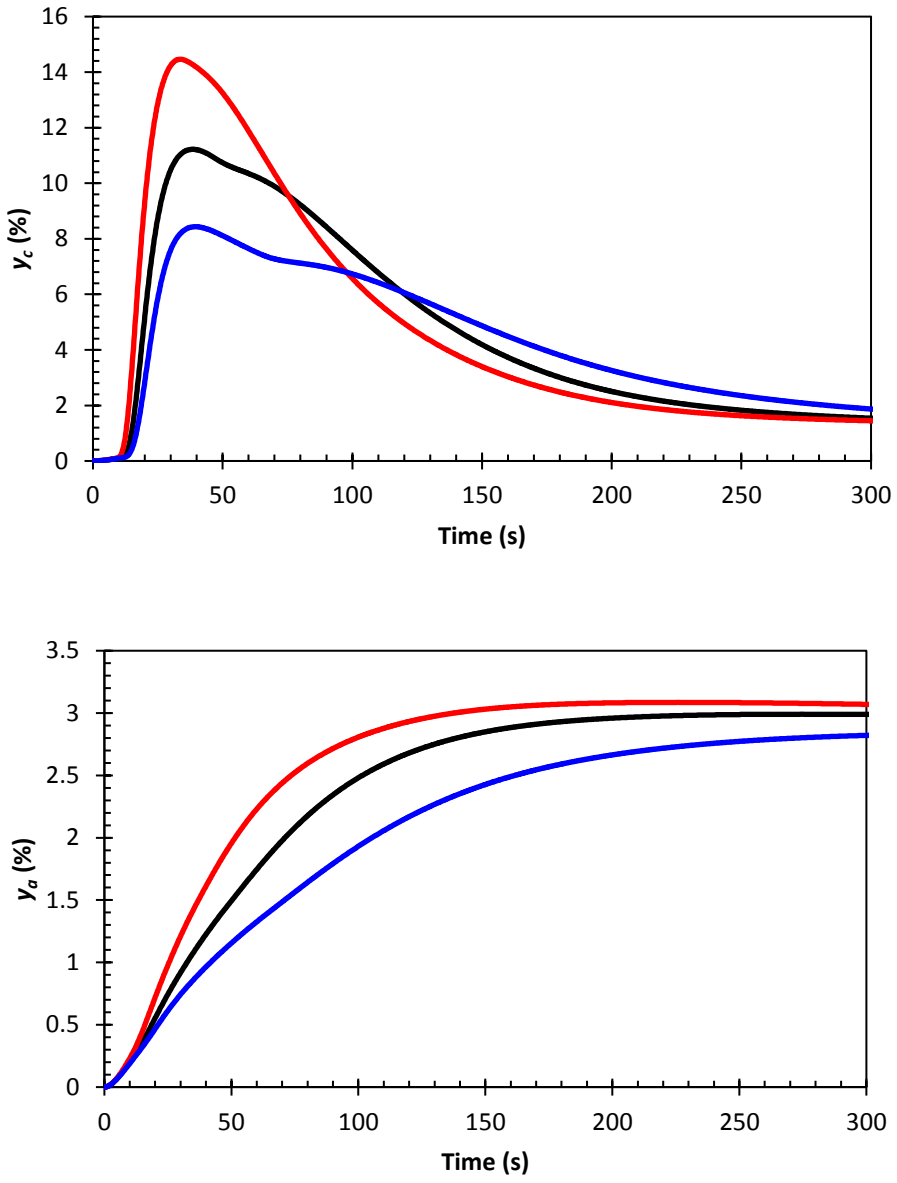

Figure 49. Model predictions of CO_2 (y_c, top) and NH_3 (y_a, bottom) gas-phase concentration histories at different values of $k_{f,hom}$ (baseline – black, x2 – red, x0.5 – blue) with m_{AC} = 40g, T_l= 70°C, and initial particle size range of -40 +50 mesh.

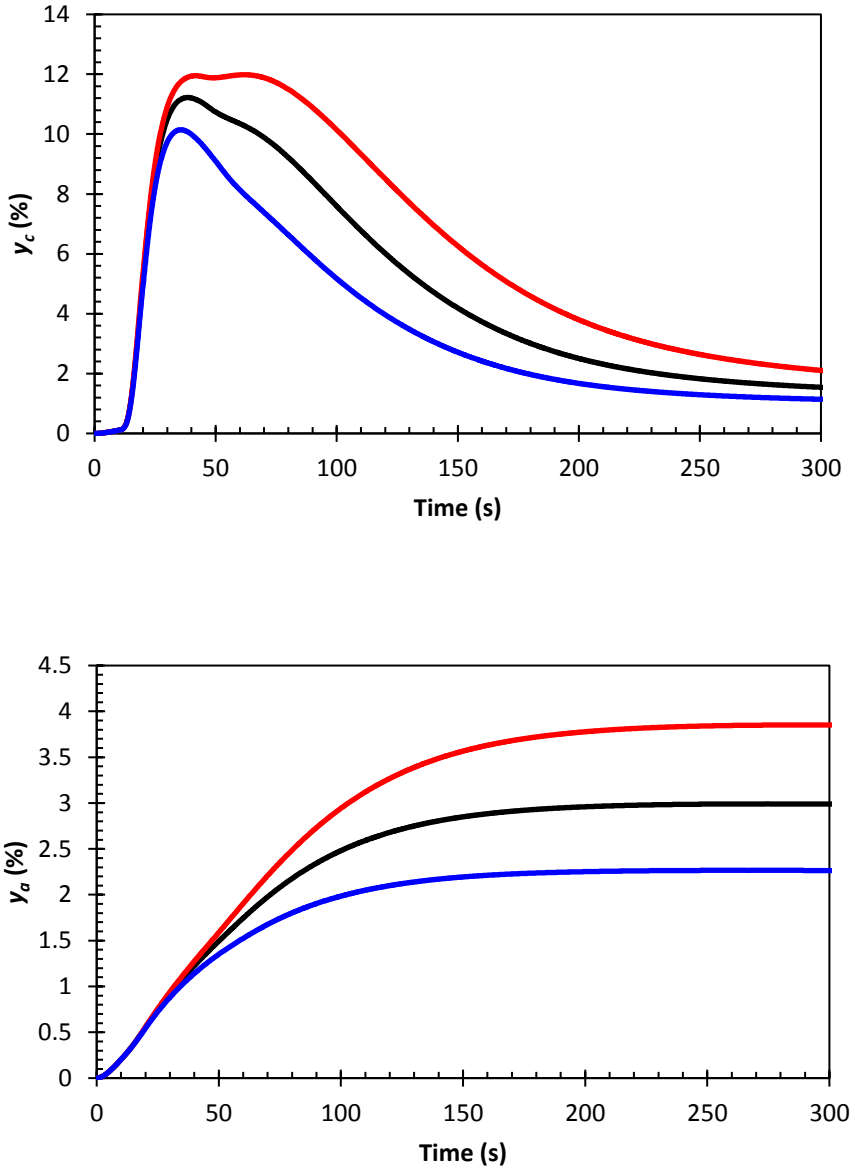

Figure 50. Model predictions of CO_2 (y_c, top) and NH_3 (y_a, bottom) gas-phase concentration histories at different values of K_{hom} (baseline – black, x2 – red, x0.5 – blue) with m_{AC} = 40g, T_l= 70°C, and initial particle size range of -40 +50 mesh.

It was argued in Chapter II that the accumulation of NH_3 in solution was primarily responsible for the rapid decrease in net reaction rate that occurs after approximately 100 s of reaction time; the accumulation of CO_2 in solution was presumed to be very small and experience only small changes, and thus have little influence on the transition from irreversible regime to mass transfer dominated regime. This hypothesis is supported by the effect of K_{hom} variation on the liquid-phase concentrations of CO_2 (x_c) and NH_3 (x_a), plotted in Figure 51.

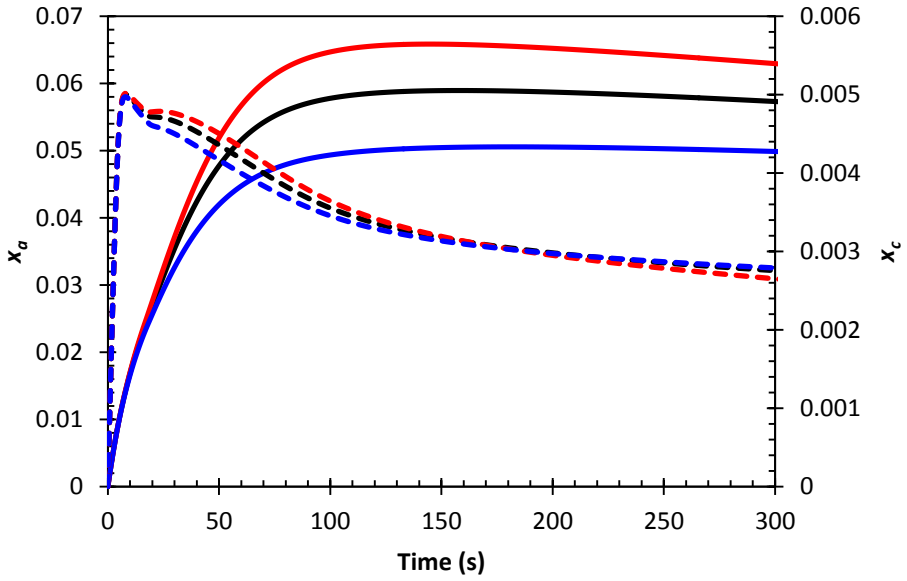

Figure 51. Model predictions for dissolved CO_2 (x_c – dashed lines) and NH_3 (x_a – solid lines) concentration subjected to perturbations of K_{hom} : baseline – black, x2 – red, and x0.5 – blue; input parameters were m_{AC} = 40g, T_l = 70°C, and particles size range was -40 +50 mesh.

One immediately notices that there are only small differences between the predictions for x_c despite two-fold variations in K_{hom} (approximately a 1.3% difference at

t = 300 s) while x_a shows nearly a 30% difference. Furthermore, since x_a shows far greater sensitivity (with respect to K_{hom}) compared to x_c, it follows that shifts in chemical equilibrium due to Le Chatelier's principle are reflected closely in changes to the amount of retained NH_3 late in the reaction.

CHAPTER V

THERMAL PARAMETER ESTIMATION

This chapter discusses the determination of the unknown heat of reaction and dissolution parameters that ultimately govern the total volumetric rate of heat absorption, which is of prime importance for any HEX reactor-based TMS scheme. There are three parameters that could not be obtained directly from the literature or experiment: the heat of reaction for heterogeneous decomposition (in PG), ΔH_{het}; the heat of dissolution for AC in PG, ΔH_{dis} and; the heat of reaction for homogeneous decomposition, ΔH_{hom}. Similar to Chapter IV, a model was developed in the Matlab/Simulink (MathWorks ver 2016a and 2016b) programming language along with MathWorks' parameter estimation utility to obtain estimates for the three aforementioned parameters. The reaction model developed in Chapter IV was included as a module in the calorimeter model, the development of which is discussed at length in this chapter. The kinetic parameters obtained in Chapter IV were input into the reaction model as functions of temperature in linear interpolated lookup tables. The parameter estimations obtained were compared to values in the literature and successfully reconciled with chemical thermodynamic theory. Additionally, the parameter estimates were used to compare model predictions to experimental liquid-phase temperature measurements across various AC sample sizes, temperatures, and particle sizes. The validation task demonstrates that the parameters obtained are appropriate for use in off-design conditions. Chapter V concludes with an analysis of the heat absorption due to individual reaction mechanisms, which shows that

under the conditions investigated in the batch reactor, nearly 30% of the available latent heat is not being utilized.

5.1 Heat of Solution of NH_3

The solubility data obtained as part of this study allows direct computation of the heat of solution for NH_3, $\Delta H_{a,des}$, per the thermodynamic relation [72]:

$$\left(\frac{\partial \ln x_a}{\partial (1/T)}\right)_P = -\frac{\Delta H_{a,des}}{\Re} \tag{5.1}$$

where $\Re$ is the universal gas constant and T is the absolute temperature in Kelvin. A plot of $\ln x_a$ as a function of $1/T$ (Figure 52) shows a linear dependence; a linear least-squares regression to the data yields $\Delta H_{a,des}$ = -22200 J/mol (~1300 J/g).

While not of immediate interest, the entropy of desorption can be computed using the same data, again following [72]:

$$\left(\frac{\partial \ln x_a}{\partial T}\right)_P = \frac{\Delta s_{a,des}}{\Re} \tag{5.2}$$

Plotting $\ln x_a$ as a function of T (Figure 53) and again applying a least-squares linear-regression, we find the entropy of desorption to be $\Delta s_{a,des}$ = -0.192 J/mol K.

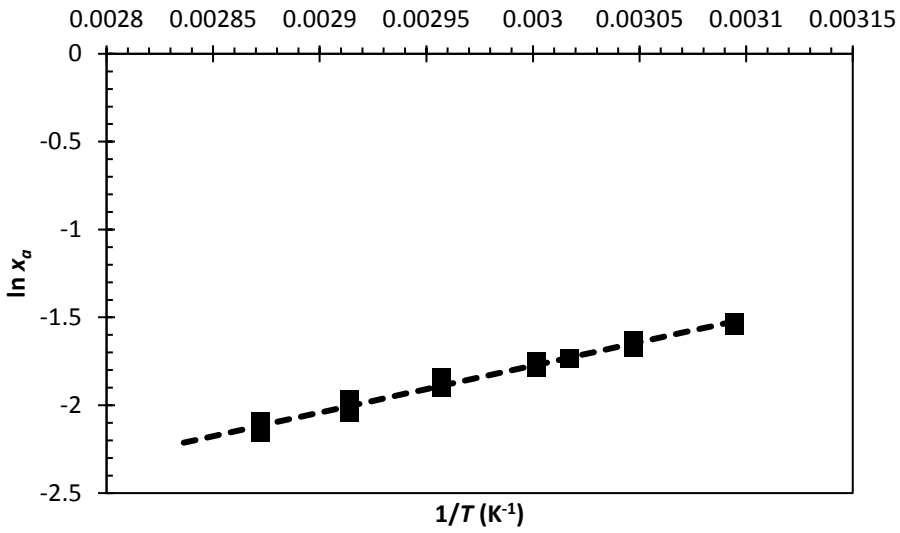

Figure 52. Plot of ln (x_a) as a function of 1/T as obtained from the solubility studies (black squares), and a least-squares linear regression to the same (dashed line). Linearity over the 50 °C- 80°C temperature range suggests that the heat of desorption for NH_3 is not a strong function of temperature

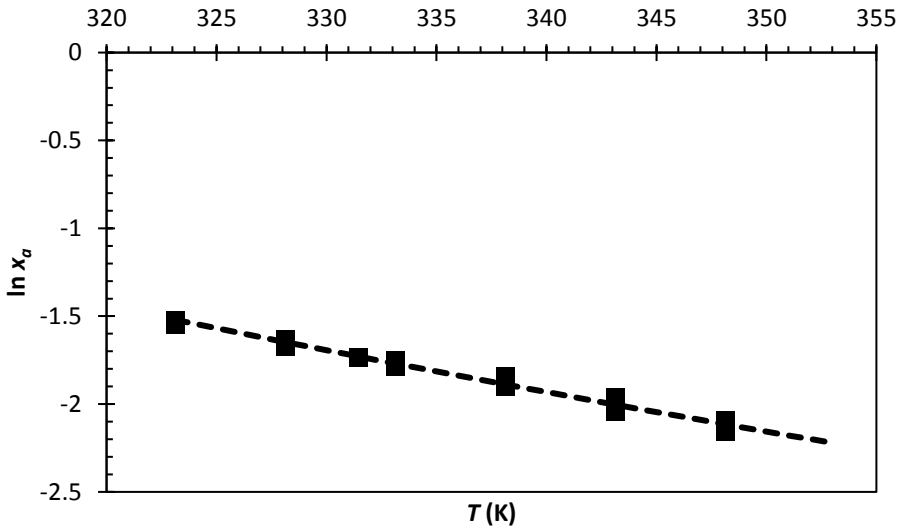

Figure 53. Plot of ln (x_a) as a function of T as obtained from the solubility study data (black squares) and a least-squares linear regression to the same (dashed line).

The heat of desorption for NH_3 is significant compared to the 1800 – 2100 J/g range for decomposition of AC [Schmidt thesis]. Eq. (5.1) was also applied to the data of Galvão and Francesconi [30] to calculate heat of solution of CO_2, which came to $\Delta H_{c,des} \approx$-9700 J/mol, or about 220 J/g. It is anticipated that the net contribution of CO_2 desorption to total heat absorbed will be small, and perhaps negligible under most conditions.

As an additional spot-check for the validity these calculations, a simple experiment was devised to obtain a rough estimate of the heat of desorption. 600 mL of NH_3 – loaded PG was placed into a 1-L Erlenmeyer flask; the flask was fitted with a stainless-steel ¼" tube through which dry nitrogen was fed to remove the dissolved NH_3. The mouth of the flask was fitted with a custom rubber stopper that allowed escaping gasses to be routed to the FTIR analyzer for NH_3 concentration measurement. While the desorption process occurred, a 1/8" T-type thermocouple probe (Omega Engineering, USA +/- 0.1°C) was inserted into the flask to continuously monitor temperature. A magnetic stirring bar provided agitation to ensure an approximately uniform temperature in the sample at any given time. Assuming negligible losses to the environment (the experiments were conducted at room temperature to minimize such losses), the heat of desorption is:

$$\Delta H_{a,des} = \frac{\int_0^t c_p(T)\,dT}{\Delta m_a} \tag{5.3}$$

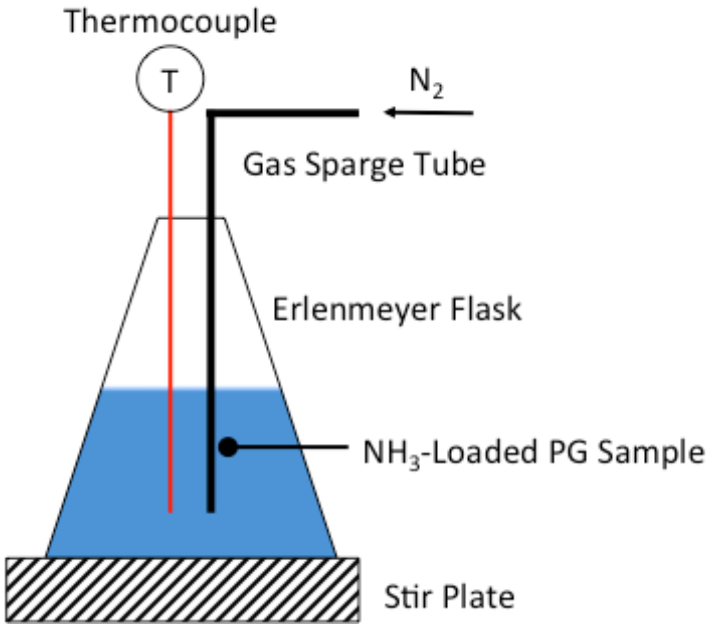

Figure 54. Simplified layout diagram of NH_3 desorption test apparatus

where t is the duration of the desorption experiment and Δm_a is the mass of NH_3 desorbed. Two protocols were used to measure Δm_a: for sample (1), Δm_a was measured by subtracting the mass of the flask assembly in Figure 54 measured after the experiment from that measured before the experiment; for sample (2), Δm_a was measured by integrating the FTIR measurements for NH_3 concentration and the known N_2 flow rate. In the latter case, desorption was allowed to continue until nearly all of the NH_3 was removed. This allowed the determination to be made when parasitic heat transfer from the environment became 'too significant" to ignore. In addition, Eq. (5.3) could be monitored as a function of time rather than simply initial and final conditions. The second measurement protocol therefore represents a more refined approach than the first

measurement protocol, although we present the results of both here for the sake of completeness.

Four runs were conducted – two with each measurement protocol -- with temperature differences sufficiently small to ensure that c_p did not vary by more than 2%. The results of these runs are summarized in Table 3:

Table 3. Experimental results for $\Delta H_{a,des}$ spot-check using both FTIR (2) and gravimetric (1) measurement methods

Protocol	Δm_a (g)	$T_{initial}$ (°C)	T_{final} (°C)	$\Delta H_{a,des}$ (J/g)
2	2.2	14.93	13.39	1013
2	2.2	19.97	17.63	1590
1	4.43	25.08	20.93	1398
1	8.55	20.56	13.66	1154

The results tabulated in Table 3 are within the neighborhood of the predicted value for $\Delta H_{a,des}$ obtained using Eq. (5.1) (+/- 200 W, approximately). We therefore confirm that $\Delta H_{a,des}$ is indeed a significant fraction of the total latent heat realizable through the reaction in PG.

From the standpoint of designing a HEX reactor to obtain the maximum possible usage of latent heat, it is not only the antagonistic effect on the reaction kinetics posed by dissolved NH_3, but also the non-trivial fraction of latent thermal energy retained that are critical to reactor performance. Thus, it is becoming evident that promoting the rapid desorption of dissolved NH_3 will perhaps prove to be the technical challenge that must be surmounted to make the AC HEX reactor-based TMS realizable in a practical setting.

5.2 Calorimeter Model

Due to the rapid kinetics and dynamic temperature controller, the assumption of quasi-steady heat transfer between the coil and reactor contents cannot be applied with reasonable accuracy. Therefore, a transient heat transfer model of the resistive heat coil and reactor wall was developed to account for transient thermal energy storage effects in the reactor energy balance. The calorimeter model is an extension of the batch reactor model of Chapter IV, subjected to the same assumptions of a well-mixed liquid-phase. In addition to the kinetic and mass transfer model, there are three additional sub-models for thermal energy conservation in the reaction vessel, the liquid-phase (which includes the solid-phase), and the heat source. The sub-models were formulated in such a fashion that they could construct a single overall linear system of first-order ODEs that are easily solvable in the Matlab/Simulink programming language. In this section we discuss the mathematical underpinning and assumptions applied to each of the sub-models, including validation and eventual integration into a complete model of the coupled thermal and chemical behavior in the batch reactor.

5.2.1 Heater Model

The thermostating function of the batch reactor/calorimeter relies on a resistive heater element to respond to rapid changes in thermal load upon the introduction of solid AC into the reactor. The heater coil consists of a stainless steel sheath having a thickness of 0.635 mm, a layer of MgO insulation, and a Nichrome wire at its core with a nominal diameter of 0.724 mm. The outer diameter of the coil is 7.37 mm. Because the sheath is

very thin and has low specific heat capacity in addition to relatively high thermal conductivity, the temperature gradient and energy storage within the sheath is negligible compared to those of the insulation layer.

5.2.1.1 Mathematical Model

To compensate for the dynamic behavior of the heater coil when subjected to variable loading, the heater is modeled as a 1-dimensional cylinder subjected to a known, uniform heat flux at $r = R_o$, and a uniform convection coefficient at $r = R$. Because the sheath is very thin and has low specific heat capacity in addition to relatively high thermal conductivity, the temperature gradient and energy storage within the sheath is negligible compared to those of the insulation layer. A schematic of the math model domain is shown in Figure 55:

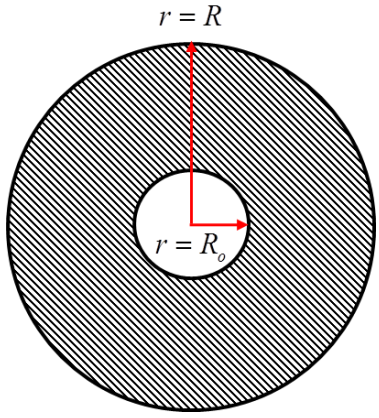

Figure 55. Domain for heater coil mathematical model; the Nichrome resistive element is represented by the region from the center to $r = R_o$; the MgO insulation is represented from $r = R_o$ to $r = R$. The presence of the stainless steel sheath was neglected

Thus, the governing equation for heat conduction and storage in a cylinder with uniform, constant properties is:

$$\frac{1}{a_h}\frac{\P T_h}{\P t} = \frac{\P^2 T_h}{\P r^2} + \frac{1}{r}\frac{\P T_h}{\P r} \tag{5.4}$$

where T_h is the heater temperature, r is the radial coordinate, and α_h is the effective thermal diffusivity. The Nichrome resistive heater element has a very small diameter in addition to high thermal conductivity and low specific heat capacity; it is reasonable, then, to neglect energy storage within the wire resistive element at the heater core. This assumption allows the Nichrome wire to be represented as a boundary condition at $r = R_o$:

$$\left.\frac{\partial T_h}{\partial r}\right|_{r=R_o} = -\frac{q_h''}{k_h} \tag{5.5}$$

where q_h'' is the heat flux from the Nichrome wire, and k_h is the effective thermal conductivity of the MgO insulation layer. q_h'' was calculated by assuming the total electrical power delivered to the heater by the DC power supply is uniformly distributed throughout the heater length. The condition at the surface of the heater coil is:

$$\left.\frac{\partial T_h}{\partial r}\right|_{r=R} = \frac{h_h}{k_h}\left(T_h\left(r=R,t\right) - T_l(t)\right) \tag{5.6}$$

Where h_h is the convection coefficient at the heater surface and T_l is the bulk liquid temperature of the PG.

To solve Eqs. (5.4)-(5.6), the domain was discretized spatially by a radial increment $\Delta r = \left(R - R_o\right)/K$, where K is an integer representing the number of discrete cells, but allowed to remain continuous in time. This allowed to the governing equations to be re-cast in state-space form:

$$\frac{d\mathbf{T}_h}{dt} = \mathbf{A}\mathbf{T}_h + \mathbf{b}_h \tag{5.7}$$

The first cell (with index $i=1$) is subjected to a time dependent heat flux; defining $\varepsilon = \Delta r/(R - R_o) = 1/K$, the discretized energy balance for the inner boundary cell reads:

$$\frac{dT_{h,1}}{dt} = \frac{\alpha_h}{\Delta r^2}\frac{\varepsilon+1}{\varepsilon+0.5}\left(T_{h,2} - T_{h,1}\right) + \dot{Q}_h\left(\frac{\alpha_h}{2\pi L k_h \Delta r^2\left(\varepsilon+0.5\right)}\right) \tag{5.8}$$

Where L is the length of the heater coil containing the nichrome element. For all interior cells having indices $i = 2,\cdots,K-1$, the time derivatives are given by:

$$\frac{dT_{h,1}}{dt} = \frac{\alpha_h}{\Delta r^2}\frac{\varepsilon+i}{\varepsilon+i-0.5}\left(T_{h,i+1} - T_{h,i}\right) - \frac{\alpha_h}{\Delta r^2}\frac{\varepsilon+i-1}{\varepsilon+i-0.5}\left(T_{h,i} - T_{h,i-1}\right) \tag{5.9}$$

The outer boundary cell ($i = K$) is subjected to a convection boundary condition; if we designate $T_{h,s}$ as the surface temperature of the heater coil, the time derivative for the K-th cell is:

$$\frac{dT_{h,K}}{dt} = \frac{a_h}{\Delta r^2}\frac{2(\varepsilon + K)}{\varepsilon + K - 0.5}\left(T_{h,s} - T_{h,K}\right) - \frac{a_h}{\Delta r^2}\frac{\varepsilon + K - 1}{\varepsilon + K - 0.5}\left(T_{h,K} - T_{h,K-1}\right) \tag{5.10}$$

where the convection boundary condition at the heat coil surface is derived from a control surface (zero thickness) energy balance to equate the rate of conduction to that of convection:

$$T_{h,surf} = -\frac{0.5Bi_h}{0.5Bi_h + 1}T_l + \frac{1}{0.5Bi_h + 1}T_{h,K} \tag{5.11}$$

where $Bi_h = h_h \Delta r / k_h$ is the heater Biot number. Rendering the governing equation in this manner allowed solutions to be rapidly computed using the MatLAB/Simulink software package.

5.2.1.2 Thermophysical Parameter Estimation

There are three parameters in Eqs. (5.8) - (5.11): The heater Biot number Bi_h, the effective thermal diffusivity, α_h, and the effective thermal conductivity, k_h. The deduction of α_h and k_h was fairly straightforward; if the reaction vessel was completely devoid of fluid, and subjected to vacuum conditions, the only mode of heat transfer from the surface of the heater is radiation, which is small at the temperatures of interest. Thus, the boundary condition in Eq. (5.6) is reduced to:

$$\left.\frac{\partial T_h}{\partial r}\right|_{r=R} = 0 \tag{5.12}$$

From Eq. (5.19) it follows immediately that $T_{h,surf} = T_{h,K}$. The surface temperature of the heater could be easily measured and used as an objective function to parametrically estimate α_h. A K-type thermocouple probe with a nominal diameter of 0.01" was attached to the surface of the heater coil with a small hose clamp. To ensure uniform contact between the probe and the heater surface, a thin (<0.001") stainless steel shim was placed between the probe and the hose clamp. The reaction vessel was evacuated and held at ~8 Torr, and a fixed DC voltage was imposed on the heater coil. The surface temperature was permitted to climb until at least 30 seconds had lapsed; normalized surface probe temperature $(T - T_{min}) / (T_{max} - T_{min})$ data are plotted against normalized time (t / t_{max}) for heater inputs of 50W, 100W, and 500W in Figure 56.

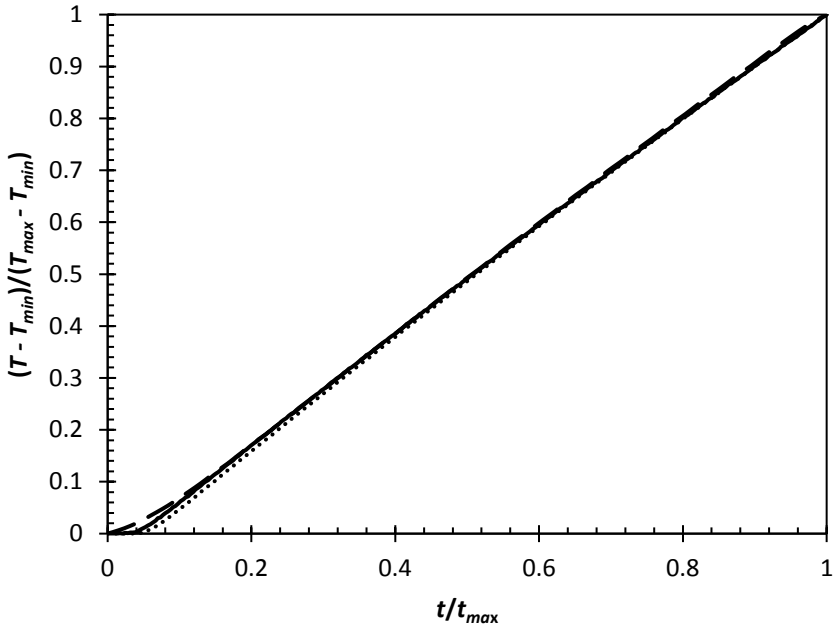

Figure 56. Plot of normalized temperature (T - T_{min}) / (T_{max} – T_{min}) vs. normalized time t / t_{max} for heater inputs of 50W (solid), 100W (dashed), and 500W (dot).

The objective function for fitting α_h and k_h is:

$$F(\alpha_h, \kappa_h) = \int_0^{t_{\max}} \sqrt{T_{h,surf}^2 - T_{h,surf}^{2*}}\, ds \tag{5.13}$$

where $T_{h,surf}^*$ is the experimentally measured heater coil surface temperature. The fitting procedure was accomplished as follows:

1) An experimental data set (e.g., corresponding to heater power inputs of 50W, 100W, etc) is chosen for fitting
2) An initial guess for α_h and k_h is chosen

3) Eq. (5.7), subject to boundary conditions in Eqs. (5.11) and (5.12) is solved numerically using the finite volume method with fully implicit discretization

4) The objective function (Eq. (5.13)) is computed using the model output and experimental data points

5) α_h and k_h are incremented and the computations (steps 2 and 3) are repeated to span a range of α_h and k_h values

6) The $F(a_h, k_h)$ data is tabulated; α_h and k_h are chosen such that $F(a_h, k_h) = \min(\{F\})$, where $\{F\}$ is the set of tabulated $F(a_h, k_h)$ values.

The above procedure was executed using the data set for a 500W heater input, which was chosen since it was at the middle of the heater's output range. The heater was not subjected to full power due to safety concerns about the use of un-wetted immersion heaters. Using 10 α_h and k_h increments and 200 control volumes, the best fitting parameters were $\alpha_h = 1.69E-6 m^2/s$ and $k_h = 6.04 W/m^2K$. To check the validity of the results, model results using the optimized parameters were compared against the data for a "high" (700W) and "low" (50W) heater power setting. A plot of this comparison is presented in Figure 57

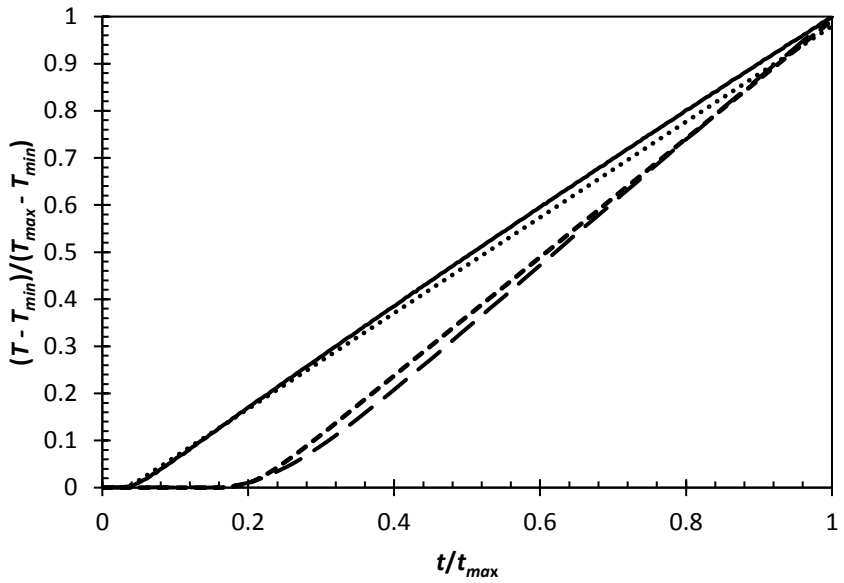

Figure 57. Comparison of normalized heater surface temperature measurements $(T - T_{min}) / (T_{max} - T_{min})$ to model predictions using parametrically optimized α_h and k_h values at two different heater settings: 50W (solid: experiment, dot: model) and 700W (dashed: experiment, short dash: model)

The agreement between experiment and predictions over a wide range of heater power settings is excellent and warranted no further refinement in the fitting procedure.

5.2.3 Reactor Wall Model

The highly endothermic reaction considered in this study necessitates considerable power input into the calorimeter in order to maintain the reaction temperature within reasonable limits. Sudden changes in fluid temperature can result in parasitic heat flow transients as high as 80-100w, and therefore introduce additional dynamics into the reactor energy balance. Hence, in this section, a dynamic reactor wall model similar to that of the heater coil is developed.

Because the wall is thin (3mm) compared to the inner diameter of the reaction vessel, it is approximated as a 1-D slab (Figure 58):

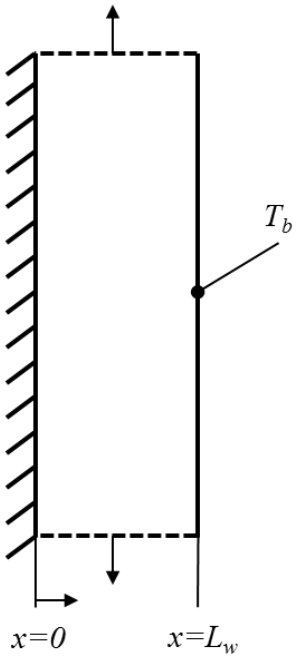

Figure 58. Domain for mathematical model of reactor wall

It is assumed, initially, that the wall is subjected to uniform convective heat transfer over both its wetted surface and outer surface. In the Cartesian coordinate system, the 1-D transient conduction equation to be solved is:

$$\frac{\partial T_w}{\partial t} = a_w \frac{\partial^2 T_w}{\partial z^2} \tag{5.14}$$

where x is the coordinate indicating the distance from the wetted surface at $x=0$ normal into the wall. The boundary conditions at the wetted surface ($x=0$) and the outer surface ($x=L_w$), respectively, are:

$$\left.\frac{\partial T_w}{\partial z}\right|_{x=0} = \frac{h_w}{k_w}\left(T(0,t) - T_l(t)\right) \tag{5.15}$$

$$\left.\frac{\partial T_w}{\partial z}\right|_{x=L_w} = -R_{th,loss}^{-1}\left(T_w(L_w,t) - T_{amb}\right) \tag{5.16}$$

where h_w and $R_{th,loss}$ are the convection coefficient at the wetted and thermal resistance of the outer surfaces, respectively; k_w is the thermal conductivity of the wall; and T_{amb} is the temperature of the surrounding environment, which is constant throughout the experiment. In the same fashion as with the heater, a finite volume, time continuous method was used to solve Eq. (5.14) numerically. Discretizing the wall into N equal sized volumes, defining $\Delta z = L_w / N$, and again letting i denote index for each finite volume cell, we obtain the following system of linear ODEs:

$$\frac{dT_{w,1}}{dt} = \frac{a_w}{\Delta z^2}\left[2T_{w,s} - 3T_{w,1} + T_{w,2}\right] \tag{5.17}$$

$$\frac{dT_{w,i}}{dt} = \frac{\alpha_w}{\Delta z^2}\left[T_{w,i-1} - 2T_{w,i} + T_{w,i+1}\right] \tag{5.18}$$

$$\frac{dT_{w,N}}{dt} = \frac{\alpha_w}{\Delta z^2}\left[T_{w,N-1} - 3T_{w,N} + 2T_{w,out}\right] \tag{5.19}$$

The boundary conditions for the wetted surface ($T_{w,surf}$) and outer surface ($T_{w,out}$) give two algebraic relations for their respective surface temperatures:

$$T_{w,surf} = \frac{0.5Bi_w}{0.5Bi_w + 1}T_{w,1} + 0.5Bi_w T_l \tag{5.20}$$

$$T_{w,out} = \frac{0.5Bi_{loss}}{0.5Bi_{loss} + 1}T_{amb} + \frac{1}{0.5Bi_{loss} + 1}T_{w,N} \tag{5.21}$$

where $Bi_w = h_w \Delta z / k_w$ and $Bi_{loss} = \Delta z / R_{th,loss} k_w$ are the Biot numbers for the wetted surface and outer surface of the reactor wall, respectively.

5.2.4 Liquid-Phase Thermal Model and Sub-Model Integration

Figure 59 shows a diagram of the control volume that serves as the basis for applying conservation of energy to the reactor. It is assumed that the solid AC dispersed in the liquid phase and the gas present in the reactor headspace to not contribute

significantly as sinks for thermal energy, as both have low heat capacity compared to the liquid phase.

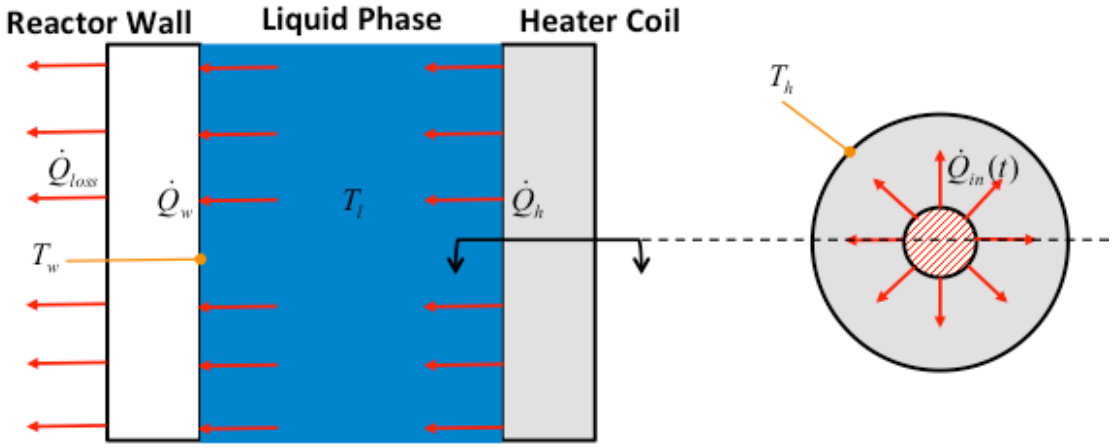

Figure 59. Diagram representing the model's three domains (reactor wall, liquid-phase, and heater coil) and the assumed direction of heat flow.

We assume the liquid phase is well stirred, and its temperature is a function of time only. The net energy balance on the liquid phase is:

$$\left(\rho c_p V\right)_l \frac{dT_l}{dt} = h_h A_h \left(T_{h,surf} - T_l\right) - h_w A_w \left(T_l - T_{w,surf}\right) - \dot{Q}_{rxn} \tag{5.22}$$

where $\dot{Q}_{rxn}$ is the heat consumed by the *net* decomposition of AC and V_l is the volume of the liquid phase. One can see that combining Eq. (5.22) with the system of ODEs represented by Eqs. (5.17) – (5.21), the reactor energy balance can be represented in state-space form:

$$\frac{d\mathbf{T}}{dt} = \mathbf{AT} + \mathbf{b} \tag{5.23}$$

where $\mathbf{T} = \left\{T_{h,1}, \cdots, T_{h,K}, T_{h,s}, T_l, T_{w,s}, T_{w,1}, \cdots, T_{w,N}, T_{w,out}\right\}^T$ is the state vector containing the time-dependent temperature of each finite volume cell in the heater coil and reactor wall, in addition to the liquid-phase bulk temperature; $\mathbf{A}$ is the coefficient matrix arising from the spatial discretization, and $\mathbf{b}$ is a vector to handle the inhomogeneous terms arising from the boundary conditions at the center of the heater coil ($r = R_o$) and at the outer surface of the reactor wall.

It is important to note that the surface temperatures $T_{h,surf}, T_{w,surf}$ and $T_{w,out}$ are, according to Eqs. (5.11), (5.20) and (5.21) respectively, algebraic constraints. The presents a problem for the numerical solvers in Simulink, which must now employ an iterative algorithm at each timestep to solve the algebraic constraints in the system, significantly slowing simulation time. A simple method was used in this study to remedy this issue; the aforesaid surface temperature variables were approximated as dynamic states (and hence their inclusion on the state vector of Eq. (5.23)):

$$\frac{dT}{dt} = K^* \left(T^* - T\right) \tag{5.24}$$

Where T represents $T_{h,s}, T_{w,s}$ or $T_{w,out}$,; T^* represents the RHS of Eqs. (5.11), (5.20), or (5.21) respectively; and K^* is a "large" constant chosen such that the artificial dynamics

associated with $T_{h,surf}, T_{w,surf}$ or $T_{w,out}$ are significantly faster than the rest of the system. This effectively approximates the algebraic constraint dictated by Eqs. (5.11), (5.20), and (5.21). In this case, a value of $K^* = 10^6$ was found to give sufficiently fast dynamics for $T_{h,surf}, T_{w,surf}$ and $T_{w,out}$ without noticeably slowing the execution speed of the Simulink model.

Not including the effect of chemical reaction, there are three unknown parameters that must be determined: h_h, h_w and $R_{th,loss}$. Over the range of temperatures considered in this study, the liquid phase (PG) experiences significant changes in viscosity, which in turn suggests that the heater coil and reactor wall convection coefficients will also differ with reaction temperature, even at the same stirring speed. It was presumed that the convection coefficients for the wetted surfaces would follow:

$$h = \frac{k_l}{L_c} \mathrm{Re}^m \mathrm{Pr}^n \left(\frac{\mu_l}{\mu_s} \right)^p \tag{5.25}$$

where μ_l and μ_s are the viscosities of the liquid phase evaluated at the bulk liquid temperature and surface temperature, respectively; Pr is the Prandtl number of the liquid phase; Re is the Reynolds number; k_l is the thermal conductivity of the liquid phase; and L_c is the characteristic length scale. With the exception of μ_s, all properties are evaluated at the bulk liquid phase temperature, T_l. With the stirring speed constant at 1000 RPM,

and no significant changes in the Prandtl number, liquid phase density, or thermal conductivity of PG over the temperature range of interest, Eq. (5.25) may be reduced to:

$$h = A^* \frac{\eta_l^{p-m}}{\eta_s^p} \tag{5.26}$$

where A^* is a constant whose value is to be determined by parameter fitting to experimentally obtained temperature histories. The functional dependence of η_l on temperature was obtained from the data of Sun and Teja [74] and implemented as a piecewise linear lookup table in the Simulink model.

Reactor temperature histories were obtained by monitoring a low thermal mass T-type temperature probe immersed in the bulk liquid (absent AC) while applying 500W – 900W from an initial temperature (typically ~22°C) up to set points ranging from 55°C to 70°C, where the temperature is maintained for 10 minutes by modulating the heater coil terminal voltage. The 10-minute hold sequence reveals the steady-state losses to the environment and thence allows the determination of $R_{th,loss}$. As will be soon discussed, the steady-state losses are important for fitting the heats of desorption during the mass transfer limited stage of the reaction.

Simulink's parameter estimation tool was used to fit $R_{th,loss}$, A, and m; the objective function chosen was the root-sum-square (RSS) error between the predicted and experimentally measured value for T_l. Values for $R_{th,loss}$ ranged between 0.67 and 0.40 m^2K/W – these high values likely stem from the presence of the vacuum jacket

between the wetted reactor wall and the ambient environment, which poses an additional and significant thermal resistance that is not explicitly accounted for in the model. These values were consistent across preconditioning (i.e., heating and holding) cycles conducted on different days and under varying laboratory temperatures, and so the approach adopted herein was deemed sufficient. The predicted values obtained for A and m were such that physically unrealistic values for h_w (as high as 10^6 W/m^{2}K) and h_h (on the order of 10,000 W/m^{2}K) were attained. The implication of these findings are that heat transfer is dictated predominantly by conduction through the heater and reactor wall, and thus disproportionally large changes in h_w and h_h were required to perturb the liquid-phase energy balance. This was confirmed by observing that changing h_h to 10^8 (4 orders of magnitude from the estimated value) had no significant effect on the prediction of T_l. It is possible to proceed with the assumption that the heater coil and wetted reactor wall surface temperatures are essentially identical to T_l. Exemplary comparisons between model predictions and experimental measurement for liquid-phase temperature ratio $(T - T_i)/(T_i - T_f)$ - where T_i is the initial temperature and T_f the maximum measured temperature - are shown in Figure 60:

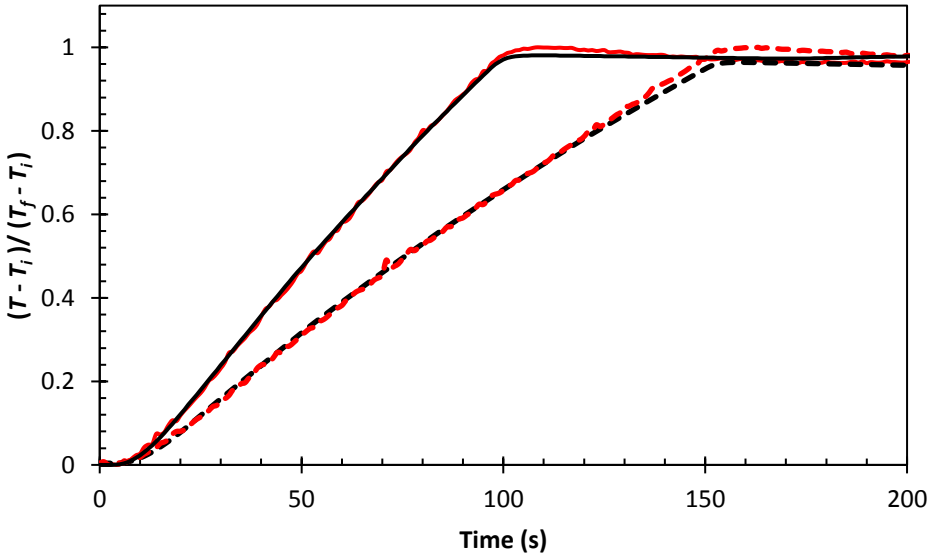

Figure 60. Plot comparing temperature ratio $(T - T_i)/(T_i - T_f)$ measured experimentally (red) and predicted by the model (black) as a function of time. Two cases are shown: heating to 55°C (solid) and heating to 70°C (dashed).

The maximum deviation from experiment observable in Figure 60 is approximately 4%. Thus, the selected empirical parameters provide excellent accuracy over large temperature ranges.

5.2.4.1 Thermochemical Energy Balance

Each chemical or mass transfer process in the multi-step reaction scheme is associated with the release/absorption of thermal energy according to the differences in inter- or intra- molecular bonds, respectively. The combined effect on the liquid phase's sensible energy content is:

$$\dot{Q}_{rxn} = \sum \left(\Delta H_j \dot{n}_j \right)_{rxn} + \sum \left(\Delta H_j \dot{n}_j \right)_{phys} + \dot{Q}_p \tag{5.27}$$

where ΔH_j is the latent heat of reaction (subscript *rxn*) or desorption/dissolution (subscript *phys*) for species *j*; $\dot{n}_j$ is the molar reaction/transfer rate of the respective process for species *j*. Absorption/desorption tests with CO_2 and PG in a 1000 ml nitrogen-sparged Erlenmeyer flask (Dow Corning) showed no measureable change in temperature, which permits the heat of desorption for CO_2 to be neglected. Additionally, Schmidt measured the heat of dissolution for solid AC in PG at room temperature, and found it to be small (~100 J/g) compared to the heat of decomposition; it is nevertheless included in this study, assuming that it does not vary significantly with temperature. The remaining unknown terms are the heterogeneous heat of reaction ΔH_{het}, the homogeneous heat of reaction ΔH_{hom}, and the heat of dissolution for solid AC ΔH_{dis}. Expressed as individual volumetric heat source/sink terms, we have:

$$\dot{q}'''_{het} = \Delta H_{het}\left(\frac{\rho_l}{M_l}\right)\dot{r}_{het} \tag{5.28}$$

$$\dot{q}'''_{dis} = \Delta H_{dis}\left(\frac{\rho_l}{M_l}\right)\dot{r}_{dis} \tag{5.29}$$

$$\dot{q}'''_{\text{hom}} = \Delta H_{\text{hom}}\left(\frac{\rho_l}{M_l}\right)\dot{r}_{\text{hom}} \tag{5.30}$$

$$\dot{q}'''_{des} = \frac{\rho_l}{M_l}\left(\Delta H_{a,des}\left(\dot{r}_a^{l-b} + \dot{r}_a^{l-g}\right) + \Delta H_{c,des}\left(\dot{r}_c^{l-b} + \dot{r}_c^{l-g}\right)\right) \quad (5.31)$$

where the sum-total of Eqs. (5.28) – (5.31) yields the net heat absorbed per-unit-volume.

5.2.4.2 Sensible Energy Storage in the Solid-Phase

Upon introduction into the reaction vessel, the AC particles are initially at the ambient temperature of the laboratory (~20°C). The sudden presence of the solid-phase in the liquid-phase, which during that is held at the desired reaction temperature, causes in sharp drop in temperature as the particles receive thermal energy from the liquid-phase via convective heat transfer. Assuming an initial particle temperature, $T_{s,i}$, of 20°C, the energy required to bring a 40g sample to a reaction temperature of 70°C (assuming solid AC has a specific heat of ~1.92 J/g [10]), is ~3800 J. While this number is small compared to the latent heat content of the AC, the sudden introduction of the AC particles into the reactor has the potential to create a large (over 1000 W), albeit brief, thermal energy sink that must be accounted for in the calorimetric measurements. Since this occurs at the onset of the reaction – where the largest endothermic heat absorption occurs -- this effect is especially critical because the parameter estimation routine will attempt to match this sudden decrease in liquid-phase temperature by increasing ΔH_{het} and ΔH_{dis}, thereby skewing the parameters at higher reaction temperatures and AC sample sizes.

With this potential complication in mind, the prudent approach is to provide compensatory logic in the model in order mitigate the effect of this experimental non-ideality. Thankfully, we are able to leverage the particle size tracking functions of Eqs. (3.32) – (3.33) to provide a first-order approximate method to compensate for sensible energy storage in the solid-phase at the onset of the experiment. First, let us assume that the period of time ('sensible heating period') over which this consideration is relevant is small compared to the lifetime of the smallest AC particle – if this is the case, we may assume that during the 'sensible heating period', the size of any given particle is approximately unchanged. The total heat transfer by convection to the solid-phase is:

$$\dot{Q}_s = 4\pi \int_{r_{i,\min}}^{r_{i,\max}} h_s r_i^2 \left(T_l - T_{s,surf}\right) n_s''' dr_i \tag{5.32}$$

where h_s is the heat transfer coefficient, which may or may not be a function of the particle size, and $T_{s,surf}$ is the surface temperature of a particle having a radius r_i. Assuming that h_s is independent of particle size, as was the case with the mass transfer coefficient, and using Eq. (3.32) to substitute for n_s''', we obtain:

$$\dot{Q}_s = \frac{3 h_s m_{AC}}{\rho_s \Delta r_i} \int_{r_{i,\min}}^{r_{i,\max}} \left(T_l - T_{s,surf}\right) \frac{dr_i}{r_i} \tag{5.34}$$

For a particle of (initial) radius r_i, the energy equation, assuming 1-dimensional conduction, is:

$$\frac{\partial T_s}{\partial t} = \frac{1}{a_s r}\frac{\partial}{\partial r}\left(r\frac{\partial T_s}{\partial r}\right) \tag{5.37}$$

where $T_s = T_s(r,t)$ is the local instantaneous temperature within the solid particle. Hence, $T_p(r_i,t) = T_s$. The boundary and initial conditions for Eq. (5.37) are:

$$\left.\frac{\partial T_s}{\partial r}\right|_{r=r_i} = \frac{h_s}{k_s}\left(T_l - T_{s,surf}\right) \tag{5.38}$$

$$\left.\frac{\partial T_s}{\partial r}\right|_{r\to 0} = 0 \tag{5.39}$$

$$T_s(r,0) = T_{amb} \tag{5.40}$$

Note that we have also assumed in the boundary condition Eq. (5.38) that the energy obtained by convection during the sensible heating period is *not* consumed, in whole or in part, by solid-liquid dissolution or heterogeneous decomposition at the particle surface. We adopt this assumption in recognition of the short timescales

involved and that the reaction processes, which are slow at temperatures below 60°C, would only be significant for a small portion of the sensible heating period.

Normally, one would be required to solve Eq. (5.37) subject to Eqs. (5.38)-(5.40) over the particle size distribution to compute $T_{s,surf}$, which would then require the integral in Eq. (5.34) to be approximated as the sum of discrete particle size groups. This would be computationally expensive, and slow the parameter estimation routine by an unacceptable degree. It was determined that a more simplified approach would be used first: the ratio $h_s/c_{p,s}$ was left as a fitting parameter, and the entire particle population was lumped into a single mass with a single effective temperature $T_{s,surf} = T_s$ and the same total volumetric interfacial area as the original particle population:

$$\frac{dT_s}{dt} = \frac{3h_s}{r_s c_{p,s} \Delta r_i}\left(T_l - T_s\right)\ln\left(\frac{r_{i,\max}}{r_{i,\min}}\right) \tag{5.41}$$

Eq. (5.41) is the familiar lumped-capacitance approximation [75], which is typically used for solid materials with high thermal conductivity; allowing $h_s/c_{p,s}$ to be adjusted accounts for this in part because the low thermal conductivity of the AC particles would confine the majority of the sensible energy storage to a region near the particle surface, thereby decreasing the effective heat capacity of the solid phase. To determine if implementing a more complicated approach was necessary, the parameter fitting routine was attempted using Eq. (5.41) and Eq. (5.34) as an additional sink term in the energy equation, Eq. (5.27).

An initial pass at fitting the experimental data to T_l using what was considered to be the most severe cases -- m_{AC} = 40g at 70 °C for various particle sizes – the value for $h_s/c_{p,s}$ was on the order of 0.01 - 0.1 $kg \times K / s \times m^2$, meaning that the sensible heating period lasted for, at most, only the first few seconds of the reaction. The effect of this small period of time on the gross dynamics of the reaction is small, and requires only an approximate correction for the portion of the initial liquid-phase temperature drop that is due to sensible heating of the solid-phase. At least for the purpose of estimating enthalpies of reaction in the batch reactor, the simplified approach adopted here is sufficient. The added complexity of solving the 1-dimensional transient energy equation for a discrete collection of particle sizes would not be warranted for this small timeframe. $h_s/c_{p,s}$ was subsequently fixed at 0.1 $kg \times K / s \times m^2$ for the thermal parameter estimation study.

5.2.4.3 Solution Method

The thermal model was implemented in the Simulink environment in a modular fashion by separating the reaction kinetics ("Reaction Model" block), endothermic heat absorption ("Heat of Reaction" block), and time integration of the energy equation ("Liquid-phase Energy Balance" block) into federated subsystems, as can be seen in Figure 61. This allowed data flow to be tracked more easily, in addition to facilitating diagnostic and debugging tasks.

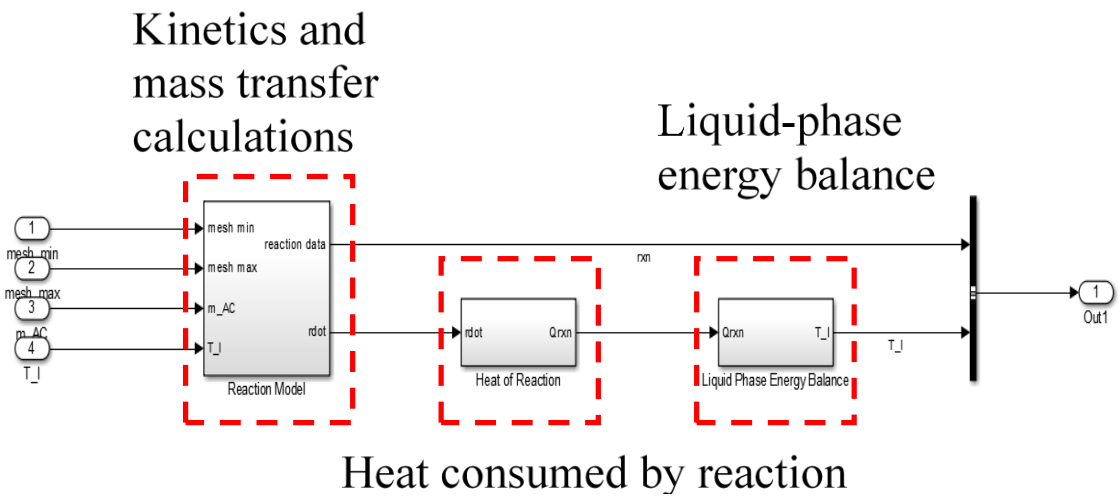

Figure 61. Simulink block diagram of batch reactor model with reaction rate, thermochemistry, and energy balance sub modules. The 'Liquid-phase energy balance' block contains the state-space models for the heater and reactor wall.

The reaction model block contains the state-space equations for solid-phase surface area, liquid-phase concentrations, and gas-phase concentrations, accepting as inputs the nominal minimum and maximum mesh size, initial AC mass, and reaction temperature setpoint. The heat of reaction block pulls instantaneous reaction rate data from the reaction model block to compute Eq. (5.27), which then passes the result, $\dot{Q}_{rxn}$ to the liquid-phase energy balance block; finally, the liquid-phase energy balance block integrates Eq. (5.23) to compute the liquid-phase temperature T_l. The liquid-phase temperature can be fed back to the reaction model block for the change in any temperature dependent parameters, but for the thermal parameter estimation task here, the T_l input to the reaction block model was held constant at the setpoint temperature for the experimental dataset under consideration. This simplification is justified in light of

the small and fleeting temperature excursions that occurred immediately upon introduction of the solid AC into the reactor. Heater coil power input is loaded to the liquid-phase energy balance block automatically from an external file containing logged data for a specified experiment; linear interpolation is used in a lookup table block to supply the heater coil power as a piecewise continuous function of time.

5.2.4.4 Endothermic Heat Absorption Estimation

The calorimetric 'measurement' of $\dot{Q}_{rxn}$ is accomplished indirectly by combining the wall and heater dynamic models with experimental measurements of the liquid-phase bulk temperature and heater power input. Accordingly, $\dot{Q}_{rxn}$ was *not* used for tuning the model parameters. The value of these estimates lies in providing a secondary check for the parameterized batch reactor and a sense of relevant timescales and patterns to inform the design of future experiments.

The inherent difficulty in obtaining numerical derivatives from experimental data introduced considerable uncertainty into the $\dot{Q}_{rxn}$ calculation, which could be as high as 500-800 W. Variations of such a magnitude made it nearly impossible to discern any meaningful information, and hence it was necessary to condition the data. Two conditioning approaches were attempted: smoothing the experimental data with a 1st order filter ("filter conditioning") or fitting a high-order polynomial to the data so dT_l/dt could be obtained analytically ("polynomial conditioning"). A time constant of 2 seconds was selected by trial-and-error for the first-order filter until the "ripple" in the

calculated $\dot{Q}_{rxn}$ was approximately +/- 50 W, which is on the order of the convective losses from the reactor at steady state. The filtering operation itself introduces uncertainty since it tends to attenuate sharp peaks and introduce phase-lag relative to the original data. The alternative method, polynomial conditioning, required, at a minimum, a 20th- order polynomial to resolve satisfactorily the sudden dip in liquid-phase temperature occurring at the onset of the reaction. The polynomial coefficients were obtained by a least-squares regression using the MatLab function *polyfit*.

The liquid-phase energy balance module of the overall calorimeter model was modified to solve Eq. (5.27) using the following procedure:

1) The model reads the T_l data from the designated data file, which was sampled at 3 Hz.
2) The experimental T_l data is smoothed via a signal conditioning function (1st order filter or polynomial fit). The conditioned temperature data is designated by the variable $\tilde{T}_l$.
3) For filter conditioning, $\tilde{T}_l$ is input to a numerical derivative block. For polynomial conditioning, the derivative could be obtained analytically.
4) The $\tilde{T}_l$ data is supplied as a time-dependent boundary condition to both the heater and wall models; these models output their total heat flow rates $\dot{Q}_h$ and $\dot{Q}_w$ respectively.
5) dT_l/dt is multiplied by the total heat capacity of the liquid-phase to obtain $\dot{Q}_l$

6) $\dot{Q}_h$, $\dot{Q}_w$ and $\dot{Q}_l$ are summed to obtain $\dot{Q}_{rxn}$, which is output as a 1-dimensional array to the MatLab workspace

A simplified representation of the Simulink block diagram is shown in Figure 62. Figure 63 compares the conditioned temperature data obtained using both the filter approach and polynomial fit.

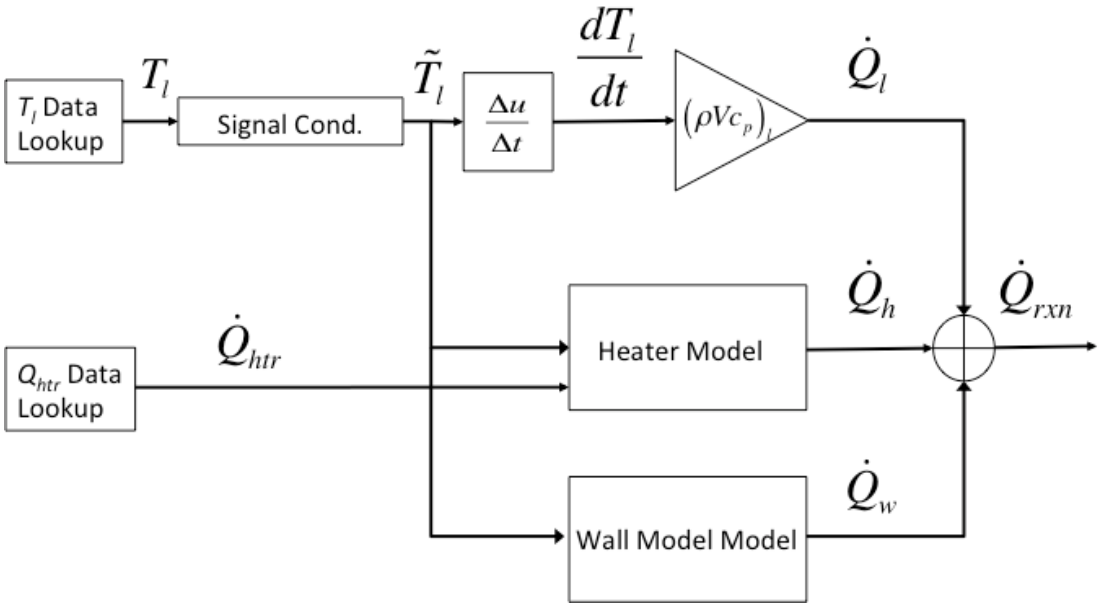

Figure 62. Simplified illustration of Simulink block diagram used to calculate experimental endothermic heat absorption.

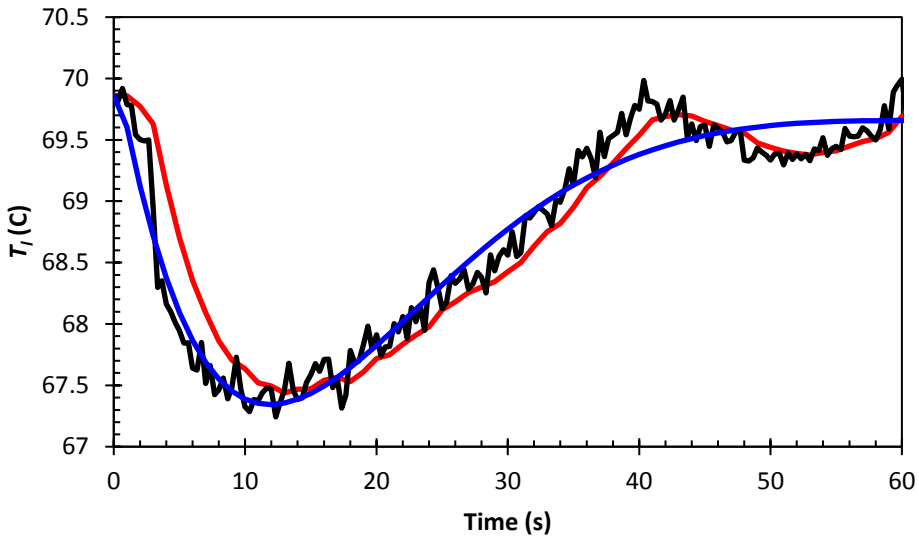

Figure 63. Conditioned temperature data obtained using 1st – order filter with a time constant of 2 seconds (red) and 20th – order polynomial fit (blue); the actual T_l data is also depicted (black).

The filtered data more-or-less preserves the sharper slopes and is also able to reproduce the low frequency ripple that is due to hunting behavior in the underdamped temperature controller. There is a slight phase-shift of about 2-3 seconds. The polynomial fit also performs well in tracking the experimental curve, but is unable to capture the hunting behavior. The resultant calculations for $\dot{Q}_{rxn}$ are shown in Figure 64:

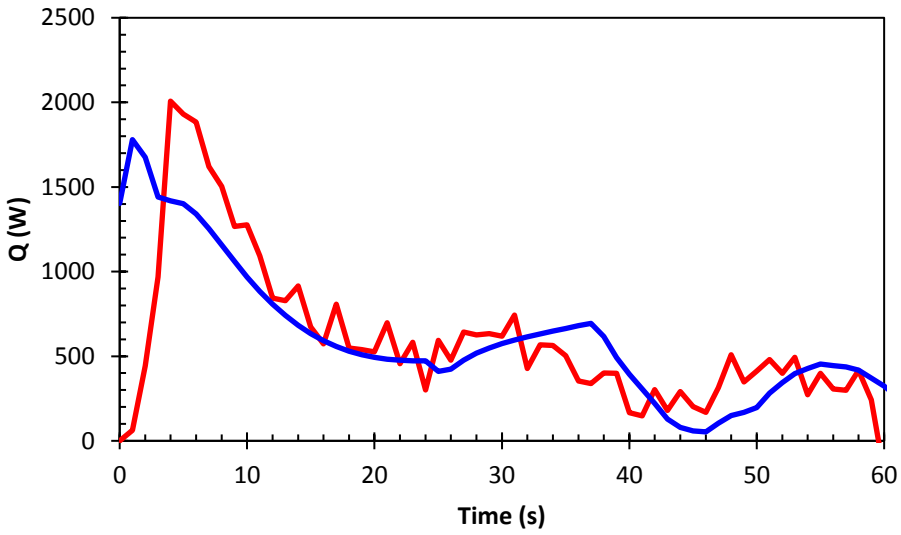

Figure 64. Calculated endothermic heat absorption obtained using 1st – order filter with a time constant of 2 seconds (red) and 20th – order polynomial fit (blue)

Both data conditioning techniques give reasonable results, but the filtered data gives more realistic curves at the onset of the reaction (from t = 0 to ~8 seconds). Specifically, there will be a slight delay in the reaction as the particles are initially at a low temperature, as discussed in section 5.2.4.2, before the reaction rapidly accelerates --- this nuance is absent in the polynomial fit case. This distinction encouraged adoption of

the filter method over the polynomial method. Thus, all calorimetric estimates of $\dot{Q}_{rxn}$ derived from the experimental data from this point onward employ the process depicted in Figure 62.

5.3 Calorimetric Results and Discussion

The following section presents the thermal parameter estimation results, comparison between model and experiment, comparison between the trends observed experimentally and predicted by the model, and a parametric sensitivity analysis. As in the previous section, the fitted parameter results obtained from experiments having m_{AC} = 40g and were used; additionally, the parameter fitting routine was utilized with data from the smallest available initial particle size distribution, i.e. -40 + 50 mesh, to reduce the mass transfer complications introduced by large particle sizes. The results were validated by comparing the model predictions to data sets with m_{AC} = 30g or 20g, at various initial particle size range. The overall agreement was judged to be acceptable.

5.3.1 Wall Heat Transfer and Heater Coil Dynamics

Figure 65 shows a representative history of the heat delivered from the coil and wall to the liquid-phase compared to the power input to the heater as measured by the DC programmable power supply.

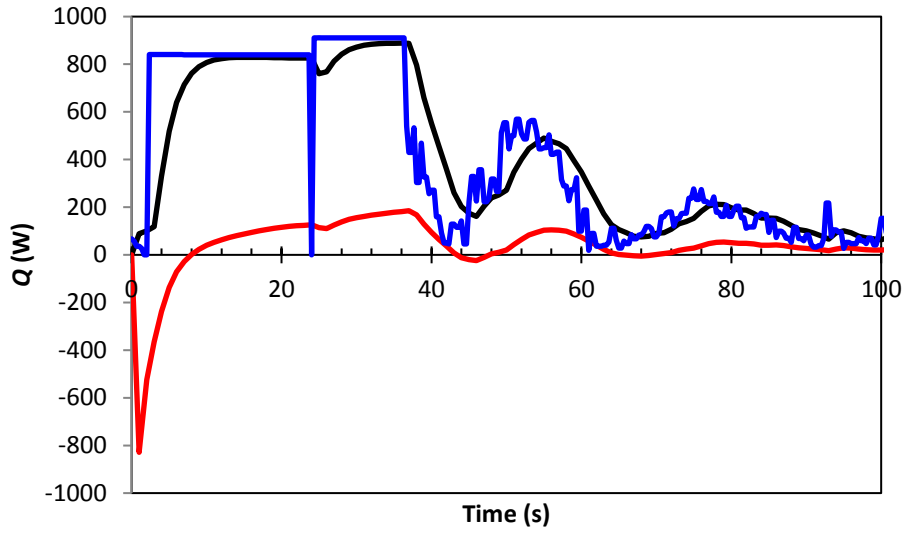

Figure 65. Plot of model-calculated heat flow from heater surface (black) and wetted reactor wall (red) compared to experimental heater input (blue). The positive direction of heat flow is defined in Figure 59. Source of the experimental data was the test m_{AC} = 40g, T = 70°C, 40 – 50 mesh particle size

For the first minute of the reaction, there is a non-trivial exchange of thermal energy with the reactor wall, which initially *delivers* heat when the AC is introduced (in response to the sudden drop in liquid temperature), but soon begins to act as a parasitic heat sink after about 10 seconds to the tune of about 20% of the heater input. There is also a marked delay between the heater coil input and conveyance to the liquid-phase; the rise time is approximately 6 seconds, and there is a phase-shift of about 4 seconds. The lesson to be learned from this comparison is that one would be ill advised to neglect the inherent dynamic behavior of the reaction vessel and the means of introducing heat into the system when performing calorimetric measurements on rapid, energy intensive reactions. Unacceptably large errors would be incurred, particularly early in the reaction,

if one were to simply compare the measured heater power to the sensible energy change in the liquid-phase.

5.3.2 Thermal Parameter Estimation Results

In contrast to the kinetic parameter fitting, the estimated thermal parameters showed considerable scatter and a non-monotonic trend between 55°C and 70°C. While this may at first seem like an indictment of the kinetic parameters obtained in the previous chapter, the following aspects must be weighed when interpreting these results:

1) At low temperatures (55°C and 60°C), the reaction rates are comparatively slow, and thus large variations in the enthalpies of reaction are necessary to adjust the model output to match the experiment. For this same reason, as was discovered in the kinetic parameter estimation work, there is also greater uncertainty associated with the parameters estimated for at these temperatures.
2) Only the bulk liquid-phase temperature data was available for a direct experimental comparison to the model predictions, which represents the cumulative contribution of the individual reaction mechanisms. This increases the likelihood for local minima in the objective function to occur. One particularly vexing consequence of this is that parameters effecting processes dominant early in the reaction (i.e., heterogeneous decomposition and dissolution) tended to create offsets in the temperature predictions *later* in the reaction when other mechanisms were dominant (i.e., homogeneous decomposition and NH_3 desorption). Simulink's optimization algorithms would then attempt to adjust the latter group

of parameters to compensate for errors in the former, leading to anomalous variations in the estimates from experiment to experiment.

The kinetic parameter fitting work indicated that large sample sizes (40g) with smaller particles (40 mesh and below) at high temperatures (70°C) typically exhibited the least variation. Unlike the kinetic parameters, however, in many cases, enthalpies of reaction vary only over comparatively large temperature ranges [76]. In consideration of the points discussed above, it would seem that finding a coherent pattern in the enthalpy of reaction estimates for all the datasets is unlikely. Instead, the strategy we employ here is to conduct the parameter estimation against a dataset at 70°C and an AC sample size of 40g with the smallest available particle sizes (40 – 50 mesh), and then compare the model predictions using the parameters thus obtained to the remaining datasets. It shall be demonstrated that this approach provides good agreement across all available experimental datasets.

5.3.2.1 Heterogeneous Reaction

In this context, the term "heterogeneous reaction" encompasses all solid-liquid pathways (i.e., heterogeneous decomposition and dissolution). The estimated value for ΔH_{het} is 80.8 kJ/mol, or approximately 1000 J/g, which is much lower than the values for dry AC reported in the literature [10]. In Figure 66, the Born-Haber cycle for the proposed AC decomposition reaction in PG shows the reason for this discrepancy:

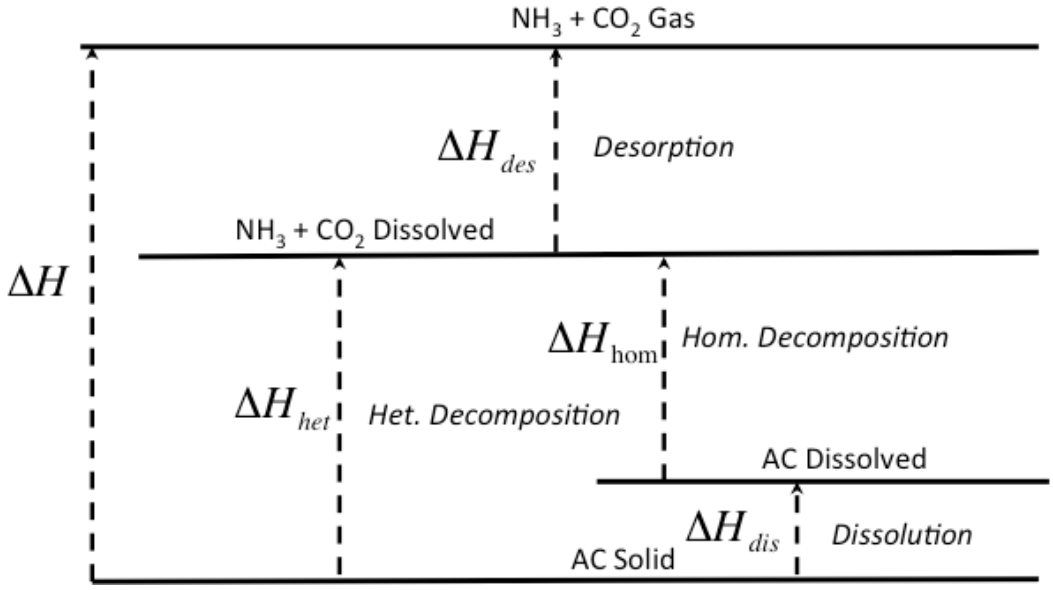

Figure 66. Born-Haber Cycle for decomposition of solid AC suspended in PG

The 'intermediate' state of dissolved NH_3 and CO_2 that must be attained prior to the final 'end' state of gaseous NH_3 and CO_2 dictates that $|\Delta H| > |\Delta H_{het}|$, where ΔH is the enthalpy of reaction for the decomposition of (dry) solid AC to its gas-phase decomposition products.

Schmidt [10] measured the heat of dissolution of AC in ethylene glycol at room temperature, which was reported as approximately 10 kJ/kmol at infinite dilution. Heat of solution is, in general, a function of concentration. Without any data specific for PG available, and assuming that ΔH_{dis} in PG would be on the same order of magnitude at that in ethylene glycol, the parameter estimation was bounded at a maximum of 10 kJ/kmol. Knowing that ΔH_{dis} may be a function of concentration (x_{AC}), we deviated from the fitting strategy discussed previously and attempted to fit two additional datasets at the same temperature and particle size: m_{AC} = 30g and 20g. It is possible that ΔH_{dis}

may increase with temperature, as is the case with some soluble solids [73], but there is not sufficient data at this point to confirm. In any case, from the standpoint of selecting 'best-fitting' (although perhaps not necessarily correct) parameters for the model, we submit that it is acceptable to utilize a single value – 5.34 kJ/kmol -- for ΔH_{dis}.

5.3.2.2 Homogeneous Reaction

The estimated value of ΔH_{hom} was -83.2 kJ/mol, or ~1100 J/g. Recalling that $\Delta H_{des} = 2\Delta H_{a,des} + \Delta H_{c,des}$, we find that ΔH = 1820 J/g when following the heterogeneous decomposition - desorption path, and ΔH = 1890 J/g when following the dissolution-homogenous decomposition - desorption path. With a disagreement of about 4%, these results were considered acceptable. We note that the value ΔH = 1800 J/g is what was assumed by Johnson *et al.* [70] in their AC HEX reactor experiments.

5.3.2.3 Comparison to Experiment

The results discussed above are summarized in Table 4:

Table 4. Thermochemical parameters used in model for validation. Asterisks indicate the value was obtained from experiment

Parameter	Symbol	Value (kJ/mol)
Enthalpy of Reaction, Heterogeneous	ΔH_{het}	-84.8
Enthalpy of Dissolution	ΔH_{dis}	-5.34
Enthalpy of Reaction, Homogeneous	ΔH_{hom}	-84.9
Enthalpy of Desorption, NH3*	$\Delta H_{a,des}$	-22.2
Enthalpy of Desorption, CO2 [30]	$\Delta H_{c,des}$	-9.3

Figure 67 and Figure 68 show comparisons of predicted and experimental liquid-phase temperature history and net heat absorbed by the reaction, respectively, for the experiment with m_{AC} = 40g, T = 70°C, and 40 – 50 mesh particles. The agreement shown between model and experiment in this case is acceptable – the RSS error between the curves in Figure 67 was less than 1% -- and similarly exhibited for T = 70°C, m_{AC} = 30g and particle sizes 50 – 60 mesh (Figure 69 and Figure 70).

Despite the underestimate from t = 0 – 30 s, the error in the temperature history does not at any point exceed 1°C. Figure 68 and Figure 70 show that the experimental $\dot{Q}_{rxn}$ curves show an abrupt rise, followed by and peak and descent; on the other hand, the model-predicted $\dot{Q}_{rxn}$ start at their peak value and decrease monotonically thereafter. The sharp rise/peak pattern is a common occurrence among the experimental data, and most likely results from the heterogeneous reaction accelerating as the solid-phase comes up to temperature. The model does not account for initial transient in the solid-phase temperature when calculating the temperature-dependent rate coefficients, assuming instead that the initial solid-phase temperature is equal to that of the liquid-phase. The timeframe over which this occurs is on the order of 1-2 seconds, and thus does not impose an appreciable error.

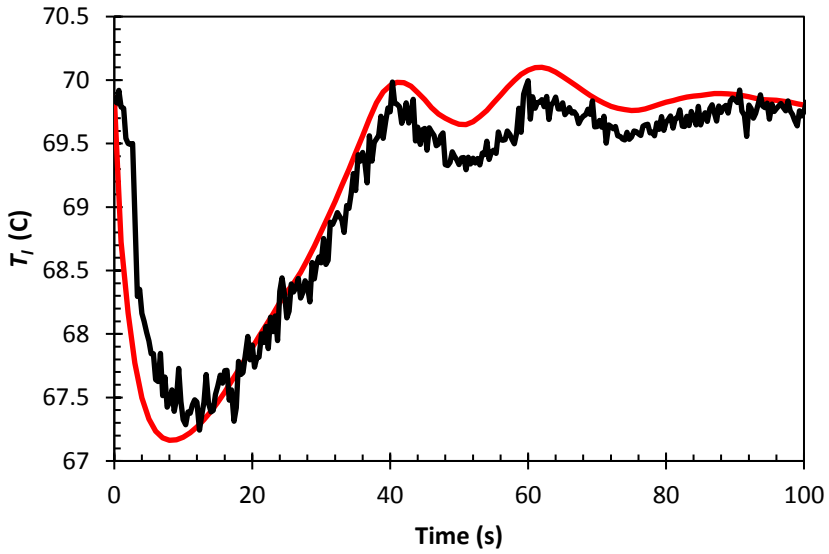

Figure 67. Comparison of temperature histories measured experimentally (black) and predicted by the model (red) for m_{AC} = 40g, T = 70°C, 40 – 50 mesh particles

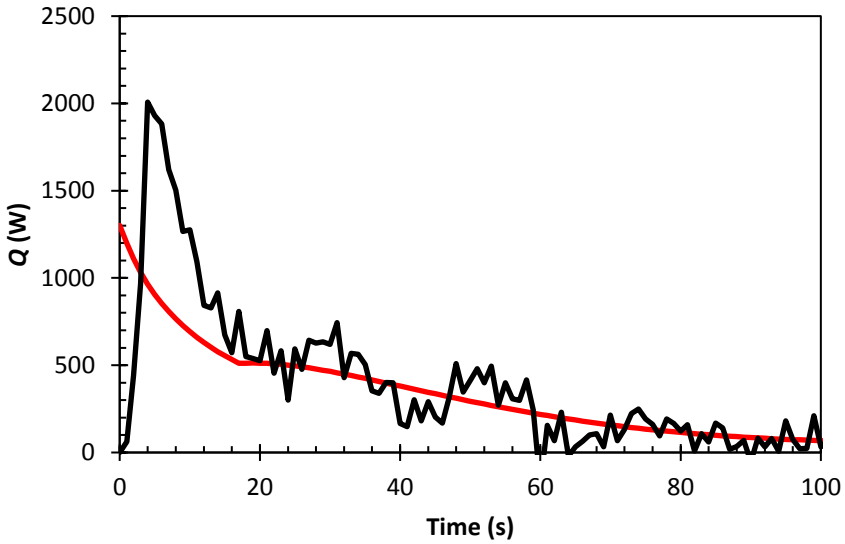

Figure 68. Comparison of heat absorbed by the reaction calculated using calorimetric calculations (black) and predicted by the model (red) for m_{AC} = 40g, T = 70°C, 40 – 50 mesh particles

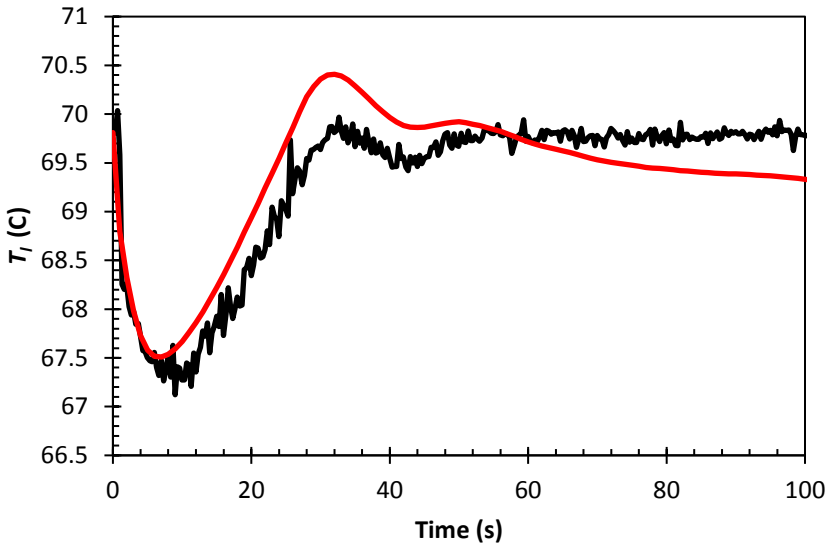

Figure 69. Comparison of temperature histories measured experimentally (black) and predicted by the model (red) for m_{AC} = 30g, T = 70°C, 50 – 60 mesh particles

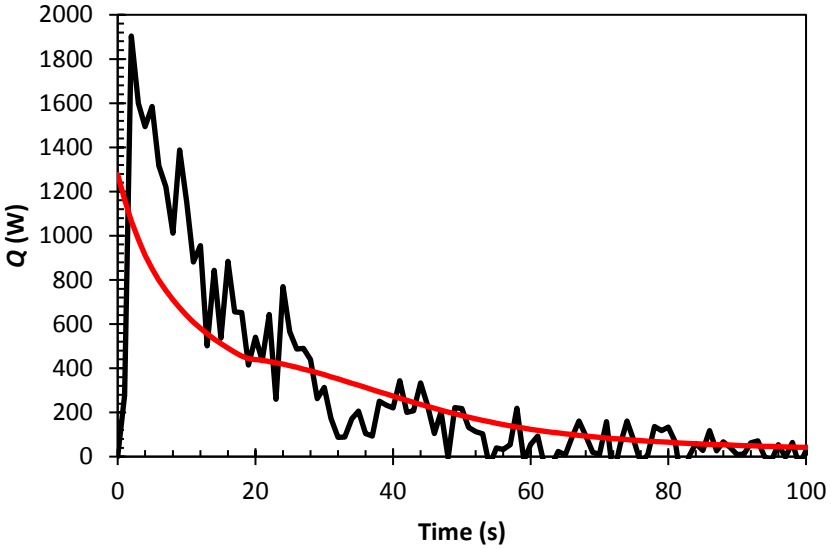

Figure 70. Comparison of heat absorbed by the reaction calculated using calorimetric calculations (black) and predicted by the model (red) for m_{AC} = 30g, T = 70°C, 50 – 60 mesh particles

Figure 71 - Figure 74 depict representative comparisons between model and experiment at lower temperatures (55°C and 60°C) with the same particle size range as that presented in Figure 67 and Figure 68. The fit quality for $\dot{Q}_{rxn}$ suffers somewhat at 55°C and 60°C, but does not appear to noticeably affect the agreement between the measured and predicted liquid-phase temperature histories. Having demonstrated satisfactory agreement over a broad range of temperatures, sample sizes, and particles sizes, we conclude that the parameter estimates shown in Table 4 are appropriate for inclusion in the model for off-design predictions.

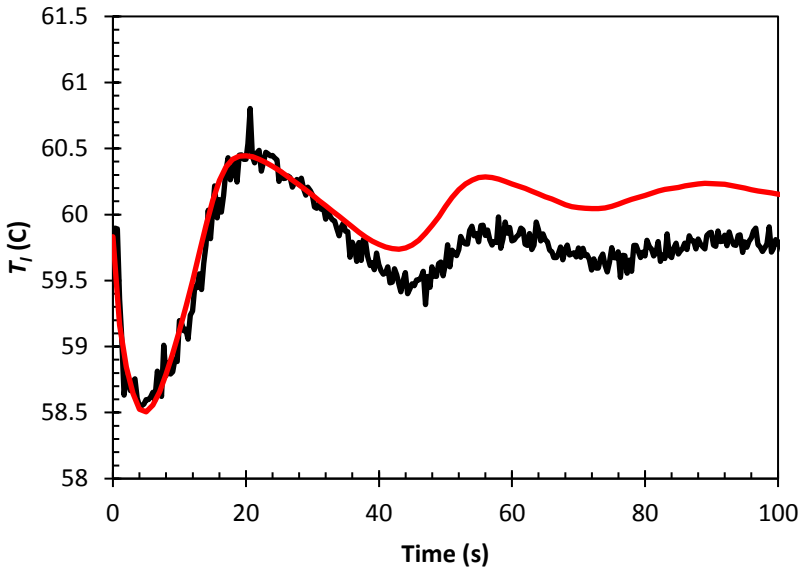

Figure 71. Comparison of temperature histories measured experimentally (black) and predicted by the model (red) for m_{AC} = 30g, T = 60°C, 40 – 50 mesh particles

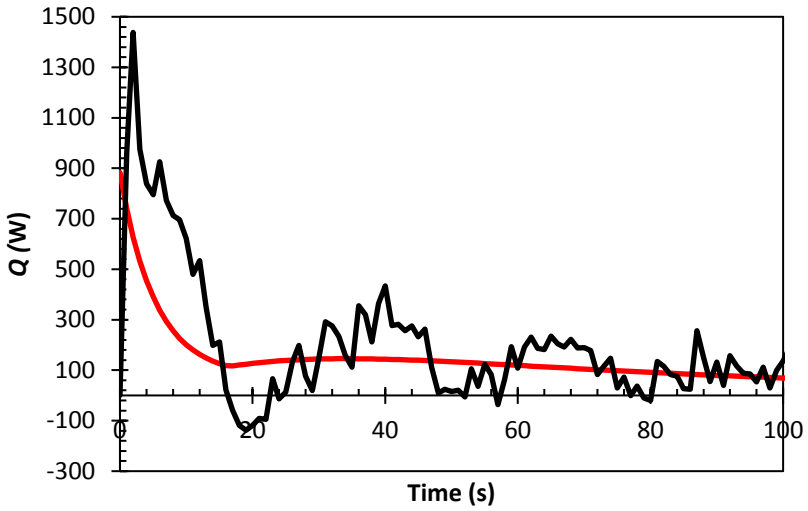

Figure 72. Comparison of heat absorbed by the reaction calculated using calorimetric calculations (black) and predicted by the model (red) for m_{AC} = 40g, T = 60°C, 40 – 50 mesh particles

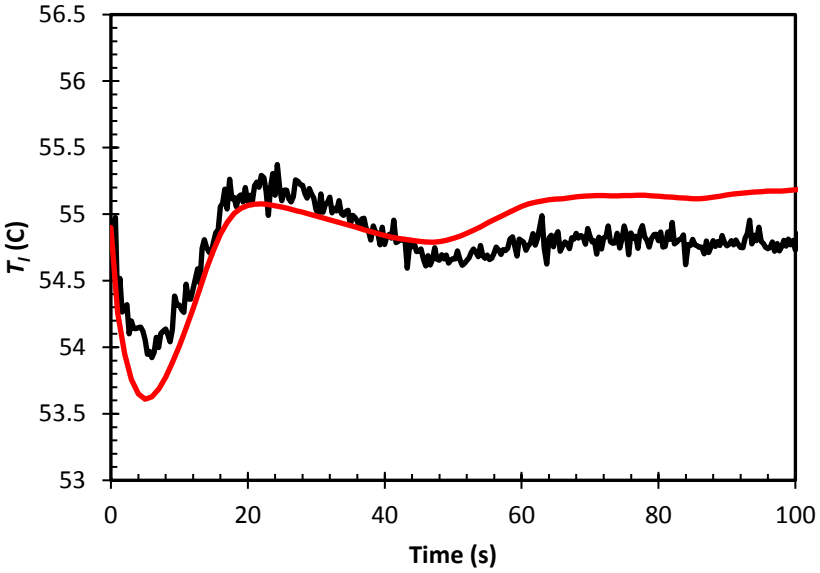

Figure 73. Comparison of temperature histories measured experimentally (black) and predicted by the model (red) for m_{AC} = 30g, T = 55°C, 40 – 50 mesh particles

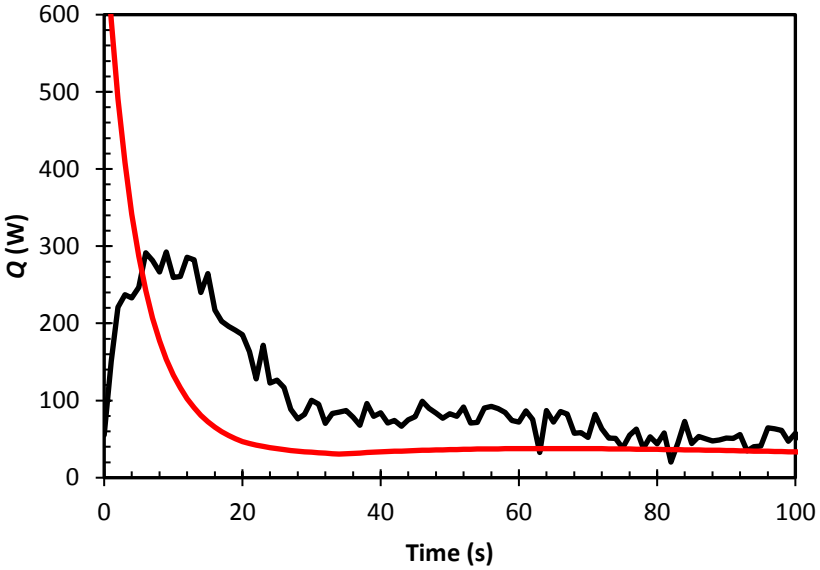

Figure 74. Comparison of heat absorbed by the reaction calculated using calorimetric calculations (black) and predicted by the model (red) for m_{AC} = 30g, T = 55°C, 40 – 50 mesh particles

5.3.2.4 Analysis

It is also of interest to investigate the contributions of the individual reaction mechanisms to $\dot{Q}_{rxn}$. Figure 75 shows for a reaction temperature of 70°C exemplary time traces of the heat absorbed by dissolution, heterogeneous decomposition, and homogeneous decomposition.

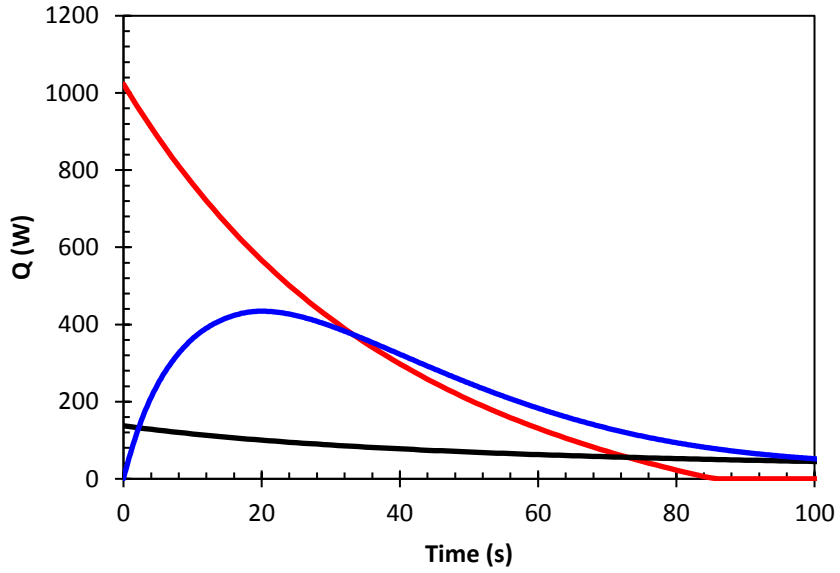

Figure 75. Heat absorption predicted by model for heterogeneous decomposition (red), dissolution (black), and homogeneous decomposition (blue) for m_{AC} = 40g, T = 70°C, 40 – 50 mesh particle size

It is immediately apparent that, early in the reaction, the dominant contributor to $\dot{Q}_{rxn}$ is heterogeneous decomposition. This lends credence to the hypothesis that the initial temperature transient in the solid- and liquid-phases is responsible for the sharp rise/peak observed in the experimental $\dot{Q}_{rxn}$ curves. $\dot{r}_{het}$ has much stronger temperature

dependence than $\dot{r}_{dis}$ and, because it is the dominant consumer of heat, an initially low reaction temperature would suppress $\dot{Q}_{rxn}$ but then rapidly rise with the solid-phase temperature. The homogeneous reaction, as was seen in the kinetic parameter estimation study, is initially small, but rises in an effectively first-order fashion as the dissolved AC concentration increases due to dissolution of the solid-phase. Figure 76 shows the effect of temperature on the instantaneous heat absorption due to homogeneous decomposition and corresponding relative contribution to $\dot{Q}_{rxn}$ is shown in Figure 77.

As temperature increases, the homogeneous reaction plays an increasing important role in the total heat absorption. However, we may infer from the change in slope from concave at 55°C to convex at 60°C in Figure 77 that the growth in relative contribution to $\dot{Q}_{rxn}$ may be approaching a limiting value since the preceding dissolution step does not exhibit the same acceleration with respect to temperature.

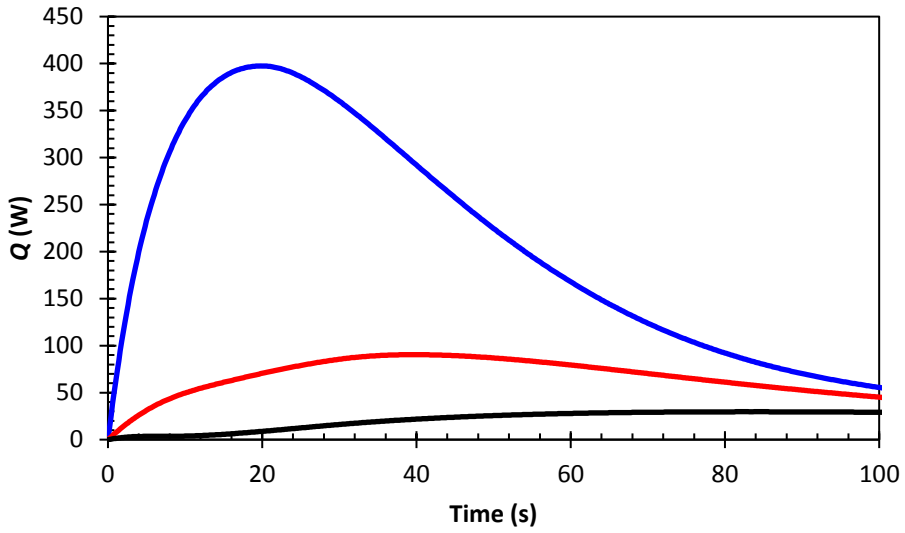

Figure 76. – Heat absorption by homogeneous decomposition as a function of time at different temperatures: T = 70°C (blue), 60°C (red), and 55°C (black). In all three cases, m_{AC} = 40g with 40 – 50 mesh particle size

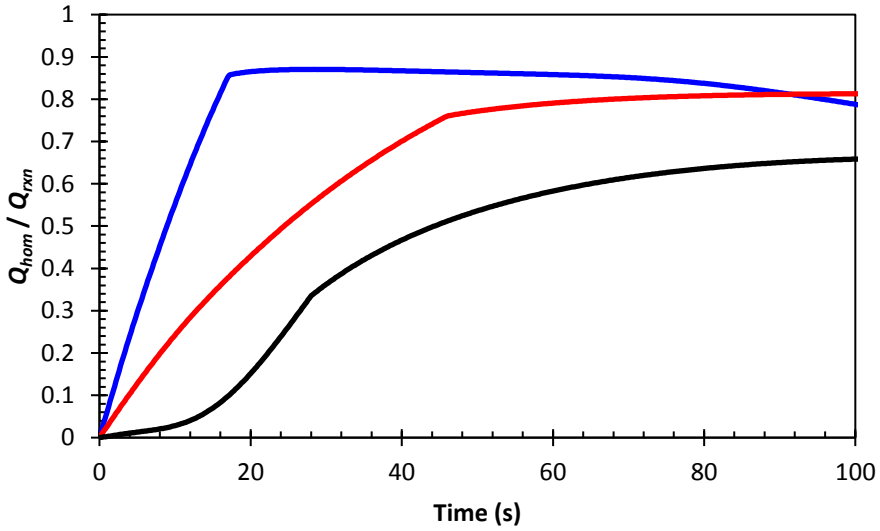

Figure 77. Fraction of heat absorbed by homogeneous decomposition relative to total heat absorbed as a function of time at different temperatures: T = 70°C (blue), 60°C (red), and 55°C (black). In all three cases, m_{AC} = 40g with 40 – 50 mesh particle size

Lastly, Figure 78 shows the instantaneous rate of heat absorption due to release of NH_3 into liberated CO_2 bubbles.

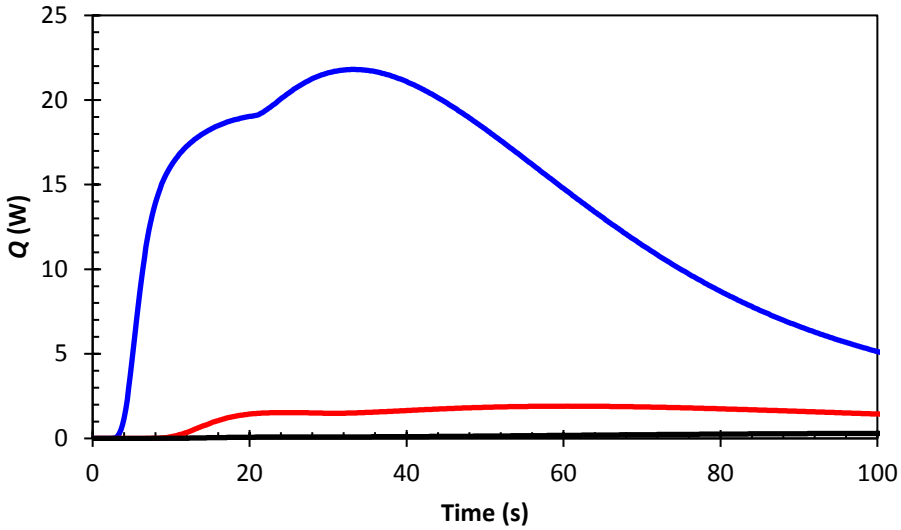

Figure 78. Heat absorption due to NH_3 desorption into CO_2 bubbles as a function of time at different temperature: T = 70°C (blue), 60°C (red), and 55°C (black). In all three cases, m_{AC} = 40g with 40 – 50 mesh particle size

While a remarkable increase with temperature is evident in Figure 78, it is also clear that only a small – almost negligible – quantity of heat is being absorbed. Due to the high heat of solution for NH_3 in PG and referring to the Born-Haber cycle illustrated in Figure 66, the model predictions point to a major penalty to efficiency (defined as the ratio of heat absorbed to total possible heat absorption) of nearly 30%. It is obvious at this point that relying on CO_2 bubbles released from solution to strip the NH_3 is not sufficient.

CHAPTER VI

HEX REACTOR MODEL

This chapter demonstrates the implementation of the reaction source term and species conservation equations, heretofore analyzed via the Lagrangian reference frame, into a continuous flow HEX reactor. The resultant model is compared to the experimental results of Johnson *et al*. [70] for a chevron plate heat exchanger HEX reactor subjected to high (70 second) and low (10 second) residence times and temperatures ranging from 70°C to 90°C. The results reported in [70] stem from an experimental program designed and conducted by AFRL to demonstrate a proof-of-concept for a continuous flow, high energy density reaction vessel to leverage AC as an expendable heat sink for thermal management. In a previous study, Niedbalski *et al*. [25, 26] had characterized the flow behavior of a gas-evolving chemical reaction in AFRL's HEX reactor vessel and proposed a general hierarchical HEX reactor modeling framework based on the separated flow model [80]. By modeling the reactor as a stack of 1-dimensional individual channels, it is possible to simulate a reactor with multiple passes and/or different flow configurations (parallel flow or counter flow); different heat exchanger surface types (offset fin, louvered fin, etc.) are represented by selecting appropriate correlations for heat transfer, mass transfer, and momentum transfer. The previously established HEX reactor modeling framework was sound, but source term representing the decomposition of AC in PG was based on a simple, single-equation reaction model [27] without accounting for the solubility of NH_3. Lastly, there was no data available at the time of publication to which the model could be compared and

adjusted to. This limitation aside, the separated flow-based hierarchical model enabled the solid, liquid, and gas phases to be analyzed as interacting continua with distinct temperatures and velocities. We have adapted the aforesaid 1-dimensional HEX reactor model framework from Niedbalski *et al.* [26], with the following improvements:

1) The newly proposed multi-step, parallel pathway reaction model for the decomposition of AC in PG replaces the simple algebraic relation originally due to Claudel and Boulamri
2) The original assumption of insoluble AC and gas-phase reaction products is abandoned in favor of tracking dissolved AC, CO_2, and NH_3
3) The solid-phase model accounts for a continuous size distribution rather than a single particle size

As in [26], the overall framework for the HEX reactor remains generic in nature and easily adaptable as the application requires. The model's degree of consistency with the data of Johnson *et al.* [70] is judged in the context of a general engineering tool that provides insight into reactor scaling trends and the effect of operating conditions on conversion (yield) and heat rejection, but may not be suitable for precise, high-fidelity predictions (e.g., optimizing reactor geometry or other detailed component-level design activities). Although compromises in fidelity were necessary in view of the available data of Johnson *et al.* [70], it is clear from the outset that the model developed in this study represents a vast improvement over the previous reported attempts [26].

6.1 Mathematical Model

The HEX reactor model was developed in a similar vein to Niedbalski *et al.* [26] and several other papers examining chemical reactions in compact heat exchangers [77-79]. The HEX reactor in Johnson *et al.*'s work was assembled in a vertical counter-flow configuration with one set of channels containing a three-phase slurry of solid AC, liquid PG, gaseous NH_3 and CO_2 flowing upward, while the other set contains water [70]. To maintain a consistent vernacular: "reactant-side" refers to the channels containing the three-phase slurry and "load-side" refers to the channels containing water. A pair of reactant- and load-side channels, along with the relevant dimensions, is depicted in the diagram of Figure 79.

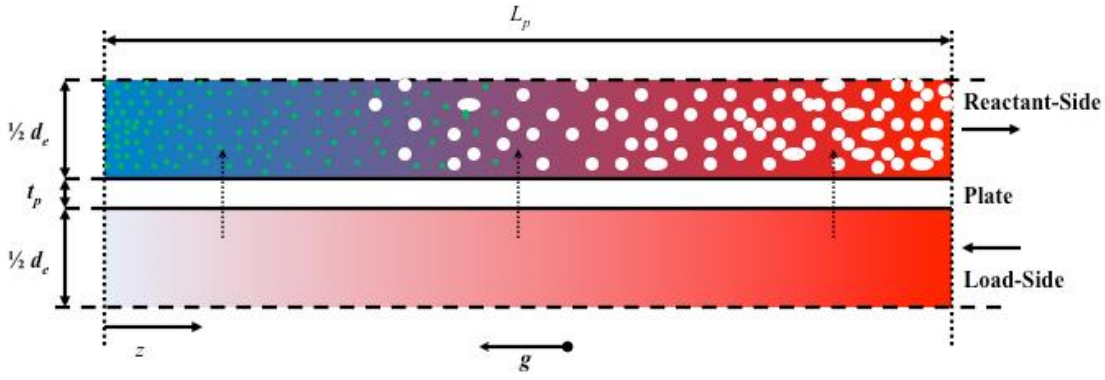

Figure 79. Diagram depicting pair of reactant and load channels; the long dashed lines represent symmetry adiabats; the vector g is in the direction of gravity. The white particles represent the gas-phase; green particles represent the solid-phase

The following assumptions are implicit in the model's framework [26]:

- Temperature-dependent physical properties are (namely, viscosity, Prandtl number, and density) are taken to be at the local bulk temperature
- Flow is uniform across the width of the channel; earlier flow visualization studies with the HEX reactor of interest [25] have confirmed this to be true except at very high flow rates

The 1-dimensional approach does not account for gradients in temperature, concentration, or velocity transverse to the direction of flow. Knowledge of local heat transfer coefficients, void fractions, and bubble desorption are presumed to be adequately represented by correlations to the appropriate cross-sectional averaged variables such as bulk temperature, pressure, and mass flux.

The operating conditions in Johnson *et al.* [70] allowed for a number of simplifying assumptions to be made as well:

- The reactor is operating at steady-state
- Axial diffusion (mass or thermal energy) is neglected; this assumption is typically acceptable for Péclet number (*Pe*) well in excess of unity, as is the case here.
- There is no flow distribution, i.e. the total flow into the manifold is evenly distributed among the channels. While the modeling framework does allow for maldistribution to be accounted for by adjusting the inlet flow rates to individual channels, it was not necessary for the small Alfa Laval MF3 chevron PHE.

- The flow is both thermally and hydraulically fully-developed
- Both liquid and gas phases behave as Newtonian fluids
- The gas and solid-phases are, at any given axial location *z*, in thermal equilibrium with the liquid-phase; this is discussed further in section 6.1.1.4

The multi-phase nature of the problem is described by the well-established separated flow model [80, 81], which does not account explicitly for the interfaces between phases in the flow field, but instead assumes the phases to be separated by an artificial boundary. Conceptually, this is an extension of the 1-dimensional plug flow model, which has seen extensive use for multi-phase contactors such as packed beds or bubble columns [82, 83]. The segregated flow model allows each phase to retain its 'identity', in a sense, by prescribing area-averaged variables for each phase. The obvious advantage of this approach is that inter-phase gradients in temperature and concentration – which are common in chemical reactors [84] – can be captured and combined with constitutive expressions to model local exchanges in mass, energy, and momentum between phases. In contrast, the simplest possible approach is to model the multi-phase flow as a homogeneous mixture with effective thermophysical properties [80], but information about phase-to-phase interactions is essentially lost. More sophisticated approaches, such as the generalized two-fluid model [85], are more suited to 2-D or 3-D CFD calculations and introduce a number of parameters which must be obtained empirically; hence, with only one applicable source of data [70] available, it would not be feasible to populate the model's parameters. The segregated flow approach was

determined to be the best compromise between fidelity, computational expediency, and ease of tuning to limited experimental data.

Gas-liquid hydrodynamic interactions are of course modeled through the use of appropriate correlations. The parameters describing these interactions are the void fraction, effective heat/mass transfer coefficients, and friction factor (often described in terms of a two-phase multiplier). The solid-phase is modeled as a homogenously dispersed suspension of spherical particles whose motion matches exactly that of the surrounding liquid. Hence, there is no axial 'diffusion' of the solid phase due to buoyancy or inertia. This assumption is justified on account of the similar densities between the liquid and solid phase, as well as the small size of the particles (below 40 mesh, or ~0.62 mm diameter), both of which tend to diminish velocity differences between the suspended solids and surround liquid [86]. For small particles, the precise geometry is of secondary importance with respect to the prediction of mass transfer behavior, and thus it is an acceptable approximation to assume the particles are spherical [42].

6.*1.1 Governing Equations*

The model's mathematical foundation lies in conservation of mass, energy, momentum, and species -- all of which must be solved simultaneously. For 1-dimensional, steady flow absent axial diffusion, the conservation equations take the form of a system of 1st order, non-linear ordinary differential equations (ODEs) and their associated boundary (inlet) conditions. For all analysis that follows, the subscript *R*

denotes the reactant-side (that is, the side containing the AC-PG slurry), and *L* the load-side of the HEX reactor.

6.1.1.1 Conservation of Mass

Assuming the HEX reactor is operating at steady-state, the 1-dimensional separated flow expression for conservation of mass is:

Liquid-phase:

$$r_R \frac{d}{dz}\left(u_R\left(1- \beta\right)\right) = 0 \tag{6.1}$$

Gas-phase:

$$\frac{d}{dz}\left(u_g \beta \rho_g\right) = \left(1-\beta\right)\left(\frac{\rho_R}{M_R}\right)\left(\dot{r}_{a,des} M_a + \dot{r}_{c,des} M_c\right) \tag{6.2}$$

where β is the void fraction, u_R is the liquid-phase bulk velocity and u_g is the gas-phase velocity. The convention from Chapter III is adopted here to recast the volumetric reaction rates and concentrations in terms of liquid-phase mole fraction. Integration of Eq. (5.1) is trivial since the liquid-phase does not undergo any phase change process, and hence its mass flux at any axial position *z* in the reactor is determined by the inlet condition:

$$u_R\left(1- \beta\right) = U_R \tag{6.3}$$

where U_R is the inlet velocity of the liquid-phase, which is also identical to the liquid-phase superficial velocity at any axial location z.

Applying conservation of mass to the solid-phase requires a more circuitous approach; for particles having an initial particle size between r_i and dr_i, and defining $c_s = c_s(r_i;t)$ as the local mass concentration of such particles, we may write:

$$\frac{d}{dz}\left(U_R c_s\right) = -4\pi r_s^{\,2} n_s'''\left(0.5 h_{het}\Delta x_{het} + h_{dis}\Delta x_{dis}\right)\left(1-\beta\right)\left(\frac{M_{AC}}{M_R}\right)\rho_R \tag{6.4}$$

where $\Delta x_{het} \equiv 1.5P/RT_R K_{het} - x_a$, $\Delta x_{dis} \equiv x_{AC,sat} - x_{AC}$ and $n_s''' = n_s'''(r_i;t)$ is the number density of particles with initial sizes between r_i and $r_i + dr_i$. Additionally, assuming the AC particles have uniform density, c_s is simply,

$$c_s = \frac{4}{3}\pi n_s''' \rho_s r_s^{\,3} \tag{6.5}$$

therefore,

$$\frac{dc_s}{dz} = 4\pi n_s''' \rho_s r_s^{\,2}\frac{dr_s}{dz} \tag{6.6}$$

combining Equations (6.5) and (6.6) and re-arranging, the following expression results:

$$\frac{dr_s}{dz} = -\frac{\rho_R M_{AC}}{U_R \rho_s M_R}\left(0.5 h_{het}\Delta x_{het} + h_{dis}\Delta x_{dis}\right) \tag{6.7}$$

the total mass concentration of solid AC at axial location *z* is

$$c = \pi\rho_s\left(\frac{4}{3}\right)\int_{r_{i,\min}}^{r_{i,\max}} n_s''' r_s^{\,3}\, dr_i \tag{6.8}$$

utilizing the shrinking core assumption discussed in Chapter III, the number density is

$$n_s''' = \frac{c_i f\left(r_i\right)}{\left(4/3\right)\rho r_s r_i^3} \tag{6.9}$$

finally, if we again assume a uniform initial size distribution, the distribution function becomes $f\left(r_i\right) = 1/\left(r_{i,\max} - r_{i,\min}\right)$. Making the substation into Eq. (6.9), and then subsequently into Eq. (6.8), one obtains:

$$c = \frac{c_i}{r_{i,\max} - r_{i,\min}}\int_{r_{i,\min}}^{r_{i,\max}}\left(\frac{r_s}{r_i}\right)^3 dr_i \tag{6.10}$$

On the condition that k_{het} and k_{dis} are independent of *r*, and the integral of Eq. (6.7) has been obtained, it is possible to solve Eq. (6.10) analytically upon substituting for *r*:

$$c(z) = \frac{c_i}{\Delta r_i}\left\{\Delta r_i + 3N_s(z)\ln\left(\frac{r^*_{i,\min}}{r_{i,\max}}\right) + 3N_s^2(z)\left(\frac{1}{r^*_{i,\min}} - \frac{1}{r_{i,\max}}\right) + \frac{1}{2}N_s^3(z)\left(\frac{1}{r^2_{i,\max}} - \frac{1}{r^{*2}_{i,\min}}\right)\right\} \quad (6.11)$$

where $N_s(z)$ is the integral of the RHS of Eq. (6.7), and;

$$r^*_{i,\min} = \begin{cases} r_{i,\min} & N_s(z) \le r_{i,\min} \\ N_s(z) & N_s(z) > r_{i,\min} \end{cases} \quad (6.12)$$

Eq. (6.12) simplifies the task of ensuring that mass is conserved in the numerical scheme; we shall elaborate on this in Section 6.1.3.

6.1.1.2 Conservation of Species

Conservation of species for AC, NH_3 and CO_2 (respectively) dissolved in the liquid-phase are as follows:

$$\frac{dx_{AC}}{dz} = \frac{1-\beta}{U_R}\left(\dot{r}_{dis} - \dot{r}_{\text{hom}}\right) \quad (6.13)$$

$$\frac{dx_a}{dz} = \frac{1-\beta}{U_R}\left(2\dot{r}_{\text{hom}} + 2\dot{r}_{het} - \dot{r}_{a,des}\right) \quad (6.14)$$

$$\frac{dx_c}{dz} = \frac{1-\beta}{U_R}\left(\dot{r}_{\text{hom}} + \dot{r}_{het} - \dot{r}_{c,des}\right) \tag{6.15}$$

In the gas-phase, conservation of species for NH_3 reads,

$$\frac{d}{dz}\left(u_g \beta \bar{\rho}_g y_a\right) = \left(\frac{\rho_R}{M_R}\right)(1-\beta)\dot{r}_{a,des} \tag{6.16}$$

where $\bar{\rho}_g$ is the molar density of the gas-phase mixture composed of NH_3 and CO_2, which is assumed to behave as an ideal mixture:

$$\bar{\rho}_g = \frac{P}{\Re T_g} \tag{6.17}$$

Note that in accordance with the assumptions stated in the previous section, $T_g = T_l$. If CO_2 is the only other gas-phase species present (i.e., no air entrainment in the PG), its gas-phase mole fraction is given by $y_c = 1 - y_a$. However, determination of y_a requires it to be separated from the terms on the LHS of Eq. (6.16). In the stirred batch reactor, it was determined that the bubble's residence time in the liquid-phase far exceeded the time for a pure CO_2 bubble to become saturated with NH_3. For a single spherical bubble composed initially of CO_2, the time constant for desorption of dissolved NH_3 from the liquid-phase is given approximately by:

$$\tau = \frac{d_b H_a}{6 k_{a,des}} \tag{6.18}$$

where the mass transfer coefficient $k_{a,des}$ may conservatively be estimated by approximating the bubble as a rigid sphere rising in a liquid expanse at terminal velocity u_t:

$$u_t = \frac{d_b^2 g \rho_R}{9 \mu_R} \tag{6.19}$$

The mass transfer coefficient may be estimated by the Ranz-Marshall correlation for rigid spheres (applicable to small bubbles at low *Re*) [87]:

$$k_{a,des} = \frac{D_a}{d_b}\left(2 + 0.6\,\mathrm{Re}^{1/2}\, Sc^{1/3}\right) \tag{6.20}$$

In reality, interactions with neighboring bubbles and localized turbulence produced by bubble motion [88] would result in higher average mass transfer coefficients than an isolated bubble rising in a stagnant fluid. Taking the maximum bubble diameter of ~1 mm observed in the flow visualization study of Niedbalski *et al.* [25], and estimating the diffusion coefficients from the modified Einstein correlation as in Derks and Versteeg [53], we estimate the time constant for a bubble to reach NH_3 saturation as $t \approx 0.02$s; the operating conditions of Johnson *et al.*'s [70] HEX reactor

places the residence time of the PG-AC slurry on the order of several seconds, and hence we may safely assume that bubbles released from the chemical reaction exist in a state of complete NH_3 saturation at any given axial location:

$$y_a = H_a x_a \frac{\Re T_R}{P}\left(\frac{\rho_R}{M_R}\right) \tag{6.21}$$

Now, upon recognizing that

$$r_g = \bar{r}_g\left(y_a M_a + y_c M_c\right) \tag{6.22}$$

we may substitute for the product $u_g \bar{r}_g b$ (after some algebraic manipulation) from the conservation of mass expression, Eq. (6.2), apply the derivative operator *d/dz*, and solve Eq. (6.16) for $\dot{r}_{a,des}$:

$$\dot{r}_{a,des} = \frac{M_c}{1 - y_a M_a}\dot{r}_{c,des} + \frac{j_g / \bar{\rho}_g}{(1-\beta)(1 - y_a M_a)}\frac{d}{dz}\left(H_a x_a\right) \tag{6.23}$$

where the term $j_g \equiv u_g b \bar{r}_g$ signifies the molar flux at a given reactor channel cross section. The RHS of Eq. (6.23) reveals two contributors to desorption of NH_3: release of additional CO_2 bubbles (i.e., $\dot{r}_{c,des}$) and spatial changes in the equilibrium gas

concentration of NH_3 (i.e. $\frac{d}{dz}\left(H_a x_a\right)$). The second contributor to $\dot{r}_{a,des}$ was not present in the batch reactor model since the bubble residence time in the liquid-phase was very short, and the concentration of NH_3 spatially uniform. An interesting facet of this expression comes to light when the product rule is applied to the second term:

$$\frac{d}{dz}\left(H_a x_a\right) = \frac{dH_a}{dT}\frac{dT_R}{dz}x_a + H_a\frac{dx_a}{dz} \tag{6.24}$$

As the temperature of the reactant-side of the HEX reactor rises along the length of the channel, the solubility of NH_3 tends to decrease (i.e., dH_a/dT is positive), which promotes further desorption of NH_3. During the later segment of the reaction, when additional dissolved NH_3 contributed by the homogeneous and heterogeneous reactions is small, x_a tends to decrease; this has an antagonistic effect on the first term of the RHS of Eq. (6.24). This permits the possibility of decelerating NH_3 desorption under certain conditions, suggesting that an additional use for the model is to map where these conditions occur so as to avoid them.

6.1.1.3 Conservation of Momentum

In the context of 1-dimensional continuous flow reactor models, the momentum equations are generally employed to predict the axial pressure profile [81], whereas quantities of interest relating to the motion of the various phases (velocity, acceleration, void fraction, etc.) are calculated using a combination of conservation of mass, conservation of species, and empirical correlations. Under steady-state conditions, conservation of momentum for the slurry (gas-liquid-solid mixture) reads:

$$\frac{dP}{dz} = \frac{dP_F}{dz} + \frac{dP_G}{dz} + \frac{dP_A}{dz} + \frac{dm_g'''}{dz}\left(u_R - u_g\right) \tag{6.25}$$

where the subscript *F* indicates the contribution of frictional pressure drop; *G* hydrostatic (or gravitational) pressure drop, and; *A* acceleration pressure drop. The last term on the RHS of Eq. (5.25) is a source term representing the acceleration that occurs as gas bubbles are liberated from the liquid-phase and joins the gas-phase.

The hydrostatic pressure drop is given by:

$$\frac{dP_G}{dz} = -g\left[\rho_R^*(1-\beta) + \rho_g\beta\right] \tag{6.26}$$

where ρ_R^* is an effective liquid-phase density including the contribution of dissolved species and the solid-phase, which were assumed to travel at the velocity of the liquid-

phase:

$$r_R^* \circ r_R + c + \left(\frac{r_R}{M_R}\right)\left(x_{AC}M_{AC} + x_a M_a + x_c M_c\right) \tag{6.27}$$

The frictional pressure drop is given by:

$$\frac{dP_F}{dz} = -\frac{1}{2d_h} U_R^2 \rho_R^* \lambda_{SP} \Phi_{TP}^2 \tag{6.28}$$

where d_h is the hydraulic diameter of the channel (approximately 3 mm) , f is the single-phase Fanning friction factor evaluated at the liquid-phase superficial velocity and utilizing effective slurry properties, and Φ_{TP}^2 is the so-called two-phase multiplier, defined as [80]:

$$\Phi_{TP} = \sqrt{\frac{\frac{dP_{F,TP}}{dz}}{\frac{dP_{F,SP}}{dz}}} \tag{6.29}$$

where the subscript designations , *TP* and *SP* signify two-phase and single-phase (i.e., slurry in the absence of a gas-phase), respectively.

Lastly, the acceleration pressure drop is given by:

$$\frac{dP_A}{dz} = -\left[r_R^* u_R \frac{du_l}{dz}(1 - \beta) + r_g u_g \frac{du_g}{dz} \beta \right] \tag{6.30}$$

The HEX reactor operating conditions considered as part of this validation study are such that the contribution from frictional and acceleration may be neglected. This practice is common for low Reynolds number reactors, such as slurry and two-phase bubble column reactors [89]; the HEX reactor flow conditions reported by Johnson *et al.* [70] give a range of *Re* on the slurry-side that is quite low (between 0.5 and 10). Under these conditions, hydrostatic pressure drop dominates. Therefore, we arrive at:

$$\frac{dP}{dz} = -g\left[r_R^* (1 - \beta) + r_g \beta \right] \tag{6.31}$$

Despite these simplifications, estimation of the local void fraction remains a critical component for accurate determination of the pressure field, and thence the gas-phase properties. In point of fact, because both α and ρ_g are strong functions of pressure, Eq. (6.31) can be a significant source of non-linearity in the overall reactor model.

It is also possible to use Eq. (6.31) in conjunction with inlet and outlet pressure data to estimate the mean void fraction in a slurry channel, which we define as:

$$\bar{\beta} = \frac{\int_0^L \beta \, dz}{L} \tag{6.32}$$

Integrating Eq. (6.31) and substituting from Eq. (6.32):

$$\bar{b} = \frac{r_g g L_p - \Delta P}{\left(r_R - r_g\right) g L_p} \tag{6.33}$$

where g is the gravitational acceleration , ΔP is the pressure drop measured between the inlet and outlet of the slurry-side of the HEX reactor. Note that we have made the approximation $r_R^* \gg r_R$.

6.1.1.4 Conservation of Energy

1-Dimensional analysis (both steady-state and transient) of heat exchange equipment is a well-established practice. For the liquid-phase, consider a general 1-dimensional representation of the energy equation for an incompressible fluid, assuming steady-state and neglecting viscous dissipation effects is:

$$U_R C_R \frac{dT_R}{dz} = \frac{A'_w}{A_c} q''_w - \left(q'''_g + q'''_s\right)\left(1 - \bar{b}\right) + \left(S'''_{\text{hom}} + S'''_{des}\right)\left(1 - \bar{b}\right) \tag{6.34}$$

where A_c is the channel cross sectional area, A'_w is the wall area per-unit channel length, C_R is the heat capacity of the liquid-phase, q''_w is the channel wall heat flux, q'''_g is the volumetric heat exchange with between the liquid -and gas-phases, q'''_s is the volumetric

heat exchange between the liquid- and solid-phases, S'''_{hom} is the volumetric heat sink/source from the homogeneous reaction, and S'''_{des} is the volumetric heat source/sink due to release of dissolved gas. Note that the volumetric terms in Eq. (6.34) are on a per-unit-volume of liquid basis, hence the appearance of the term $(1-\beta)$. The energy balance for the gas-phase reads:

$$C_g \frac{d}{dz}\left(u_g \beta T_g\right) = q'''_g (1-\beta) \tag{6.35}$$

In considering the solid-phase, we must consider the range of particle sizes present at any particular axial position *z*, which necessitates an integral over the entire local particle population to obtain the total reaction and sensible energy storage contribution. The rate of change in sensible energy of the entire AC particle population is due to combination of the heat transferred to the surface from the liquid-phase via convection, less the heat consumed by the endothermic chemical reaction occurring at the surface:

$$U_R C_s \frac{d}{dz}\int_{r_{i,\min}}^{r_{i,\max}} \overline{T}_s r^3 n'''_s (1-\beta)\, dr_i = \int_{r_{i,\min}}^{r_{i,\max}} \left[3r^2 \left\{ h_s \left(T_s - T_R\right) + S''_s \right\}\right] n'''_s (1-\beta)\, dr_i \tag{6.36}$$

where T_s is the surface temperature of an AC particle or radius *r*, $\overline{T}_s$ is the bulk temperature of a solid particle of radius *r*, h_s is the convective heat transfer coefficient at

the solid-liquid interface, and S_s'' is the heat flux consumed by the dissolution and heterogeneous decomposition reactions. Note that Eq. (6.36) is linked to Eq. (5.35) via:

$$q_s''' = -\int_{r_{i,\min}}^{r_{i,\max}} 4\pi r^2 h_s \left(T_s - T_R\right) n_s''' dr_i \tag{6.37}$$

Assuming that the reaction takes place entirely on the surface of any AC particle, and recalling the poor thermal conductivity of solid AC, we posit that:

1) The surface temperature – rather than the bulk temperature – of the particle governs S_s'' and;
2) The majority of the thermal energy delivered to the particle's surface via convection is consumed by the chemical reaction, with only a small fraction of the heat causing a sensible energy change in the solid particle.

From assumption (2) above, it follows that the integral on the LHS of Eq. (6.36) is negligible and the energy equation for any given particle becomes:

$$h_s \left(T_s - T_R\right) \approx -S_s'' \tag{6.38}$$

and thus, using the definitions of $\dot{r}_{het}$ and $\dot{r}_{dis}$,

$$q_s''' = \int_{r_{i,\min}}^{r_{i,\max}} 4\pi r^2 n_s''' S_s'' dr_i = \left(\Delta H_{dis}\dot{r}_{dis} + \Delta H_{het}\dot{r}_{het}\right)\left(\frac{\rho_R}{M_R}\right) \tag{6.39}$$

Because the heterogeneous reaction term is a strong function of temperature, it is necessary to also calculate T_s, which turn requires h_s to be known. The determination of the heat transfer coefficient h_s is a complicated affair, owing in large part to the rapid dissolution and reaction processes causing the solid-liquid interface to constantly renew. For this same reason, it is expected to be similar to heat transfer coefficients encountered in turbulent flow, and so the difference between T_s and T_R is likely to be small. As a first approximation, it is assumed that $T_s \approx T_R$, as was the case with the batch reactor. This simplification also alleviates a significant numerical burden since T_s would need to be iteratively calculated.

Substituting Eqs. (6.39) and (6.35) into Eq. (6.34), we obtain a single expression for the slurry energy balance:

$$\frac{dT_R}{dz} = \frac{A_w'}{U_R C_R A_c} q_w'' - \frac{C_g}{U_R C_R}\frac{d}{dz}\left(u_g \alpha T_g\right) + \Delta\mathbf{H}^T \bullet \dot{\mathbf{r}}\frac{(1-\beta)}{U_R C_R} \tag{6.40}$$

where, for convenience, we have defined the vectors $\dot{\mathbf{r}} = \left\{\dot{r}_{het}, \dot{r}_{dis}, \dot{r}_{\text{hom}}, \dot{r}_{des}\right\}^T$ and $\Delta\mathbf{H} = \left\{\Delta H_{het}, \Delta H_{dis}, \Delta H_{\text{hom}}, \Delta H_{des}\right\}^T$. Due to the small heat capacity of gasses relative to liquids, C_g/C_R is very small compared to $\Delta\mathbf{H}/C_R$, and so we may plausibly neglect the

small amount of thermal energy lost by the liquid-phase to the gas-phase; the liquid-phase energy balance becomes:

$$\frac{dT_R}{dz} = \frac{A'_w}{U_R C_R A_c} q''_w + \Delta \mathbf{H}^T \bullet \dot{\mathbf{r}} \frac{(1-\beta)}{U_R C_R} \tag{6.41}$$

To calculate the temperature of the gas-phase, we recognize that $q'''_g(1-b)$ may be expressed as:

$$q'''_g(1-b) = h_g a'''_b (T_R - T_g) \tag{6.42}$$

where the quantity $h_g a'''_b$ is the volumetric heat transfer coefficient per-unit-channel volume from the liquid-phase to the gas-phase. The combination of low heat capacity and the generally high gas-liquid interfacial area a'''_b means that $T_g \gg T_R$.

6.1.2 Correlations and Physical Properties

With concurrent liquid, gas, and particulate solids flowing through tortuous minichannels, the flow situation encountered in the HEX reactor is exceedingly complex. There are no readily applicable heat, mass, and/or momentum correlations for this specific situation, although there are a scant few concerning gas-liquid flows in PHEs [90 - 93] and many more for single-phase flows [14 - 17] at various *Re*.

For the purposes of selecting the appropriate correlations, there are three possible 'zones' that may exist in a slurry channel according to which combination of phases are present:

1) Liquid-solid (LS) zone – the liquid-phase has not yet been saturated with CO_2, and thus no gas bubbles have evolved. The dispersed solid AC is in the process of dissolving and undergoing heterogeneous decomposition.
2) Liquid (L) zone – the solid AC particles have completely dissolved/reacted, but the dissolved CO_2 remains below the saturation limit. This only occurs under special circumstances – at low temperatures when heterogeneous and homogeneous decomposition are slow compared to the residence time, and/or when the solid AC loading is low.
3) Liquid-solid-gas (LSG) zone – gas bubbles are evolving from a supersaturated liquid-phase, and the solid AC particles have not yet completely dissolved/reacted.
4) Liquid-gas (LG) zone – the solid AC particles have completely dissolved/reacted, and only the liquid-phase and gas-phase are present

Following the natural progression of the reaction, it is obvious that these zones occur in numerical order proceeding from the inlet of the slurry channel to the outlet. The correlations utilized for each zone will be discussed in the subsections that follow.

6.1.2.1 Mass Transfer Parameters

For the batch reactor model, the nucleation, growth, and release of CO_2 bubbles was modeled via an effective volumetric mass transfer coefficient $k_{c,des}a_b'''$ correlated to the Reynolds number, Weber number, and supersaturation ratio. Physically, such a correlation would be appropriate for a HEX reactor as well, since both *Re* and *We* are measures of the intensity of turbulent mixing (which would promote the aggregation of dissolved CO_2 molecules at nucleation sites), and stability of bubbles in the liquid flow field (which determines the volumetric gas-liquid interfacial area), both of which can generally describe the two-phase flow characteristics in an open-flow reaction vessel. Certainly, one would also expect the degree of supersaturation to play a significant role as well, regardless of reactor type. Nevertheless, the HEX reactor presents a number of additional difficulties to adapting such a correlation, chief among which is the large variation in viscosity along the length of the channel, and the axial change in liquid and gas-phase velocities. It also bears considering that the void fractions encountered in the HEX reactor, due to its small volume, are much larger than typically observed in a stirred tank reactor. The development of a generally applicable correlation for bubble desorption in a PHE HEX reactor is well beyond the scope of this work; adapting this correlation introduces three unknown parameters to be adjusted for this particular correlation, and with only the limited data of Johnson *et al.* [70], it is not feasible to attempt a fit of all three parameters. Instead, we shall write the correlation as:

$$k_{c,des} a_b''' = C^* g^{2.2} \tag{6.43}$$

where C^* is a constant representing an effective value for the term $\mathrm{Re}^n We^m$ in Eq. (3.53) and $g = \left([CO_2] - [CO_2]_{sat}\right) / [CO_2]_{sat}$ is the supersaturation ratio, with the exponent 2.2 taken from Kierzkowska-Pawlak *et al.* [66] as an initial estimate. To be consistent with the definition in [66], the volumetric mass transfer coefficient in Eq. (6.43) is on a per-unit-volume of mixture (gas and liquid) basis, rather than liquid alone. The value for C^* is estimated by adjusting its assumed value until the calculated average void fraction was reasonably close to the estimated average void fraction from the data of Johnson *et al*. [70], specifically the high residence time data where the void fraction could be estimated analytically. Generally, the average void fraction increases with C^*; however, the model predictions became insensitive to C^* at large values. Even in this limiting case, there was still significant under-estimation of the load-side heat transfer and heat consumed by AC decomposition. It was found that this underestimation could be remedied satisfactorily by choosing a single, 'average' value of $x_{AC,sat}$ which was within the range estimated from the batch reactor experiments. We shall elaborate upon this further in Section 6.2.

In a similar vein, the mass transfer coefficients for the dissolution and heterogeneous decomposition processes could not be fit to the experimental HEX reactor data due to the limited range of conditions tested and the absence of any species concentration measurements. Given the low Reynolds number compared to the batch reactor, it is probable that the assumption of mass transfer-limited heterogeneous

decomposition still holds. Data reported for three-phase bubble column reactors [88, 89] give some insight into the orders of magnitude to be expected – provided that the bubbles are small enough to behave as rigid spheres and thus provide a reasonable analogy to the solid spheroid particles. This data – and the model in the study – does not take into account nucleation of bubbles on the particle surface or the possibility of microeddies generated by rapid dissolution. Initially, the values for k_{dis} and k_{het} were taken from the batch reactor model parameter fit for m_{AC} = 40g and T = 70°C and held constant.

6.1.2.2 Thermal-Hydraulic Parameters

The energy balance equation (Eq. (6.41)) requires a constitutive relation for the wall heat flux, which for 1-dimensional models is realized by Newton's law of cooling:

$$q''_w = h_{eff}\left(T_L - T_R\right) \tag{6.44}$$

where T_L is the load fluid temperature and h_{eff} is the overall heat transfer coefficient accounting for both load and slurry sides of the HEX reactor. For steady-state conditions, h_{eff} is given by:

$$h_{eff} = \left(\frac{1}{h_R} + \frac{l_w}{k_w} + \frac{1}{h_L}\right)^{-1} \tag{6.45}$$

Johnson *et al.* [70] reported single-phase correlations for their HEX reactor -- both the load (water) side and slurry (PG) side Nusselt number were correlated as a function of Reynolds number and Prandtl number. The said correlations were obtained using the Wilson plot method (further details are in the Appendix). For the load side, the following correlation for *Nu* was developed for *Re* from 100 to 330, with an uncertainty of 6%:

$$Nu_L = 0.18\,\mathrm{Re}_L^{0.67}\mathrm{Pr}_L^{1/3}\left(\mu/\mu_w\right)^{0.14} \tag{6.46}$$

For the reactant-side, the *Nu* correlation reads:

$$Nu_R = 0.082\,\mathrm{Re}_R\mathrm{Pr}_R^{1/3}\left(\mu/\mu_w\right)^{0.14} + 6.79 \tag{6.47}$$

where μ_w is the liquid-phase viscosity evaluated at the local wall temperature. These correlations were validated against Johnson *et al.*'s [70] data for baseline single-phase experiments conducted prior to each AC decomposition run. A comparison is presented in Section 6.2.1 of the data for both high residence time (~70 s) and low residence time (~10 s) to those predicted by the model in the absence of chemical reaction or multiphase flow.

The LS zone is viewed as a liquid-solid slurry wherein the fluid properties are unaffected by the presence of dissolved species in the liquid-phase. A number of authors have considered liquid-solid slurry flows [94 - 98], and while none appear to be specific

to PHEs, there is a consensus that the presence of *small* particles tends to enhance heat transfer and frictional pressure drop. Small-particle slurries also tend to exhibit rheological behavior describable by a shear-thickening power law model [94]. The enhancement to heat transfer would apply to the wall heat flux in this region; Charunyakorn *et al.* [94], in their study of small encapsulated phase-change particles in laminar flow in a circular tube, modeled the particle-motion induced heat transfer enhancement by means of an adjustment to the liquid-phase thermal conductivity. However, Charunyakorn *et al*. also pointed out that the presence of particles had only a minor effect on the Nusselt number (compared to a liquid-only flow), once phase-change was taken into account. In accordance with the assumption that heat transfer in the LS-zone is not affected to a great degree by the solid-phase, Eq. (6.47) is utilized to calculate the local slurry-side heat transfer coefficient for both the LS-zone and liquid-zone.

In the case of the LSG- and LG-zones, there is a wealth of evidence to show that the effect of gas-liquid interactions on the reactant-side heat transfer coefficient must be accounted for. The literature for two-phase gas-liquid flows in heat exchangers show substantial enhancements in heat transfer over those of single-phase flows with the same liquid-phase mass flux – even without phase-change or bubble nucleation – that increases monotonically with gas-phase mass flux [93].

In such instances where there is no condensation or evaporation (such as the HEX reactor considered here), the heat transfer surfaces would remain wetted even at very high gas-phase mass fluxes. Accordingly, the threat of dry out is essentially non-

existent. The enhancement in frictional pressure drop that also occurs with increasing gas-phase mass flux [90 - 93] suggests, by heat-momentum transfer analogy, that turbulence and/or secondary flows generated by bubble motion in the liquid-phase is responsible for the enhancement. This effect has also been studied numerically [99] as an analogy to turbulence.

Niedbalski *et al.* [26] derived a modified Leveque analogy similar to that which Martin [16] developed for turbulent flow in chevron PHEs. The Leveque analogy was originally proposed for thermally-developing, hydrodynamically fully-developed flows where the thermal boundary layer is significantly smaller than the channel diameter [100]. In the case of turbulent flows and/or high Prandtl number fluids, this is certainly a reasonable assumption; this line of reasoning can be extended [26] to that of gas-liquid bubbly flow owing to the mixing action produced by bubbles as they displace the liquid-phase. This would tend to disrupt the development of the thermal boundary layer and limit it to a thin region in a manner similar to high-*Re* turbulence. The modified Leveque analogy yields a correlation of the form [26]:

$$Nu = A^{*}\left(\mathrm{Re}^{2} / {}_{SP}F_{TP}^{2}\right)^{m} \mathrm{Pr}^{1/3} \tag{6.48}$$

where λ_{SP} is the Darcy friction factor evaluated as though the liquid-phase were flowing alone at the same superficial velocity; m = 2/3 can be adjusted empirically as necessary (Martin [16] found a m = 0.374 worked well for single-phase turbulent flow in chevron PHEs), and the leading coefficient A^{*} is also an empirical constant. This correlation has a

unique advantage in that it relates two-phase pressure drop data – which can be obtained using a single channel – to thermal performance of a heat exchanger operating in two-phase flow conditions with a non-condensable gas; when no gas-phase is present, Eq. (6.48) reduces to the original Leveque analogy (with $m = 2/3$). The difficulty in adapting this correlation to describe flow in the LSG or LG regions of the HEX reactor arises from the requirement that *Nu* should be at least piecewise continuous along the length of the channel, i.e. Eq. (6.48) and Eq. (6.47) must be equal at the interface between the LS (or liquid-only) and LSG (or LG) zones. Complicating this challenge further is the presence of additional fitting parameters in Eq. (6.48). The plot in Figure 80 compares *Nu* calculated using Eq. (6.48) (using Martin's [16] parameters) to that of Eq. (6.47) over the course of a typical 10-second residence time baseline experiment from Johnson *et al.* [70].

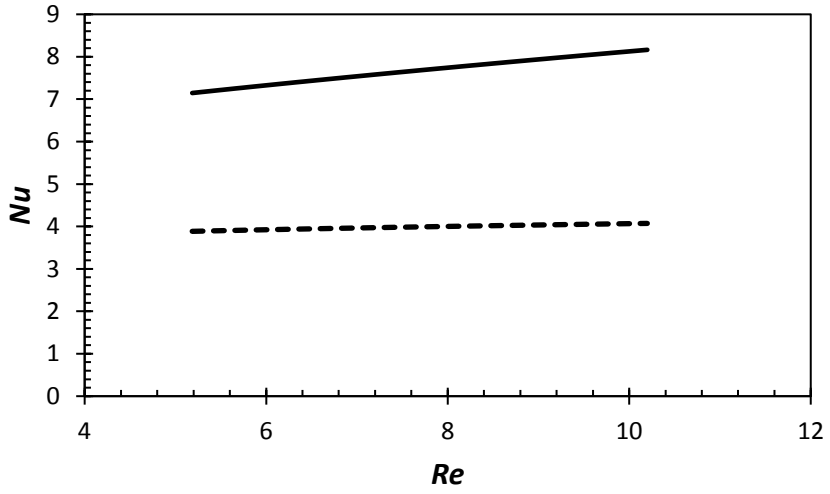

Figure 80. Plot of Eq. (6.47) (solid line) and Eq. (6.48) (dashed line) as a function of Reynolds number in single phase flow.

Even a cursory examination of Figure 80 shows that it is not possible to satisfy the requirement for piecewise continuity in *Nu* along the length of the channel using the modified version of Martin's correlation (Eq. (6.48)) as suggested originally (at least under the conditions considered here) [26]. Additionally, it is practically impossible to adjust the empirical constants of both equations so that they are piecewise continuous regardless of at what value of *Re* the transition from the LS/L zone to LSG/LG zone occurs. The variation in (liquid-phase) *Re* along the length of the channel from ~5 to ~10 occurs are a result of PG's viscosity being strongly temperature dependent – as concentrations of AC introduced into the reactor change, so too would the transition point between zones. Because the dependency on *Re*, a different set of empirical coefficients for Eq. (5.48) would be needed for each change in HEX reactor operating conditions. It is therefore unlikely that the two separate correlations can be utilized in a piecewise continuous fashion. There are two relatively straightforward choices to resolve this issue:

1) Adjust the empirical constants in Eq. (6.47) so that when $F_{TP}^2 = 1$, it is nearly equal to that of Eq. (6.48) over the range of *Re* encountered, or;
2) Introduce a dependency on F_{TP}^2 into Eq. (6.47) and adjust the fitting parameters such that satisfactory agreement with experiment is attained.

The presence of the single-phase friction factor λ_{SP}, which is also dependent upon *Re*, means that option (1) would only be feasible over a limited range of *Re*. Apart from this limitation, it is unrealistic to suppose that there is a 'sharp' interface between the zones; as supersaturation is initially small, the assumption that the micro-pumping effect

of the bubbles is sufficient to maintain a small thermal boundary layer is inapplicable. This consideration suggests that use of Eq. (6.48) in the AC HEX reactor might only be advisable when flow in the LS/L zone is already turbulent, as opposed to when there is a transition from laminar creeping flow to a self-agitating bubbly flow. Option (2) is essentially a purely empirical approach that is not founded on any underlying assumption apart from the observation that

$$h_{TP}/h_{SP} = h(l_{TP}/l_{SP}) \tag{6.49}$$

where h is a function whose form depends on the channel geometry, fluid properties, and so forth. The simplest case is to presume, based on the form of Eq. (6.47), that:

$$h_{TP} = \Phi_{TP}^{n} h_{SP} = \Phi_{TP}^{n}\left[0.082\,\mathrm{Re}_R \mathrm{Pr}_R^{1/3}\left(m/m_w\right)^{0.14} + 6.79\right] \tag{6.50}$$

where n is an empirical fitting parameter, which we have taken to be 2/3 for consistency with theory. With only two ranges of *Re* to compare the model against, this approach was judged to be an appropriate first-cut that is consistent across all HEX reactor operating conditions considered, and accounts for the heat transfer coefficient enhancement with increasing gas-phase mass flux.

The remaining task is to select an appropriate correlation for the two-phase multiplier Φ_{TP}. Tribbe and Muller-Steinhagen investigated air-water flow in a chevron PHE, reporting pressure drop data under various liquid- and gas-phase mass fluxes [91,

92]. They proposed a relation correlating their two-phase multiplier data to the Lockhart-Martinelli parameter [91]:

$$\Phi_{TP} = 1.423 - 0.0724 \ln X + \frac{1.031}{X} \tag{6.51}$$

where X is the Lockhart-Martinelli parameter, defined as [80]:

$$X = \sqrt{\frac{dP_{F,R}}{dz} \Big/ \frac{dP_{F,g}}{dz}} \tag{5.52}$$

where the frictional pressure gradients $\frac{dP_{F,R}}{dz}$ and $\frac{dP_{F,g}}{dz}$ are evaluated according to the corresponding mass flux as though liquid (or gas) were flowing in the channel alone. Eq. (6.51) appears to be a promising candidate for estimating the local two-phase multiplier, since it represented data for PHEs with different chevron angles and hydraulic diameters, and could be applied locally with only a minor compromise in accuracy [91]. Tribbe and Muller-Steinhagen suspected that variations in geometry (i.e., chevron angle and trough depth/channel diameter) were accounted for via the single-phase friction factors used to compute X for a given liquid- and gas-phase mass flux combination. For this model, a correlation suggested by Martin [16] was used to calculate the single-phase friction factor for use in Eqs. (6.52) and (6.51).

Niedbalski *et al*. [25] conducted a flow visualization study using the same the chevron PHE as Johnson *et al*. [70], but using the reaction between sodium bicarbonate and acetic acid as a surrogate for the decomposition of AC. A two-phase multiplier correlation was also proposed:

$$\Phi_{TP} = \frac{13}{\sqrt{X}} \tag{6.53}$$

Interestingly, Niedbalski *et al.*'s [25] correlation yields a nearly three-fold greater estimate for Φ_{TP} than Tribbe and Muller-Steinhagen's correlation (Eq. (6.51)). This may be explained, perhaps, by the comparatively low liquid-phase *Re* studied in ref. [25], while Tribbe and Muller Steinhagen [91] examined flows with liquid-phase *Re* in the turbulent range. With existing bulk liquid turbulence, the relative influence of gas bubble motion on mixing in the transverse direction of the channel would be considerably less pronounced than in flows that would be laminar if the flow were single-phase.

Most of the conservation equations discussed in Section 6.1.1 require an estimation of the local area-averaged void fraction, α. In addition to directly effecting liquid-phase volumetric source terms (e.g., the homogeneous reaction rate and solid-phase decomposition reactions), it is evident from Eq. (6.3) that the residence time of the reactants – being inversely proportional to liquid-phase velocity – is strongly dependent upon the void fraction. Tribbe and Muller-Steinhagen recommended a correlation attributed to Rouhani [101] to predict the void fraction in chevron PHEs:

$$\beta = \frac{\chi}{\rho_g}\left\{\left[1+0.12(1-\chi)\right]\left[\frac{\chi}{\rho_g}+\frac{1-\chi}{\rho_R}\right]+\frac{1.18}{j\rho_R^{0.5}}\left[g\sigma\left(\rho_R-\rho_g\right)\right]^{1/4}\right\}^{-1} \tag{6.54}$$

where $j = j_g + j_R + j_s$ is the total mass flux, $\chi = j_g / j$ is the mass quality, and σ is the surface tension. By conservation of mass (Eqs. (6.1) and (6.2)) , we can express the total mass fluxes in terms of the primitive variables:

$$j = U_R c_i\left(1+\frac{\rho_R}{c_i}\right) \tag{6.55}$$

$$j_g = U_R c_i\left[1-\frac{\chi}{c_i}-\rho_R\left(\frac{M_{AC}}{M_R}\right)\left(x_{AC}+n_c x_c+n_a x_a\right)\right] \tag{6.56}$$

whence χ can be readily computed. Rouhani's correlation, according to ref. [91], appeared to perform satisfactorily for chevron plate heat exchangers. With no demonstrably superior alternative, and recognizing that the PHE used by Tribbe and Muller-Steinhagen was very similar to the HEX reactor studied by Johnson *et al.* [70], Eq. (6.54) was implemented to calculate the void fraction in this study as well.

6.1.3 Numerical Methodology

The finite-volume formulation of the HEX reactor model follows the discretization procedure detailed in Niedbalski *et al*. [26], which is discussed briefly here. Broadly, the (1-dimensional) finite volume method re-casts the differential equations representing conservation of mass, energy, species, and momentum as an algebraic system of equations. The HEX reactor channels are divided into *N* uniformly segments along the axial (*z*) direction, over which the governing equations are integrated. Since many of the primitive variables are coupled across the mass/energy/momentum domains (e.g., temperature and concentration via the temperature dependency of the rate coefficients), the finite volume representation of the governing equations can either by fully-coupled (one linear system), or partially coupled (one linear system for each primitive variable). Since most of the governing equations are non-linear, an iterative prediction-correction approach was implemented after [26]. As an illustrative example, consider primitive variables q_A, q_B, q_C, q_D, q_E with a HEX reactor having *K* channels, each of which is discretized into *N* volumes. The fully coupled approach, written in Matrix form, reads:

$$\begin{bmatrix} AA_{1,1} & \cdots & AA_{1,J} & & AE_{1,1} & \cdots & AE_{1,J} \\ \vdots & \ddots & \vdots & \cdots & \vdots & \ddots & \vdots \\ AA_{J,1} & \cdots & AA_{J,J} & & AE_{J,1} & \cdots & AE_{J,J} \\ & \vdots & & \ddots & & \vdots & \\ EA_{1,1} & \cdots & EA_{1,J} & & EE_{1,1} & \cdots & EE_{1,N} \\ \vdots & \ddots & \vdots & \cdots & \vdots & \ddots & \vdots \\ EA_{J,1} & \cdots & EA_{J,N} & & EE_{K,1} & \cdots & EE_{K,N} \end{bmatrix} \begin{Bmatrix} \delta\theta_{A,1} \\ \vdots \\ \delta\theta_{A,J} \\ \vdots \\ \delta\theta_{E,1} \\ \vdots \\ \delta\theta_{E,J} \end{Bmatrix} = \begin{Bmatrix} X_{A,1} \\ \vdots \\ X_{A,J} \\ \vdots \\ X_{E,1} \\ \vdots \\ X_{E,J} \end{Bmatrix} \tag{6.57}$$

where $AA_{i,j}$ is the link coefficient between $dq_{A,i}$ and $dq_{A,j}$, $AE_{i,j}$ the link coefficient between $dq_{A,i}$ and $dq_{E,j}$, and so forth; $dq_{A,i}$ is a small perturbation of the conservation equation about the present value of the variable q_A, in the *i*-th finite volume cell, and; $X_{A,j}$ is the 'error' in the conservation equation of the *i*-th finite volume cell at the current value of $q_{A,i}$. Note that the cell indices $i, j \hat{\imath} (1, J)$, where $J = N \times K$ is the total number of finite volume cells. In each iteration cycle, the system in Eq. (6.57) is solved and the coefficient matrix is subsequently updated. While this approach is fairly robust, it carries significant computational expense not only due the matrix's size (5*J* x 5*J*) but also to the abundance of off-diagonal elements arising from the non-linear chemical reaction terms, which makes inversion decidedly difficult and resource-intensive.

The de-coupled approach splits the system in Eq. (6.57) into multiple *J x J* systems corresponding to each primitive variable. In addition to being smaller, the matrices themselves become much easier to invert since most of the off-diagonal elements are no longer present. At each iteration cycle, the following systems are solved sequentially:

$$AA_{i,j}\,dq_{A,j} = X_{A,j} \tag{6.58}$$

$$BB_{i,j}\,dq_{B,j} = X_{B,j} \tag{6.59}$$

$$CC_{i,j}\,dq_{C,j} = X_{C,j} \tag{6.60}$$

$$DD_{i,j}\,dq_{D,j} = X_{D,j} \tag{6.61}$$

$$EE_{i,j}\,dq_{E,j} = X_{E,j} \tag{6.62}$$

At the end of the iterative cycle, each coefficient matrix **AA** through **EE** is then updated using the newly obtained values $q_{new} = q_{prev} + dq$. The non-linear terms are simply treated as inhomogeneous source terms and included in the appropriate vector **X**. This method was used to conduct the simulations presented in this chapter.

The volumetric source terms representing dissolution and heterogeneous reaction of the solid-phase presented a challenge in implementation. The solid-phase transport equation solved at each finite volume was Eq. (6.7), which would give the change in radius of all particles in the flow field. The solid-phase source terms, $\dot{r}_{het}$ and $\dot{r}_{dis}$ are proportional to a_s''', and for a given finite volume cell of size Δz, conservation of mass for the solid-phase gives:

$$c(z_i + \Delta z_i) - c(z_i) = \int_{z_i}^{z_i+\Delta z} -\left(\frac{M_{AC}}{M_R}\right)\left(\frac{\rho_R}{U_R}\right)\left(\dot{r}_{het} + \dot{r}_{dis}\right) dz \tag{6.63}$$

Difficulty arises when $\dot{r}_{het}$ and $\dot{r}_{dis}$ -- which are volumetric terms -- are evaluated using an average value of *r*, which is known only at the faces of the cell (i.e. at $z = z_i$ and $z = z_i + \Delta z$), while the change in solid-phase mass concentration is evaluated exactly at the known values of *r*. This causes an error between the LHS and RHS of Eq. (6.63) which grows in severity with Δz, thereby forcing unnecessarily small cell sizes. One method to remediate this problem was to exploit the assumption that the solid-phase mass transfer coefficients are approximately independent of particle size, which allows us to write

$$\int_{z_i}^{z_i+\Delta z} \dot{r}_{het} dz = \left(\frac{U_R M_R}{M_{AC}\rho_R}\right)\left[c(z_i + \Delta z) - c(z_i)\right]\frac{k_{het}\Delta x_{het}}{k_{het}\Delta x_{het} + k_{dis}\Delta x_{dis}} \tag{6.64}$$

$$\int_{z_i}^{z_i+\Delta z} \dot{r}_{dis}\, dz = \left(\frac{U_R M_R}{M_{AC}\rho_R}\right)\left[c(z_i + \Delta z) - c(z_i)\right]\frac{k_{dis}\Delta x_{dis}}{k_{het}\Delta x_{het} + k_{dis}\Delta x_{dis}} \tag{6.65}$$

With the volume integral of the solid-phase source terms approximated in this way, conservation of mass between the solid-phase and liquid-phase is guaranteed regardless of Δz.

6.2 Model Predictions and Comparison to Experiment

The objective of this section is to compare model predictions for total convective heat transfer and endothermic heat absorption to experimental measurements reported by Johnson *et al.* [70] to validate and gauge the models quantitative accuracy (and limitations). It is also of practical interest to examine the effect of HEX reactor operating parameters – inlet AC solids concentration, load fluid temperature, particle size, and residence time – on overall reactor performance (i.e. conversion, total heat removed, total heat consumed by reaction). The resultant predictions for axial concentration and temperature profiles reveal indispensable insights into the factors that promote optimal operating conditions.

6.2.1 Single-Phase Validation

The low (reactant-side) flow rates and high temperature differences presented unique challenges to the canonical approach to heat exchanger analysis. For most industrial applications, the established practice in the literature [17] involves the log-mean temperature difference (LMTD) method [75], which expresses an average heat transfer coefficient in terms of an average hot-side to cold-side temperature difference:

$$h_{eff} = \frac{\dot{Q}}{A_w \Delta T_{lm}} \tag{6.66}$$

where A_w is the total heat exchange area, $\dot{Q}$ is the total heat transfer, and ΔT_{lm} is the LMTD. The LMTD is defined as:

$$\Delta T_{lm} = \frac{\Delta T_2 - \Delta T_1}{\ln\left(\frac{\Delta T_2}{\Delta T_1}\right)} \tag{6.67}$$

For a counter-flow heat exchanger, $\Delta T_1 = T_{L,in} - T_{R,out}$ and $\Delta T_2 = T_{L,out} - T_{R,in}$. The LMTD method is derived assuming that thermophysical properties remain approximately constant, as is the case in most heat exchanger applications when the temperature of the process fluid does not change by more than several degrees Celcius. In this application, the reactant-side temperature can change by as much as 45°C – over such a large temperature difference, with a nominal reactant-side inlet temperature of 55°C, *Pr* may decrease by over 70% [74]. For precisely this reason, applying the LMTD-method globally to predict single-phase heat transfer is inappropriate.

The approach used in this study was to develop a single-phase correlation at higher *Re* – Eq. (6.47) – where the temperature differences on the reactant-side were less severe, and then apply the correlation locally in the numerical model for the low-*Re* cases. We stress that the objective is not to obtain an optimal single-phase heat transfer correlation that can be used generally, but rather a *reasonably accurate* relation that can be used in conjunction with Eq. (6.50) to predict the reactant-side heat transfer coefficient in the presence of decomposing AC. The author was granted a request to

AFRL for single-phase characterization data for the PHE used by Johnson *et al*. [70]; note that the data presented in this section and in the Appendix is attributable to AFRL; the author's participation was limited to operating the test apparatus and analyzing the data.

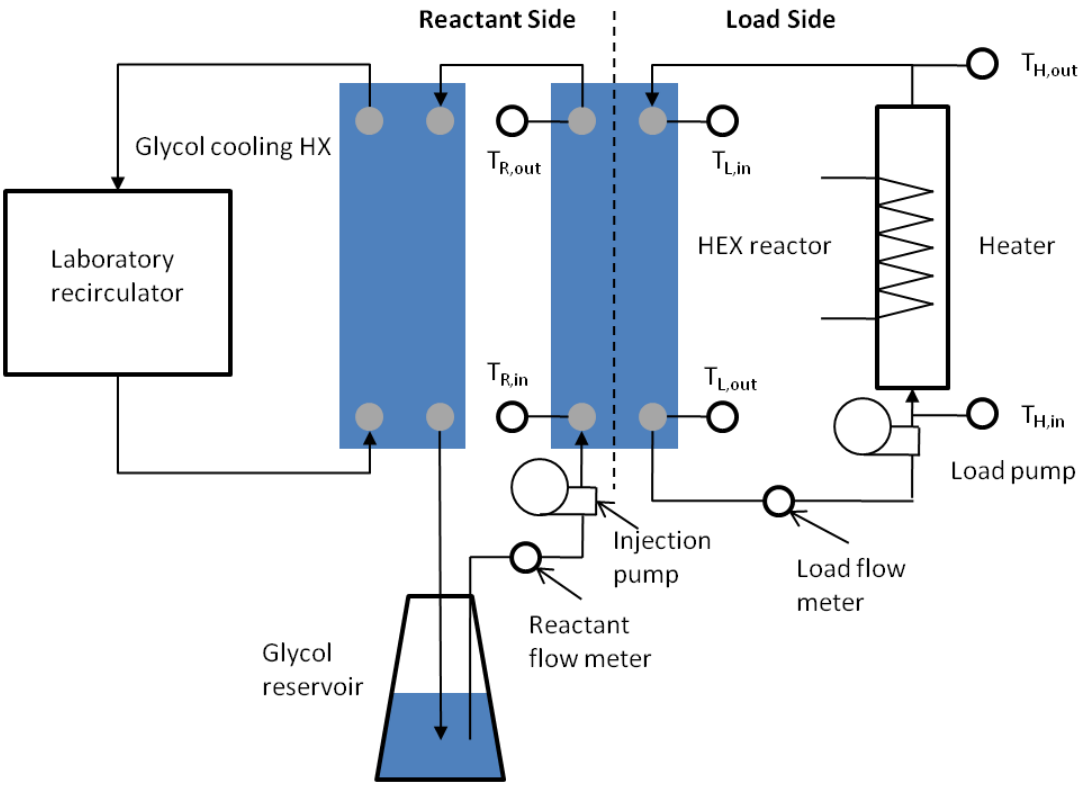

Figure 81. AFRL's Alfa Laval HEX reactor as configured for single-phase heat transfer characterization

The HEX reactor was operated in a closed-loop mode according to the diagram in Figure 81. The reactant-side inlet temperature was held at 50 +/- 0.5°C by modulating in-line heater input with a custom PID controller developed by Johnson *et al.* [13, 70]. The load-side mass flow rate was held at 112 g/s so that the reactant-side heat transfer

coefficient was the dominant contributor to the overall heat transfer coefficient. A secondary heat exchanger was used on the reactant-side to reject heat to the facility water supply and operate continuously until steady-state flow conditions were achieved. Two cases were tested, each with load-side inlet temperatures set to 70°C, 80°C, 90°C:

1) *Low Residence Time*: 12 plates were installed on the HEX reactor, giving 7 reactant channels and 6 load channels. The reactant flow rate was held at 3 L/min (~53 g/s) to give an approximate residence time of 20 seconds
2) *High Residence Time*: 24 plates were installed on the HEX reactor, giving 13 reactant channels and 12 load channels. The 'slurry pump' was removed and flow was provided by the 'charge pump' alone, which provided a reactant-side flow rate of 0.6 L/min (~13 g/s) to give an approximate residence time of 70 seconds.

Table 5 compares measured values for total heat transfer $\dot{Q}_L$ obtained from experiment and predicted by the model with Eqs. (6.47) and (6.50). Residence time was calculated based on the volume of the reactant-side, that is, $t_{res} = \dot{m}_R / \rho_R V_R$, where V_R is the total volume of the reactant-side; each channel contributed approximately 0.072 L.

Table 5. Load-side heat rejection measured during single-phase heat transfer characterization experiments compared to model predictions

Residence Time	$T_{L,in}$ (°C)	$\dot{Q}$Experiment (W)	$\dot{Q}$ Model (W)	Error (%)
20 sec	70.1	1682	1737	-3.3
	80.2	2535	2623	-3.5
	90.2	3474	3570	-2.8
70 sec	70.1	833	643	22.8
	80.2	1272	994	21.9
	90.2	1736	1331	23.3

Good agreement was obtained for t_{res} = 20s, but degrades for t_{res} = 70s, although it is still within acceptable bounds. These results confirm that the error incurred by adopting Eq. (6.47) for the low-*Re* conditions reported by Johnson *et al.* [70] would not exceed that typical of two-phase flow correlations. Some of the disagreement at t_{res} = 70s may be attributable to experimental uncertainty; the maximum possible heat transfer, given fixed inlet temperatures and flow rates, is

$$\dot{Q}_{\max} = \left(\dot{m}c_p\right)_{\min}\left(T_{in,L} - T_{in,R}\right) \tag{6.68}$$

where the subscript *min* denotes the minimum of either $\dot{m}_R c_{p,R}$ or $\dot{m}_L c_{p,L}$, which in all cases considered in this study is the former. Evaluating $c_{P,R}$ at $T_{L,in}$ (yielding a maximum possible heat capacity ~2800 J/kg K) and computing Eq. (6.68) for the t_{res} = 70s cases tabulated in Table 5, one obtains the results in Table 6:

Table 6. Predicted maximum attainable heat transfer, per Eq. (6.68), for 70 s residence time single-phase validation experiments

$\dot{m}_R$ **(g/s)**	$T_{L,in}$ **(°C)**	$T_{R,in}$ **(°C)**	$\dot{Q}_{\max}$ **(W)**
13.3	70.1	50.5	722
13.6	80.2	50.6	1131
13.5	90.2	51.0	1530

Comparing $\dot{Q}_{\max}$ to the corresponding experimental $\dot{Q}_L$ values in Table 5, one notices that it is not possible to obtain the measured $\dot{Q}_L$ data using the reported $\dot{m}_R$ measurements. We suspect that the reactant-side flow meter may be responsible for this discrepancy, as an error of 1 or 2 g/s could amount to 100 – 200 W in calculated heat transfer at the flow rates used in the high residence time experiments. In fact, if one were to assume 100% effectiveness ($\dot{Q}_L = \dot{Q}_{\max}$) and use Eq. (6.68) to calculate $\dot{m}_R$, the following results (Table 7) are obtained:

Table 7. Load-side heat rejection measured during 70s residence time single-phase heat transfer characterization experiments compared to model predictions; $\dot{m}_R$ was estimated using Eq. (6.68) and setting experimental $\dot{Q}_L = \dot{Q}_{\max}$

$\dot{m}_R$ (g/s)	$T_{L,in}$ (°C)	$T_{R,in}$ (°C)	$\dot{Q}$ Exp. (W)	$\dot{Q}$ Model (W)	Error (%)
15.4	70.1	50.5	833	748	10.2
15.2	80.2	50.6	1272	1142	10.2
15.3	90.2	51.0	1736	1530	11.9

The nearly uniform estimation of reactant-side flow rate and subsequent improvement in model and experimental agreement gives credence to the above hypothesis.

6.2.2 Low Residence Time Validation

Low residence time tests were conducted with 12 chevron plates installed (7 reactant channels and 6 load channels) and a PG flow rate $\dot{m}_R$ of ~50 g/s, giving a residence time of approximately 10 seconds [70]. Table 8 shows the collection of steady-state low residence time test conditions reported by Johnson *et al.* [70] that serve as inlet boundary conditions for the model. For each case considered, Johnson et al used a particle size range of 40 – 60 mesh; no size distribution was reported, so it was assumed to be uniform.

Table 8. Experimental conditions for low residence time (10 second) tests reported in [70]

c_i (g/L)	$T_{L,i}$ (°C)	$T_{R,i}$ (°C)	$\dot{m}_L$ (g/s)	$\dot{m}_R$ (g/s)
22.1	80.1	52.2	116.1	52.0
31.7	80.1	52.3	114.9	50.9
49.5	80.0	51.4	114.5	48.7
48.5	80.0	50.9	129.2	53.2
45.5	80.0	51.1	116.1	47.8

The total heat rejected by the load fluid ($\dot{Q}_L$) and the total heat absorbed by the reaction ($\dot{Q}_{rxn}$) serve as the basis for validation; Figure 82 and Figure 83 compare $\dot{Q}_{rxn}$ and $\dot{Q}_L$ (respectively) reported by Johnson *et al.* [70] to the model predictions.

The model predictions for $\dot{Q}_{rxn}$ are just outside of the experimental uncertainty, but appear to follow the same trend; increasing c_i yields a monotonically increasing curve with a gradually decaying slope. This trend is consistent with Johnson *et al.*'s [70] observation of diminishing gains in $\dot{Q}_{rxn}$ even as the AC feed rate was increased. The model also appears to under-predict $\dot{Q}_L$ by about 20% on a consistent basis.

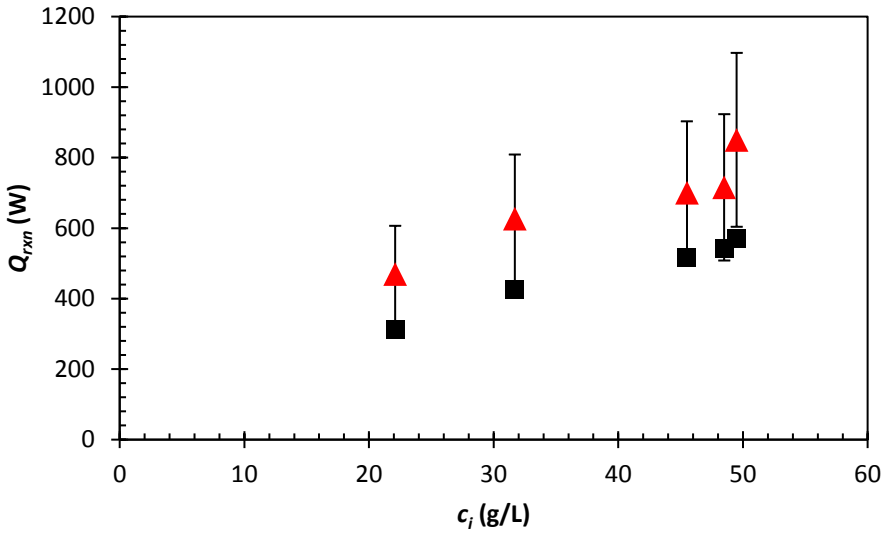

Figure 82. Heat absorbed by endothermic reaction as a function of solid AC concentration predicted by model (black squares) and from Johnson *et al.* 's 10 second residence time experiments [70] (red triangles). Particle size was between 420µm and 250µm (40-60 mesh)

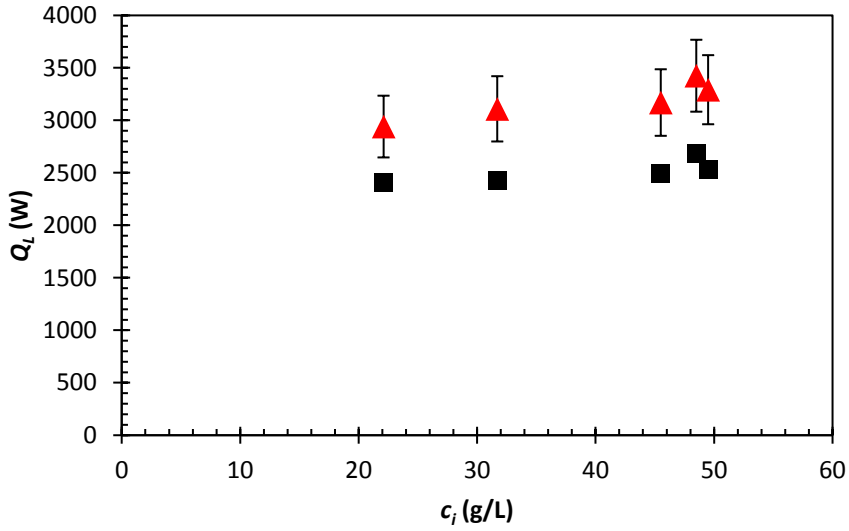

Figure 83. Load-side heat rejection as a function of solid AC concentration predicted by model (black squares) and from Johnson *et al.*'s 10 second residence time experiments [70] (red triangles). Particle size was between 420µm and 250µm (40-60 mesh)

6.2.3 High Residence Time Validation

The high residence time tests were conducted with 24 chevron plates installed (13 reactant channels and 12 load channels) and the reactant flow rate set to minimum attainable value of ~12 g/s, although it apparently varied by +/-20% between experiments [70]. Johnson *et al*. [70] used the same solid AC feed rate (~2.4 g/s) as in the low residence time tests, which increased the solids concentration an average of 5-fold. Hence, direct comparisons between high and low residence time operating conditions could only be accomplished through simulation, and will be addressed in the analysis and discussion section that follows. Table 9 tabulates the inlet temperatures, flow rates, and AC concentration inputs to the model. Note that there are two tests with different temperatures

Table 9. Experimental conditions for high residence time (70 second) tests reported in [70]

c_i(g/L)	$T_{L,i}$(°C)	$T_{R,i}$(°C)	$\dot{m}_L$(g/s)	$\dot{m}_R$(g/s)
188	70.0	47.6	111.1	13.8
84.8	80.3	50.4	112.1	15.3
169	79.9	48.2	112.9	11.6
211	80.2	47.1	112.1	11.4
221	90.0	42.6	112.7	11.0

Figure 84 and Figure 85 compare experimental measurement of $\dot{Q}_{rxn}$ and $\dot{Q}_L$, respectively, corresponding to the conditions in Table 9.

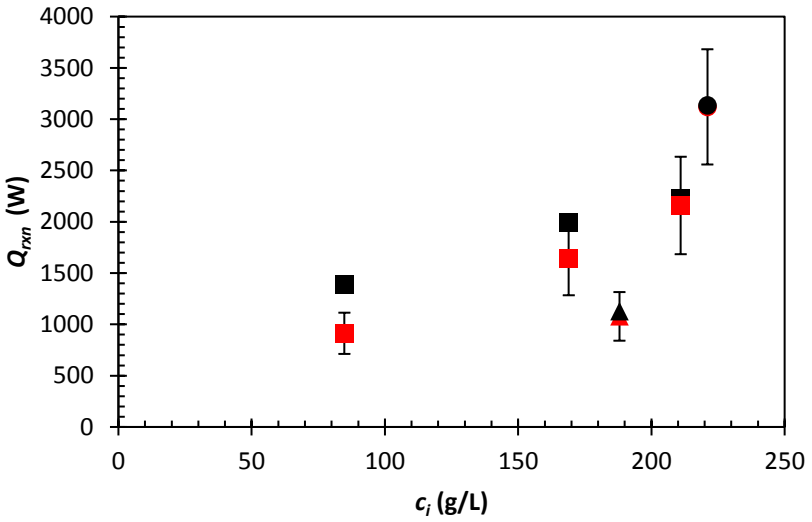

Figure 84. Heat absorbed by endothermic reaction as a function of solid AC concentration predicted by model (black) and from Johnson *et al.*'s 70 second residence time experiments [70] (red); load-side inlet temperature was 70°C (triangle), 80°C (square), and 90°C (circle); particle size was between 420µm and 250µm (40-60 mesh)

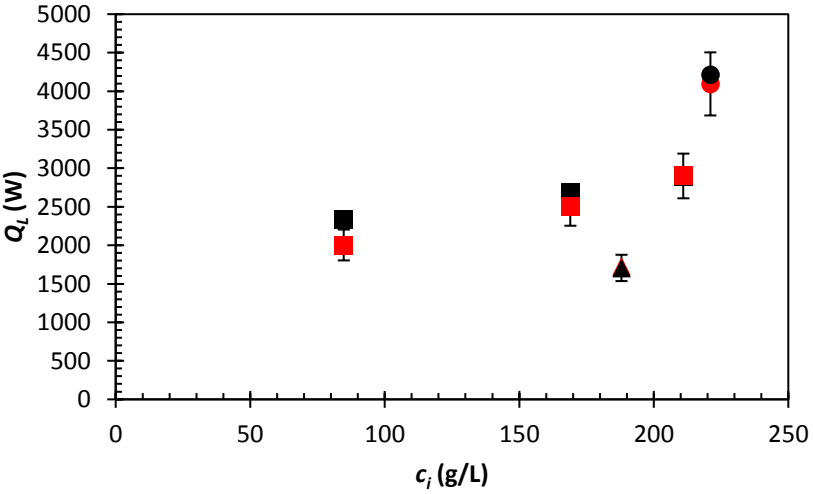

Figure 85. Load-side heat rejection as a function of solid AC concentration predicted by model (black) and from Johnson *et al.*'s 70 second residence time experiments [70] (red); load-side inlet temperature was 70°C (triangle), 80°C (square), and 90°C (circle); particle size was between 420µm and 250µm (40-60 mesh)

Measurements and predictions for $\dot{Q}_{rxn}$ agree within experimental uncertainty, with the single exception of the case c_i = 80 g/L. The model tends to over-predict $\dot{Q}_L$ at lower concentrations, but accuracy is improved immensely as the concentration increases.

Since it is appropriate to assume negligible frictional pressure drop for these tests, the void fraction was estimated using Eq. (6.54) and the inlet and outlet static pressure measurements [70]. Figure 86 shows a comparison of model-predicted average void fraction and that estimated from Johnson *et al.*'s high residence time data [70]:

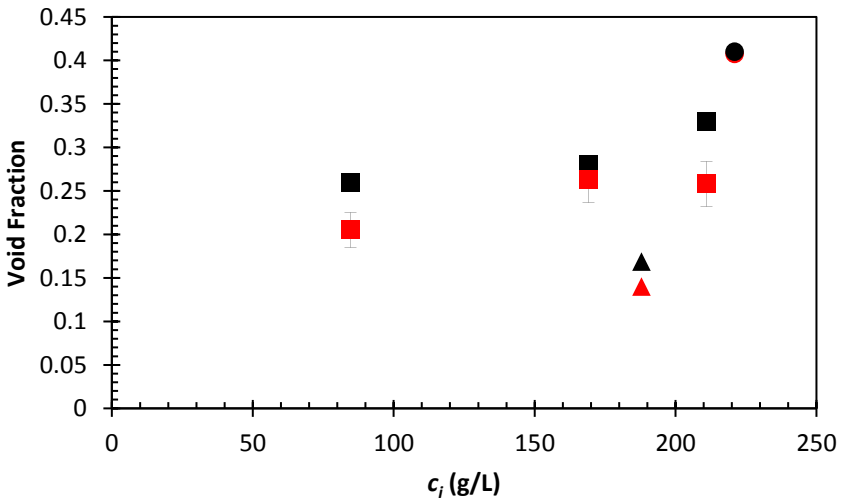

Figure 86. Estimated average void fraction as a function of solid AC concentration predicted by model (black) and from Johnson *et al.*'s 70 second residence time experiments [70] (red); load-side inlet temperature was 70°C (triangle), 80°C (square), and 90°C (circle); particle size was between 420µm and 250µm (40-60 mesh)

Agreement with experimental void fraction estimates was obtained by setting the leading coefficient C^* in Eq. (6.43) to 0.1 1/s; no further refinement was deemed necessary.

6.2.4 Discussion

6.2.4.1 Low Residence Time

Comparison with Johnson *et al.*'s [70] $\dot{Q}_{rxn}$ and $\dot{Q}_L$ measurements show consistent under-prediction in the low residence time case, and thus warrants further examination. Thankfully, the favorable comparison between [Johnson et al] and the model's predictions for the high residence time $\dot{Q}_{rxn}$ provides confidence that inaccuracy in rate coefficients and/or heats of reaction are not responsible. Instead, the reason for underestimating the total heat transfer capacity is most likely embodied in the reactant-side heat transfer coefficient, h_R. For the low residence time simulations, the axial concentration profiles suggest that this is due to underestimation of the reactant-side heat transfer coefficient in the LS zone, which occupies the majority of the reactant channel. Figure 87 shows a dual plot of dimensionless solid-phase mass concentration and gas-phase mass flux along the non-dimensional axial coordinate for c_i = 22, 32, and 50 g/L.

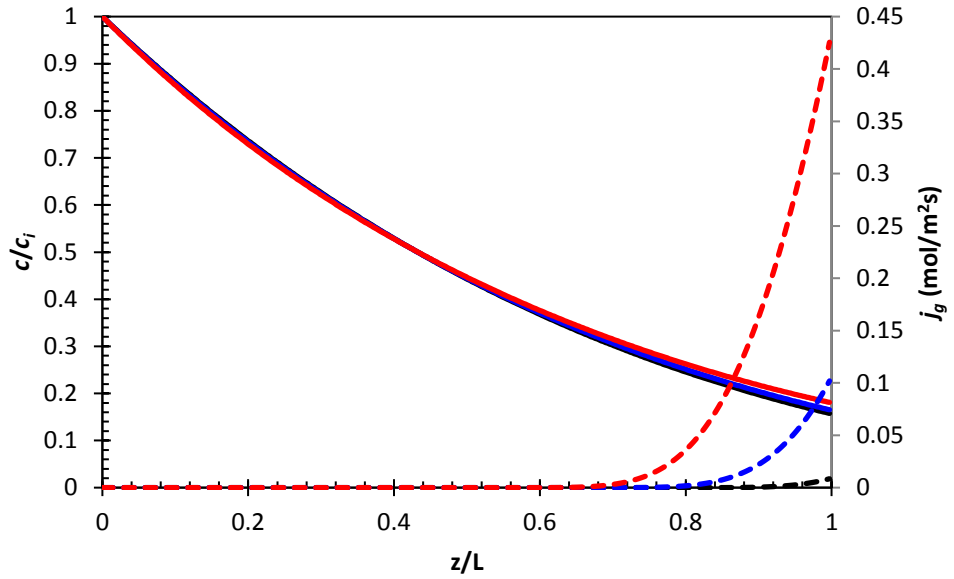

Figure 87. Axial gas-phase mass flux (j_g – dashed line) and dimensionless solid-phase concentration (c/c_i – solid line) simulated for different 10 second residence time tests: c_i = 22 (black), 32 (blue), and 50 (red) g/L.

The LS-zone is comprised of the region where the gas-phase mass flux is zero (dissolved CO_2 is below saturation) while the dimensionless solid-phase concentration c / c_i is greater than zero. The transition to the LSG-zone occurs where the j_g curves depart abruptly from the horizontal axis as the liquid-phase becomes saturated with CO_2. As one would expect, the LS-to-LSG transition occurs further upstream as the inlet solid AC concentration is increased, causing the CO_2 saturation limit to occur sooner. It is clear from Figure 87 that, at most, bubble release occurs in only 20% of the channel, and therefore the overall volume-averaged heat transfer coefficient would be governed by the single-phase correlation. It was pointed out in the preceding discussion that Charunyakorn *et al*. [94], Sohn and Chen [96, 97], and several other investigators [95,

98]] have documented increases in the effective heat transfer coefficient when small solid particles are present. Thus, it is certainly plausible that there is an enhancement to h_R in the LS-zone, or when the gas-phase mass flux is small in the LSG-zone.

One additional possibility is that experimental non-idealities inherent in Johnson *et al.*'s HEX reactor facility were sufficient to affect the reactant-side heat transfer coefficient, namely:

1) The PG and AC are mixed into a slurry *outside* of the reactor, and so in cases of high residence time, there could be several seconds prior to entry into the reactor in which the AC could react, and thus render the inlet condition inaccurate. This would result in non-zero inlet conditions for x_c, x_a, and x_{AC}, and therefore an expedited transition from LS to LSG/LG zones, increasing the reactant-side heat transfer coefficient
2) Air entrainment into the mixing pump could have introduced LSG-type flow at the reactor inlet, which could potentially enhance the reactant-side heat transfer coefficient as well – this would be highly dependent on the operating conditions of the charge pump, and thus would be extremely difficult to accurately compensate for in the model
3) The mixing pump could have pulverized the larger particles, which would decrease the effective mesh size and thus enhance the heterogeneous and dissolution reaction mechanisms. This appears unlikely since it would impact $\dot{Q}_{rxn}$ more than

$\dot{Q}_L$, both of which have approximately the same consistent level of disagreement with [70].

It is not possible with the available information to confirm or dismiss experimental non-idealities (except perhaps for (3)) as either the sole or contributing source of the discrepancy between measured and predicted total heat transfer. We can be certain that there is merit to (1) simply by noting the decrease in reactant-side inlet temperature with increasing c_i, which could be explained by endothermic reaction occurring prior to entering the reactor.

6.2.4.2 High Residence Time

Adjustments to the correlations/fitted parameters were necessary to achieve the agreement with the high residence time data reported in the literature [70], the justification for which is presented here. For consistency, these same adjustments were applied to obtain the results analyzed in section 6.2.4.1. Per the discussion in Section 6.1.2.1, the leading coefficient C^* of Eq. (6.43) served as an approximate fitting parameter to attain the forgoing predictions for $\dot{Q}_L$, $\dot{Q}_{rxn}$, and the average void fraction $\bar{b}$. Uncertainty as to the temperature dependence of $x_{AC,sat}$ led to its re-casting as a fixed parameter representing an effective "average" value. This approach affords an additional degree of freedom for reconciling the model and experiment, and was found to provide acceptable agreement over all concentrations and residence times considered. Given the limited breadth of experimental results available, the objective was not to find optimal

fits for all conceivably adjustable parameters; rather, the intent was to demonstrate that even with rough estimates for a minimal number of parameters, satisfactory agreement with experiment such as that presented in Sections 6.2.2 and 6.2.3 could be achieved. To guide the adjustments, a high residence time 'test case' was selected for comparison with the model predictions, namely: c_i = 211 g/L and $T_{L,in}$ = 80°C.

Figure 88 shows the gas-phase mass flux and dimensionless solid-phase ratio c/ci as a function of dimensionless axial position for three exemplary high residence time simulations (ci = 85, 169, and 211 g/L and $T_{L,i}$ = 80°C). In contrast to the low residence time tests, approximately 80% of the channel length is comprised of either LSG or LG (in the case of ci = 85 g/L, after z/L = 0.58) zones, which implies that the overall heat transfer coefficient is dominated by Eq. (6.50).

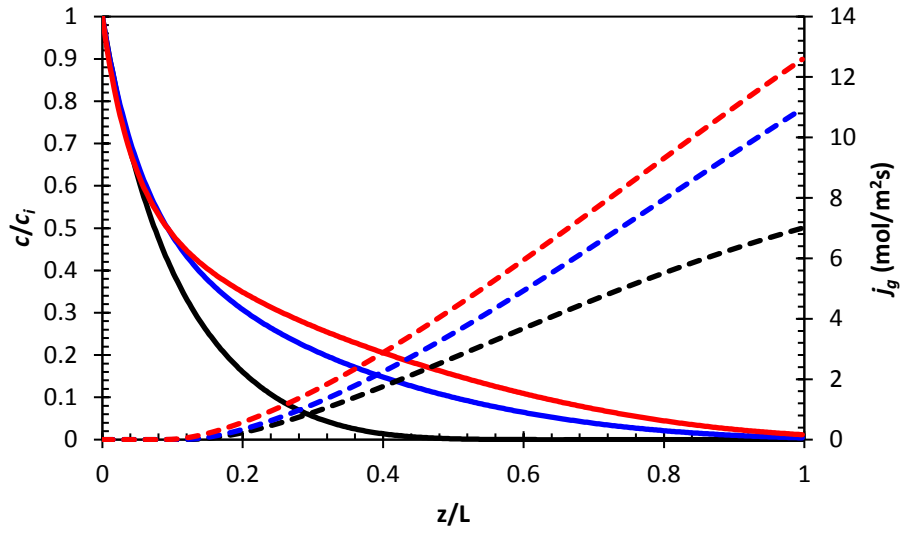

Figure 88. Axial gas-phase mass flux (j_g – dashed line) and dimensionless solid-phase concentration (c/c_i – solid line) simulated for different 70 second residence time tests: c_i = 85 (black), 169 (blue), and 211 (red) g/L.

Thus, Figure 88 demonstrates that the agreement shown in Figure 84 and Figure 85 was strongly dependent on F_{TP}, which is in turn dependent on the sum total of liberated CO_2. Accordingly, any combination of parameters affecting the reaction steps prior to desorption could potentially be adjusted to improve agreement with the experimental results. In the interest of minimizing the number of adjustable parameters, we focused on parameters estimated in the batch reactor study that had a greater degree of uncertainty due to being dependent on hydrodynamic conditions (i.e., k_{het} and k_{dis}), or could not be fitted in a such a way that extrapolations to higher temperature could be reliably made (i.e., $x_{AC,sat}$). In particular, the solid-phase mass transfer coefficients k_{het} and k_{dis} were not well established for the HEX reactor, and were therefore explored as possible fitting parameters. On the basis of the results in Figure 88, one can infer that the mass k_{het} and k_{dis} would have comparatively little impact on the time necessary for the

solid-phase to deplete, and thus minimal impact on F_{TP}. This is evidenced by the fact that c_i / c follows an approximately linear trend over the majority of the channel length for c_i = 169 g/L and 211 g/L. A parametric sensitivity analysis with respect to both k_{het} and k_{dis} on the model predictions for the c_i = 211 g/L experiment was conducted to provide confirmation. The results of this analysis represented in terms of percent change in predicted Q_L or Q_{rxn} as a function of multiples of k_{dis} and k_{het} are plotted, respectively, in Figure 89 and Figure 90. There is virtually no change (<0.2%) in predicted $\dot{Q}_L$ or $\dot{Q}_{rxn}$ despite order-of-magnitude perturbations in k_{het}, indicating dissolution of AC is the dominant solid-phase mechanism. However, the only appreciable change that could be affected by perturbing k_{dis} was a reduction in $\dot{Q}_L$ or $\dot{Q}_{rxn}$, which would amount to only about -15% when k_{dis} is reduced by a factor of 0.1. This vindicates the decision to only treat k_{het} and k_{dis} with rough approximations.

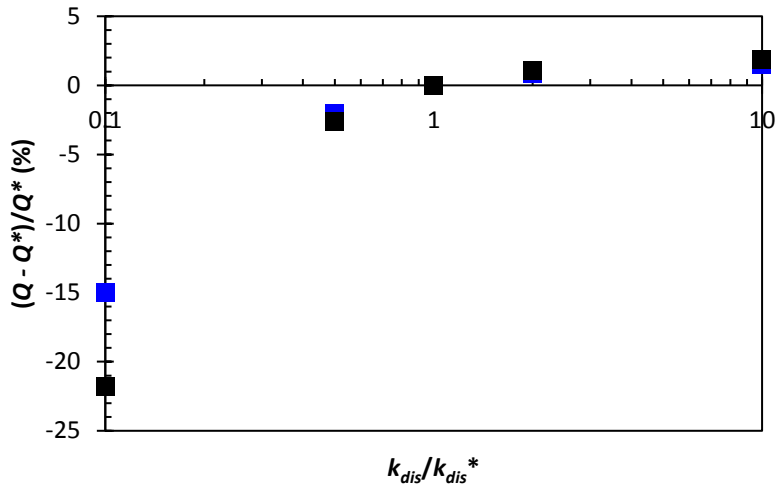

Figure 89. Sensitivity of predicted Q_L (black) and Q_{rxn} (blue) as a function k_{dis} . k_{dis}* is the nominal value of k_{dis} for the experiment c_i = 211 g/L, t_{res} = 70 s; Q* is the model-predicted value of Q_L or Q_{rxn} corresponding to k_{dis}*.

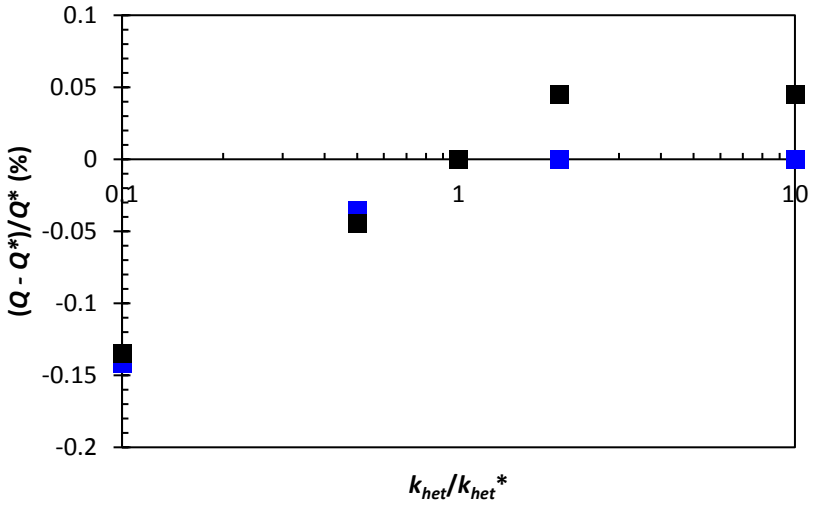

Figure 90. Sensitivity of predicted Q_L (black) and Q_{rxn} (blue) as a function k_{het} . k_{het}* is the nominal value of k_{het} for the experiment c_i = 211 g/L, t_{res} = 70 s; Q* is the model-predicted value of Q_L or Q_{rxn} corresponding to k_{het}*.

The only other estimated parameter that did not follow a predictable pattern (which could be safely extrapolated to higher temperatures) was the solubility of AC in PG, $x_{AC,sat}$. Thus, to avoid the possibility of spurious results at operating temperatures above 70°C, $x_{AC,sat}$ was held constant and its value adjusted until satisfactory agreement with the test case (c_i = 211 g/L, t_{res} = 70 s) was attained. As the validation results in the prior sections indicate, this approximation gives very good accuracy at high residence time and high concentration operating conditions over several different load-side temperatures and fair agreement at lower concentration and/or low residence times. Through trial-and-error, a value of $x_{AC,sat}$ = 0.14 was chosen because it matched $\dot{Q}_{rxn}$ at high c_i and t_{res} (where the HEX reactor would realistically operate for thermal management [70]), while also predicting $\dot{Q}_L$ within experimental error margins.

Average void fractions calculated with C^* set to 0.1 s^{-1} showed consistency with estimates derived from the experimental data at three different load temperatures and solid AC concentrations. Incidentally, it was found that void fraction predictions – as well as heat transfer and heat absorption – became insensitive to further adjustments in C^* beyond 0.1 s^{-1}. A plot of average void fraction calculations for assumed values of C^* is shown in Figure 91:

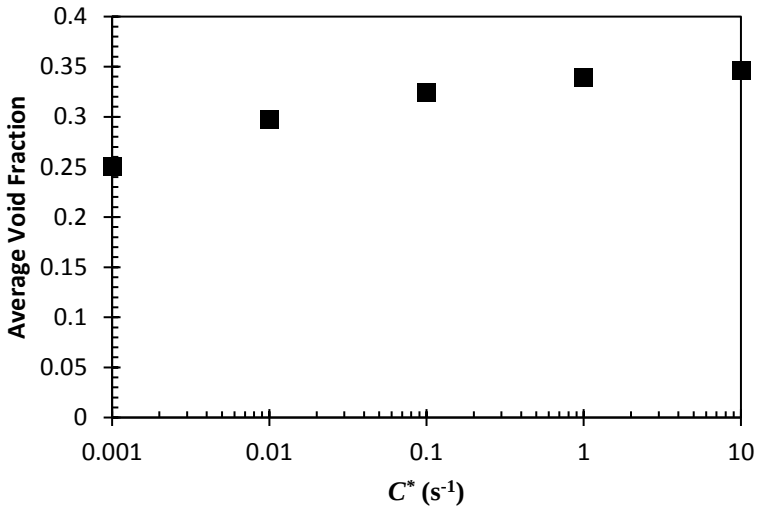

Figure 91. Average void fraction predicted by model for the 70 second residence time case as a function of assumed C^* in Eq. (6.43); c_i = 169 g/L and $T_{L,in}$ = 80°C.

After reaching saturation, the dissolved CO_2 concentration profile traces $x_{c,sat}(z)$ In the limit of large C^*, as depicted in Figure 92. The liquid-phase's "capacity" for supersaturation asymptotically tends to zero, and as such, the amount of dissolved CO_2 available to potentially affect the void fraction is vanishingly small. This also implies that CO_2 retention has only a minor effect on the kinetics; the released CO_2 influences the reaction by physical means viz. convective heat transfer enhancement.

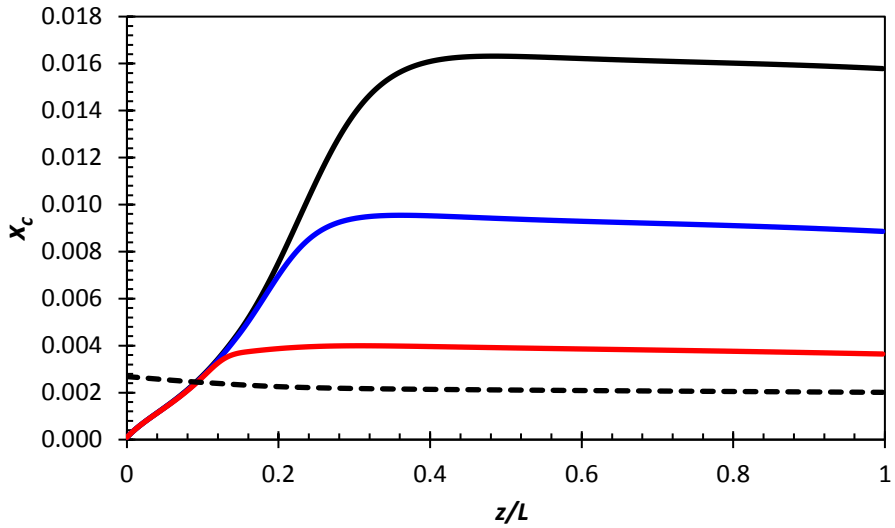

Figure 92. x_c as a function of z/L for assumed values of C^* in Eq. (6.43): 0.001 1/s (black), 0.1 1/s (blue) and 1.0 1/s (red); the dashed black line indicates local $x_{c,sat}$. All other simulation conditions were for a 70 second residence time test with c_i = 169 g/L and $T_{L,in}$ = 80°C.

A favorable comparison to data in the literature for a chevron PHE HEX reactor for two vastly different operating conditions and wide temperature ranges has demonstrated the model, along with the parameters and correlations selected, provides reasonably accurate prediction for both total heat transfer and heat absorption by AC decomposition.

6.2.4.3 Axial Heat Flux/Absorption Profiles

It has been shown previously [26] that there exists a tradeoff between total heat transfer rate/capacity and the fraction of that heat which can be rejected to decomposing AC, which, for a fixed temperature and AC mass flow rate, is related to both the residence time and concentration. Therefore, there are effectively two characteristic

operating regimes: one where convective heat transfer dominates the total heat transfer rate, and another where the reaction and convective heat transfer are of comparable importance.

Johnson *et al.* [70] showed that, based on their experimental results, residence times in excess of one minute were needed to sink at least 50% of the total heat load to AC, if the load temperature remained fixed. The model developed in this study corroborates this claim, and offers an explanation as to why this is the case.

Figure 93 shows local per-unit-channel length heat flux endothermic heat absorption for a low residence time experiment with an AC concentration of 50 g/L, a load-side inlet temperature of 80°C and reactant-side inlet temperature of 50°C compared to its baseline single-phase prediction (i.e., without any chemical reaction).

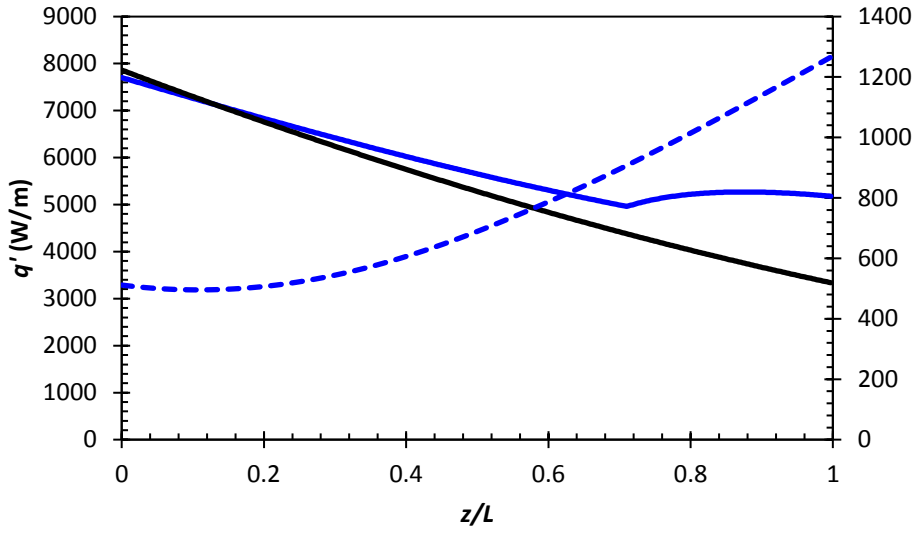

Figure 93. Local heat flux per-unit-length-per-channel for c_i = 50 g/L, $T_{L,in}$ = 80°C, $T_{R,in}$ = 50°C, t_{res} = 10 s; contribution of load-side rejection (blue solid line) and reaction (blue dashed line) compared to load-side rejection of single-phase case with identical inlet conditions (solid black line)

The single-phase case actually enters the channel with a higher heat flux than the decomposition case due to the higher exit temperature of the load fluid (and thus greater local ΔT), which would normally be expected of a counter-flow heat exchanger such as this. Most prominently, there is a sudden change in the slope of q' at z/L = 0.7; the reason for this becomes clear upon examination of Figure 87, which shows that the liquid-phase becomes supersaturated with CO_2 at this point. This causes an increase in the overall reaction rate, as can be seen from the dotted line in Figure 93, but it also causes a rapid rise in h_R as CO_2 gas is liberated. Hence, there is both an enhancement in convection and the reaction rate. The rise in the reaction rate alone appears to be only a small contributor to the sudden and dramatic rise in heat flux as the slurry enters the LSG-zone, indicating that the convection enhancement from the reaction becomes the

dominant contributor to increase in total heat transfer. A plot of q'_{rxn} / q'_L as depicted in Figure 94 demonstrates that the reaction only contributes at most to 20% of the total heat flux:

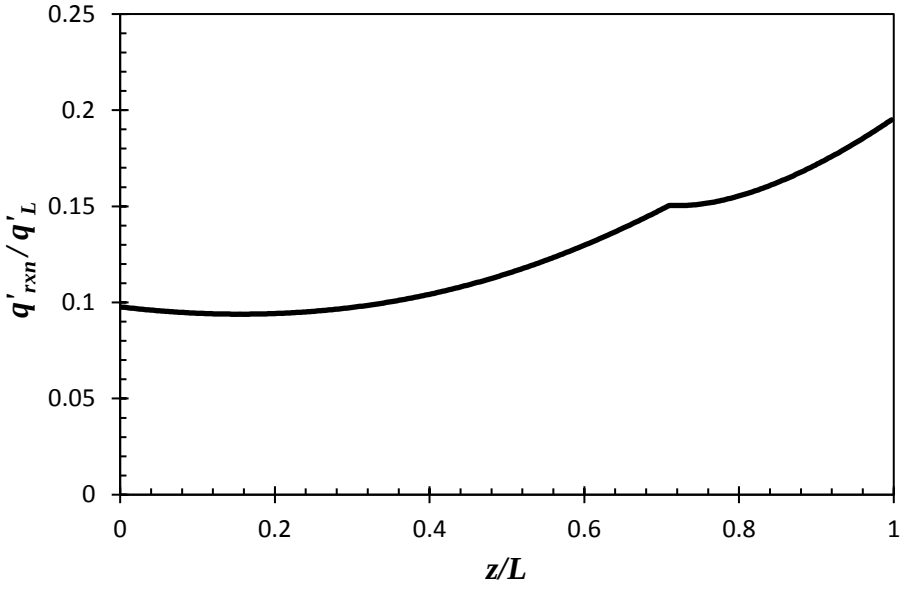

Figure 94. Local fraction of heat absorbed by reaction to heat rejected by load-side for c_i = 50 g/L, $T_{L,in}$ = 80°C, $T_{R,in}$ = 50°C, t_{res} = 10 s

Perhaps the most curious aspect of the curve in Figure 94 is the bicuspid shape assumed where the LSG-transition occurs. We note that in Figure 94 the reaction rate appears almost constant for nearly a quarter of the channel length prior to $z/L = 0.7$, while the total heat flux continues to decrease. The result of this initial trend is that the reaction is apportioned a slightly increasing share of the total heat flux up until CO_2 saturation is reached. Following this point, the enhancement in convection again causes

q'_{rxn} / q'_L to decrease briefly before finally resuming a steady rise for the remainder of the channel as the increasing reactant temperature accelerates the homogeneous reaction. The simulation results for this test case show that even when relatively low amounts of latent heat are utilized, the reaction actually provides a sizeable increase in total heat transfer simply by gas generation.

It is also of interest to identify the presence and spatial distribution of reaction regimes identified in Chapter IV (Irreversible and mass transfer-limited). Notably, unlike with the batch reactor, the homogeneous reaction is a significant contributor even in low residence times. The local rate of heat absorption due to heterogeneous decomposition, dissolution, and homogeneous decomposition mechanisms are plotted in Figure 95.

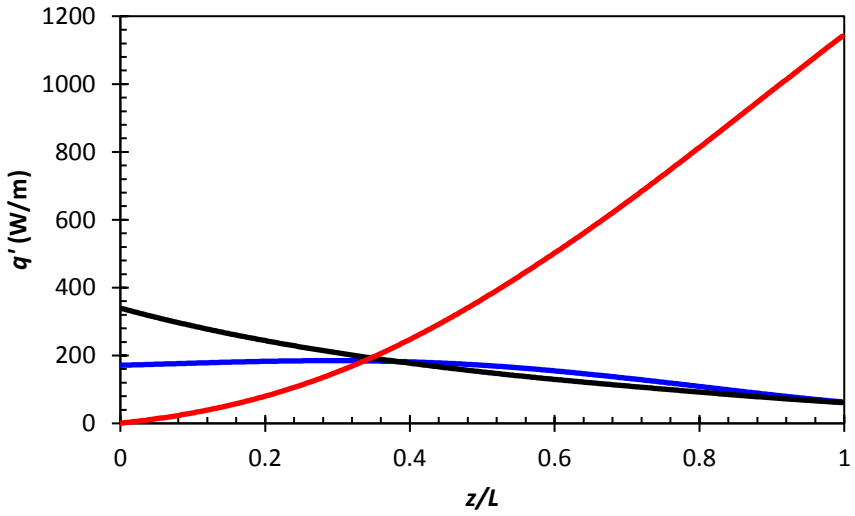

Figure 95. Local heat flux per-unit-length per channel due to dissolution (black), heterogeneous decomposition (blue) and homogeneous decomposition (red) for c_i = 50 g/L, $T_{L,in}$ = 80°C, $T_{R,in}$ = 50°C, t_{res} = 10 s.

Qualitative similarities between the HEX reactor and batch reactor are present, particularly with respect to curve shapes. The key distinguishing features lie in the changing reactant temperature along the channel length and the persistence of NH_3 saturated bubbles, which in the batch reactor are vented immediately.

For the purpose of comparison, the nearest 'equivalent' batch reactor case had an identical concentration of 50 g/L, a particle size range of 40-50 mesh and a reaction temperature of 70°C (which is approximately the average reactant-side temperature). Comparing Figure 75 to Figure 95 above, the homogeneous reaction reaches its peak in the batch reactor after about 25 seconds (corresponding approximately to $z/L = 1.25$), which was well before the heterogeneous reaction and dissolution curves had abated substantially; in the HEX reactor, the heterogeneous and dissolution mechanisms comprise only a small fraction of the total heat absorption by the time the homogeneous reaction has become significant. In addition, the heterogeneous reaction was responsible for nearly twice the heat absorption rate due to dissolution in the batch reactor, whereas in the HEX reactor these roles appear to be reversed. The axial temperature profile, plotted in Figure 96, shows the reason this change in pattern:

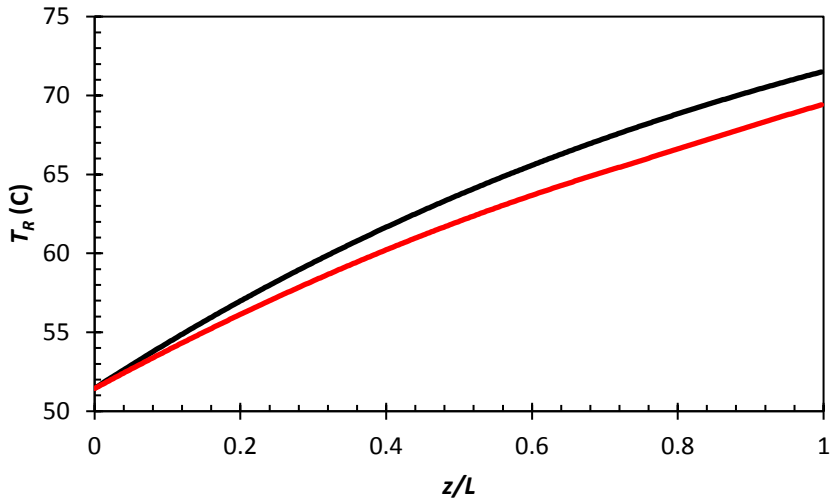

Figure 96. Local reactant-side temperature for c_i = 50 g/L, $T_{L,in}$ = 80°C, $T_{R,in}$ = 50°C, t_{res} = 10 s (red) and corresponding single-phase case (black)

The dissolution process is approximated as temperature independent over the range of temperatures considered; the temperature dependence of K_{het}, on the other hand, means that upon entering the reactor at 51°C the heterogeneous reaction is slow. Due to the gradual rise in temperature that can be seen in Figure 96, the dissolution mechanism depletes most of the solid-phase before a significant reaction temperature is attained. Thus, in the case considered here, the primary pathway is the dissolution → homogeneous reaction → desorption pathway. The preference for the dissolution pathway gives homogeneous reaction rates higher than those obtained in the batch reactor for the same concentration, but at the expense of a slow rise time. It may be said that a secondary effect of the slow rise in temperature is the delay in attaining the peak homogeneous reaction rate such that it did not occur within the length of the channel. In effect, the rate of heat transfer relative to the reactant fluid residence time dictated the

overall time constant of the reaction, which resulted in the poor conversions reported by Johnson *et al*. [70].

The operating regime in which convection and reaction phenomena are of comparable magnitude represents the 'best-yield/efficiency' performance that Johnson *et al*. [70] endeavored to achieve with their HEX reactor design. The two factors promoting this operating condition are concentration and residence time, both of which were quite high in the high residence time series of experiments [70]. For further examination, we consider the case c_i = 211 g/L, t_{res} = 70 s, $T_{L,in}$ = 80°C; this experiment used the same AC mass flow rate (2.5 g/s) as the low residence time experiment shown in Figure 97, but with nearly a four-fold increase in concentration due to the lower PG flow rate. Calculated local heat flux and heat absorption per-unit-length are compared against the single-phase baseline for the aforesaid experiment in Figure 97:

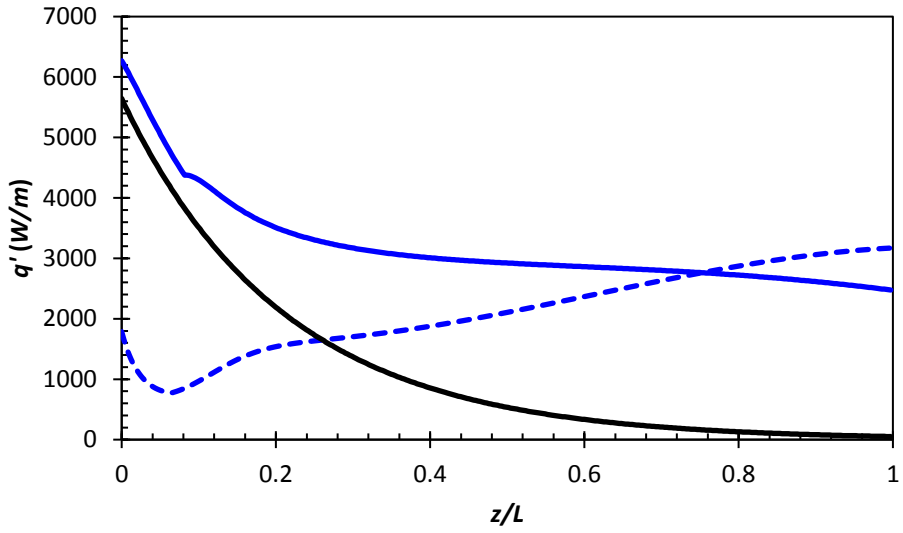

Figure 97. Local load-side heat flux per-unit-length per channel due to dissolution (solid blue: with reaction, solid black: single-phase baseline) and heat absorption by reaction (dashed blue) for c_i = 211 g/L, $T_{L,in}$ = 80°C, $T_{R,in}$ = 50°C, t_{res} = 70 s

Similar to the low residence time heat flux profile in Figure 93, there is an abrupt change in the q'_L slope corresponding to the axial position at which CO_2 saturation is first reached. Unlike the previous case, q'_{rxn} grows at a more rapid clip than the low residence time counterpart, and the decrease in q'_L appears to cease and slowly rise after the transition to the LSG-zone occurs before gradually declining again near the channel outlet. Indeed, the heat flux profile resembles in many respects that which might be produced by refrigerant condensation [80]. A plot of q'_{rxn} / q'_L is shown in Figure 98:

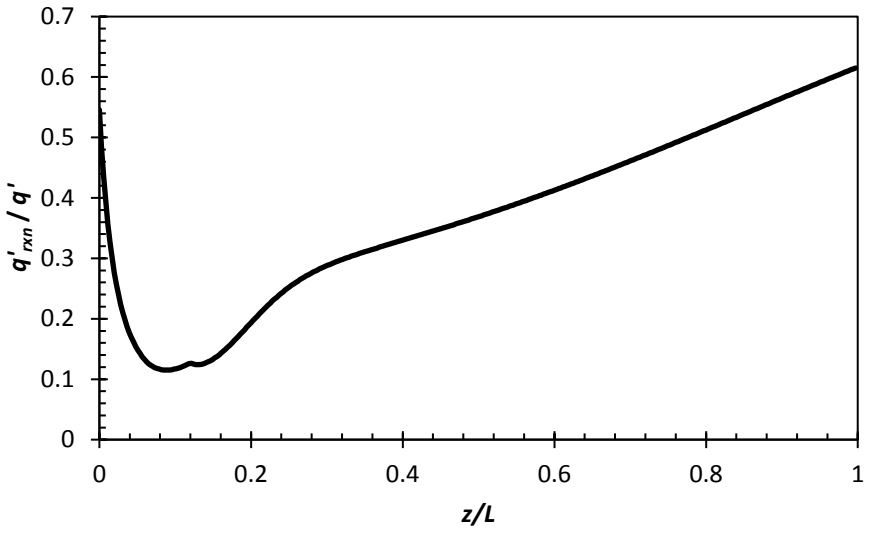

Figure 98. Local fraction of heat absorbed by reaction to heat rejected by load-side for c_i = 211 g/L, $T_{L,in}$ = 80°C, $T_{R,in}$ = 50°C, t_{res} = 70 s

The sudden drop in q'_{rxn} / q'_L is due to the rapid reaction and dissolution of smaller particles. Comparing Figure 98 to Figure 94, there is a far greater fraction of the total heat transfer consumed by the reaction compared to the low residence time scenario at the same AC feed rate. As will be discussed in section 6.3, the increase in conversion over the low residence time counterpart is due in large part to the extended residence time, which permits the homogeneous reaction to develop completely and reach its peak value within the reactant channel.

Despite the significantly higher residence time and concentration, the heat absorption rates of the heterogeneous decomposition, dissolution, and homogeneous decomposition mechanisms follow very similar trends to the low residence time counterparts in Figure 95. These local heat absorption rates are plotted as a function of dimensionless axial coordinate *z/L* in Figure 99

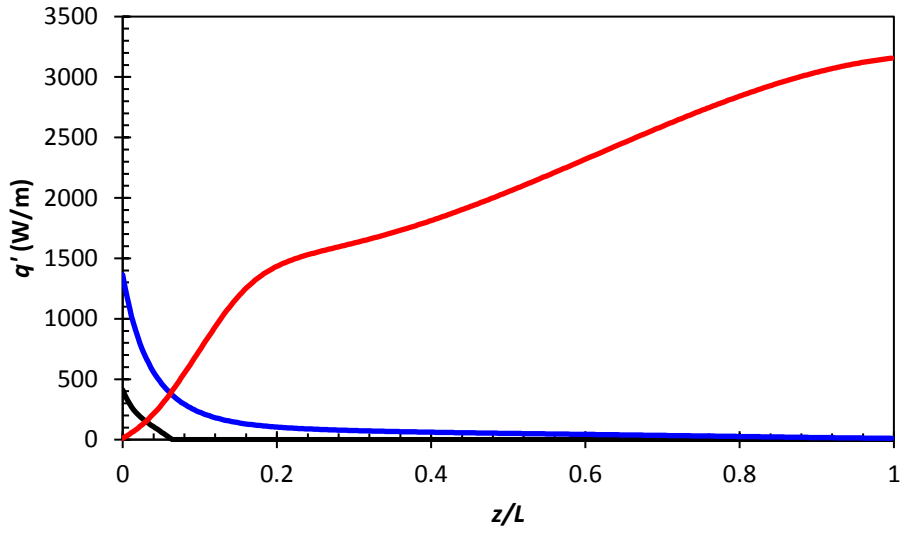

Figure 99. Local heat flux per-unit-length per channel due to dissolution (blue), heterogeneous decomposition (black) and homogeneous decomposition (red) for c_i = 211 g/L, $T_{L,in}$ = 80°C, $T_{R,in}$ = 50°C, t_{res} = 70 s

One notices in Figure 99 that again the homogeneous reaction suffers a slow rise time and just barely reaches its peak within the channel. The homogeneous reaction is responsible for the majority of heat absorption. There is a significant increase in the peak dissolution rate at x/L = 0, but only a slight rise in the heterogeneous reaction rate as the reactant-side inlet temperature is still low. Therefore, as in the low residence time experiment, the comparatively slow dissolution → homogeneous reaction → desorption route is the dominant pathway.

On a side note, the heterogeneous reaction actually terminates at the point where $(2P_{eq}/3RT)/K_{het} \pounds x_a$, at which point $\dot{r}_{het}$ was assumed to be zero. This assumption was derived from the stipulation that the solid-phase would not spontaneously reform within the liquid-phase (indeed, such an event was never observed in this work, nor was it

reported by Schmidt [10], even at very high concentrations). The possibility of a liquid-to-solid reverse reaction is also unlikely because it would be highly exothermic, and none of the experimental data in Johnson *et al*. [70] gave evidence of such. However, the concentration of 211 g/L is far greater than the maximum concentration that could be characterized in the batch reactor experiments, and thus it is possible that the relative contribution of the heterogeneous reaction is being underestimated.

The axial temperature profile in Figure 100 reveals a situation where there is initially a sharp rise in temperature, followed by a gradual rise as the reaction accelerates:

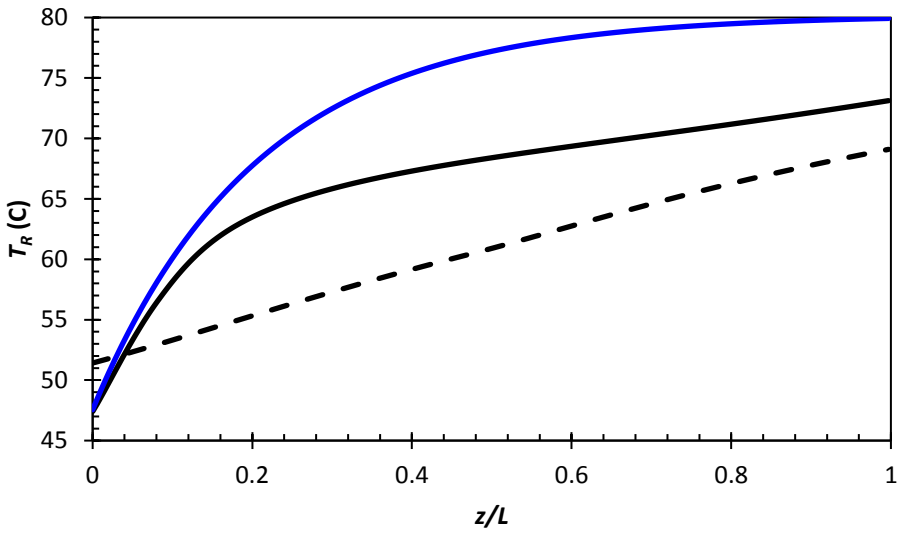

Figure 100. Local reactant-side temperature for c_i = 211 g/L, $T_{L,in}$ = 80°C, $T_{R,in}$ = 50°C, t_{res} = 70 s (solid black) and corresponding single-phase case (solid blue) compared to the case c_i = 50 g/L, $T_{L,in}$ = 80°C, $T_{R,in}$ = 50°C, t_{res} = 10 s (dashed black)

For comparison, the single-phase baseline for $T_{L,in}$ = 80°C and t_{res} = 70 seconds was also plotted in Figure 100; it is clear that the rates of heat absorption by endothermic reaction and dissolution are at least comparable to heat delivered to the reactant fluid by convection, hence the noticeably more gradual rise in temperature along the reactant channel. Despite the generally higher temperatures compared to the low residence time case, which was also plotted in Figure 100 for comparison, the heterogeneous decomposition and dissolution mechanisms occur within a region where the temperature is below 60°C, and so the dissolution pathway is still preferred. However, the solid-phase is almost completely depleted (less than 10% of the total reaction rate) by z/L = 0.2, as compared to z/L = 0.6 in the low residence time case; this implies a greater effective channel length available for the homogeneous reaction to occur, which mitigates the impact on conversion of the "slower" reaction pathway taking precedent.

The homogeneous reaction occurs predominantly where the temperature profile has become almost linear and flat-- its slope is actually lower than the low residence time temperature profile. As this segment of channel corresponds to when the homogeneous reaction is consuming an increasing share of the total thermal load, the immediate conclusion is that the reaction is limiting temperature rise. This represents a peculiar situation where the reaction is essentially self-limiting, since the delayed temperature rise ultimately results in incomplete conversion and thus wasted cooling potential. Such a scenario was predicted by Niedbalski *et al.* [26] in instances where the latent heat capacity, which is directly proportional to inlet concentration, far exceeds the heat transfer capacity of the reactor. While this particular set of operating conditions (

$T_{L,in}$ = 80°C, t_{res} = 70 s, c_i = 211 g/L) offers improved conversion over the low residence time case at the same operating temperature and AC feed rate, it does not yield the *optimal* usage of the AC's latent heat capacity.

6.3 Parametric Analysis

Utilizing the lessons gained via comparison to the data of Johnson *et al.* [70], this section shall demonstrate the model's application to exploring the operating parameter spaces for a fixed HEX reactor design – the Alpha Laval MF3 chevron PHE used in [70] is used as a representative test case, assuming a counter-flow arrangement with vertical upward flow on the reactant side to facilitate gas escape. The objective of this analysis is to explore the relationship between HEX reactor operating conditions and thermal performance metrics. In most cases, the performance metrics of interest are competing, inviting the adoption of an objective function to describe the shifting balance between said competing metrics as the operating conditions are varied.

The analysis of Section 6.2.4.3 has shown that the mixed reaction/convection-dominated regime is generally conducive to higher conversions compared to the convection-dominated regime. While we have established this as a rule-of-thumb for AC HEX reactor design, the tradeoff between total capacity $\dot{Q}_L$ and conversion $\eta = \dot{Q}_{rxn} / \dot{m}_{AC} \Delta H$ means that for any fixed HEX reactor design (length, number of plates, plate geometry, etc.) there exists a 'best-value' compromise between these two performance metrics. Subsections 6.3.1 – 6.3.5 shall analyze the trends in capacity and

conversion with respect to the following operating conditions and constraints thereto (Table 10):

Table 10. Range of conditions considered for parametric study

Parameter	Symbol	Min	Max
Reactant-side Inlet Temp.	$T_{R,in}$	45	90
Load-side inlet Temp.	$T_{L,in}$	90	90
Concentration	c_i	20	200
Particle size	r_i	60 mesh	40 mesh
Residence time	t_{res}	20 s	70 s

One additional metric that will be tracked is the ratio of heat absorbed by reaction to that transferred by convection, which we define as $\varepsilon \equiv \dot{Q}_{rxn} / \dot{Q}_L$ and refer to as "balance". This quantity is especially useful in determining if the reactor is in a heat transfer limited state. Ideally, ε would be as close to unity as possible – values over unity indicate that the heat absorbed by the reaction exceeds the HEX reactor's heat transfer capacity and thus cooling potential is wasted, whereas values below unity indicate that it is possible to sink a greater portion of the HEX reactor's capacity to the AC.

6.3.1 Load-Side Inlet Temperature

As Johnson *et al.*'s [70] experiments have shown, higher load-side temperatures give improvements in the three performance metrics. The practical limitation, in this case, was that the maximum safe operating temperature was 90°C to prevent boiling or possible overtemp conditions on the inline heater. Further, it may be argued that a limit

on load-side temperature is also necessary to prevent decomposition of AC into urea and water [102]; the presence of water would increase the solubility of NH_3, and therefore reduce the attainable endothermic cooling. The consideration of the system-level costs of high load-side temperatures – in particular, the energy and control requirements for lifting a low-quality thermal load at ~30°C to various load-side temperature – cannot be captured in the present analysis. Therefore, we shall fix the load-side inlet temperature at Johnson *et al.*'s upper limit of 90°C.

6.3.2 Reactant-Side Inlet Temperature

In both low and high residence time cases, the dissolution pathway was the preferred route. This suggests that some benefit may be gained by increasing the reactant-side inlet temperature so as to render the heterogeneous decomposition → desorption pathway dominant, which would lower the effective time constant of the reaction and thence increase conversion for a given load temperature and AC concentration. Practically, accomplishing this condition would present an additional challenge to HEX reactor design where solid and liquid mixing would need to occur within the reactor in order to prevent wasteful decomposition outside of the reactant channels. The AC concentration, residence time, particle size, and load temperature were fixed at the values listed in Table 11; these values were selected to represent typical operating conditions that were attainable with the experimental apparatus of Johnson *et al*. [70].

Table 11. Fixed parameters for $T_{R,in}$ study

Parameter	Value
Particle Size	40 – 60 mesh
$T_{L,in}$	90°C
$\dot{m}_R$	50 g/s
$\dot{m}_L$	120 g/s
c_i	50 g/L

The gross values for total heat exchanged, $\dot{Q}_L$; balance, $\varepsilon_q = \dot{Q}_{rxn} / \dot{Q}_L$; and conversion $\varepsilon_c = \dot{Q}_{rxn} / \dot{m}_{AC} \Delta H$ are plotted in Figure 101 as functions of reactant-side inlet temperature:

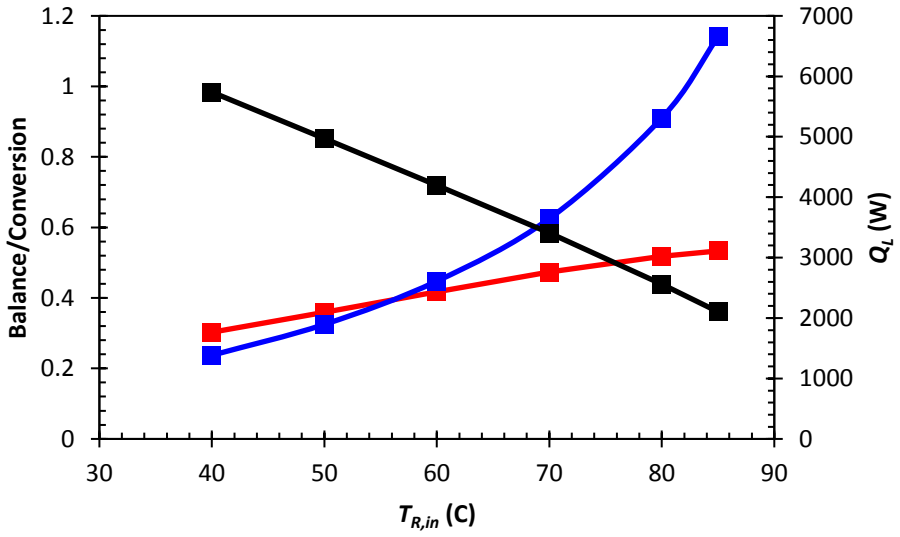

Figure 101. Total load-side heat rejection (black), conversion (red) and balance (blue) as a function for reactant-side inlet temperature; all other parameters were fixed according to Table 11

As the available load-to-reactant temperature gradient is reduced, $\dot{Q}_L$ decreases while higher inlet temperatures increase the overall reaction rate and thus increase both η and ε. The conversion and balance have an almost one-to-one correlation below 60°C, but rapidly diverge as $T_{R,in}$ increases. The rapidly increasing effectiveness is more a consequence of the decreasing $\dot{Q}_L$ than accelerating reaction rates, which are experiencing a diminishing return at higher $T_{R,in}$ as evidenced by the plateauing conversion.

Figure 101 showed that conversion appeared to asymptotically approach 55% with increasing reactant-side inlet temperature. The general upward trend in conversion results from the increase in temperature, which tends to increase the rate coefficients, but also because the heterogeneous decomposition → desorption pathway becomes increasingly important. This can be observed in the local heat absorption rates for the heterogeneous and homogeneous reaction mechanisms plotted in Figure 102:

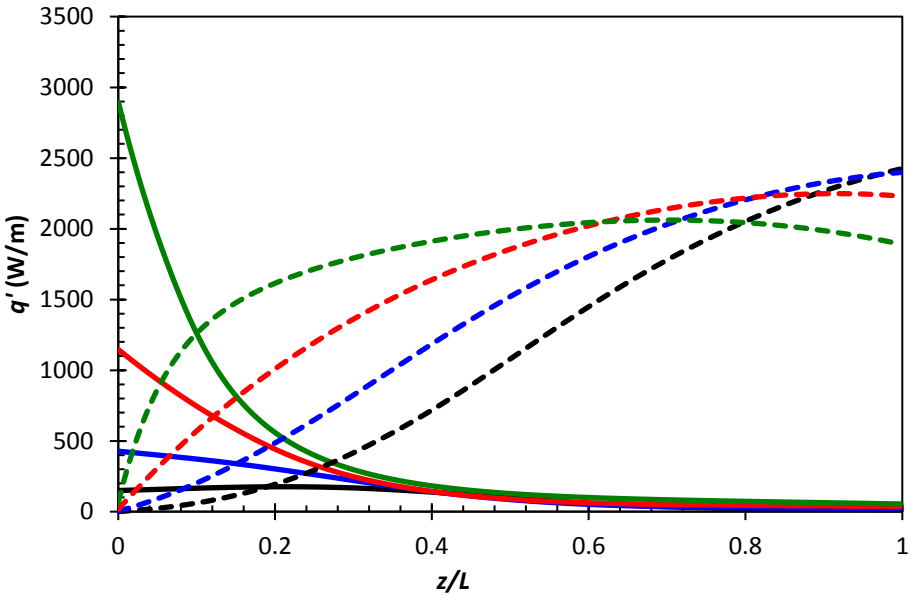

Figure 102. Local heat absorption due to homogeneous decomposition (dashed) and combined heterogeneous and dissolution mechanisms (solid) at various $T_{R,in}$: 50°C (black), 60°C (blue), 70°C (red) and 80°C (green)

As expected, the heterogeneous decomposition rate grows exponentially with temperature, and beyond $T_{R,in}$ = 60°C, exceeds that of the dissolution rate. There is very little difference in $\dot{q}'_{dis}$ as the temperature increases. The homogeneous reaction timescale decreases as well owing to the exponential increase in the forward rate coefficient k_{hom} and the equilibrium coefficient K_{hom}; there are also only minor differences in maximum $\dot{q}'_{\text{hom}}$ values. This effect tends to compensate for the increased preference for the heterogeneous decomposition→desorption pathway, which would otherwise reduce the homogeneous reaction's role.

The asymptotic behavior of conversion with respect to reactant-side inlet temperature follows from the process becoming increasingly heat transfer limited as the

available reactant-to-load temperature gradient decreases; this is reflected in the inversely related slopes of η and ε, and is most readily apparent in the dimensionless axial temperature profiles plotted in Figure 103:

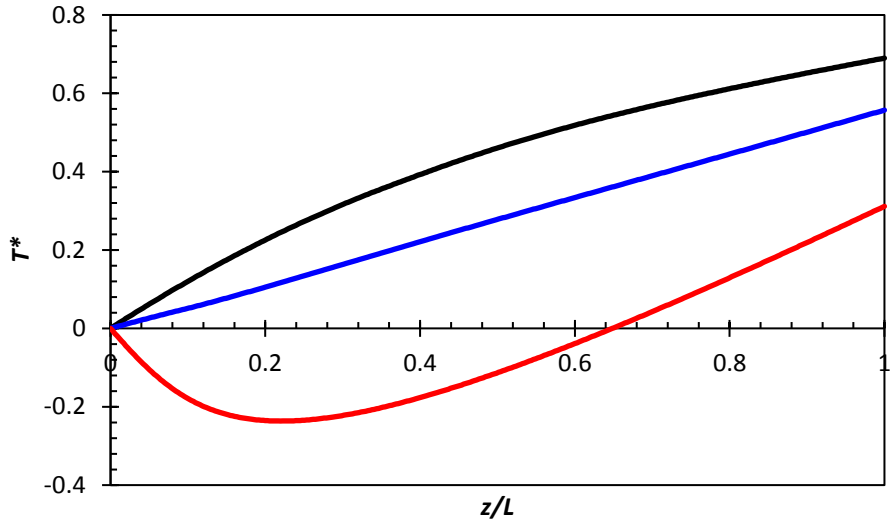

Figure 103. Dimensionless reactant-side temperature profiles at different $T_{R,in}$: 50°C (black), 70°C (blue), and 80°C (red). Negative values of T^* indicate a heat transfer-limited condition

where we have defined:

$$T^* \equiv \frac{T_R - T_{R,in}}{T_{L,in} - T_{R,in}} \tag{6.69}$$

As $T_{L,in} - T_{R,in}$ decreases (i.e. $T_{R,in}$ increases), the heat transferred from the load side becomes insufficient to sustain the reaction at the local temperature, causing the temperature to decrease. As the temperature decreases, so too does the local reaction

rate. Increasing the severity of the heat transfer limited condition further retards gains in the total reaction rate, causing the diminishing slope in η.

6.3.3 Solid AC Concentration

Johnson *et al*. [70] had claimed that as AC concentration was increased while the residence time and load temperature remained fixed, there was a diminishing return in $\dot{Q}_{rxn}$. The model is able to show that increasing concentration without changing the characteristic timescales of the reaction will cause the conversion to suffer in exchange for minor gains in $\dot{Q}_{rxn}$.

Before examining the effect of solid AC concentration on a HEX reactor of practical size, it is necessary to first consider the theoretical "infinite-length heat exchanger" case to delineate the effect of concentration on the characteristic time-scale of the reaction. Since the model is only able to simulate a bounded domain, "infinite length" is understood to mean a length sufficient for the reaction to proceed to completion, i.e. when $\dot{q}'_{rxn}$ = 0. In this study, assuming $\dot{m}_R$ = 50 g/s, a length of four meters proved sufficient. Fundamentally, this analysis reveals the greatest possible conversion that can be realized for fixed load-side conditions and concentration. As will be shown, this limit is a function of NH_3 retention.

For the present analysis, the parameters tabulated in Table 12 are held fixed while the concentration is varied from 20 g/L – 200 g/L:

Table 12. Fixed parameters for solid AC concentration study

Parameter	Value
Particle Size	40 – 60 mesh
$T_{L,in}$	90°C
$\dot{m}_R$	50 g/s
$\dot{m}_L$	120 g/s
$T_{R,in}$	50°C

Figure 104 shows predicted local heat absorption by reaction/dissolution as a function of axial distance normalized by $L^* = 0.375$ m for c_i = 20 g/L, 50 g/L, and 100 g/L. Note that for these simulations 1000 finite volumes cells were used to ensure gradients near the channel inlet were adequately resolved.

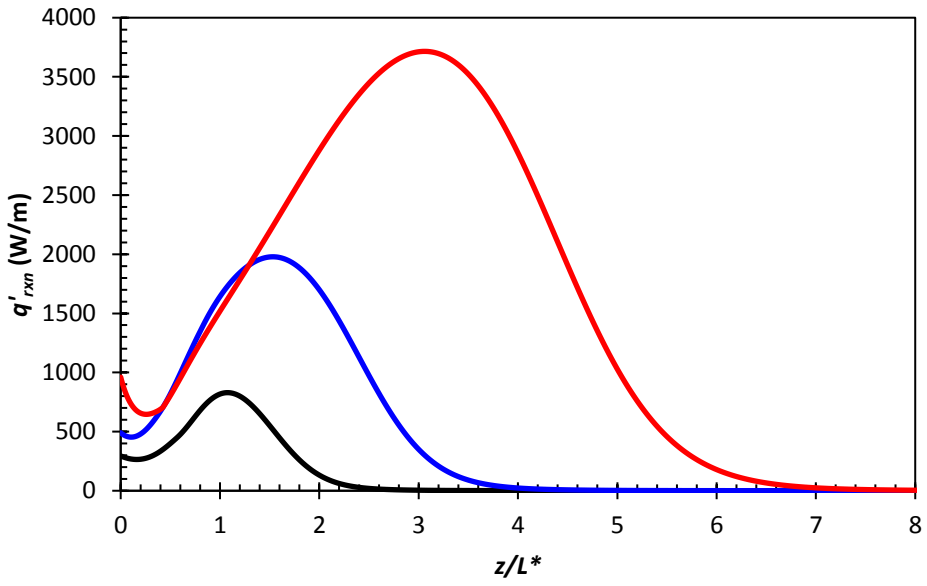

Figure 104. Local heat absorption rate due to reaction/dissolution in an "infinite length" reactor for different solid AC concentrations: 20 g/L (black), 50 g/L (blue), and 100 g/L (red)

In addition to a marked increase in maximum $\dot{q}'_{rxn}$, the location of said peak shifts further downstream by a sizeable degree. Roughly, doubling the solid AC concentration effectively doubles the length of reactor – and by extension, residence time – necessary for the reaction to proceed to completion. The homogeneous reaction, which is responsible for the peak $\dot{q}'_{rxn}$, grows in proportion to the solid AC concentration, otherwise experiences no substantial change to the rate or equilibrium coefficient. The increase in solid-phase surface area provides an initial boost to the reaction rate at the inlet, but this is short in duration and of considerably smaller magnitude than the enhancement to the peak in $\dot{q}'_{\text{hom}}$. It stands to reason, then, that if the HEX reactor does not allow sufficient residence time for the homogenous reaction to develop completely (i.e. to reach its peak value), then it will incur severe penalties to conversion.

For the three cases plotted in Figure 104, Table 13 shows the maximum attainable values for the relevant thermal performance figures of merit:

Table 13. Calculated thermal performance values for "infinite length reactor" cases plotted in Figure 105

c_i (g/L)	$\dot{Q}_L$ (W)	$\dot{Q}_{rxn}$(W)	$\dot{Q}_{rxn,\max}$(W)	η	ε
20	6217	1197	1800	0.67	0.19
50	7957	3102	4500	0.69	0.39
100	10801	6164	9000	0.69	0.57

where $\dot{Q}_{rxn,\max} \equiv \Delta H \cdot \dot{m}_{AC}$. Of note, both $\dot{Q}_{rxn}$ and $\dot{Q}_{rxn,\max}$ scale (almost) linearly with c_i, which yields a maximum possible conversion of 70%. Axial concentration

profile for dissolved AC corresponding to each of the three test cases –plotted in Figure 105 – show that the homogeneous reaction proceeds nearly to completion, and thus we may eliminate the mass transfer-limited regime as the cause for this conversion limit. Plots of the retained dissolved NH_3 – depicted in Figure 106– show that a large quantity of dissolved NH_3 remains in solution. Due to the relatively high enthalpy of solution for NH_3 in PG, the retained NH_3 represents a non-trivial store of cooling potential that is not being utilized, and thus limiting realization of 100% conversion.

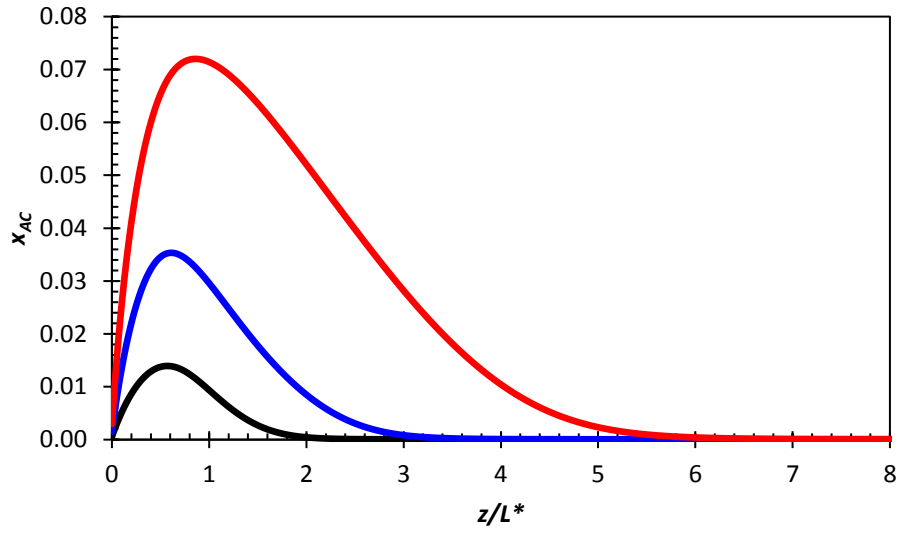

Figure 105. Local dissolved AC mole fraction x_{AC} for "infinite length reactor" at different solid AC concentrations: 20 g/L (black), 50 g/L (blue), and 100 g/L (red)

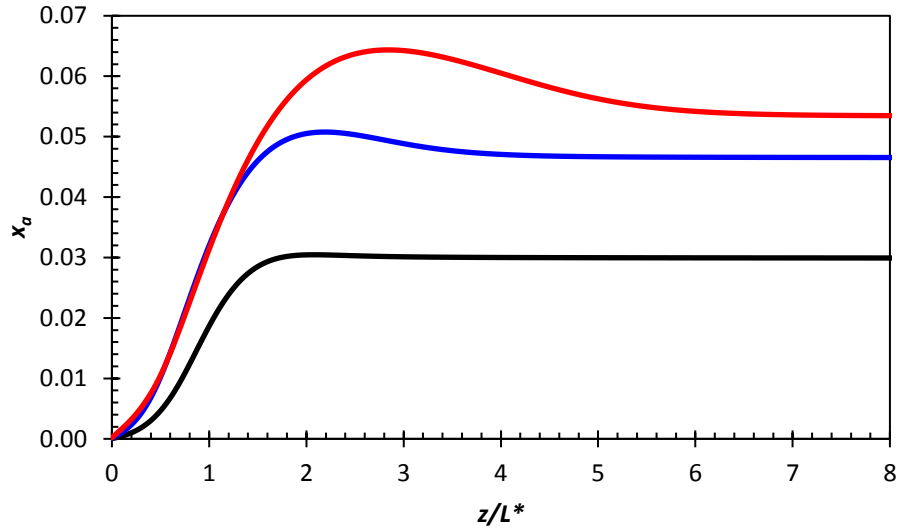

Figure 106. Local dissolved NH_3 mole fraction x_a for "infinite length reactor" at different solid AC concentrations: 20 g/L (black), 50 g/L (blue), and 100 g/L (red)

Having developed a basis for interpreting the results, we proceed with the analysis of the finite-length HEX reactor. With the selected reactant-side mass flow rate and assuming 24 plates installed in the HEX reactor, the residence time is approximately 20 seconds. Figure 107 shows the model predictions for $\dot{Q}_L$, e, and h obtained at various assumed solid AC concentrations.

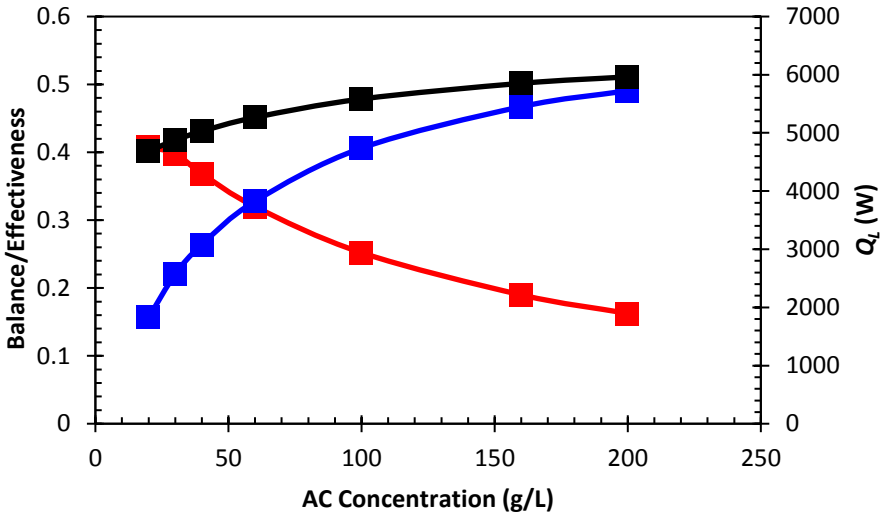

Figure 107. Total load-side heat rejection (black), conversion (red) and balance (blue) as a function of solid AC concentration; all other parameters were fixed according to Table 12

Consistent with the observations of Johnson *et al*. [70], $\dot{Q}_L$ and ε exhibit asymptotic behavior with increasing c_i. Initially, near c_i = 20 g/L, the conversion curve shows only a minor decrease as concentration is raised up until about 30 g/L, after which a precipitous drop occurs; this narrow 'flat' region corresponds to values of c_i such that the solid-phase has completely dissolved/reacted within the reactant channel. As

concentration is increased further the solid-phase is no longer depleted within the channel, leading to the rapid drop in conversion. This result is to be expected given that any remaining solid AC represents *completely* wasted cooling potential, whereas dissolved NH_3 or dissolved AC remaining at the reactor outlet would represent *partially* wasted cooling potential.

An additional but equally important cause for the reduction in conversion is that additional time/axial distance required for the homogeneous reaction to develop and enter into the mass transfer-limited stage. This was anticipated on the basis of the results plotted in Figure 107, and can likewise be seen in the axial plots of $\dot{q}'_{rxn}$ and $\dot{q}'_L$ for the finite-length HEX reactor, as shown in Figure 108:

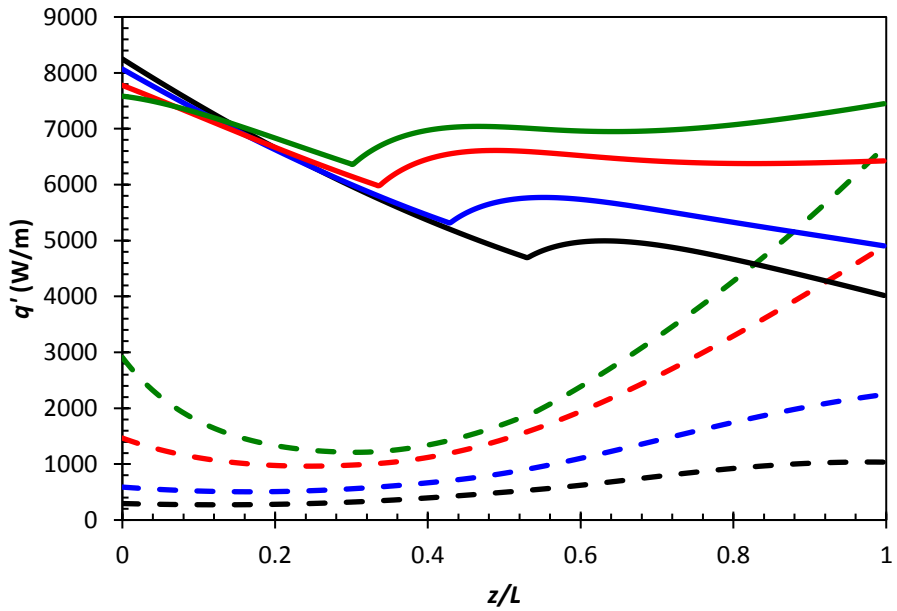

Figure 108. Local heat flux (solid line) and heat absorption (dashed line) at various solid AC concentrations: 20 g/L (black), 40 g/L (blue), 100 g/L (red), and 200 g/L (green)

At c_i = 20 g/L, $\dot{q}'_{rxn}$ assumes its peak value, which is due to the homogeneous decomposition mechanism, just prior to exiting the reactor. As concentration increases, the $\dot{q}'_{rxn}$ peak shifts further outside of the reactor, indicating that the proportion of the reaction completed within the channel is shrinking.

To confirm, the same set of simulations was repeated at a 70 second residence time ($\dot{m}_R$= 15 g/s) – at c_i = 200 g/L, for instance, conversion increased to ~60%. A plot of $\dot{q}'_{\text{hom}}$ as a function z/L, given in Figure 109, shows that the homogeneous reaction was able to attain its peak value within the reactant channel, hence the large improvement in conversion over the same case at t_{res} = 20 seconds. Additionally, the same plot shows that $\dot{q}'_{rxn}$ exceeds $\dot{q}'_L$ after z/L = 0.6, showing that the HEX reactor is well into the reaction-dominated regime.

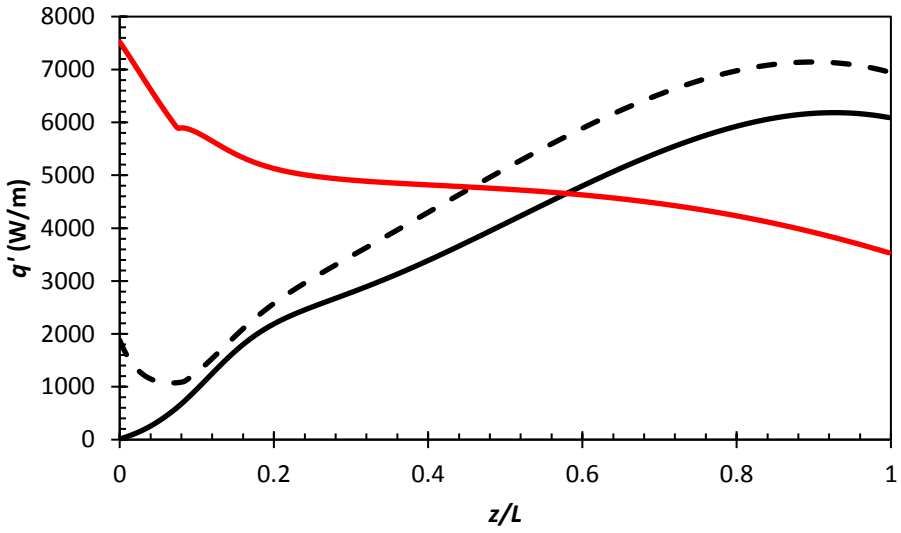

Figure 109. Local heat absorption by homogeneous reaction (solid black line), all processes combined (dashed black line), and load-side heat rejection for t_{res} = 70 seconds and c_i = 200 g/L. All other parameters are as listed in Table 13

When η is plotted as a function of c_i for the high residence time set of simulations (Figure 110), there is a non-monotonic trend: conversion increases briefly before beginning to fall in a fashion comparable to the low residence time simulations. The curves for ε and $\dot{Q}_L$ show the anticipated increase with respect to c_i. The behavior of η is actually linked to the total extent of NH_3 desorption; if one considers a reactor of infinite length, the NH_3 retention as $z \rightarrow \infty$ is given by:

$$x_a^* = \left(U_R \frac{2c_i}{M_{AC}} - j_g y_a^* \right) \left(\frac{M_R}{r_R} \right) \tag{6.70}$$

where y_a^* is the gas-phase mole fraction of NH_3 in an infinite length HEX reactor, the value of which may interpreted as the maximum attainable for fixed load-side conditions and AC solid concentration. We have assumed the load-side temperature is sufficiently high such that $x_{AC} \approx 0$ and all that remains as $z \rightarrow \infty$ is either dissolved or free gas. Let $\Delta j_a \equiv U_R \left(2c_i / M_{AC} - x_a^* \left(r_R / M_R \right) \right)$ represent the desorbed NH_3 in the limit $z \rightarrow \infty$; then, after substituting for j_g in Eq. (6.68), we find that:

$$\Delta j_a = j_{c,\max} \frac{y_a^*}{1 - y_a^*} \tag{6.71}$$

Thus, one can see that Δj_a is proportional to the molar flux of desorbed CO_2 $j_{c,max}$. In an infinite reactor, we may assume that:

$$j_{c,\max} = U_R \frac{c_i}{M_{AC}} - \left(\frac{r_R}{M_R} \right) x_{c,sat} \tag{6.72}$$

Hence, the maximum possible CO_2 released increases in direct proportion to increases in c_i. The cooling potential associated with the retained NH_3 is:

$$h_{lost,a} = \frac{\Delta H_{des}}{\Delta H} \left(2 - \left[1 - \frac{M_{AC}}{c_i} \left(\frac{r_R}{M_R} \right) x_{c,sat} \right] \frac{y_a^*}{1 - y_a^*} \right) \tag{6.73}$$

Therefore, because $x_{c,sat}$ is essentially fixed by the load-side temperature (the same is approximately true for y_a^*), there is an inverse relationship between c_i and the lost cooling potential. This behavior is seen in Figure 110 for lower values of c_i since the residence time is much larger than that required by the reaction. As c_i increases further, the timescale of the reaction becomes comparable to the residence time, resulting in unreacted AC (dissolved and solid) exiting the reactor and the subsequent decline in conversion.

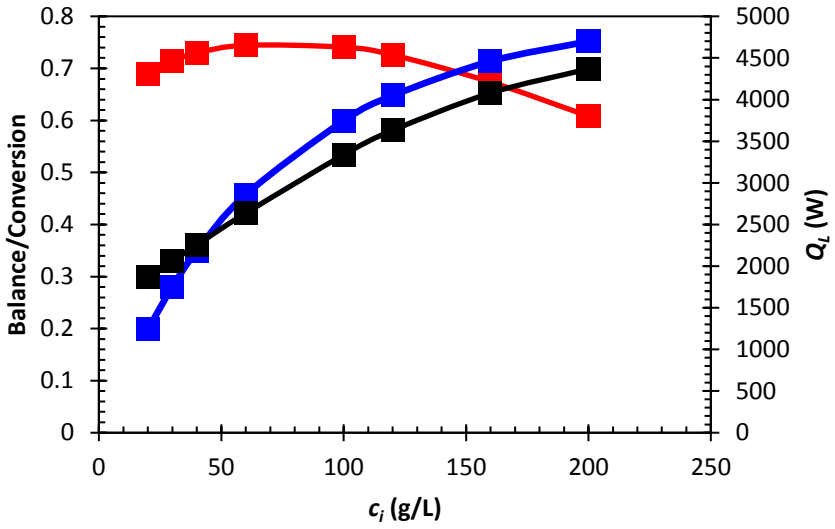

Figure 110. Total load-side heat rejection (black), conversion (red) and balance (blue) as a function of solid AC concentration; all other parameters were fixed according to Table 6.7, but with residence time set to 70 seconds

The comparison of the trends in coversion with repect to concentration at different residence times has shown that conversion is limited by residence time when operating in the convection dominated regime, as was found by Johnson *et al*. [70], and

by NH_3 retention when operating in the reaction dominated regime.

6.3.4 Particle Size

Particle size is more precisely described by a distribution function rather than a single parameter. Assuming a uniform particle size distribution, the 'particle size' parameter can be described by a distribution width Δr_i and a maximum $r_{i,max}$.. To reflect more realistic conditions, we shall use a fixed sieve-size increment in place of a fixed Δr_i,; in practice, it is much simpler to obtain a fixed, standard sieve size increment than a fixed physical size increment, since this would require more advanced separation techniques. In the batch reactor study, smaller particle sizes correlated to (initially) faster reaction rates. Interaction with the changing temperature field in the HEX reactor can, under some circumstances, produce counterintuitive results. It was demonstrated in section 6.3.2 that the dominant reaction pathway (i.e. the "slow" or "fast" routes) was determined by the prevailing conditions for the solid-phase, namely temperature. It is therefore conceivable that larger particle sizes might shift preference toward the faster heterogeneous decomposition pathway by allowing the solid-phase to persist further downstream, where the temperature is higher. Hence, the smallest possible AC particles may not necessarily yield the highest conversion and/or highest overall reaction rate. The purpose of this section is to show the dependence of load-to-reactant heat transfer and heat absorption on the mean of the initial particle size distribution. These results will establish whether the aforesaid hypothetical scenario is possible and, if so, provide guidance in selecting the optimal particle size.

In order to better discern the effects of a given particle size, it is necessary to maintain Δr_i to a minimum. This ensures that the results can be reasonably correlated with the mean particle size. Sieve size increments of 10 mesh were found to be sufficient for this; smaller increments produced no appreciable change in the results. The fixed parameters selected for this analysis are tabulated in Table 14:

Table 14. Fixed parameters in particle size study

Parameter	Value
c_i	50 g/L
$T_{L,in}$	90°C
$\dot{m}_R$	50 g/s
$\dot{m}_L$	120 g/s
$T_{R,in}$	50°C

Model predictions for $\dot{Q}_L$, ε, η are plotted in Figure 111 for mean particle mesh sizes of 25 through 95 (100 μm – 20 μm diameter).

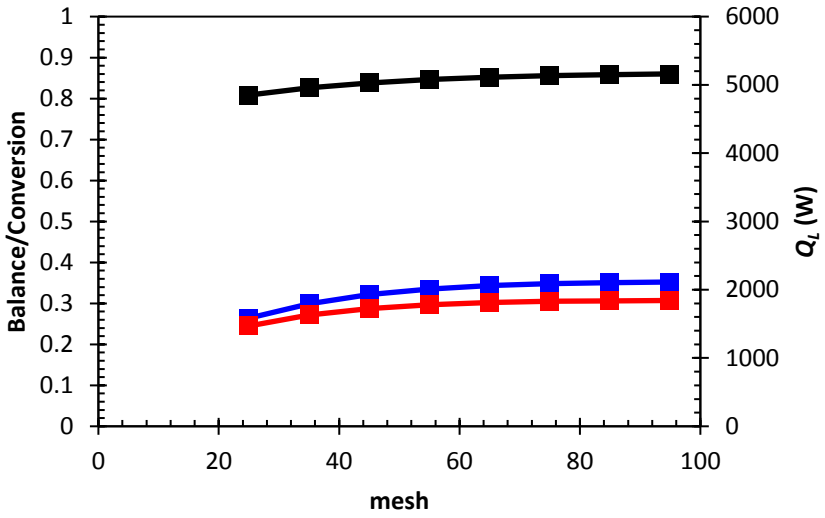

Figure 111. Total load-side heat rejection (black), conversion (blue), and balance (red) as a function of mean mesh size; all simulations used the fixed parameters listed in Table 14

Moderate improvements in all metrics are realized between 24 mesh and 45 mesh, but stagnate as the particle size is reduced further. Smaller particles increase the available surface area for heterogeneous decomposition and dissolution, but do not alter the rate/equilibrium coefficients governing the homogeneous reaction. As was observed with the batch reactor model, one can only accelerate the development of the homogeneous reaction by using smaller particles, but it will not change the peak homogeneous reaction rate, nor will it change its characteristic timescale. Hence, the main benefit is ensuring that the solid-phase is fully depleted within the channel; beyond that point, the enhancement to conversion and heat transfer capacity becomes negligible. This can be seen in the axial solid-phase concentration profiles and local endothermic heat absorption rates, which are plotted in Figure 112 and Figure 113 for particle size ranges of 20-30, 40-50, and 90-100 mesh.

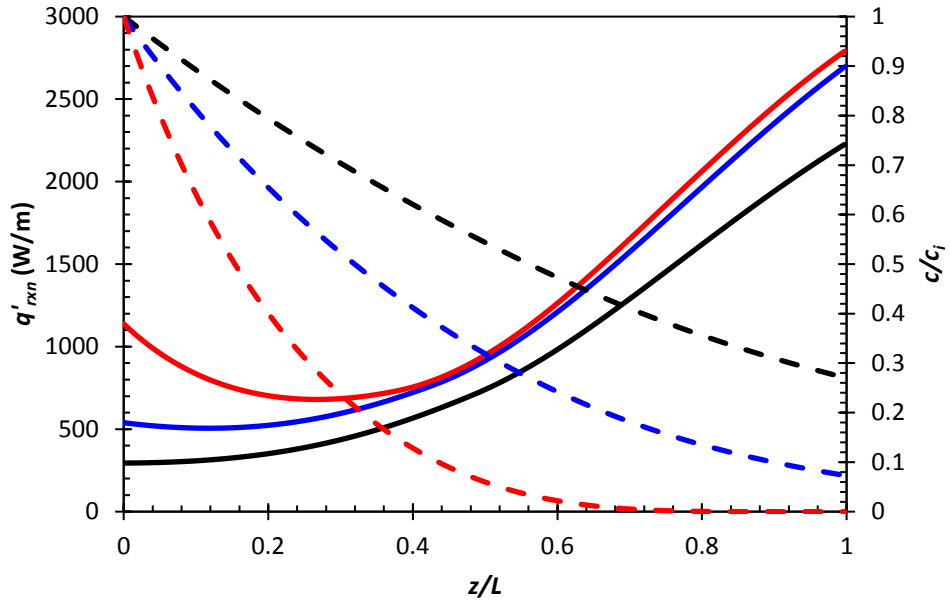

Figure 112. Local heat absorption rate due to reaction/dissolution (solid lines) and solid-phase concentration ratio c/c_i at different mean particle sizes: 20 - 30 mesh (black), 40 - 50 mesh (blue), and 90 - 100 mesh (red)

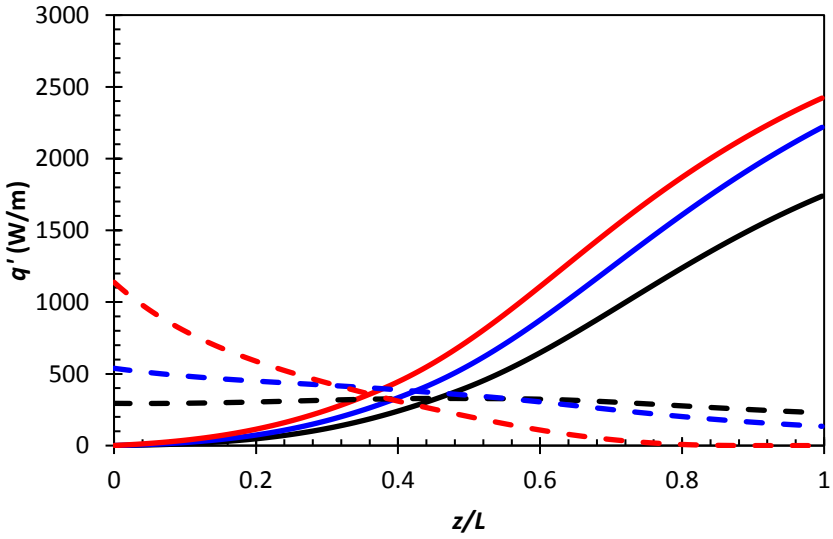

Figure 113. Local heat absorption rate due to homogeneous decomposition (solid lines) and due to combined heterogeneous reaction and dissolution (dashed lines) at different particle sizes: 20 - 30 mesh (black), 40 - 50 mesh (blue), and 90 - 100 mesh (red)

The dimensionless solid-phase concentration curve corresponding to the large particles (20-30 mesh) shows that ~30% of the solid-phase remains at the reactor outlet, whereas only ~10% remains for the intermediate particles (40-50 mesh), and 0% for the small particles (90-100 mesh). The large and intermediate particle $\dot{q}'_{rxn}$ curves show a far greater distinction throughout the channel compared to that of the intermediate and small particles, which are practically indistinguishable after $z/L = 0.3$. Prior to this point, the small particle size gives a pronounced but very brief enhancement in $\dot{q}'_s$ that contributes little to the total heat absorption rate. Therefore, the homogeneous reaction is the dominant contributor to $\dot{Q}_{rxn}$, and by extension, the conversion. Since the reaction is dominated by the dissolution → homogeneous reaction → desorption pathway, the merger of the small and intermediate particle $\dot{q}'_{rxn}$ curves implies that as particle size decreases beyond what is necessary for the solid-phase to completely dissolve/react within the channel, the homogeneous reaction becomes the overall rate-determining step. Particle sizes of 40 mesh and smaller will yield essentially the same result irrespective of the particle size distribution's form. Thus, in addition to providing an improvement in conversion and capacity, the above-referenced particle size threshold would also greatly reduce process variability associated with the particle size distribution, whose functional form is difficult to control.

To see if it was possible for conditions to develop such that larger particle sizes might be advantageous, the same set of simulations was repeated with a reactant-side inlet temperature of 70°C. The reasoning behind this selection of inlet condition follow from the observation that higher reactant-side inlet temperature would favor the 'faster'

heterogeneous pathway and therefore reduce the overall reaction timescale. This does not appear to be the case, as can be seen in Figure 114:

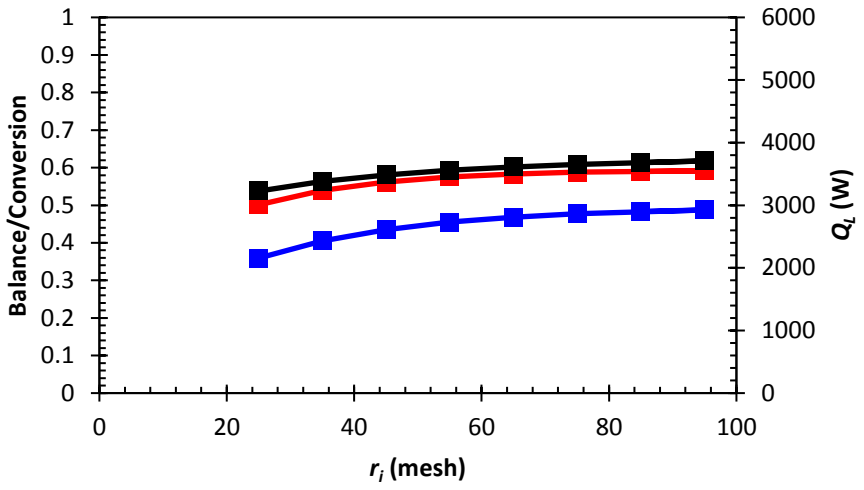

Figure 114. Total load-side heat rejection (black), conversion (blue), and balance (red) as a function of mean mesh size; all simulations used the fixed parameters listed in Table 14 but with residence time set to 70 seconds

Qualitatively, η, ε, and $\dot{Q}_L$ follow the same trends as the lower inlet temperature case. Actually, comparing η in Figure 114 to that in Figure 111 reveals that the only apparent difference is an upward shift in the higher inlet temperature case by about 0.12. Increasing the longevity of the solid-phase does indeed lead to a greater proportion of the overall reaction to favor the heterogeneous pathway, but this benefit is offset by the decrease in surface area concentration.

6.3.5 Residence Time

Residence time is perhaps the easiest operating parameter to adjust, requiring changing pump flow rates, AC feed rates, or increasing the number of plates in the PHE. However, this adjustment cannot be done independently of the Reynolds number, which is directly proportional to $\dot{m}_R$. The need for high residence times to ensure full conversion will always compete with the need for maximizing HEX reactor energy density; this section will show the dependence of capacity and conversion on residence time.

The heat transfer capacity $\dot{Q}_L$ varied as expected with residence time, taking a form similar to the single-phase (PG-only) case, as can be seen in Figure 115. The decay in $\dot{Q}_L$ with residence time becomes increasingly gradual at higher solid AC concentrations due to the combined effects of convective heat transfer enhancement by the gas-phase and augmentation of the effective heat capacity of the reactant fluid by chemical reaction/dissolution.

A plot of conversion as a function residence time for various solid AC concentrations is shown in Figure 116, and while all curves approach a limiting value as expected, there is small but non-trivial difference in the asymptotic behavior. This same behavior was described in Section 6.3.3, which is the result of a transition from an effectively "infinite length" reactor – where conversion improves with increasing solid AC concentration – to a "finite length" reactor – where conversion declines with increasing solid AC concentration.

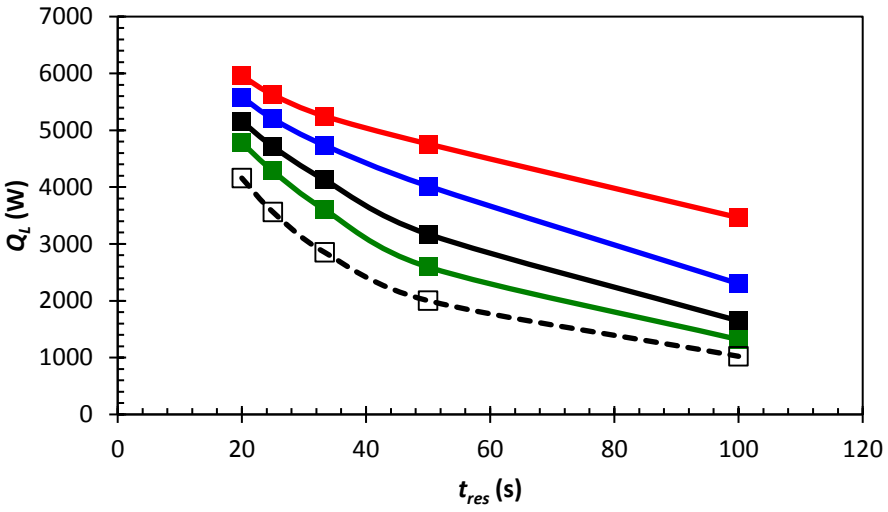

Figure 115. Total load-side heat rejection as a function of residence time for different solid AC concentrations: 0 g/L (dashed), 25 g/L (green), 50 g/L (black), 100 g/L (blue), and 200 g/L (red)

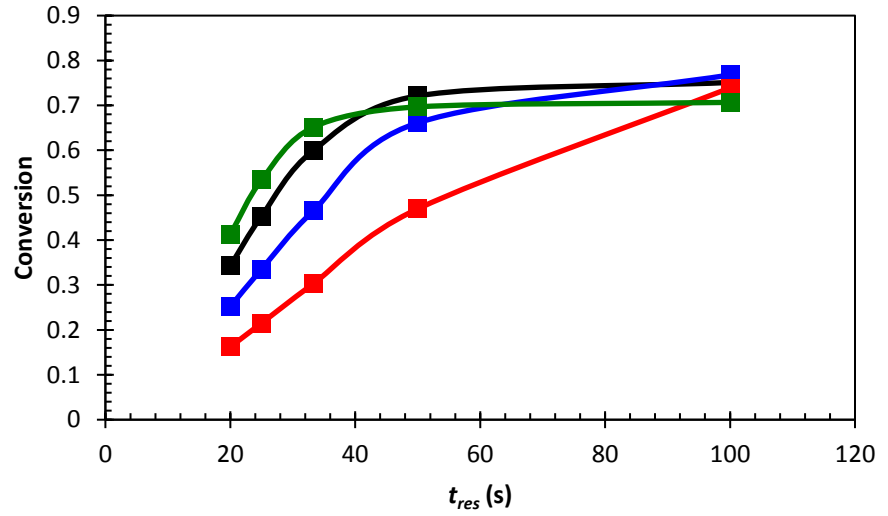

Figure 116. Conversion as a function of residence time for different solid AC concentrations: 0 g/L (dashed), 25 g/L (green), 50 g/L (black), 100 g/L (blue), and 200 g/L (red)

6.4 Optimization

Reduced order models such as the one used in this study have the advantage of allowing numerical optimization routines to be employed within reasonable execution timeframes. In general, an appropriate objective function is selected to represent the combined cost/benefit of various performance metrics, which is then perturbed by small increments until it has been minimized. As was shown previously, the measures of thermal performance for the HEX reactor are in many cases competing, and so this is a problem that is well suited to optimization. In this section, we show how the model can be combined with a numerical optimization routine to find a set of operating conditions to maximize heat transfer capacity, conversion, and ensure balance between convection and endothermic absorption.

The three performance metrics introduced in the previous discussions were rendered into the following objective function:

$$F = \sqrt{(1-\eta)^2 + (1-\varepsilon)^2 + \left(\dot{Q}_{rxn,\max} / \dot{Q}_L\right)^2} \tag{6.74}$$

where we have assumed that each metric is of equal importance. Eq. (6.74) reflects the following optimization targets:

1) Conversion as close as possible to unity
2) A balance between convection and reaction as close as possible to unity
3) Maximize heat rejection

To minimize Eq. (6.72), we seek the condition,

$$\nabla F = 0 \tag{6.75}$$

The gradient descent method [69] is perhaps the simplest optimization method, and as such is well suited to numerical implementation. The basic algorithm is as follows:

1. The parameters $\boldsymbol{\theta}$ to be optimized are given an initial guess $\boldsymbol{\theta}_o$, and the gradient ∇F is evaluated either analytically or numerically
2. The direction of greatest change is in the direction of the gradient vector; hence, an increment is applied to the parameter vector in the opposite direction of ∇F:

   $$\boldsymbol{\theta}_{new} = \boldsymbol{\theta}_{old} - \frac{\nabla F}{\|\nabla F\|}$$

3. F is evaluated at $\boldsymbol{\theta}_{new}$ and compared to F from the previous iteration. If the values of F differ by more than the specified tolerance, the procedure is repeated; otherwise, F is declared to be minimized

The above algorithm was implemented in the Maple 18 programming language (Waterloo Maple, Canada). To obtain the gradient vector, each element of the parameter vector $\boldsymbol{\theta}$ was perturbed by a small value (one) while the remaining elements were fixed

at the values obtained from the previous iteration. The model was run for each perturbation and the corresponding element in the vector ∇F was approximated as:

$$\frac{\partial F}{\partial q_j} \approx \frac{F(q_{old} + \delta_j \Delta q) - F(q_{old})}{\delta_j \Delta q} \tag{6.76}$$

Where the vector operator $\delta_j = 1$ if $I = j$ and 0 otherwise. Once Eq. (6.74) is evaluated for each element of ∇F, the increment to $\boldsymbol{\theta}$ is calculated and the next iterative cycle is started.

6.4.1 Assumptions

This analysis is conducted with a fixed HEX reactor design and load-side conditions as in Section 6.3. The operating conditions that could potentially be adjusted are particle size, reactant-side inlet temperature, AC solid concentration, and residence time. In Johnson *et al.*'s paper [13, 70], concentration and residence time were not independent parameters. In fact, the AC feed rate $\dot{m}_{AC}$ was fixed to provide a target endothermic heat absorption rate of 4.5 kW, and so as the residence time was varied the AC solid concentration was given by:

$$c_i = \frac{\dot{m}_{AC}}{\dot{m}_R / \rho_R} \tag{6.77}$$

We proceed with the optimization task assuming that one intends to react a fixed feed rate of AC to match a known quantity of heat to be rejected. Furthermore, per the results of Section 6.3.4, decreasing the particle size will generally improve the conversion in a residence time limited operating condition; it is obvious, then, that having the smallest particles possible will ensure that no limits are imposed by incomplete reaction/dissolution of the solid phase. However, Johnson *et al*. [70] reported that particles smaller then 60 mesh (240 μm) would not feed reliably through their gravimetric feeder. Therefore, this analysis assumes a particle size range of 40 to 60 mesh (420 – 240 μm) for consistency with ref. [70]. This leaves two independently adjustable parameters: reactant-side inlet temperature and residence time mediated through the reactant-side flow rate.

6.4.2 Results and Discussion

The imposed solid AC feed rate was varied between 1 g/s and 4 g/s, and the estimation routine was terminated when F changed by less than 0.01 between successive iterations. Table 6.10 shows the operating parameter set that minimizes Eq. (6.74) for different AC feed rates.

Table 15. Optimization results using Eq. (6.72) for different AC feed rates

Parameters	Solid AC Feed Rate (g/s)				
	1	**2**	**2.5**	**3**	**4**
$\dot{m}_R$ (g/s)	56.3	46.2	50.1	45.9	45.9
$T_{R,in}$ (°C)	81.8	75.3	73.4	71.1	67.2
c_i (g/L)	17.8	43.3	49.9	65.4	87.1
ε	0.64	0.66	0.65	0.62	0.59
η	0.59	0.54	0.49	0.45	0.37
$\dot{Q}_L$ (W)	1654	2971	3382	3914	4490

The performance metrics in the objective function (η, ε, $\dot{Q}_L / \dot{Q}_{rxn,\max}$) are plotted in Figure 117:

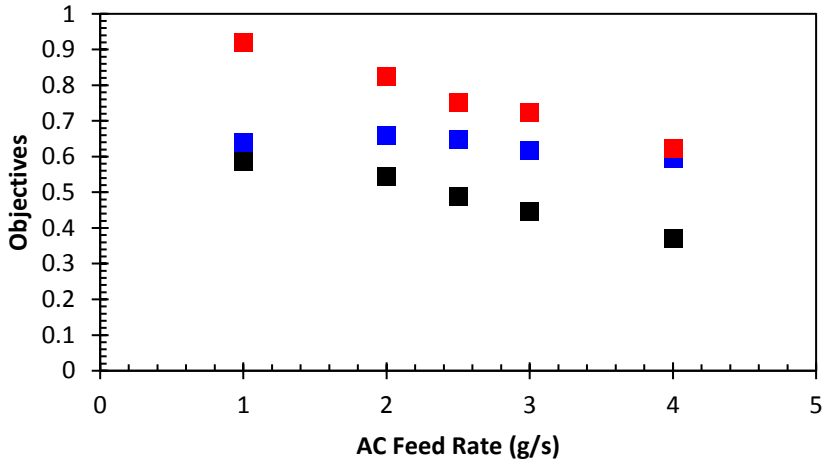

Figure 117. Optimal $\dot{Q}_L / \dot{Q}_{rxn,\max}$ (red squares), conversion (black squares), and balance (blue squares) as a function of AC feed rate.

Both η and $\dot{Q}_L / \dot{Q}_{rxn,\max}$ experienced a steady decrease as greater AC feed rates were imposed, whereas ε stayed within the vicinity of 0.6. The requirement that $\varepsilon = 1$ drove the reactant-side inlet temperature up, acting in opposition to $\dot{Q}_L / \dot{Q}_{rxn,\max}$ which tended to favor low inlet temperatures in order to increase the temperature gap between load and reactant side. As the feed rate was increased, enough latent heat via endothermic reaction became available to offset the drive for a large temperature gap somewhat, but is unable to stem the decrease in $T_{R,in}$ and thence the drop in conversion. At the same time, $\dot{Q}_L / \dot{Q}_{rxn,\max}$ also tends to drive $\dot{m}_R$ higher, while η produces the opposite effect. $\dot{Q}_L / \dot{Q}_{rxn,\max}$ and η follow nearly parallel trajectories while ε remains relatively flat, which shows that the objective function F prefers to sacrifice heat transfer capacity and conversion to maintain ε. This tendency can be corrected, if desired, with the use of weighting factors within F:

$$F = \sqrt{w_1 \left(1-\eta\right)^2 + w_2 \left(1-\varepsilon\right)^2 + w_3 \left(\dot{Q}_{rxn,\max} / \dot{Q}_L\right)^2} \tag{6.78}$$

where w_1, w_2, and w_3 are the dimensionless weighting factors whose sum is equal to one. The optimization results for $\dot{m}_{AC}$ = 2.5 g/s shows approximately the same conversion (50%) that Johnson *et al.* [70] found with $\dot{m}_R$ = 13 g/s (t_{res} = 70 s) at the same AC feed rate. The optimum conditions according to the objective function required a reactant-side inlet temperature of 73°C, whereas Johnson *et al.* [70] reported a reactant-side inlet temperature of 47°C. As was described previously, the penalty associated with higher

reactant-side inlet temperature operation – i.e., reaction occurring prior to entering the reactor – is not reflected in the model. At the system-level, the optimization procedure does not account for the considerations required to maintain such a high inlet temperature, which will certainly factor into the system engineer's decision to operate at such conditions with a closed loop reactant-side. For instance, it may become necessary for the HEX reactor to operate in an intermittent mode: if the inlet temperature of the PG begins to fall below a specified threshold, the AC feedrate is reduced or stopped until the loop temperature rises to acceptable levels, and then again restored. This process would repeat in a cyclic manner, causing excursions in heat transfer capacity and potentially impacting stable operation of the thermal management system. The results presented here are illustrative of performance trends with respect to controllable, static HEX reactor operating conditions; when placed in the broader context of an integrated thermal management *system* perspective, these conditions may not represent the optimal design points.

CHAPTER VII

CONCLUSIONS AND RECOMMENDATIONS

In this study, we have developed a new model for the decomposition of ammonium carbamate in a propylene glycol carrier fluid under both batch and continuous flow conditions. The proposed model represents the net decomposition reaction as a combination of two parallel pathways comprised of both physical (bubble generation, convective mass transfer) and chemical (heterogeneous reaction, homogeneous reaction) mechanisms mediating the interaction between a dispersed solid phase, a bulk liquid phase, and a bulk and/or dispersed gas phase. The limited expanse of prior research [10,25,26,70] demonstrated the thermal management potential of AC suspended in PG, but did not quantitatively describe the kinetics, or relied on rate equations that were developed for dry powder. This study has addressed a critical gap in understanding necessary for reliably predicting AC-PG HEX reactor performance between 45°C and 90°C at 1 atm. The reaction model framework is adaptable to other HEX reactor geometries and flow configurations.

A bench-scale experimental approach was developed to obtain kinetic and calorimetric data to parameterize the model. A one-liter, pressure and temperature controlled, stirred batch reactor with continuous headspace sampling and IR species quantification was constructed to systematically characterize the decomposition reaction. AC concentrations of 25, 37.5, and 50 g/L were reacted at 1 atm and temperatures of 55°C, 60°C, and 70°C, with particle sizes ranging from 20 mesh to 100 mesh. The reactor was designed to enable sudden introduction of a known mass and particle size

range of AC into an effectively isothermal temperature field, which in turn allowed the kinetics to be studied independent of hydrodynamics and heat transfer behavior. Transient heat consumption by the endothermic reaction was calculated using a carefully tuned and validated heat transfer model of the reactor wall, thermostat coil, and bulk liquid-phase in conjunction with power input and temperature measurements. IR concentration time traces of CO_2 and NH_3, correlated with qualitative visual observations of the reaction, evidenced two distinct stages in the decomposition process: an irreversible regime characterized by high CO_2 release with vigorous bubble formation, and a mass transfer-limited regime where NH_3 release was steady and CO_2 release was marginal.

A species balance of NH_3 and CO_2 concentration histories thus obtained indicated significant portions of NH_3 were retained in solution – this was further confirmed by measuring the solubility of NH_3 in PG at atmospheric pressure and temperature between 50°C and 75°C, which was nearly 100x more soluble than CO_2 [30]. The solubility difference was such that the bubbles nucleated during the course of the reaction were almost entirely due to supersaturation of CO_2 in the liquid-phase, which subsequently enhanced the rate of NH_3 desorption by acting as a scrubbing gas. By Le Chatelier's principle, the reversible homogeneous reaction governed the transition between the 'irreversible' regime and 'mass transfer-limited' regime; more precisely, the buildup of NH_3 in the liquid-phase drives the reverse reaction and thus reduces the net reaction rate. Because the peak heat absorption rates were observed during the

irreversible regime, the retention and removal of NH_3 from solution was identified as a major design driver for HEX reactor energy density.

A multi-objective optimization code was employed to estimate the model's kinetic and equilibrium parameters as a function of temperature. Agreement between model predictions and IR gas-phase concentration measurements was generally acceptable, and especially good at 70°C. Two characteristic timescales were identified via parametric sensitivity analysis, each associated with one of the two parallel pathways in the model: heterogeneous reaction followed by desorption (path (1)) and dissolution followed by homogeneous reaction followed by desorption (path (2)). Path (1) is generally the 'faster' reaction pathway, and thus more favorable from a reactor design standpoint. The estimated kinetic parameters allowed the kinetic model to be incorporated into a transient energy balance; subsequently, the same optimization procedure was utilized with liquid-phase temperature measurements to estimate the heats of reaction for homogeneous decomposition, heterogeneous decomposition, and the heat of dissolution for AC. The net heat of reaction for AC decomposition was estimated to be approximately 1800 J/g, which was in agreement with the estimates of Johnson *et al.* [70]. A comparison of model predictions with temperature histories showed agreement typically within +/- 1°C. Agreement with calculated heat absorption was acceptable, although the peak heat absorption rate at the onset of reaction was typically underestimated.

The parameterized model was adapted by way of a 1-dimensional separated flow framework to successfully describe a significantly more complicated reacting flow in a

compact HEX reactor [25, 26, 70]. A reasonable degree of uncertainty (+/-20%) was obtained over a range of different AC concentrations (20 g/L – 200 g/L), liquid-phase flow rates (15 g/s , 50 g/s), and load-side temperatures (70°C, 80°C, 90°C). Due to the relatively low reactant-side inlet temperatures, the homogenous reaction was the overall rate determining step and therefore responsible for the ~70 second residence time necessary to achieve conversion above 50%. As expected, NH_3 retention proved a limiting factor in attainable conversion, which could be mitigated by increasing the load temperature; however, load temperatures above 90°C were cautioned against by Johnson *et al.* [70], as thermal decomposition into urea (an exothermic reaction) begins to become significant. Even when the mass transfer-limited condition was effectively eliminated by high temperature operation, the retained NH_3 accounts for a sizeable amount of wasted cooling potential due to its high heat of solution.

For fixed HEX reactor geometry, load-side flow rate, and load-side temperature, a tradeoff between total heat transfer capacity and conversion was observed as the residence time was varied. Low residence time operation favored large overall heat transfer due to convection, but typically poor conversion; conversely, high residence time operation yields higher conversion, but lower overall heat transfer due to a reduced heat transfer coefficient and $\dot{m}_R c_{p,R}$. This penalty in heat transfer was offset at higher AC concentrations (200 g/L), which enhances the effective heat capacity of the reactant side by the latent heat of reaction, in addition to enhancing the convective heat transfer coefficient due to the greater presence of bubbles.

The temperature at the inlet of the reactant-side proved to be an important determining factor in the overall reaction timescale (and by extension, the conversion). At inlet temperatures below 60°C, the majority of the solid-phase mass entered the liquid-phase through physical dissolution, which then underwent homogeneous decomposition and then desorption. At higher inlet temperatures, the heterogeneous decomposition mechanism became the dominant pathway; this reaction pathway tended to accelerate the overall decomposition reaction since the intervening homogeneous reaction step is bypassed. The fraction of solid-phase mass that follows the heterogeneous pathway increases with increasing reactant-side inlet temperature. There is, however, a critical inlet temperature above which reactor performance begins to suffer, i.e., when the balance ε exceeds unity – further increases in inlet temperature will accelerate the reaction rate, but the rate of convective heat transfer is insufficient to match the rate of endothermic heat absorption. Implementation of the slurry generation function becomes more challenging at higher inlet temperatures since any reaction that occurs outside of the reactor constitutes wasted cooling capacity. To enable effective operation at higher reactant-side inlet temperatures, the slurry generation function (dry AC feeding and dispersion in the PG stream) could potentially be integrated into the reactor inlet port; this may not be feasible during reduced pressure operation, which would require a means of isolating the AC feed system from the low pressure slurry mixer.

A simple gradient descent code was developed to explore how the competing factors identified (i.e., conversion, total heat rejection, and balance) through parametric

analysis would govern how closely one could approach ideal performance – namely, maximum heat rejection, balance of unity, and maximum conversion. Without accounting for system-level performance tradeoffs and taking the AC federate to be the same as in Johnson *et al*. [70], the best attainable conversion was approximately 50%, the balance approximately 60%, with a total heat rejection of 3.3 kW.

The following subsections shall address specific areas to improve HEX reactor performance or to improve model fidelity as future avenues of research.

7.1 NH_3 Sequestration

At atmospheric pressure, the attainable HEX reactor energy density is ultimately limited by the retention of dissolved NH_3 in the PG carrier fluid, which accounts for an approximately 30% loss of cooling potential at load temperatures in the neighborhood of 80°C. The high solubility of NH_3 in PG also presents a difficulty from the perspective of a thermal management system where the intent is to circulate the PG in a closed loop that is recharged with AC upon returning to the reactor. At each subsequent pass, any accumulated NH_3 would inhibit both the heterogeneous reaction and homogenous reaction via Le Chatelier's principle, resulting in diminishing conversion at each cycle. Therefore, to operate in a closed loop, a method of desorbing and/or sequestering the residual NH_3 in the liquid phase is required to regenerate the PG stream.

Alternatively, Schmidt [10] and Johnson *et al*. [70] showed that operation at reduced pressure greatly enhanced the conversion; as the model results suggest, this improvement is realized by reducing the saturation limit of NH_3 in the liquid-phase such

that a state of supersaturation was achieved, which would enable desorption by nucleation of NH_3 bubbles. The obvious drawback to this approach is the need for a vacuum pump sufficient to handle the volume of gas generated by the reaction while maintaining a rough vacuum (~1 kPa); for larger HEX reactors, it is unlikely that this approach will scale favorably.

Still another alternative to expedite NH_3 desorption would be to inject a dry, inert gas into the slurry at the reactor inlet. This would effectively perform the same gas-scrubbing function as the CO_2 bubbles, except with the added advantage of being independently controllable. Dry air could potentially be supplied continuously with relatively little volume/weight cost at the system level when compared to the vacuum pump option, in addition to enhancing convective heat transfer. However, the NH_3 would still remain highly soluble in the liquid-phase and thus potentially very large volumes of air may be required. In turn, large volume flow rates of air would displace and accelerate the slurry due to the HEX reactor's small channel diameter. The resulting decrease in residence time would tend to offset improvements in conversion. In addition, the CO_2 – NH_3 – air gas mixture would need to be rapidly separated from the liquid-phase after exiting the reactor, so as to avoid re-absorption of NH_3 as the liquid-phase cools; this presents an additional challenge to designing the gas-separation equipment for Johnson *et al.*'s [70] design.

7.2 Residence Time and Heat Transfer Intensification

The removal of NH_3 addresses what is primarily a thermodynamic limitation – this is, a limit to the maximum attainable thermal performance for a fixed AC feed rate and load temperature – but does not address the rate limitations encountered by a "finite length" HEX reactor. The model demonstrated an inverse relationship between residence time, which favored greater conversion (up to the NH_3 –imposed limit), and total heat transfer rate. If the reactor geometry is fixed, increasing residence time necessitates reducing the flow rate of the slurry, which in turn reduces both the heat transfer coefficient and potentially places the reactor in a heat transfer-limited condition where heat is not delivered to the reactant-side as fast as it is consumed by the reaction. The development of such as scenario is functionally equivalent to reducing the conversion, inasmuch as more energy is extracted from the PG than from the load fluid, thereby wasting cooling potential. To avoid inordinately long reactor channels that would otherwise be required to prevent such a condition from occurring, it is necessary to introduce supplemental mechanical agitation to enhance the heat transfer coefficient without sacrificing residence time.

A relatively new area of heat transfer intensification research, commonly called "active enhancement" [103], focuses on locally imparting energy to the flow field to disrupt thermal boundary layers and promote turbulence. For instance, synthetic jets [104], oscillating plates [105], piezoelectric fans [106], or combinations thereof [107] have been investigated experimentally at the bench scale, and shown appreciable enhancement in the heat transfer coefficient. The flow field can also be manipulated by

means of a controlled electric or magnetic field [103, 108], subject to the requirement of appropriate carrier fluids.

In an oscillating flow/pulse reactor, the heat transfer coefficient can be at least partially decoupled from the residence time [109-111]. This is accomplished by superimposing a an oscillatory reversing flow rate over a small time-averaged flow rate; the oscillating motion disrupts thermal boundary layers and promoting intense localized mixing, while the 'net forward' flow rate is small enough that the requisite residence time would be attainable. Affecting the superimposed alternating flow might be accomplished by using a reversible pump, such as the peristaltic pump used by Johnson *et al*. [70], or with piston-actuated diaphragms as the inlet and outlet of the reactor as in [109]. Additionally, the alternating flow motion would likely have a synergistic effect with the passive heat transfer enhancement geometry of a chevron plate heat exchanger by intensifying secondary vortical flows in the troughs of the corrugation pattern [23]. Further, the corrugation pattern could be optimized to exploit the hydrodynamic interactions between the dispersed gas-phase with the continuous liquid-phase, which has been shown in the literature to enhance convective heat transfer [89, 93].

It is also possible to adapt the HEX reactor model framework developed in this study to describe the thermal performance of an oscillatory flow reactor. A reduced-order approach was suggested by Harvey *et al*. [111], where the reactor is treated as multiple continuous stirred tank reactors (CSTRs) in series, which is similar to the finite volume method except that the number of CSTR elements was selected to emulate the residence time distribution of the reactor. The appropriate number of CSTR elements

was correlated to a bulk flow Reynolds number and an oscillatory flow Reynolds number, which incorporates both the frequency and amplitude of the cyclic flow reversals; the velocity ratio comparing the (average) oscillating flow velocity to the bulk flow was also found to be an important parameter. However, Harvey *et al.*'s [111] model assumed that the reaction kinetics and hydrodynamics were independent, which is certainly not an appropriate assumption in the case of multi-phase reactions. It is therefore suggested that, as an initial approach to adapting the proposed HEX reactor framework for oscillatory flow situations, correlations for void fraction and the Nusselt number be developed as functions of gas-phase/liquid-phase mass flux ratio, oscillation frequency, oscillation amplitude, and steady/oscillating velocity ratio. It will also be necessary to consider over what range of amplitudes and frequencies a periodically-steady flow can be achieved; under such conditions, experimental data (pressure drop, temperature, concentration, *etc*.) used to develop said correlations can be averaged over the flow reversal cycle period, which avoids the complication of modeling the flow behavior as transient.

7.3 Improvements to Model Fidelity

The modeling framework employed in the HEX reactor model is inherently modular and flexible; therefore, improvement of individual process/sub models would allow the HEX reactor model to represent a broader range of operating conditions, carrier fluid types, or possibly to investigate and compare alternatives to the chevron PHE. The following aspects of the model that could benefit most from further investigation include, but are not limited to:

1) Heterogeneous Reaction – this would encompass both the microscale solid behavior as the interface both dissolves and reacts, and the surface chemical kinetics, which are still largely unknown and in further need of direct investigation. This limitation is especially apparent at low (< 60°C) temperatures and/or large particle sizes, where the agreement with the experimental data tended to be poor. A proper account of the solid-phase chemistry will allow the assumption of mass transfer-limited heterogeneous decomposition to be relaxed, with the benefit of extending the model's applicability to temperatures below 55°C. This will also be a pre-requisite to modeling the solid-liquid interface behavior, and obtaining the mass transfer coefficients which may be dependent on surface concentrations. It is also suggested that a population balance equation(s) be implemented – this will allow greater flexibility to incorporate different particle size-dependent reaction regimes if necessary, and also allows the HEX reactor model framework to be extended to account for transient behavior (e.g., response to a disturbance/change in reactor inlet conditions).

2) AC Solubility – the estimated solubility of AC in PG did not follow the expected increasing trend with respect to temperature, which was further complicated by the similar sensitivity of the batch reactor model's predictions to the dissolution mass transfer coefficient. Therefore, estimates of parameters associated with the solid-phase mechanisms (k_{dis}, k_{het}, K_{het}) would be improved if $x_{AC,sat}$ were experimentally characterized as a function of temperature. Such an experimental study would need to take care to ensure that the decomposition reaction is slow, which may require conducting the experiment at lower temperatures and extrapolating. Alternatively, one may conduct an equilibrium study in a sealed, temperature-regulated chamber filled completely with PG and a known amount of AC. The temperature can be slowly raised until there is no visible solid AC present; if the PG were saturated with NH_3 prior to conducting the experiment, equilibrium in the solution would favor dissolved PG.

3) Nucleation – the model in this study did not consider the possibility of nucleation on the particle surface, which has been explored by a few authors experimentally (e.g., [39]), but not with a rapidly reacting and dissolving solid particle. It would be especially fruitful if nucleation rate expressions that are not reliant on correlations for specific vessels, such as that of Fan et al [39] or Liu *et al.* [113] or Liu [114], were integrated into the model to describe both nucleation occurring on the HEX reactor surface and on the solid-phase. In addition, the Leveque analogy dependence on the two-phase multiplier, F_{TP}, does not account for the quenching [115] contribution to convective heat transfer that occurs when bubbles are

released from the reactor wall and are suddenly replaced by “fresh” liquid; an appropriate nucleation model could be combined with quenching effect correlations [115] to improve heat transfer coefficient predictions.

4) Slurry Rheological Behavior – In this study, the fluids were treated as Newtonian; however, it has been well documented [89, 94 - 98] that the presence of small suspended particles causes non-Newtonian rheological behavior to arise, in addition to enhancements in the effective thermal conductivity. An experimental investigation would be necessary to characterize and validate a model to describe the apparent viscosity and thermal conductivity in the presence of a highly soluble, reactive solid-phase. It was suspected that this effect was responsible for the underprediciton of heat transfer at low residence times, when the gas-phase had only a small and brief presence.

7.4 Parameter Space Mapping and Uncertainty Quantification

The model developed in this study could potentially be combined with high performance parallel computing to obtain multi-dimensional maps of the three HEX reactor performance parameters – balance, conversion, and capacity – as functions of operating conditions and/or design parameters. This data can be used to construct operating regime maps that visually delineate convection-dominant, reaction-dominant, or heat transfer-limited regimes as functions of the independent parameters of interest. A

compilation of operating regime maps would allow rapid interpretation of complex trends with respect to multiple parameters.

In the same vein, response surfaces approximating the input/output relationship of the model (surrogate models) could be generated and used to perform global sensitivity analyses to extend the results of the local sensitivity analyses conducted in this work [117]. Multiple approaches to developing surrogate models for this purpose are possible, including interpolation functions between tabulated model outputs, regression curves, or neural networks, among others [117].

This approach also permits variances in the HEX reactor performance metrics to be correlated to variances in the input parameters (*i.e.*, operating conditions) [117]. In this fashion, Monte-Carlo sampling of statistical distributions in the input parameters can be used as to rapidly compute statistical distributions in the performance metrics [117]. Understanding which input variance(s) are linked to the strongest model prediction variance(s) provides indispensable guidance in experimental design and further parameter estimation studies. On the other hand, the same technique may be applied to deduce statistical distributions in the estimated parameters, given knowledge of the uncertainties in the empirical correlations and the experimental measurements used to fit the model response. One could then obtain a more descriptive and comprehensive measure of the 'goodness-of-fit' for a given estimated parameter set; while the RSS error shows the extent to which the estimated parameters fit a particular experimental data set/objective function, it does not provide the statistical context necessary to judge the agreement with experiment on a global basis – *i.e.* factoring in the uncertainties in the

observed phenomena the model is intended to describe. Extracting the PDFs associated with the estimated parameters is especially useful when it is not feasible to conduct multiple trials of the same experiment, as was the case in this work and in the work of Johnson *et al*. [70].

REFERENCES

[1] I. Mudawar, Assessment of high-heat-flux thermal management schemes, Components and Packaging Technologies, IEEE Transactions on. 24 (2001) 122-141.

[2] Z.W. Ma, P. Zhang, Pressure drop and heat transfer characteristics of clathrate hydrate slurry in a plate heat exchanger, Int. J. Refrig. 34 (2011) 796-806.

[3] J. Bellas, I. Chaer, S.A. Tassou, Heat transfer and pressure drop of ice slurries in plate heat exchangers, Appl. Therm. Eng. 22 (2002) 721-732.

[4] G. Glatzmaier, Summary Report for Concentrated Solar Power Thermal Workshop, NREL (2011).

[5] J.E. Schmidt, D.S. Dudis, J. D.J. Miller, Expendable high energy density thermal management material: ammonium carbamate, J. Thermophysics Heat Trans. 26 (2012) 345-351.

[6] J. E. Schmidt, D. D. Dudis, D. J. Miller, The use of ammonium carbamate as a high specific thermal energy density material for the thermal management of low grade heat, 42nd AIAA Thermophysics Conference (2011) .

[7] R.N. Bennet, P.D. Ritchie, D. Roxburgh, J. and Thomson, The system ammonia carbon dioxide ammonium carbamate. Part I.—The equilibrium of thermal dissociation of ammonium carbamate, Transactions of the Faraday Society. 49 (1953) 925-929.

[8] E.P.J. Egan, J.E.J. Potts, G.D. and Potts, Dissociation pressure of ammonium carbamate, Industrial engineering chemistry. 38 (1946) 454-456.

[9] T.R. Briggs, V. and Migrdichian, The Ammonium Carbamate Equilibrium, J. Phys. Chem. 28 (1924) 1121-1135.

[10] J. E. Schmidt, The use of ammonium carbamate as a high specific thermal energy density material for thermal management of low grade heat, MS Thesis University of Dayton 2011.

[11] A. M. Edge, I. Pearce, C. H. Phillips, C. H., Compact Heat Exchangers as Chemical Reactors for Process Intensification (PI), Proc. Intens. (1997) 175-189.

[12] Z. Anxionnaz, M. Cabassud, C. Gourdon, P. Tochon, Heat exchanger/reactors (HEX reactors): concepts, technologies: State-of-the-art, Chemical Engineering and Processing: Process Intensification 47 (2008) 2029-2050.

[13] D. Johnson, S. Patnaik, J. Ervin, An integrated chemical reactor-heat exchanger based on ammonium carbamate, Proc. SAE (2012).

[14] W. W. Focke, Turbulent convective transfer in plate heat exchangers, Int. Comm. Heat Mass Transfer 10 (1983) 201-210.

[15] W. W. Focke, J. Zachariades, I. Olivier, The effect of the corrugation inclination angle on the thermohydraulic performance of plate heat exchangers, Int. J. Heat Mass Transfer 28 (1985) 1469-1479.

[16] H. Martin, A theoretical approach to predict the performance of chevron-type plate heat exchangers, Chem Eng. Proc. 35 (1996) 301-310.

[17] A. Muley, R. M. Manglik, Experimental study of turbulent flow heat transfer and pressure drop in a plate heat exchanger with chevron plates, ASME J. Heat Transfer 121 (1999) 110-117

[18] D-H. Han, K-J. Lee, Y-H. Kim, The characteristics of condensation in brazed plate heat exchangers with different chevron angles, J. Korean Phys. Soc. 43 (2003) 66-73.

[19] A. Jokar, M. H. Hosni, S. J. Eckels, Dimensional analysis on the evaporation and condensation of refrigerant R134a in a minichannel plate heat exchanger, Applied Therm. Eng. 26 (2006) 2287-2300.

[20] W. S. Kuo, Y. M. Lie, Y. Y. Hsieh, T. F. Lin, Condensation heat transfer and pressure drop of refrigerant R-410a flow in a vertical plate heat exchanger, Int. J. Heat Mass Transfer 48 (2005) 5205-5220.

[21] G. A. Longo, Refrigerant R134a condensation heat transfer and pressure drop inside a small brazed plate heat exchanger, Int. J. Refrigeration 31 (2008) 780-789.

[22] J. R. García-Cascales, F. Vera-García, J. M. Corberán-Salvador, J. Gonzálvez-Maciá, Assessment of boiling and condensation heat transfer correlations in the modelling of plate heat exchangers, Int. J. Refrigeration 30 (2007) 1029-1041.

[23] M. Ciofalo, J. Stasiek, M.W. Collins, Investigation of flow and heat transfer in corrugated passages—II. Numerical simulations, Int. J. Heat Mass Transfer. 39 (1996) 165-192.

[24] P. J. Heggs, P. Sandham, R. A. Hallam. C. Walton, Local transfer coefficients in corrugated plate heat exchanger channels, Trans. IChemE 75 (A) (1997) 641-645.

[25] N. Niedbalski, D. Johnson, S.S. Patnaik, D. Banerjee, Study of a multi-phase hybrid heat exchanger-reactor (HEX reactor): part I – experimental characterization, Int. J. Heat Mass Transfer 70 (2014) 1078-1085.

[26] N. Niedbalski, D. Johnson, S.S. Patnaik, D. Banerjee, Study of a multi-phase hybrid heat exchanger-reactor (HEX reactor): part II – numerical prediction of thermal performance, Int. J. Heat Mass Transfer 70 (2014) 1086-1094.

[27] B. Claudel, L. Boulamri, A new model of gas-solid kinetics: the case of ammonium carbamate formation and decomposition, Thermochim. Acta 126 (1988) 129-148.

[28] B. R. Ramachandran , A. M. Halpern, E.D. Glendening, Kinetics and mechanism of the reversible dissociation of ammonium carbamate: involvement of carbamic acid, J. Phys. Chem. A 102 (1998) 3934-3941.

[29] Alicat Scientific M-series gas flow meter operating manual, Rev. 36 (2014) DOC-ALIMAN16.

[30] A.C. Galvao, A.Z. Francesconi, Methane and carbon dioxide solubility in 1,2-propylene glycol at temperatures ranging from 303 to 423 K and pressures up to 12 MPa, Fluid Phase Equilibria 289 (2010) 185-190.

[31] S. J. Kline, F. A. and McClintock, Describing uncertainties in single-sample experiments, Mech. Eng. 1 (1953) 3-8.

[32] O. J. Schierholtz, M. L. Staples, Vapor pressure of certain glycols, J. Am. Chem. Soc. 57 (1935) 2709-2711.

[33] Y. T. Kang, T. Nagano, T. Kashiwagi, Mass transfer correlation of NH_3-H_2O bubble absorption, Int. J. Refrigeration 25 (2002) 878-886.

[34] F. Scargiali, A. D'Orazio, F. Grisafi, A. Brucato, Modelling and simulation of gas-liquid hydrodynamics in mechanically stirred tanks, Chem. Eng. Research and Design 85 (2007) 637-646.

[35] M. Petitti, M. Vanni, D.L. Marchisio, A. Buffo, F. Podenzani, Simulation of coalescence, break-up and mass transfer in a gas-liquid stirred tank with CQMOM, Chem. Eng. J. 228 (2013) 1182-1194.

[36] F. Garcia-Ochoa, E. Gomez, Theoretical prediction of gas-liquid mass transfer coefficient, specific area and hold-up in sparged stirred tanks, Chem. Eng. Sci. 59 (2004) 2489-2501.

[37] R.V. Chaudhari, P.A. Ramachandran, Three phase slurry reactors, AIChE Journal 26 (1980) 177-201.

[38] V.G. Pangarkar, A.A. Yawalkar, M.M. Sharma, A.A.C.M. Beenackers, Particle-liquid mass transfer coefficients in two- /three- phase stirred tank reactors, Ind. Eng. Chem. Res. 41 (2002) 4141-4167.

[39] Y. Fan, F. Qin, X. Luo, J. Zhang, J. Wang, H. Gui, J. Liu, A modified expression for the steady-state heterogeneous nucleation rate, J. Aerosol Science

[40] S. Kresta, Turbulence in stirred tanks: anisoptropic, approximate, and applied, Canadian J. Chem. Eng. 76 (1998) 563-576.

[41] R.L. Steinberger, R.E. Treybal, Mass transfer from a solid soluble sphere to a flowing liquid stream, AIChE Journal 6 (1960) 227-232.

[42] P. Harriot, Mass transfer to particles: Part I. Suspended in agitated tanks, AIChE Journal 8 (1962) 93-101.

[43] P.M. Armenante, E. U. Nagamine, J. Susanto, Determination of correlations to predict the minimum agitation speed for complete solid suspension in agitated vessels, Canadian J. Chem. Eng. 76 (1998) 413-419.

[44] K.S.M.S.R. Rao, V.B. Rewatkar, J.B. Joshi, Critical impeller speed for solid suspension in mechanically agitated contactors, AIChE Journal 34 (1988) 1332-1340.

[45] A. Mersmann, F. Werner, S. Maurer, K. Bartosch, Theoretical prediction of the minimum stirrer speed in mechanically agitated suspensions, Chem. Eng. Proc. 37 (1998) 503-510.

[46] R. Taylor, R. Krishna, Multicomponent Mass Transfer, John Wiley and Sons (1993).

[47] S. P. Cadogan, Diffusion of CO_2 in Fluids Relevant to Carbon Capture, Utilisation and Storage, Ph.D. Thesis, Imperial College London 2016.

[48] S. Peng, A.N. Soriano, M. Li, Ternary diffusion coefficients of diethylene glycol and lithium chloride in aqueous solutions containing diethylene glycol and lithium chloride, Fluid Phase Equilibria 297 (2010)1-5.

[49] D. M. Maharajh, J. Walkley, The temperature dependence of the diffusion coefficients of Ar, CO_2, CH_4, CH_3Cl, CH_3Br, and $CHCl_2F$ in Water, Can, J. Chem. 51 (1973) 944-952.

[50] S.P. Cadogan, G. C. Maitland, J.P. Martin-Trusler, Diffusion coefficients of CO_2 and N_2 in water at temperatures between 298.15 K and 423.15 K and pressures up to 45 MPa, J. Chem. Eng. Data 59 (2014) 519-525.

[51] M.J.W. Frank, J.A.M. Kuipers, W.P.M. van Swaaij, Diffusion coefficients and viscosities of $CO_2 + H_2O$, $NH_3 + H_2O$, and $NH_3 + CH_3OH$ liquid mixtures, J. Chem. Eng. Data 41 (1996) 297-302.

[52] E.K. Iskrenova, S.S. Patnaik, Solvent effects in the thermal decomposition reaction of ammonium carbamate: A computational molecular dynamics study of the relative solubilities of CO_2 and NH_3 in water, ethylene glycol and their mixtures, Int. J. Heat Mass Transfer 100 (2016) 224-230.

[53] P. J. W. Derks, G. F. Versteeg, Kinetics of absorption of carbon dioxide in aqueous ammonia solutions, Energy Procedia 1 (2009) 1139-1146.

[54] H. Park, Y.M. Jung, J.K. You, W. H. Hong, J.N. Kim, Analysis of the CO_2 and NH_3 reaction in an aqueous solution by 2D IR COS: formation of bicarbonate and carbamate, J. Phys. Chem. 112 (2008) 6558-6562.

[55] X. Wang, W. Conway, D. Fernandes, G. Lawrance, R. Burns, G. Puxty, M. Maeder, Kinetics of the reversible reaction of CO_2(aq) with ammonia in aqueous solution, J. Phys. Chem. A 115 (2011) 6405-6412.

[56] T.F. Hatch, R.L. Pigford, Simultaneous absorption of carbon dioxide and ammonia in water, I&EC Fundamentals 1 (1962) 209-214.

[57] B. R. W. Pinset, L. Pearson, F. J. W. Roughton, The kinetics of combination of carbon dioxide with ammonia, Trans. Faraday Soc. 52 (1956) 1594-1598.

[58] P.V. Danckwerts, The reaction of CO_2 with ethanolamines, Chem. Eng. Sci. 34 (1979) 443-446.

[59] M. Caplow, Kinetics of carbamate formation and breakdown, J. American Chem. Soc. 90 (1968) 6795-6803.

[60] V. Darde, W. J. M. van Well, P. L. Fosboel, E. H. Stenby, K. Thomsen, Experimental measurement and modeling of the rate of absorption of carbon dioxide by aqueous ammonia, Int. J. Greenhouse Gas Control 5 (2011) 1149-1162.

[61] H. Chen, B. Dou, Y. Song, Y. Xu, X. Wang, X. Du, C. Wang, X. Zhang, C. Tan, Studies on absorption and regeneration for CO_2 capture by aqueous ammonia, Int. J. Greenhouse Gas Control 6 (2012) 171-178.

[62] J. E. Crooks, J. P. Donnellan, Kinetics and mechanism of the reaction between carbon dioxide and amines in aqueous solution, J. Chem. Soc. Perkin Trans. II (1989) 331-333.

[63] E. F. da Silva, H. F. Svendsen, Ab initio study of the reaction of carbamate formation from CO_2 and alkanolamines, Ind. Eng. Chem. Res. 43 (2004) 3413-3418.

[64] J. Liu, S. Wang, G. Qi, B. Zhao, C. Chen, Kinetics and mass transfer of carbon dioxide absorption into aqueous ammonia, Energy Procedia 4 (2011) 525-532.

[65] H. Hikita, Y. Konishi, Desorption of carbon dioxide from supersaturated water in an agitated vessel, AIChE Journal 30 (1984) 945-951.

[66] H. Kierzkowska-Pawlak, A. Chacuk, Carbon dioxide desorption from saturated organic solvents, Chem. Eng. Tech. 33 (2010) 74-81.

[67] B. C. Hoke, E. F. Patton, Surface tensions of propylene glycol + water, J. Chem. Eng. Data 37 (1992) 333- 337.

[68] F. Kudrewizki, P. Rabe, Model of the dissipation of mechanical energy in gassed stirred tanks, Chem. Eng. Sci. 41 (1985) 2247- 2252.

[69] A. van den Bos, Parameter Estimation for Scientists and Engineers, John Wiley and Sons (2007).

[70] D. J. Johnson, N.P. Niedbalski, J.S. Ervin, S.S. Patnaik, Ammonium carbamate-based heat exchanger reactor as an endothermic heat sink for thermal management, Int. J. Heat Mass Transfer 91 (2015) 766-776.

[71] F. Patron, S.A. Adelman, Solvent cage effects and chemical dynamics in liquids, Chem. Phys. 152 (1991) 121-131.

[72] I. M. Klotz, R.M. Rosenberg, Chemical Thermodynamics: Basid Theory and Methods 6th Ed., John Wiley and Sons (2000).

[73] J.M. Moore, C.L. Stanitski, P.C. Jurs, Chemistry: The Molecular Science, Thompson Brooks/Cole (2005).

[74] T. Sun, A.S. and Teja, Density, viscosity and thermal conductivity of aqueous solutions of propylene glycol, dipropylene glycol, and tripropylene glycol between 290 K and 460 K, J. Chem. Eng. Data 49 (2004) 1311-1317

[75] F.P. Incropera, D.P. Dewitt, T.L. Bergman, A.S. Lavine, Fundamentals of Heat and Mass Transfer, 6th ed., John Wiley and Sons, New Jersey, 2007.

[76] M.J. Moran, H.N. Shapiro, Fundamentals of Engineering Thermodynamics, 6th Ed., John Wiley and Sons, New Jersey, 2007.

[77] M.C. Georgiadis, S. Macchietto, Dynamic modelling and simulation of plate heat exchangers under milk fouling, Chem. Eng. Sci. 55 (2000) 1605-1619.

[78] J. Wang, S. Han, F. Wei, Z. Yu, Y. Jin, An axial dispersion model for gas-liquid reactors based on the penetration theory, Chem. Eng. Processing 36 (1997) 291-299.

[79] V. Alopaeus, H. Laavi, J. Aittamaa, A dynamic model for plug flow reactor state profiles, Computers and Chem. Eng. 32 (2008) 1494-1506.

[80] J.G. Collier, J.R. Thome, Convective Boiling and Condensation, third ed., Oxford University Press, New York, 1996.

[81] V.P. Carey, Liquid-Vapor Phase-Change Phenomena: An Introduction to the Thermophysics of Vaporization and Condensation Processes in Heat Transfer Equipment, 1992.

[82] N. Hooshyar, D. Vervloet, F. Kapteijn, P.J. Hamersma, R.F. Muddle, J.R. van Ommen, Intensifying the Fischer-Tropsch synthesis by reactor structuring – a model study, Chem. Eng. J. 207-208 (2012) 885-870.

[83] D. Vervloet, F. Kapteijn, J. Nijenhuis, J.R. van Ommen, A convection-based single-parameter model for heat transport in multiphase tubular reactors packed with closed cross flow structures, Chem. Eng. J. 233 (2013) 265-273.

[84] H. A. Jakobsen, Chemical Reactor Modeling, Springer-Verlag, Berlin (2008).

[85] M. Ishii, K. Mishima, Two-fluid model and hydrodynamic constitutive relations, Nuclear Eng. Design 82 (1984) 107-126.

[86] N.P. Cheremisinoff, R. Gupta, Handbook of Fluids in Motion, (1983) 895-927.

[87] W.E. Ranz, W.R. Marshall, Evaporation from drops, Chem. Eng. Progress 48 (1952) 141-146, 173-180.

[88] S. Nedeltchev, Theoretical prediction of mass transfer coefficients in both gas-liquid and slurry bubble columns, Chem. Eng. Sci. 157 (2017) 169-181.

[89] J. Garcia-Ochoa, R. Khalfet, S. Poncin, G. Wild, Hydrodynamics and mass transfer in a suspended solid bubble column with polydispersed high density particles, Chem. Eng. Sci. 52 (1997) 3827-3834.

[89] T.M. Adams, S.M. Ghiaasiaan, S.I. Abdel-Khalik, Enhancement of liquid forced convection heat transfer in microchannels due to the release of dissolved noncondensibles, Int. J. Heat Mass Transfer 42 (1999) 3563-3573.

[90] G. Kreissig, H.M. Müller-Steinhagen, Frictional Pressure Drop for Gas/Liquid Two-Phase Flow in Plate Heat Exchangers, Heat Transfer Eng. 13 (1992) 42-52.

[91] C. Tribbe, H.M. Müller-Steinhagen, Gas/Liquid Flow in Plate-and-Frame Heat Exchangers - Part II: Two-Phase Multiplier and Flow Pattern Analysis, Heat Transfer Eng. 22 (2001) 12-21.

[92] C. Tribbe, H.M. Müller-Steinhagen, Gas/Liquid Flow in Plate-and-Frame Heat Exchangers - Part I: Pressure Drop Measurements, Heat Transfer Eng. 22 (2001) 5-11.

[93] P. Vlasogiannis, G. Karagiannis, P. Argyropoulos, V. Bontozoglou, Air–water two-phase flow and heat transfer in a plate heat exchanger, Int. J. Multiphase Flow. 28 (2002) 757-772.

[94] P. Charunyakorn, S. Sengupta, S.K. Roy, Forced convection heat transfer in microencapsulated phase change material slurries: flow in circular ducts, Int. J. Heat Mass Transfer 34 (1991) 819-833.

[95] K. Chen, M.M. Chen, An analytical and experimental investigation of the convective heat transfer of phase-change slurry flows, Proc. Int. Symp. Multiphase Flows (II) (1987) 496-501.

[96] C.W. Sohn, M.M. Chen, Microconvective thermal conductivity in disperse two-phase mixture as observed in a laminar flow, J. Heat Transfer 103 (1981) 47-51.

[97] C.W. Sohn, M.M. Chen, Heat transfer enhancement in laminar slurry pipe flows with power law thermal conductivities, J. Heat Transfer 106 (1984) 539-542.

[98] A.S. Ahuja, Augmentation of heat transport in laminar flow of polystyrene suspensions: Part I, J. Appl. Phys. 46 (1975) 3408-3416.

[99] Y. Sato, K. Sekoguchi, Liquid velocity distribution in two-phase bubble flow, Int. J. Multiphase Flow. 2 (1975) 79-95.

[100] A.S. Jones, Heat transfer in the thermal entrance region of a flat duct, Journal of the Australian Mathematical Society.Series A.Pure mathematics and statistics. 19 (1975) 146-160.

[101] S.Z. Rouhani, E. Axelsson, Calculation of void volume fraction in the subcooled and quality boiling regions, Int. J. Heat Mass Transfer. 13 (1970) 383-393.

[102] B. Claudel, E. Brousse, G. Shehadeh, Novel thermodynamic and kinetic investigation of ammonium carbamate decomposition into urea and water, Thermochimica Acta 102 (1986) 357-371.

[103] L. Leal, M. Miscevic, P. Lavieille, M. Amorkane, F. Pigache, F. Topin, B. Nogarede, L. Tadrist, An overview of heat transfer enhancement methods and new perspectives: Focus on active methods using electroactive materials, Int. J. Heat Mass Transfer 61 (2013) 505-524.

[104] L. Silva-Llanca, A. Ortega, Vortex dynamics and mechanisms of heat transfer enhancement in synthetic jet impingement, Int. J. Thermal Sciences 112 (2017) 153-164.

[105] A. Ihara, H. Watanabe, On the flow around flexible plates, oscillating with large amplitude, J. Fluids Structures 8 (1994) 601-619.

[106] J.C. Shyu, J.Z. Syu, Plate-fin array cooling using a finger-like piezoelectric fan, Applied Thermal Eng. 62 (2014) 573-580

[107] Y. Yu, T.W. Simon, M. Zhang, T. Yeom, M.T. North, T. Cui, Enhancing heat transfer in air-cooled heat sinks using piezoelectrically-driven agitators and synthetic jets, Int. J. Heat Mass Transfer 68 (2014) 184-193.

[108] M. Sheikholeslami, M.G. Bandpy, R. Ellahi, A. Zeeshan, Simulation of MHD CuO-water nanofluid flow and convective heat transfer considering Lorentz forces, J. Magnetism Magnetic Materials 369 (2014) 69-80.

[109] P. Stonestreet, A.P. Harvey, A Mixing-based design methodology for continuous oscillatory flow reactors, Chem. Eng. Research Design 80 (2002) 31-44.

[110] A.P. Harvey, M.R. Mackley, T. Seliger, Process Intensification of biodiesel production using a continuous oscillatory flow reactor, Chemical Tech. Biotech. 78 (2003) 338-341.

[111] A.P. Harvey, M.R. Mackley, P. Stonestreet, Operation and optimization of an oscillatory flow continuous reactor, Ind. Eng. Chem. Res. 40 (2001), 5371-5377.

[112] J.P. Solano, R. Herrero, S. Espin, A.N. Phan, A.P. Harvey, Numerical study of the flow pattern and heat transfer enhancement in oscillatory baffled reactors with helical coil inserts, Chem. Eng. Research Design 90 (2012) 732-742.

[113] X.Y. Liu, K. Maiwa, K. Tsukamoto, Heterogeneous two-dimensional nucleation and growth kinetics, J. Chem. Phys. 106 (1997) 1870-1879.

[114] X.Y. Liu, A New kinetic model for three-dimensional heterogeneous nucleation, J. Chem. Phys. 111 (1999) 1628-1635.

[115] E. Chen, Y. Li, X. Cheng, CFD simulation of upward subcooled boiling flow of refrigerant-113 using the two-fluid model, Applied Thermal Eng. 29 (2009) 2508-2517.

[116] J. Fernandez-Seara, F.J. Uhia, J. Sieres, A. Campo, A general review of the Wislon plot method and its modifications to determine convection coefficients in heat exchange devices, Applied Thermal Eng. 27 (2007) 2745-2757.

[117] Assesing the Reliability of Complex Models, National Research Council of the National Academies, Washington, D.C., 2012.

APPENDIX

A.1 Single-Phase Characterization

The experimental facility consists of two fluid loops: the load side, which carries distilled water; and the reactant side, which carries propylene glycol (PG). The water circulating on the load side is heated by an in-line resistance heater to the desired operating temperature, which subsequently passes through the HEX reactor and heats the circulating PG. The glycol is kept at a constant inlet temperature ($T_{R,in}$) by passing through a secondary glycol cooling heat exchanger (GCHX), which is cooled by a fan-cooled laboratory recirculator. A schematic representation of the experimental facility is provided in Figure 118:

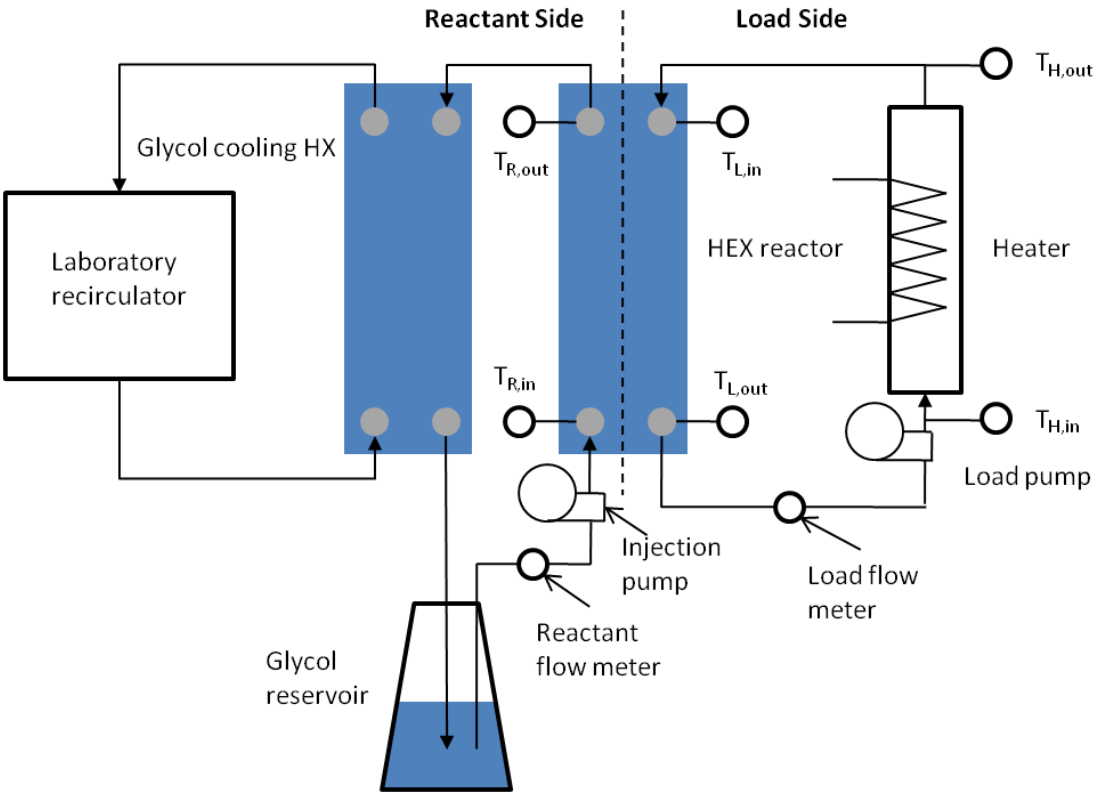

Figure 118. Diagram of experimental apparatus used in single-phase heat transfer characterization

The HEX reactor is an Alfa Laval MF3 gasketed plate heat exchanger with 30° chevrons and total of 12 heat transfer plates (and two end plates). The total available heat transfer surface area is approximately 0.327 m^2, with maximum plate clearance of 3 mm. The GCHX is a Danfoss brazed plate heat exchanger (B3-052-20-4.5-H) run in a counterflow configuration. The power output of the heater is adjusted by a PID controller; the $T_{L,out}$ probe is used as the controller input. The flow meters, temperature probes, heater current and heater voltage readings are captured by a National Instruments data acquisition module and fed to a digital computer, where the readouts are displayed and recorded by LabVIEW (8.6) (National Instruments) software. The HEX reactor and

heater are enclosed within a plexiglass chamber to minimize the effect of ambient convection on the reactor energy balance. Steady-state losses follow an approximately linear relationship with respect to average load temperature. At the desired operating range (60°C-70°C), assuming an ambient convection coefficient of 5 $w/m^2/K$ and environment temperature of ~23°C, losses from the reactor are expected to be on the order of 50 W.

A.1.1 Load-side heat transfer characterization

A set of water-to-water heat transfer characterization tests were performed using the facility illustrated in Figure 118, except with the glycol reservoir, glycol cooling heat exchanger, and injection pump replaced with a single water loop through the laboratory recirculator. Tests were conducted by fixing the load-side outlet temperature and holding both the load-side and reactant-side flow rates constant so that the system could reach a steady-state condition. The system was judged to be at steady-state once the PID output stabilized, and the load-side outlet temperature did fluctuate by more than 0.2°C. Temperature, flow rate, and absolute pressure data were subsequently recorded at a rate of 2Hz for at least 10 minutes to ensure that time-averaged quantities were representative of sustained operation. The following analysis was used to obtain the heat transfer characteristics of the load-side in the form of a Nusselt number correlation.

For steady-state heat exchanger operation, Newton's law of cooling is recast in terms of an overall thermal resistance and an effective average temperature difference to compute the heat flux:

$$\dot{Q}_L = h_{eff} A_w (N-2) \Delta T_{lm} \tag{A.1}$$

where, h_{eff} is the overall heat transfer coefficient, A_w is the area of a corrugated plate, N is the total number of plates in the PHE, and ΔT_{lm} is the log-mean temperature difference defined as:

$$\Delta T_{lm} = \frac{\Delta T_2 - \Delta T_1}{\ln\left(\frac{\Delta T_2}{\Delta T_1}\right)} \tag{A.2}$$

Where, for a counterflow heat exchanger,

$$\Delta T_1 = T_{L,in} - T_{R,out} \tag{A.3}$$

$$\Delta T_2 = T_{L,out} - T_{R,in} \tag{A.4}$$

Assuming negligible fouling and the same plate surface area on both hot (load) and cold (reactant) sides, the overall thermal resistance ($1/h_{eff}$) is the algebraic sum of the thermal resistances due to convection in the working fluids and conduction through the plate:

$$\frac{1}{h_{eff}} = \frac{1}{h_R} + \frac{l_w}{\kappa_w} + \frac{1}{h_L} \tag{A.5}$$

If h_L is known, and h_{eff} is computed experimentally according to Eq. (A.1), Eq. (A.5) may be readily used to obtain h_R. Hence, a correlation is needed that relates h_L to known load-side operating conditions (i.e., flow and temperature). A popular method for obtaining such a correlation in PHEs is the modified Wilson plot technique [115], which is employed herein. The basis for the modified Wilson plot is a transformation of Eq. (A.5), which is obtained by assuming a power law relationship for the Nusselt number:

$$h = C\left(\frac{\kappa}{d_e}\right)\mathrm{Re}^n \mathrm{Pr}^m \left(\frac{\mu}{\mu_w}\right)^p \tag{A.6}$$

where, κ is the thermal conductivity, d_e is the mean channel spacing, μ is the dynamic viscosity evaluated at the fluid bulk temperature, μ_w is the dynamic viscosity evaluated at the wall temperature, Pr is the Prandtl number, and Re is the Reynolds number, defined as:

$$\mathrm{Re} = \frac{\dot{m} d_e}{\mu A_c N^*} \tag{A.7}$$

where, $\dot{m}$ is the mass flow rate, A_c is the cross sectional area of the channel (defined here as the product of plate width and mean channel spacing), and N^* is the number of channels (6 for the load side and 7 for the reactant side). Note that this definition does not consider flow maldistribution.

Substituting Eq. (A.6) into Eq. (A.5), multiplying by $\left(\kappa_L / d_e\right)\mathrm{Re}_L^n \,\mathrm{Pr}_L^m \left(\mu_L / \mu_{L,w}\right)^p$ and rearranging yields the following:

$$\left[\frac{1}{h_{eff}} - \frac{l_w}{\kappa_w}\right]\left(\frac{\kappa_L}{d_e}\right)\mathrm{Re}_L^n \,\mathrm{Pr}_L^m \left(\frac{\mu_L}{\mu_{L,w}}\right)^p = \frac{1}{C_L} + \frac{1}{C_R}\left(\frac{\mathrm{Re}_L}{\mathrm{Re}_R}\right)^n \left(\frac{\mathrm{Pr}_L}{\mathrm{Pr}_R}\right)^m \left(\frac{\kappa_L}{\kappa_R}\right)\left(\frac{\mu_L \mu_{R,w}}{\mu_R \mu_{L,w}}\right)^p \tag{A.8}$$

Defining the following variables:

$$X = \left(\frac{\mathrm{Re}_L}{\mathrm{Re}_R}\right)^n \left(\frac{\mathrm{Pr}_L}{\mathrm{Pr}_R}\right)^m \left(\frac{\kappa_L}{\kappa_R}\right)\left(\frac{\mu_L}{\mu_R}\frac{\mu_{R,w}}{\mu_{L,w}}\right)^p \tag{A.9}$$

$$Y = \left[\frac{1}{h_{eff}} - \frac{l_w}{\kappa_w}\right]\left(\frac{\kappa_L}{D}\right)\mathrm{Re}_L^n \,\mathrm{Pr}_L^m \left(\frac{\mu_L}{\mu_{L,w}}\right)^p \tag{A.10}$$

One obtains:

$$Y = \frac{1}{C_R} X + \frac{1}{C_L} \tag{A.11}$$

The implementation of this technique may be simplified if water is used as the working fluid on both the load and reactant sides for obtaining Wilson plot data. Assuming both sides are operating in the same flow regime, the Reynolds and Prandtl number dependence (i.e., the exponents and leading multiplier) should be identical. The

leading multiplier, *C*, can be obtained by plotting *Y* as a function of *X* and computing the slope of a best-fit linear regression to the data. The exponents *m* and *p* were set to 1/3 and 0.14, respectively, for consistency with similar correlations in the literature [75]. The exponent *n* was selected such that the R^2 goodness-of-fit coefficient of a linear regression to the data was at a maximum for the data set obtained. It was determined that a value of $n = 0.67$ provided the best linear fit:

$$Nu_L = 0.187\,\mathrm{Re}_L^{0.67}\,\mathrm{Pr}_L^{1/3} \tag{A.12}$$

The Wilson plot constructed with these parameters is shown in Figure 119, and the resulting correlation for $Nu_L Pr_L^{-1/3}$ is plotted in Figure 120:

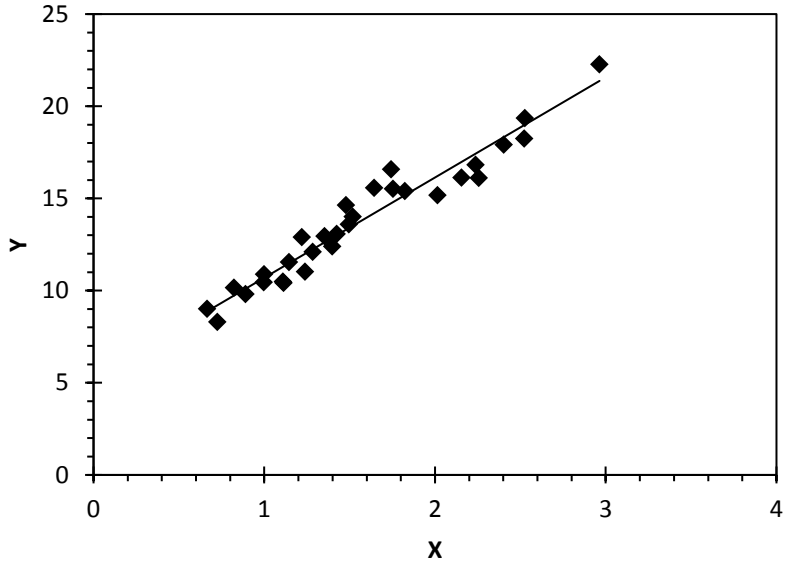

Figure 119. Wilson plot obtained from water-water single-phase testing

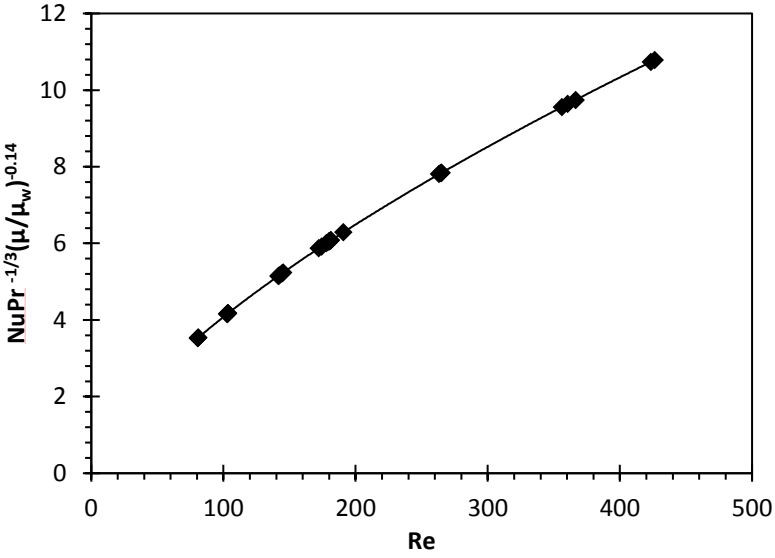

Figure 120. Plot of $NuPr^{1/3}(\mu/\mu_w)$ as function of Re for the load side of the HEX reactor

With the load pump, Reynolds numbers ranging from 200 – 430 could be realized; load-side inlet temperatures varied between 50 and 56 °C, and reactant-side inlet temperatures varied between 43 and 52°C. All fluid properties were evaluated at the average bulk temperature ((T_{in}+T_{out})/2). Figure 121 shows a parity plot with the experimentally measured overall heat transfer coefficient plotted against the predicted value using Eq. (A.12), demonstrating acceptable agreement. The maximum and average errors (between experimental and calculated h_{eff}) observed were 9.3% and 4.5%, respectively; the standard deviation was 3.2%.

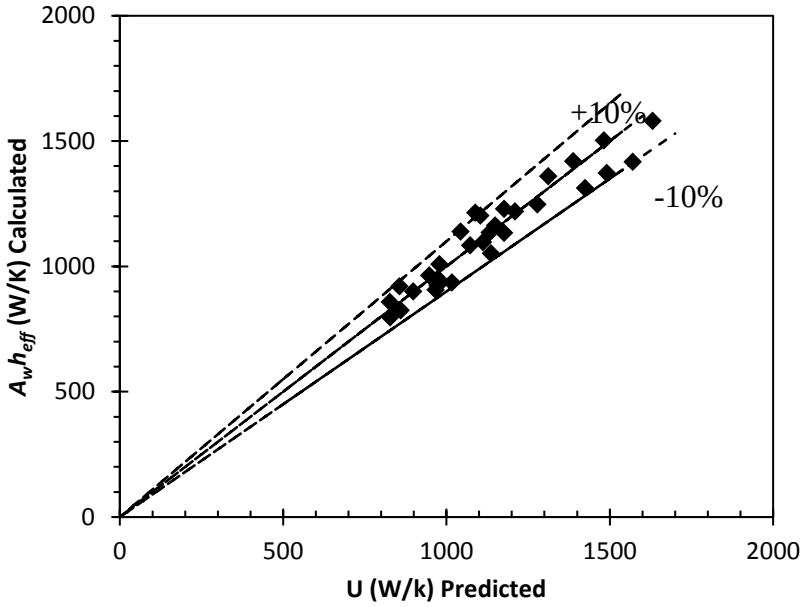

Figure 121. Parity plot comparing overall heat transfer coefficient *U* calculated experimentally with predictions using Eq. (11)

It should be noted that Eq. (A.12) is a calibration equation valid only for the above stated experimental conditions and the specific PHE model used as the HEX reactor.

A.1.2 Reactant-side heat transfer characterization

The experimental facility illustrated in Figure 118 was employed, using the same testing procedure described above, to extract a single-phase Nusselt number correlation for the reactant-side with glycol as the working fluid. This correlation serves as a thermal performance baseline to which the multi-phase reacting flow may be compared. Such an approach allows for the effect of gas evolution on convective heat transfer to be discerned when compared to single-phase heat transfer at the same flow rate and temperature. From Eq. (A.5), the reactant-side heat transfer coefficient may be calculated by using the load-side correlation developed previously (Eq. (A.12)):

$$h_R = \left[\frac{1}{h_{eff}} - \frac{1}{h_L} - \frac{l_w}{\kappa_w} \right]^{-1} \tag{A.13}$$

Because the viscosity of propylene glycol is a strong function of temperature, tests were conducted at mean glycol bulk temperatures ranging from 58°C to 70°C, with Reynolds numbers from 2 to 40. Fluid properties were again evaluated at the mean bulk temperature. The reactant-side Nusselt number was then plotted against the group $Re_R^n Pr_R^{1/3}$ as depicted in Figure 122; the Reynolds number exponent n was adjusted iteratively until the plot was linearized:

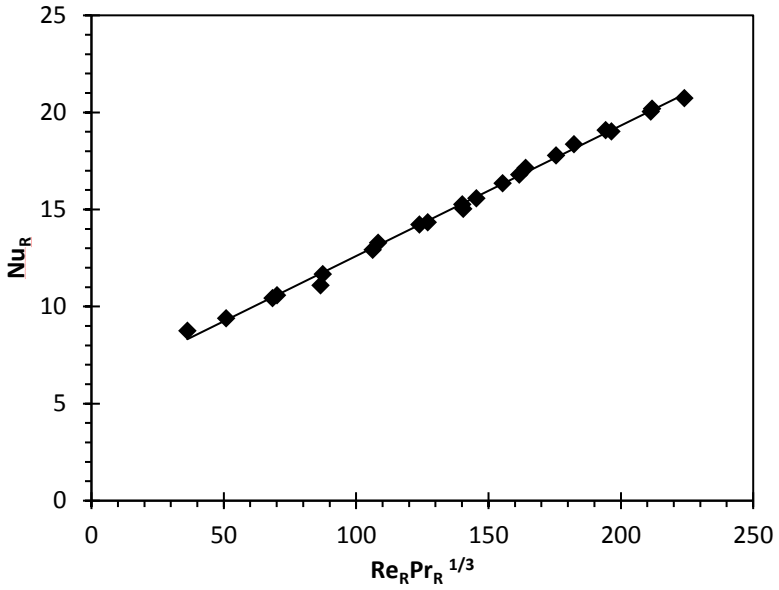

Figure 122. Plot of reactant-side Nusselt number as a function of Reynolds-Prandtl product

The resulting correlation is as follows:

$$Nu_R = 0.067\,\mathrm{Re}_R\,\mathrm{Pr}_R^{1/3} + 5.93 \tag{A.14}$$

The maximum and average error between Eq. (A.14) and the experimentally measured Nusselt number was 6% and 1%, respectively. Eq. (A.14) was adjusted to obtain Eq. (6.47) so maximize agreement with the data in Table 5.

It was observed, at glycol mass flow rates below 80 g/s, that the discrepancy between the load-side and reactant-side energy balances, $\Delta\dot{Q} = \dot{m}_L c_{p,L} \Delta T_L - \dot{m}_R c_{p,R} \Delta T_R$, tended to increase in severity. Because this disagreement was ameliorated at higher glycol flow rates, it was judged that imperfect mixing in the HEX reactor manifold was

responsible. The outlet temperature probes were moved outside of the manifold and into the downstream pipeline to allow for additional mixing to occur in the fluid before reaching the probe tip, thereby furnishing a more representative measurement of the bulk fluid temperature. Tests repeated with this new arrangement confirmed a reduction in $\Delta\dot{Q}$ for the same temperature set points and flow rates.

A.1.3 Uncertainty Analysis

The uncertainties associated with independent experimental variables were assumed to be the instrument manufacturers reported limits of error.

Table 16. Instrument uncertainties claimed by manufacturer

Instrument	Model/mfg.	Uncertainty	Range
Load flow meter	110-039 Turbine/ Omega	± 0.32%	2.3-11.4 LPM
Reactant flow meter	FTB2005 Turbine/ Omega	± 3%	2-30 LPM
Temp. Probes	K-type / Omega	± 0.1 °C	-
Absolute Pressure Transducers	PX409-050 A5V/ Omega		0-50 PSI

Uncertainty propagation was estimated using the Klein-McKlintock method [31]:

$$\varepsilon = \sqrt{\sum_{i}^{K} \varepsilon_{x_i}^2} \tag{A.15}$$

where, ε_{x_i} is the relative uncertainty associated with the *i*-th independent experimental variable x_i, which is defined as:

$$\varepsilon_{x_i} \equiv \frac{\delta x_i}{x_i} \tag{A.16}$$

Thus, neglecting the uncertainty in fluid properties, the uncertainty for the load- or reactant-side heat transfer rate is estimated as:

$$\varepsilon_{\dot{Q}} = \sqrt{\varepsilon_{\dot{m}}^2 + \varepsilon_{\Delta T}^2} \tag{A.17}$$

where, ΔT is the inlet-to-outlet temperature change on the load- or reactant-side:

$$\delta \Delta T^2 = \delta T_{in}^2 + \delta T_{out}^2 \tag{A.18}$$

The total heat transfer rate $\dot{Q}$ is estimated as an average of $\dot{Q}_L$ and $\dot{Q}_R$, therefore:

$$\varepsilon_{\dot{Q}} = \sqrt{\frac{\delta \dot{Q}_L^2 + \delta \dot{Q}_R^2}{\dot{Q}^2}} \tag{A.19}$$

Similarly, the uncertainty of overall heat transfer coefficient calculations may be estimated as:

$$\varepsilon_{h_{eff}} = \sqrt{\varepsilon_{\dot{Q}}^2 + \varepsilon_{\Delta T_{lm}}^2} \tag{A.20}$$

Using Eqs. (2) and (15), the log-mean temperature difference (absolute) uncertainty is calculated as:

$$\delta\Delta T_{lm}^2 = \left[\left(\frac{\partial}{\partial T_2}\Delta T_{lm}\right)\delta\Delta T_2\right]^2 + \left[\left(\frac{\partial}{\partial T_1}\Delta T_{lm}\right)\delta\Delta T_1\right]^2 \tag{A.21}$$

Thus, after some manipulation,

$$\varepsilon_{\Delta T_{lm}}^2 = \left\{\frac{\delta\Delta T_2}{\Delta T_2 - \Delta T_1}\left[1 - \frac{\Delta T_{lm}}{\Delta T_2}\right]\right\}^2 + \left\{\frac{\delta\Delta T_1}{\Delta T_2 - \Delta T_1}\left[-1 + \frac{\Delta T_{lm}}{\Delta T_1}\right]\right\}^2 \tag{A.22}$$

Table 17 shows the average and maximum relative uncertainties calculated from the water-water Wilson plot tests. The load-side heat transfer coefficient uncertainty (ε_{h_L}) was estimated to be that of h_{eff}, which is ±11.8%. This value is in good agreement with the deviation from the calibration curve (Eq. (A.12)), where h_{eff} is predicted to within 10%. Table 18 shows the average and maximum calculated uncertainties for the water-glycol tests. The Klein-McKlintock method appears to over-estimate the uncertainty of the reactant-side heat transfer coefficient; the maximum error between Eq. (A.14) and the experimental results was 6%.

Table 17. Estimated relative uncertainties for water-water characterization tests

Quantity	Average ε	Maximum ε
ΔT_L	7.1%	12.2 %
ΔT_R	5.3%	10.0 %
$\dot{Q}_L$	7.2%	12.2%
$\dot{Q}_R$	7.4%	14.0 %
$\dot{Q}$	10.8%	14.9 %
ΔT_{lm}	4.8%	5.9 %
h_{eff}	11.8%	15.8 %

Table 18. Estimated relative uncertainties for water-glycol characterization tests

Quantity	Average ε	Maximum ε
ΔT_L	10.7 %	12.3 %
ΔT_R	8.0 %	13.3 %
$\dot{Q}_L$	10.8 %	12.4 %
$\dot{Q}_R$	9.0 %	13.7 %
$\dot{Q}$	14.3 %	18.2%
ΔT_{lm}	2.6 %	3.7 %
h_{eff}	14.5 %	18.6 %

A.2 Batch Reactor Model Parameter Estimates

A.2.1 Mass Transfer and Solubility Parameters

Table 19. Estimated mass transfer and solubility parameters as a function of temperature at different solid AC loadings

k_a^{l-g} (s^{-1})	**20g**	**30g**	**40g**	**Average**
55 °C	5.84E-05	2.06E-04	1.14E-04	1.60E-04
60 °C	3.39E-05	4.50E-05	4.37E-05	4.44E-05
70 °C	2.24E-05	2.13E-05	2.18E-05	2.15E-05
$x_{AC,sat}$	**20g**	**30g**	**40g**	**Average**
55 °C	2.62E-01	1.82E-01	1.82E-01	1.82E-01
60 °C	2.03E-01	1.57E-01	1.75E-01	1.66E-01
70 °C	4.99E-02	5.91E-02	5.91E-02	5.91E-02
k_{het} (s^{-1})	**20g**	**30g**	**40g**	**Average**
55 °C	2.99E-04	3.55E-04	3.50E-04	3.53E-04
60 °C	6.16E-04	1.78E-04	2.48E-04	2.13E-04
70 °C	1.25E-04	1.35E-04	1.35E-04	1.35E-04
k_{dis} (s^{-1})	**20g**	**30g**	**40g**	**Average**
55 °C	4.00E-06	4.46E-06	5.02E-06	4.74E-06
60 °C	4.01E-06	1.46E-05	6.28E-06	1.04E-05
70 °C	4.58E-05	5.51E-05	5.50E-05	5.51E-05

A.2.2 Kinetic Parameters

Table 20. Estimated kinetic (rate and equilibrium coefficients) as a function of temperature at different solid AC loadings

$k_{f,\mathrm{hom}}$ (s^{-1})	**20g**	**30g**	**40g**	**Average**
55 °C	1.57E-03	3.26E-03	2.19E-03	2.19E-03
60 °C	2.49E-02	1.21E-02	1.41E-02	1.41E-02
70 °C	3.07E-02	3.43E-02	3.43E-02	3.43E-02
K_{hom}	**20g**	**30g**	**40g**	**Average**
55 °C	1.22E-05	1.91E-05	2.16E-05	2.16E-05
60 °C	4.70E-05	5.90E-05	9.71E-05	9.71E-05
70 °C	5.83E-04	8.80E-04	8.80E-04	8.80E-04
K_{het}	**20g**	**30g**	**40g**	**Average**
55 °C	2.69E-01	2.56E-01	2.47E-01	2.52E-01
60 °C	2.51E-01	1.64E-01	1.95E-01	1.80E-01
70 °C	6.04E-02	7.40E-02	7.40E-02	7.40E-02

A.3 Experimental Comparisons

A.3.1 Low Residence Time (10 s)

Table 21. Comparison between results of Johnson *et al.* [70] and HEX reactor model predictions for heat absorbed by endothermic reaction (Q_{rxn}) and heat transferred by convection (Q_L) ; 10 second residence time.

		Experiment [70]		Model	
c_i (g/L)	$T_{in,L}$ (°C)	Q_{rxn} (W)	Q_L (W)	Q_{rxn} (W)	Q_L (W)
22.1	80.1	470	2941	293	2405
31.7	80.1	627	3110	402	2427
49.5	80.0	850	3292	554	2536
48.5	80.0	716	3425	542	2687
45.5	80.0	700	3170	518	2496

A.3.2 High Residence Time (70 s)

Table 22. Comparison between results of Johnson *et al.* [70] and HEX reactor model predictions for heat absorbed by endothermic reaction (Q_{rxn}) and heat transferred by convection (Q_L) ; 70 second residence time.

		Experiment [70]		Model	
c_i (g/L)	$T_{in,L}$ (°C)	Q_{rxn} (W)	Q_L (W)	Q_{rxn} (W)	Q_L (W)
188	70.01	1078	1731	1128	1706
84.8	80.3	913	2004	1385	2331
169	79.9	1646	2504	1997	2854
211	80.2	2159	2900	2225	2894
221	89.99	3120	4095	3135	4213